

**STRUCTURE & DYNAMICS OF RADIONUCLIDE -
LIGAND-SOLVENT SYSTEMS IN THE FUEL
REPROCESSING: MOLECULAR DYNAMICS
SIMULATIONS STUDIES**

By

ARYA DAS

(ENGG01201604003)

BHABHA ATOMIC RESEARCH CENTRE, MUMBAI

A thesis submitted to the

Board of Studies in Engineering Sciences

In partial fulfilment of requirements

for the Degree of

DOCTOR OF PHILOSOPHY

of

HOMI BHABHA NATIONAL INSTITUTE



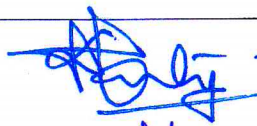
July 2021

Homi Bhabha National Institute

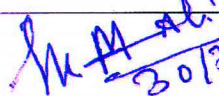
Recommendations of the Viva Voce Committee

As members of the Viva Voce Committee, we certify that we have read the dissertation prepared by Shri Arya Das entitled "Structure and Dynamics of Radionuclide-Ligand-Solvent systems in the Fuel Reprocessing: MD Simulation Studies" and recommend that it may be accepted as fulfilling the thesis requirement for the award of Degree of Doctor of Philosophy.

Chairman – Prof. D. K. Maity


30/07/2021

Guide / Convener - Prof. Sk. Musharaf Ali


30/7/2021

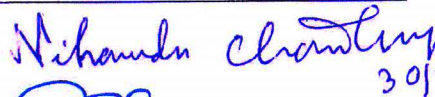
Examiner - Prof. V.G. Gaikar

THROUGH WEB
MEETING

Member 1- Prof. A. Arya


30/07/2021

Member 2- Prof. N. Choudhury


30/7/21

Member 3- Prof. S. Mukhopadhyay


30/7/21

Final approval and acceptance of this thesis is contingent upon the candidate's submission of the final copies of the thesis to HBNI.

I/We hereby certify that I/we have read this thesis prepared under my/our direction and recommend that it may be accepted as fulfilling the thesis requirement.

Date: 30.07.2021

Place: Mumbai


30/7/2021

Signature
Guide

STATEMENT BY AUTHOR

This dissertation has been submitted in partial fulfilment of requirements for an advanced degree at Homi Bhabha National Institute (HBNI) and is deposited in the Library to be made available to borrowers under rules of the HBNI.

Brief quotations from this dissertation are allowable without special permission, provided that accurate acknowledgement of source is made. Requests for permission for extended quotation from or reproduction of this manuscript in whole or in part may be granted by the Competent Authority of HBNI when in his or her judgment the proposed use of the material is in the interests of scholarship. In all other instances, however, permission must be obtained from the author.



Arya Das

DECLARATION

I, hereby declare that the investigation presented in the thesis has been carried out by me. The work is original and has not been submitted earlier as a whole or in part for a degree / diploma at this or any other Institution / University.

Arya Das.

Arya Das

List of Publications arising from the thesis

Journals

(1) Molecular Dynamics Simulation for the Calibration of the OPLS Force Field Using DFT Derived Partial Charges for the Screening of Alkyl Phosphate Ligands by Studying Structure, Dynamics, and Thermodynamics.

Das, A.; Sahu, P. and Ali, Sk. M. *J. Chem. Eng. Data* **2017**, 62, 2280–2295.

(2) Molecular dynamics simulation for the test of calibrated OPLS-AA force field for binary liquid mixture of tri-iso-amyl phosphate and n-dodecane.

Das, A. and Ali, Sk. M. *The J. Chem. Phys.* **2018**, 148, 074502.

(3) Understanding of interfacial tension and interface thickness of liquid/liquid interface at a finite concentration of alkyl phosphate by molecular dynamics simulation.

Das, A. and Ali, Sk. M. *J. Mol. Liq.* **2019**, 277, 217–232.

(4) Molecular Dynamics Simulation Studies on Structure, Dynamics, and Thermodynamics of Uranyl Nitrate Solution at Various Acid Concentrations.

Das, A. and Ali, Sk. M. *J. Phys. Chem. B* **2019**, 123, 4571–4586.

(5) Unusual behaviour of Stokes–Einstein relation in liquid mixtures.

Das, A. and Ali, Sk. M. *AIP Advances* **2020**, 10, 045327.

Conferences

1. Free energy of solvation of ligands in polar and non-polar diluents using thermodynamic integration techniques; Das, A. and Ali, Sk. M.; *The Eighth Asia Pacific Conference in Theoretical and Computational Chemistry (APCTCC-8)*, **2017**, IIT Bombay.
2. Molecular dynamics simulation for the screening of composition of tri-isoamyl phosphate and dodecane for use in PUREX process; Das, A. and Ali, Sk. M.; *SESTEC*, **2018**, Goa, Maharashtra.
3. Determination of Limiting Concentration of Uranyl Nitrate Solution – Insight from MD Simulation and Experiment; Das, A. and Ali, Sk. M.; *DAE Computational Chemistry Symposium (DAECCS)*, **2019**, BARC, Mumbai.
4. Unusual Behavior of Slipping and Sticking Conditions in Liquid Phase; Das, A. and Ali, Sk. M.; *DAE Computational Chemistry Symposium (DAECCS)*, **2019**, BARC, Mumbai.
5. Molecular Dynamics Simulations on Interfacial Structure in Presence of Third Component; Das, A. and Ali, Sk. M.; *Molecular Simulations of Complex Fluids and Interfaces (MOLSIM)*, **2020**, IIT Kanpur.
6. Unusual behavior of Stokes-Einstein relation in liquid phases; Das, A. and Ali, Sk. M.; *Statistical Mechanics in Chemistry and Biology (SMCB 2021)*, **2021**, IIT Tirupati, IIT Goa & IISER Tirupati.

DEDICATED
TO
MA & BABA

ACKNOWLEDGEMENTS

Standing near the shore after a long four years voyage, I commence to contemplate about my PhD expedition in theoretical computational chemistry. In the very beginning, I would like to thank Almighty for the kindness by fulfilling me in such an extent in every aspects of my life by simply overlooking the fact that I don't worthy for all these. Herby, I gracefully accept that I am a person with limited capabilities both as a student and a person. Thus, I owe to everyone who directly or indirectly helped me during this journey. Expression of the gratitude by words about my own feeling is not possible because I am highly indebted and no word is simply sufficient to articulate my emotion towards each and every one of them.

First and foremost, I would like to thank my PhD guide Prof. Sk. Musharaf Ali without him it would never ever be possible for me to even begin this work. I express my sincere gratitude to them for offering me the opportunity to work in their research group. I am deeply indebted to them for their continuous inspiration, never ending guidance, infinite patience, unconditional help and extraordinary trust on me in difficult phases of my life.

I am also thankful to Mr. K. V. Ravi (CE, Nuclear Recycle Board) and Mr. H. R. Pimparkar (GM, INRPRD, Nuclear Recycle Board) for their guidance and enthusiastic support during my PhD. I am deeply grateful to Mr. K. Jayanarayan, Mrs. Bidisha Mitra Biswas, Mr. Soumya Sarkar for their continued inspiration during this journey. I express my deep gratitude towards Mr. Amitava Roy (former CE, Nuclear Recycle Board), Mr. DAS Rao (former GM, INRPRD, NRB) and Mrs. Lata Mishra (former AGM, INRPRD, NRB) for getting opportunity and their important supports. I would specially thank to Dr. Ashish Kr. Singhadeb, Mrs. Puja Sahoo, Mr. Sandip Bhowmick and Dr. Anil Boda for unconditional help, inspiration and encourage all the time. I would like to thank all the members of Nuclear Recycle Board for their constant help and encouragement and sharing their vast knowledge

with me. It is a great pleasure to thank all the members of the doctoral committee Prof. D. K. Maity (chairman), Prof. A. Arya (member), Prof. N. Choudhury (member), Prof. Sulekha Mukhopadhyay (member) for their guidance and help throughout this journey. I would also like to thank Raghuda, Mondalda, Sabyada, Arkada, Sourav, Sanat, Deboda, Avikda, Tipu, Soumen, Abhijit, Srijit and Rahul for their help and constant encouragement.

I would like to express my deepest gratitude to my ma (Mrs. Bijali Das), my baba (Mr. Sibananda Das) and my sister (Miss Ananya Das) for giving me unconditional support, endless sacrifice, relentless motivation and boundless love. There is no word in the dictionary which can express my parent's devotion in the making of us. I can only say that whatever I am today is just because of them. Thank you God for blessing me with such wonderful parents.

I would like to extend my gratitude and affection towards my family members. I would like to express my deep gratitude to my mother in law (Mrs. Shivani Das). Last but not the least I would like to thank my wife (Mrs. Gargi Das) for all her efforts and sacrifice. Our family life completes a mini-cycle with the arrival of my son (Mr. Souharda Das).

There are many others, who have provided support and inspiration in this wonderful reward journey. I should be excused since I cannot list them all here but I am grateful to all of them.

The very fact that I am getting the opportunity to write this acknowledgement as a part of PhD thesis is due to my teacher and my mentor Dr. Sk. M. Ali, who appeared in my life as a ray of light in a room full of darkness and changed my perception not only in the field of science but also in day to day real life. There are no words to put my emotion towards him, I can only say thank you for appearing as guide, philosopher and friend.

Arya Das

CONTENTS

	Page No.
SUMMARY	i
SYNOPSIS	iii
LIST OF FIGURES	xix
LIST OF TABLES	xxix
Chapter 1 Introduction	1
1.1 Indian Nuclear Power Program & Nuclear Fuel Cycle	1
1.2 Nuclear Fuel Cycle	4
1.3 TBP As Ligand In Reprocessing Application	8
1.4 Selection of Novel Ligand Or Alternative Of TBP	9
1.5 Necessity of Simulation	10
1.6 Background & Motivation Of Thesis	12
1.7 Objective of Thesis	13
1.8 Structure of Thesis	14
Chapter 2 Model & Methodology	17
2.1 Introduction To Molecular Dynamics Simulation	17
2.2 Model & Methodology	21
2.3 Statistical Mechanics	27
2.4 Time Average (Method of Boltzmann)	28
2.5 Ensemble Average (Method of Gibbs)	29
2.5.1 Canonical Ensemble (NVT)	30
2.5.2 Isothermal-Isobaric (NPT) Ensemble	31
2.6 Selection Of Partial Charge Model	32
2.7 Pair Correlation Function	34
2.8 Self-Diffusion Coefficient	35
2.9 Free Energy Of Hydration & Solvation	36
2.10 Partition Coefficient	37
2.11 Free Energy Of Extraction	39
2.12 Dipole Moment	39

2.13	Shear Viscosity	40
2.14	Interfacial Tension (IFT)	42
2.15	Interface Thickness Or Width (IFW)	43
2.16	Surface Tension	44
2.17	Water Transport In Organic Phase	45
2.18	Hydrogen Bond Dynamics	46
Chapter 3	Calibration of Force Field & Screening of Ligand	49
3.1	Introduction	49
3.2	Simulation Systems	50
3.3	Results & Discussion	51
3.3.1.	Liquid state structure of the ligands and the solvents	51
3.3.2.	Mass density of the pure ligands and solvents	53
3.3.3.	Pair correlation function (PCF) of pure liquid TBP, TiAP and TEP	58
3.3.4.	Dynamical properties of liquid TBP, TiAP and TEP: Diffusion coefficient	65
3.3.5	Free Energy of Solvation of TBP, TiAP and TEP in Aqueous and Organic Environment	69
3.3.6.	Partition coefficient (P) of TBP, TiAP and TEP in water-dodecane bi-phasic system	72
3.3.7.	Liquid state dipole moment of TBP, TiAP and TEP	74
3.3.8	Heat of vaporisation	76
3.3.9.	Application to nuclear fuel cycle	76
3.3.10.	Free energy of extraction of UO_2^{2+} ion in water-dodecane system using DFT/COSMO-RS approach	78
3.4	Summary	79
Chapter 4	Test of Calibrated Force Field in Binary Mixture	81
4.1	Introduction	81
4.2	Simulation Systems	84
4.3	Results & Discussion	86
4.3.1.	Structure of the pure liquids and mixtures	86
4.3.2	Dipole moment of TiAP/n-dodecane mixture	86

4.3.3	Mass density of TiAP/dodecane mixture	88
4.3.4	Excess volume of mixing	92
4.3.5	Diffusion coefficient of binary mixture	94
4.3.6	Pair Correlation Functions (PCFs)	97
4.3.7	Excess enthalpy of mixing of TiAP/ n-dodecane mixture	103
4.3.8	Shear viscosity	105
4.3.9	Selection of composition for binary mixture of TiAP and dodecane	109
4.3.10	Test of Stokes-Einstein relation in TiAP-dodecane mixture	112
4.4	Summary	113
Chapter 5	Interfacial Phenomena of Biphasic Mixture	115
5.1	Introduction	115
5.2	Simulation Systems	120
5.3	Results & Discussion	123
5.3.1	Water system	123
5.3.2	Pure nitric acid & 3M nitric acid system	125
5.3.3	Biphasic System	130
5.3.3a	Water–dodecane system	130
5.3.3b	Neutral water/ (TiAP + dodecane) system	132
5.3.3c	Acidic water/ (TiAP + dodecane) system	143
5.3.4	Relation between interface thickness and interfacial tension	150
5.3.5	Preferential orientation of TiAP at the interface	159
5.3.6	Water Solubility in TiAP/dodecane System	160
5.4	Summary	162
Chapter 6	Structure & Dynamics of Uranyl Nitrate Solution	165
6.1	Introduction	165
6.2	Simulation Systems	169
6.3	Experimental Procedure	172
6.3.1	Solution preparation	172
6.3.2	Density measuring principle	172
6.3.3	Dynamic light scattering (DLS) experiments	173
6.4	Result & Discussion	173

6.4.1. Type 1: Uranyl ion in water	173
6.4.2. Type 2: Uranyl nitrate in 3M nitric acid	185
6.4.3. Type 3: Uranyl nitrate in varying nitric acid concentrations	207
6.6 Summary	217
Chapter 7 Conclusions & Future Work	219
7.1 Conclusions	219
7.2 Future Work	225
REFERENCES	227
APPENDIX	I-VIII

SUMMARY

Molecular dynamics (MD) simulations were performed to calibrate the all atom optimized potential for liquid simulations (OPLS-AA) force field using partial quantum charges calculated from four different population analysis methods: Mulliken, Löwdin, NPA and ChelpG for predicting the structural, thermodynamical and dynamical properties of pure liquid like tri-n-butyl-phosphate (TBP), tri-iso-amyl-phosphate (TiAP) and tri-ethyl-phosphate (TEP) and dodecane to determine the potential ligand-solvent system for nuclear fuel cycle. The calculated structural and dynamical properties were affected by the different atomic partial charges on TBP, TiAP and TEP which are reflected on the estimated physical and dynamical properties and Mulliken population analysis with OPLS force field found an excellent agreement with the experimental data. The diffusivity and the pair correlation function (PCF) for all the ligands have been calculated and validated. Free energy of hydration and solvation for all the ligands were evaluated using thermodynamic integration (TI) method indicates TiAP is more hydrophobic and more partitioning in dodecane among the other ligands and also compared with the experimental value. The partition coefficient of the ligands calculated from MD simulations using free energy difference between water-dodecane systems resembles the trend predicted by DFT/COSMO-RS calculations and found TiAP has better partitioning. Furthermore, the superiority of TiAP over TBP for the extraction of uranyl (UO_2^{2+}) ion has been demonstrated by free energy of extraction using DFT/COSMO-RS calculations. The studies were further extended on the various molecular properties of TiAP and TiAP/dodecane binary mixture with different composition of TiAP-dodecane mixture using MD simulations. The excess volume of mixing was found to be positive for the entire range of mole fractions and the excess enthalpy of mixing was shown to be endothermic for TBP/dodecane mixture as well as TiAP/dodecane mixture as reported experimentally. The spatial pair correlation functions (PCFs) are evaluated between TiAP–TiAP and TiAP–dodecane molecules. Further, shear viscosity has been

computed by performing the non-equilibrium molecular dynamics (NEMD) employing periodic perturbation method. The effective composition of binary mixture is also decided based on the dynamic properties for efficient extraction. The simulation results demonstrate that Stokes-Einstein (SE) relation breaks down at the molecular level. Additionally, the works were extended on the simple and complex biphasic systems to evaluate the interfacial properties like interface structure, interfacial tension, interface thickness using MD simulations. Total interface thickness is found increasing with mole fraction of TiAP and decreasing with acid molarities. The interfacial tension is found to be decreased with increasing mole fraction of TiAP whereas increased with the acid concentrations. The inverse relation between interface thickness and interfacial tension has been established. The surface tension computed from pressure tensor was found to be in excellent agreement with the experimental results, which is then used to determine the interface thickness employing capillary wave theory (CWT) using a simple scheme of finding the bulk correlation length by adopting COSMO-RS. Furthermore, a simple equation has been obtained by fitting the MD simulation results of total interface thickness for a wide range of composition of third component. The optimum selection of mole fraction of TiAP and the aqueous phase acidity has been decided for metal ion extraction system. In addition to that, the structural and dynamical behaviour of uranyl ion in water has been investigated by performing MD simulations using different force fields. The super-saturation effect has been captured by an inflection in the plot of surface tension and shear viscosity against concentration due to the solution heterogeneity which was correlated by an inflection in the scattering intensity observed by performing dynamic light scattering (DLS) experiment. Finally, the breakdown of Stokes-Einstein relation has been also found for acidic uranyl nitrate solution which followed far sticking boundary condition. Hence, the versatility of single force field has been established and the efficient biphasic system can be designed from the studies of binary mixture, biphasic mixture and the interfacial properties.

SYNOPSIS

Among the various sources of energy, nuclear energy shares ~15-20% of the total energy consumption worldwide. In view of the growing energy demand, fission-based nuclear power will play a vital role in meeting this need. One aspect of nuclear power that still provides significant technical challenges is the management of irradiated nuclear fuel (fuel discharged from a nuclear reactor after its utilization).¹ The management of continuously increasing used nuclear fuel in large volumes which contains un-burnt uranium, fissile plutonium, transuranic actinides and fission products (FP), necessitates the development of an effective and selective methodology to reuse fissile content by separating actinides and FP.^{2,3} Reprocessing is the series of processes for separation of uranium and plutonium from the FP and transuranic actinides in back-end operation. The radionuclides present in spent fuel should be reprocessed for its safe disposal. The reprocessing of used nuclear fuel is of practical interest not only to reduce the high-active solid waste but also to produce the fresh fuel for 2nd generation nuclear reactor which can give dependable supply of fuel.²⁻⁶ The decay of radiotoxicity of the spent fuel needs several thousand years to reach its natural level.⁷ Hence, spent fuel reprocessing is also important to remove the radionuclide from the waste so that the time required to reach an acceptable activity level will be minimized.

Various conventional separation processes are available but they are not suitable due to high temperature and pressure, difficult to manage the generated waste and needs much effort to get product in desired form. Besides this, some non-conventional and non-traditional processes are also developed by resolving various issues present in the conventional processes. But again, they are not well established. So, among the well-established processes the solvent extraction is the best choice for reprocessing.

The key role of the solvent extraction technologies is the selective transfer of valuables between aqueous and organic phases using liquid phase contractor.^{8,9} Liquid – liquid extraction based technology is used to address the fuel reprocessing. The extent of reprocessing depends on the efficiency of the liquid-liquid extraction processes which are widely used for separation and recovery of radionuclide from spent nuclear fuel. Further, the extraction method includes two immiscible liquids, mainly one aqueous phase which contains the metal ions and other is the organic phase consists of a mixture of a suitable ligand and a solvent. In this context, the most commonly practised extraction process is PUREX (Plutonium Uranium Recovery by Extraction) where the metal ions are extracted by organic ligand from acidic feed solution. Initially, the used nuclear fuel undergoes de-cladding and dissolution processes. The irradiated fuels containing fissile and fertile materials, have been chopped in small pieces and then dissolved in 12M boiling nitric acid to prepare the nitrates of Uranium (U) and Plutonium (Pu) which has been used as feed solution.¹⁰

This liquid – liquid extraction process is a multi-stage and multi-solute process which possesses several challenges for modelling the extraction phenomena and also for understanding the processes from molecular level. The most commonly used extractant molecules in solvent extraction process are organo-phosphorus ligands which bind the metal ions via their phosphoryl group. TBP (tri-n-butyl phosphate) is the most popular one used with n-dodecane as an inert solvent and commonly used as diluent for TBP¹¹ and also thoroughly understood extracting agent among the organo-phosphorus ligands because of its pivotal role in various stages of nuclear fuel cycle.^{9,11,12} TBP has advantages of the (1) adequate extraction power for uranium and plutonium, (2) good selectivity for uranium and plutonium in comparison to the elements present in the fission products, (3) amenability to stripping with dilute nitric acid, and (4) good phase separation. TBP makes

complexes selectively with Uranium and Plutonium.³⁻⁹ 30% TBP/n-dodecane ligand-solvent composition is used universally for recovery of uranium and plutonium from spent nuclear fuels.

Although TBP is widely used in industrial scale also, it has some inherent limitations. For the reprocessing of fast reactor fuel involving Plutonium (Pu) rich spent fuel with high level of radioactivity, TBP has the limitation of third phase formation at high metal loading.¹³ Also, the separation process is interfered by the formation of degradation products principally DBP (di-butyl phosphate) and MBP (mono-butyl phosphate) by radiological and chemical effects on TBP which reduces the fission product decontamination factor (DF). The fuel reprocessing is also affected by the significant aqueous solubility of TBP. So, this is high time to think of alternative of TBP to pursue the reprocessing of fast reactor as well as thermal reactor fuel.

There is continuing search of an alternative novel ligand which has the merits of TBP and at the same time overcomes the above mentioned demerits of TBP. Suresh *et al* discussed the effect of elongation of alkyl chain and introduction of branching on alkyl group of phosphate ligand on extraction process.⁸ Sometimes branching on first carbon atom significantly alters the extraction efficiency or the mutual solubility of water. Among many synthesized ligands, tri-iso-amyl phosphate (TiAP) has been shown to be quite promising. In recent past many researchers reported that TiAP, a homologous of TBP, is a potential ligand in many aspects: such as TiAP has the lesser tendency towards third phase formation for extraction of tetravalent actinides, lower aqueous solubility (0.019 kg/m^3) compared to TBP (0.40 kg/m^3), high extraction ability and better resistance to degradation.¹⁴ Sreenivasulu and co-workers carried out the radiolytic degradation studies on TIAP and they reported that the degradation behaviour of TiAP is similar to TBP and TiAP can be used as potential extractant because of its lower third phase formation

tendency and lower aqueous solubility.¹⁵ Again, mixture settler experiments have been carried out by Suresh and co-workers with TiAP as an extractant for reprocessing applications and they reported that TiAP can be used as alternate extractant over TBP for both fast reactor and thermal reactor fuel reprocessing.¹⁶ So, TiAP might be a replacement of TBP and is being used for thermal reactor fuel reprocessing as well as fast reactor fuel reprocessing.¹⁷⁻¹⁹ In addition to that the experimental studies also confirm the similar potentiality of TiAP in extraction, scrubbing and stripping and it mitigates the limitations.^{16,17, 19-21} Moreover, TiAP has more thermal resistant compared to TBP when red oil formation is concerned. TiAP found to be safer under drastic temperature and concentrated acid conditioning process evaporator. Again, Das and co-researcher also confirmed from the TGA test that the red oil prepared from TiAP is absence of exothermic reaction during heating from 30°C to 200°C which indicates TiAP is safer than TBP.²² The extraction behaviour of U(VI) from nitric acid medium using 1.1M TiAP/n-dodecane as solvent along with scrubbing and stripping behaviour of U(VI) also have been investigated and found that both the TBP and TiAP ligands are comparable.¹⁹ Again, the extraction behaviour of Th(IV) from nitric acid medium was also studied using TiAP – KO as extractant and a good separation factor [$D_{U(VI)}/D_{Th(IV)}$] of 88.25 was reported at 6M HNO₃. The extraction of U(VI) by TiAP was an exothermic process whereas the extraction of Th(IV) was an endothermic process. It was also noted that the stripping of U(VI) from TiAP organic phase was comparatively easier than that of Th(IV).¹⁸ Further, the cost of TBP and TiAP are also very similar.²³⁻²⁴ Hence, TiAP is shown to be comparatively better ligand over TBP in reprocessing applications.

In order to predict and explain the behaviour of proposed ligands to develop an efficient extraction system, one can pursue either the experimental or theoretical route. From an experimental point of view, though one can get very accurate predictions but one should

have laboratory infra-structure, radionuclide handling system and chemicals which are quite expensive and time consuming also. Even it sometimes can be completely impossible or dangerous also to measure what is desired. The complementary alternative to experiment is the use of computational techniques like: molecular dynamics (MD) simulations and Quantum electronic structure calculations (QESC), which are principle tools for theoretical studies in biological as well as in chemical molecules. This computational method calculates the time dependent behaviour of a molecular system based on Newton's laws of motion. Molecular dynamics simulations have evolved into a mature technique that can be used effectively to understand macromolecular structure-to-function relationships. These methods are now regularly used to investigate the microscopic structure, dynamics and thermodynamics of biological or chemical molecular systems and their complexes.

A wide range of chemical/physical processes can be modelled using MD simulation²⁵ which help in planning the experiments and thus reduce the cost and time of experiments. So, elaborate molecular dynamic simulations studies are required to establish the liquid – liquid extraction processes with TiAP as an extractant for implementation and to address the issues in commercial scale. Therefore, a detailed investigation on the structural and thermo-physical properties of these ligands and the related dynamical and thermodynamic properties for the metal ion extraction is of utmost necessary for which molecular level studies are essential to predict structural and thermo-physical properties with an aim to have better understanding of the extraction process.

Therefore, MD simulations were conducted for pure TBP, TiAP, TEP (belongs to alkyl phosphate group) and dodecane to determine the various structural, thermodynamical and dynamical properties.²⁶⁻²⁷ The accuracy of physical and dynamical properties strongly depends on the performance of force field and it is very crucial to select the good one

which can able to arrest all the properties. Though tri-ethyl phosphate (TEP) has not been reported in the literature for its use as metal ion extractant, few experimental values related to thermo-physical properties are available for TEP which are useful to calibrate the atomistic force field.

Thus, the present thesis reports the force field for the pure ligands based on the calculation of physical and dynamical properties. For calibration of force field, four types of atomic charge models have been used. They are Mulliken, Löwdin, NPA (orbital population analysis methods) and ChelpG (a grid based method using electrostatic potential). Along with the calibration of force field, the comparative studies of ligands have been done to find out an efficient ligand for liquid-liquid extraction process. Subsequently, the calibrated force is to be tested for TiAP/dodecane binary mixture to see whether the single force field is able to capture all the physical and dynamical properties of binary mixture using MD simulations. Next, the compatibility of developed force field has been checked for water – TiAP/dodecane biphasic mixture by computing respective properties at liquid – liquid interface as third goal. In addition to that an attempt has been made for the calculation of total and intrinsic interface thickness for simple as well as complex biphasic mixture using the concepts of QM, MD and statistical mechanics. The versatility of single force field is the main attraction of the current studies. Further, the effect of partial charges on the structural and dynamical properties of actinides in water and then to calculate the various structural and dynamical properties of uranyl nitrate in acidic medium with wide range of uranyl nitrate as well as acid concentration. The MD simulation studies of aqueous feed solution at various uranyl nitrate concentration have been carried out to understand the limiting concentration of uranyl nitrate in feed solution used in PUREX process. The overall thesis is composed of seven chapters and a brief discussion of each chapter is given below.

Chapter 1:

This chapter deals with a general introduction about demand of nuclear energy and associated irradiated nuclear fuel reprocessing and the role of ligand-solvent system in the field of extraction of radionuclides from spent nuclear fuel. It includes necessity of molecular modelling and simulations for process parameters optimization, the motivation behind the thesis, objectives and scope of thesis.

Chapter 2:

This Chapter deals with model and methodology used in the present thesis to perform the molecular dynamics simulations studies of the chemical species involved in the PUREX process. It also includes the methodology of statistical mechanics for determination of various thermophysical, dynamical and thermodynamical properties of liquid phases (pure liquids, mixture of organic liquids and mixture of aqueous solution).

Chapter 3:

The main objective of this chapter is to calibrate the OPLA – AA force field and screening of ligand. In Chapter 3, molecular dynamics (MD) simulations were performed to calibrate the all atom optimized potential for liquid simulations (OPLS-AA) force field using partial quantum charges calculated from four different population analysis methods: Mulliken, Löwdin, NPA (Natural population analysis) and ChelpG (CHarges from ELectrostatic Potentials using a Grid-based method) for predicting the thermophysical properties of pure liquid like tri-n-butyl-phosphate (TBP), tri-iso-amyl-phosphate (TiAP) and tri-ethyl-phosphate (TEP) and dodecane to determine the potential solvent for nuclear fuel cycle. The calculated structural and dynamical properties were affected by the different partial charges on TBP, TiAP and TEP. The Mulliken embedded force field was found better

among the others based on the estimation of liquid density, diffusivity, structural parameters and dipole moment. The accuracy of developed force field is checked by calculating the heat of vaporization, free energy of hydration and solvation and partition coefficient and the calculated values are in excellent agreement with available experimental values. Free energy of hydration and solvation for all the ligands were evaluated using thermodynamic integration (TI) technique and TiAP exhibits higher hydrophobic nature and higher degree of partitioning in organic phase which is suitable as a ligand for solvent extraction. Furthermore, the partition coefficient of the ligands have been calculated from MD using free energy and from QM using DFT/COSMO-RS method and found better partitioning for TiAP. So, the lesser density, lower solubility, higher partitioning and higher dipole moment compared to TBP and TEP indicates TiAP may be the suitable ligand for nuclear applications. Finally, the superiority of TiAP over TBP as extracting agent for UO_2^{2+} ion has been demonstrated by higher calculated free energy of extraction using DFT. Overall the Mulliken charge embedded calibrated OPLS-AA force field is perhaps the most reliable one for evaluation of the liquid state properties of pure alkyl phosphates and n-alkanes.²⁸

Chapter 4:

Tri-isoamyl phosphate (TiAP) has been proposed to be an alternative for tri butyl phosphate (TBP) in PUREX process. TiAP like TBP also cannot be used in pure form due to its high viscosity and hence a diluent is mixed at appropriate composition to make it suitable for solvent extraction. Hence, the objective of Chapter 4 is to test the developed force field in TiAP/n-dodecane and TBP/n-dodecane binary mixture and to determine the suitable composition of binary mixture which can be used for metal ion extraction. Therefore, the MD simulations have been carried out to understand the structural, dynamical and thermodynamical properties with different mole fraction of TiAP-dodecane

and TBP-dodecane binary mixture at the entire range of mole fraction of 0 to 1 employing our calibrated Mulliken embedded OPLS force field. The calculated electric dipole moment of TiAP was seen to be almost unaffected with the TiAP mole fraction. The calculated liquid densities of TiAP-dodecane mixture with the effect of mole fraction and temperature are in good agreement with the experimental data which signifies the accuracy of force field and simulation methods. The excess volume of mixing was found to be positive for the entire range of mole fraction and the excess enthalpy of mixing was shown to be endothermic as reported experimentally. The diffusivities for TiAP and dodecane against mole fraction in the binary mixture intersect at a composition in the range of 25-30% of TiAP in dodecane. Further, shear viscosity has been computed by performing the non-equilibrium molecular dynamics (NEMD) and found excellent agreement with the experimental values. The diffusivities and shear viscosities of TiAP against mole fraction also intersect in the range of 20 – 30% composition. Both are very much closer to the TBP/n-dodecane composition used in the PUREX process. Finally, the objective is fulfilled by establishing that the Mulliken embedded force field is equally reliable for the binary mixture without incorporating any arbitrary scaling in the force field and also suggests the suitable composition of binary mixture. Further, the present MD simulations results demonstrate that Stokes-Einstein (SE) relation breaks down for the organic mixture.²⁹

Chapter 5:

The objective of this chapter is to apply the Mulliken embedded force field in simple and complex biphasic system and to understand the interfacial properties which are responsible for metal-ligand complex formations and its transport through interface. For this reason, the physical properties at the interface like interface structure, interfacial tension, interface thickness have been studied for a wide range of mole fraction of TiAP and with various

aqueous phase acidity. The interface thickness has been investigated in the presence of finite concentration of third component, a lipophilic ligand, tri-isoamyl phosphate (TiAP) and nitric acid employing MD simulations. The interface thickness is an increasing function of mole fraction of TiAP and a decreasing function of acid concentration. The interfacial tension computed from pressure tensor method is exhibiting the opposite effect. The inverse relation between interface thickness and interfacial tension has been established which is similar to the capillary wave theory (CWT) which relates the interface thickness and interfacial tension for two component system. The two component methodology of CWT is also applicable for three component system using weighted average scheme of finding the bulk correlation length by adopting conductor like screening model for realistic solvents (COSMO-RS). Furthermore, a simple equation has been obtained by fitting the MD results of total interface thickness for a wide range of composition of third component. The value of interface thickness calculated from the model equation was found to be in good agreement with the available experimental and MD results for a wide variety of oil-water biphasic systems. In addition to that the P=O-P=O dimer of TiAP has been found more stable among the other orientations based on the calculation of dimerization energy using DFT and also captured in the MD simulations. Furthermore, the present MD data shows that the water extraction is enhanced at higher mole fraction of TiAP because of wider interface thickness at higher composition of TiAP whereas decreased at higher aqueous phase acidity due to lower interface thickness. So, the present chapter concludes the proper optimization in composition of TiAP/dodecane and aqueous phase acidity leads to an efficient extraction system for partitioning of metal ions.³⁰

Chapter 6:

The structural and dynamical characteristics of uranyl ion in aqueous acidic environment are of immense importance in the field of nuclear fuel reprocessing. In this context,

different atomic partial charges have been used to parameterize the force field in the last few decades. The objective of Chapter 6 is whether the different charge models are really required to understand the uranyl ion in water system or whether the partial charges have an important implication on the physical and dynamical properties and finally what will be the right choice. The second objective is to perform MD simulations with the screened force field and to calculate the various structural and dynamical properties of uranyl nitrate in acidic medium with wide range of uranyl nitrate as well as acid concentration to model the PUREX process more realistically. It has been found that all the models have depicted similar structural and dynamical properties except the free energy of hydration where the Gulibaud-Wipff (GW) model performs well over the others. The calculated density using MD simulations is found to be in excellent agreement with the measured experimental density which ensures the accuracy of the adopted GW force field. The calculated surface tension and shear viscosity are seen to be increased with uranyl nitrate concentrations. At higher concentration of about 4.0 moles/lit, super-saturation effect has been captured by an inflection in the plot of surface tension and shear viscosity against concentration due to the solution heterogeneity which was correlated by an inflection in the scattering intensity observed by performing dynamic light scattering (DLS) experiment. The binding mode of nitrate ions with uranyl ion is found to be concentration dependent and at higher concentration, it is predominantly mono-dentate. This chapter suggests the limiting concentration of uranyl nitrate in feed solution.³¹⁻³²

Chapter 7:

Finally, the work is briefly summarized and logically concluded in Chapter 7. The heart of conclusion is that the OPLS – AA force field calibrated with Mulliken atomic partial charges is capable to capture and explain all the thermophysical, dynamical and thermodynamical properties of pure liquids, binary mixtures and biphasic mixtures

successfully. So, our main objective of the thesis is the versatility of a single refined force field in the field of radionuclide – ligand – solvent systems pertaining to the fuel reprocessing is achieved. In addition to that TiAP is established as a potential alternative ligand of TBP which can be applied in thermal reactor as well as fast reactor fuel reprocessing. Favourable interfacial properties for metal ion transfer have been suggested and the characteristics of uranyl nitrate along with the limiting concentration of uranyl nitrate in feed solution have been established which useful informations are for fuel reprocessing. Next, the present work can be extended in the direction of extraction of heavy metals with the suggested composition of ligand – solvent system, multicomponent system to understand the co-extraction process, recovery of FP from the waste stream in near future.

References:

- 1) Zabunoglu, O. H., Reprocessing of long-cooled nuclear fuel: Process description and plant design. *Retrospective Theses and Dissertations* **1988**, Digital Repository @ Iowa State University, <http://lib.dr.iastate.edu>.
- 2) Lo, C. T.; Baird, M. H. I.; Hanson, C., *Handbook of Solvent Extraction*, New York : Wiley, ©1983.
- 3) Simpson, M. F.; Law, J. D., *Nuclear Fuel Reprocessing*, Idaho National Laboratory, February, **2010**.
- 4) Paiva, A. P.; Malik, P., Recent advances on the chemistry of solvent extraction applied to the reprocessing of spent nuclear fuels and radioactive wastes. *J. Radioanal. Nucl. Chem.* **2004**, 261, 485 - 496.
- 5) McKay, H. A. C.; Miles, J. H.; Swanson, The Purex Process. *In Science and Technology of Tributyl Phosphate, Vol III, Applications of Tributyl Phosphate in Nuclear*

Fuel Reprocessing; J. L.; Schulz, W. W.; Burger, L. L.; Navratil, J. D.; Bender, K. P., Eds.; CRC Press: Boca Raton, FL 1990; p 8 - 37.

6) Arm, S. T.; Bush, R. P.; McGurk, J. C., Concept for the Reduction of Waste Volumes from Nuclear Fuel Reprocessing. *Prog. Nucl. Energy* **1998**, 32, 389 - 396.

7) Piotr Mazgaj, P. D., Transmutation: reducing the storage time of spent fuel. *Journal of Power Technologies* **2014**, 94, 27 - 34.

8) Suresh, A.; Srinivasan, T. G.; Rao, P. R. V., The Effect of the Structure of Trialkyl Phosphates on Their Physicochemical Properties and Extraction Behavior. *Solvent Extr. Ion Exch.* **2009**, 27, 258 – 294.

9) Sawant, R. M.; Rastogi, R. K.; Chaudhuri, N. K., Study on the Extraction of U(IV) Relevant to PUREX Process. *J. Radioanal. Nucl. Chem.* **1998**, 229, 203 - 206.

10) Spent Nuclear Fuel Reprocessing Flow sheet. **June 2012**, NEA/NSC/WPFC/DOC (2012) 15, Organisation for Economic Co-operation and Development, NEA.

11) Schulz, W. W.; Navratil, J. D.; Bess, T. E., Eds. *Science and Technology of Tributyl Phosphate*; CRC Press: Boca Raton, FL, 1984; Vol. 1, 1984.

12) Wright, A.; Paviet-Hartmann, P., Review of Physical and Chemical Properties of Tributyl Phosphate/Diluent/Nitric Acid Systems. *Sep. Sci. Technol.* **2010**, 45, 1753 - 1762.

13) Chiarizia, R.; Jensen, M. P.; Borkowski, M.; Ferraro, J. R.; Thiyagarajan, P.; Littrell, K. C., Third Phase Formation Revisited: The U(VI), HNO₃-TBP, n-Dodecane System. *Solvent Extr. Ion Exch.* **2003**, 21, 1 - 27.

14) Hassan, S. H.; Shukla, J. P., Tri-iso-amyl phosphate (TAP): An Alternative Extractant to Tri-butyl Phosphate (TBP) for Reactor Fuel Reprocessing. *J. Radioanal. Nucl. Chem.* **2003**, 258, 563 - 573.

- 15) Sreenivasulu, B.; Suresh, A.; Rajeswari, S.; Ramanathan, N.; Antony, M. P.; Sivaraman, N.; Joseph, M., Physicochemical properties and radiolytic degradation studies on tri-iso-amyl phosphate (TiAP). *Radiochim. Acta.* **2017**, 105, 249 – 261.
- 16) Suresh, A.; Sreenivasulu, B.; Jayalakshmi, S.; Subramaniam, S.; Sabharwal, K. N.; Sivaraman, N.; Nagarajan, K.; Srinivasan, T. G.; Vasudeva Rao, P. R., Mixer-settler runs for the evaluation of tri-iso-amyl phosphate (TiAP) as an alternate extractant to tri-n-butyl phosphate (TBP) for reprocessing applications. *Radiochim. Acta.* **2015**, 103, 101–108.
- 17) Singh, M. L.; Tripathi, S. C.; Lokhande, M.; Gandhi, P. M.; Gaikar, V. G., Density, Viscosity, and Interfacial Tension of Binary Mixture of Tri-iso-amyl Phosphate (TiAP) and n-Dodecane: Effect of Compositions and Gamma Absorbed Doses. *J. Chem. Eng. Data* **2014**, 59, 1130 – 1139.
- 18) Kong, F.; Liao, J.; Ding, S.; Yang, Y.; Huang, H.; Yang, J.; Tang, J.; Liu, N., Extraction and Thermodynamic Behaviour of U (VI) and Th (IV) From Nitric Acid Solution With Tri-isoamyl Phosphate. *J. Radioanal. Nucl. Chem.* **2013**, 298, 651 – 656.
- 19) Rakesh, K. B.; Suresh, A.; Rao, P. R. V., Extraction and Stripping Behaviour of Tri-iso-amyl Phosphate and Tri-n-butyl Phosphate in n-Dodecane With U (VI) In Nitric Acid Media. *Radiochim. Acta.* **2014**, 102, 619 – 628.
- 20) Das, D.; Juvekar, V. A.; Roy, S. B.; Bhattacharya, R., Co-Extraction of U(VI) and HNO₃ Using TBP and its Higher Homologues TiAP and TEHP: Comparison of Equilibria, Kinetics, and Rate of Extraction. *Separation Science and Technology* **2015**, 50, 411 - 420.
- 21) Singh, D. K.; Garg, S. K.; Bharadwaj, R. K., Removal of Cr (VI) using tri-isoamyl phosphate. *Indian Journal of Chemical Technology* **2000** 7, 205 – 206.

- 22) Das, B.; Kumar, S.; Mondal, P.; Mudali, U. K.; Natarajan, R., Synthesis and characterization of red-oil from tri iso-amyl phosphate/n-dodecane/nitric acid mixtures at elevated temperature. *J Radioanal Nucl. Chem.* **2012**, 292, 1161 - 1171.
- 23) Suresh, A.; Brahmmananda Rao, C. V. S.; Srinivasulu, B.; Sreenivasan, N. L.; Subramaniam, S.; Sabharwal, K. N.; Sivaraman, N.; Srinivasan, T. G.; Natarajan, R.; Vasudeva Rao, P. R., Development of alternate extractants for separation of actinides. *Energy Procedia* **2013**, 39, 120 – 126.
- 24) Pal, K. K.; Mishra, S.; Mallika, C.; Mudali, U. K., Evolution in the physiochemical properties of alternate PUREX solvent on hydrolytic and chemical treatment. *Separation Science and Technology* **2017**, 52, 2715 - 2720.
- 25) Allen, M. P.; Tildesley, D. J., *Computer Simulation of Liquids*. Clarendon Press, Oxford, **1987**.
- 26) Ye, X.; Cui, S.; de Almeida, V. F.; Khomami, B., Interfacial Complex Formation in Uranyl Extraction by Tributyl Phosphate in Dodecane Diluent: A Molecular Dynamics Study. *J. Phys. Chem. B* **2009**, 113, 9852 – 9862.
- 27) Sahu, P.; Ali, S. M.; Shenoy, K. T., The Passage of TBP-Uranyl Complexes From Aqueous-Organic Interface To The Organic Phase: Insights From Molecular Dynamics Simulation. *Phys. Chem. Chem. Phys.* **2016**, 18, 23769 – 23784.
- 28) Das, A.; Sahu, P. and Ali, Sk. M., Molecular Dynamics Simulation for the Calibration of the OPLS Force Field Using DFT Derived Partial Charges for the Screening of Alkyl Phosphate Ligands by Studying Structure, Dynamics, and Thermodynamics. *J. Chem. Eng. Data* **2017**, 62, 2280 – 2295.
- 29) Das, A. and Ali, Sk. M., Molecular dynamics simulation for the test of calibrated OPLS-AA force field for binary liquid mixture of tri-iso-amyl phosphate and n-dodecane *J. Chem. Phys.* **2018**, 148, 074502.

- 30) Das, A. and Ali, Sk. M., Understanding of interfacial tension and interface thickness of liquid/liquid interface at a finite concentration of alkyl phosphate by molecular dynamics simulations. *J. Mol. Liq.* **2019**, 277, 217–232.
- 31) Das, A. and Ali, Sk. M., Molecular Dynamics Simulation Studies on Structure, Dynamics, and Thermodynamics of Uranyl Nitrate Solution at Various Acid Concentrations, *J. Phys. Chem. B* **2019**, 123, 4571 – 4586.
- 32) Das, A. and Ali, Sk. M., Unusual behaviour of Stokes–Einstein relation in liquid mixtures, *AIP Advances* **2020**, 10, 045327.

LIST OF FIGURES

Figure No.	Figure Caption	Page No.
Figure 1.1	Schematic of the three stage Indian Nuclear Energy Program	2
Figure 1.2	Flow diagram of open fuel cycle and closed fuel cycle	3
Figure 1.3	Flow chart for various applications of nuclear energy	4
Figure 1.4	Decay of radiotoxicity of fission products (FP) and transuranic actinides with time	5
Figure 1.5	Block diagram of PUREX process. FP - Fission product, SNF – Spent nuclear fuel, La – Lanthanides and An – Actinides.	7
Figure 2.1	Inputs to molecular dynamics simulations	19
Figure 2.2	Flow chart for molecular dynamics simulations	20
Figure 2.3	Schematic representation of TiAP and dodecane molecules with atom number	23
Figure 2.4	Typical diagram of rectangular simulation box extended towards z-direction used for calculation of surface tension of pure component	45
Figure 3.1	Optimized structures of ligand/solvent (red sphere: Oxygen atom; orange sphere: Phosphorous atom; grey sphere: Carbon atom and white sphere: Hydrogen atom)	51
Figure 3.2	Snapshot of equilibrated structure of pure (a) TBP (b) TiAP (c) TEP (d) Dodecane after 10ns simulation run (Red: Oxygen atom; Olive green: Phosphorous atom; Cyan: Carbon atom and Orange: Hydrogen atom).	52
Figure 3.3	Density profile of pure TBP, TiAP and TEP with time	53
Figure 3.4	Density profile of pure dodecane	57
Figure 3.5	Intermolecular pair correlation functions between the pairs of atoms of P – P, P – O and O – O for pure TBP, TiAP and TEP ligands. (a) PCF's of O – O atoms (b) PCF's of P – P atoms (c) PCF's of P – O atoms.	58

Figure 3.6	Intermolecular pair correlation functions between the pairs of atoms of P–P for different charged model of three ligands. (a) PCF's of P–P atoms of two TBP molecules (b) PCF's of P–P atoms of two TiAP molecules (c) PCF's of P–P atoms of two TEP molecules.	60
Figure 3.7	Intermolecular pair correlation functions between the pairs of atoms of P–O for different charged model of three ligands. (a) PCF's of P–O atoms of two TBP molecules (b) PCF's of P–O atoms of two TiAP molecules (c) PCF's of P–O atoms of two TEP molecules.	62
Figure 3.8	Intermolecular Pair Correlation functions between the pairs of atoms of O – O for different charged model of three ligands. (a) PCF's of O – O atoms of two TBP molecules (b) PCF's of O – O atoms of two TiAP molecules (c) PCF's of O – O atoms of two TEP molecules.	63
Figure 3.9	Plot of PCFs between the pairs of atoms of C–C of dodecane after 10ns production run in NVT	64
Figure 3.10	MSD profiles of Pure TBP, TIAP and TEP liquids and their respective molecular structures.	65
Figure 3.11	MSD profiles of TBP, TiAP and TEP for four different charge models illustrating the partial charges on atom has significant dependency on MSD	66
Figure 3.12	MSD profile of dodecane after 10ns production run in NVT	68
Figure 3.13	The calculated free energy of hydration and solvation in water and dodecane respectively for three ligands illustrating the energy gap between hydration and solvation.	70
Figure 3.14	Free energy change (ΔG) for TiAP, TBP and TEP as a function of coupling parameter (λ) evaluated using thermodynamic integration in (a) water as free energy of hydration and (b) dodecane as free energy of solvation.	71
Figure 3.15	Optimized structures of complexes of (a) $\text{UO}_2(\text{NO}_3)_2(\text{TiAP})_2$ and (b) $\text{UO}_2(\text{NO}_3)_2(\text{TBP})_2$	78
Figure 4.1	Snapshot of (a) pure TiAP, (b) pure dodecane and (c) 50% TiAP/dodecane mixture after the production run in NVT. Red: TiAP, Blue: Dodecane.	86

Figure 4.2	Dipole moment of TiAP as a function of the mole fraction	87
Figure 4.3	Density of TiAP and dodecane as a function of time	88
Figure 4.4	Density of binary mixture as a function of the mole fraction of TiAP	89
Figure 4.5	Calculated and experimental density of pure TiAP as a function of temperature	90
Figure 4.6	Effect of temperature on density of TiAP-dodecane mixture with various compositions	91
Figure 4.7	Excess volume of mixing of the TiAP/dodecane mixture as a function of mole fraction of TiAP	93
Figure 4.8	(a) MSD of TiAP and (b) MSD of dodecane in TiAP/dodecane binary mixture	95
Figure 4.9	MSD of TBP in TBP/dodecane binary mixture	97
Figure 4.10(a)	Pair correlation function of P – P atoms of two interacting TiAP molecules	98
Figure 4.10(b)	Pair correlation functions of P – O atoms of two interacting TiAP molecules	100
Figure 4.10(c)	Pair correlation functions of O – O atoms of two interacting TiAP molecules	100
Figure 4.10(d)	Trend of the first peak appeared in PCF of P – P atoms as a function of mole fraction of TiAP	101
Figure 4.11	Pair correlation functions of (a) P – C atoms of two interacting TiAP and dodecane molecules and (b) O – C atoms of two interacting TiAP and dodecane molecules	102
Figure 4.12	Behaviour of the first peak height in the PCF between P-C atoms and between O-C atoms as a function of mole fraction of TiAP	103
Figure 4.13	Excess enthalpy of mixing of (a) TBP/dodecane binary mixture and (b) TiAP/dodecane binary mixture	104
Figure 4.14	Shear viscosity of TBP as a function of external force in NEMD	105

Figure 4.15	Shear viscosity of (a) TBP/dodecane binary mixture as a function of mole fraction of TBP in dodecane and (b) TiAP/dodecane mixture as a function of mole fraction of TiAP in dodecane.	107
Figure 4.16	Shear viscosity of TiAP/dodecane binary mixture with corresponding density of the mixture.	109
Figure 4.17	Diffusivity of binary mixture as a function of mole fraction	110
Figure 4.18	Diffusivity of TiAP and shear viscosity of TiAP-dodecane mixture as a function of density of the mixture	111
Figure 4.19	Plot of product of diffusivity and shear viscosity of (a) TiAP/dodecane mixture as a function of mole fraction and (b) TBP/dodecane mixture as a function of mole fraction of TBP in dodecane.	112
Figure 5.1	A typical biphasic simulation box containing TiAP in dodecane as organic phase and water as aqueous phase. The colour code and number of molecules for liquids are followed as red: water – 3000 molecules, blue and red: TiAP – 100 molecules and cyan: dodecane – 400 molecules.	121
Figure 5.2	(a) Density profile and liquid structure of Water (SPC/E Model). Oxygen: Red balls and Hydrogen: Olive balls and (b) Plot of intermolecular pair correlation function between pairs of atoms of OW – OW, OW – HW, HW - HW of two water molecules.	125
Figure 5.3	Density profile and liquid structure of (a) Dissociated form of pure nitric acid: H_3O^+ - Blue balls, NO_3^- - Red balls, (b) Associated form of pure nitric acid: O-Red balls, N-Blue balls and H-Orange balls and (c) 3M nitric acid. O: Red balls, N: Blue balls, H: Orange balls and Water: Cyan dots.	127
Figure 5.4	Plot of intermolecular pair correlation function between pairs of atoms of NA – NA, OA – OA, HA - HA of two nitric acid molecules of pure nitric acid.	127
Figure 5.5	Plot of intermolecular pair correlation function for 3M nitric acid (a) PCFs between pairs of atoms of NA – NA, OA – OA, HA - HA of two nitric acid molecules and (b) PCFs between water and acid molecules of OA – OW, OA – HW, HA – OW and HA – HW pairs of atoms.	129

Figure 5.6	Density profile of water–dodecane system with snapshot representing the biphasic mixture of water (left side: red/white) and dodecane (right side: blue).	130
Figure 5.7	Snapshot of interfacial region of water–dodecane system illustrating surface roughness	131
Figure 5.8	MSD of water and dodecane for water–dodecane biphasic system along with MSD of pure water.	132
Figure 5.9	(a) Snapshot of water/(TiAP + dodecane) system at different simulation length representing the TiAP accumulation at neutral interface. System: water-20%TiAP in dodecane. Colour code: red-O, yellow-phosphorous, white-H, cyan-dodecane and (b) orientation of phosphoryl group of TiAP molecules at neutral interface	133
Figure 5.10	Snapshot of liquid structure and its corresponding density profiles for 10%, 20%, 30% and 40% mole fraction of TiAP/dodecane-water biphasic system. Cyan: dodecane, red & white: water, red & grey: phosphoryl group of TiAP.	135
Figure 5.11	Schematic density profile for various mole fraction of TiAP from 10 % to 40%, representing the interface thickness which increases with mole fraction of TiAP.	136
Figure 5.12	Total interface thickness as a function of mole fraction of TiAP representing an increasing trend of interface thickness.	137
Figure 5.13	Pair correlation function (a) between O – HW atoms and (b) between O – OW atoms of two interacting TiAP and water molecules.	139
Figure 5.14	Snapshot of phosphoryl group of TiAP and water molecules at interface representing the orientation of phosphoryl group towards water surface and a schematic diagram of that phenomenon. Yellow: P, red: O, cyan: water.	141
Figure 5.15	Optimized structure of TiAP-H ₂ O and H ₂ O-H ₂ O at the B3LYP/SVP level of theory to exhibit the hydrogen bond.	142
Figure 5.16	PMF along the coordinates of (a) P–P atoms, (b) P–O atoms, (c) O–HW atoms and (d) O–OW atoms between two interacting TiAP–TiAP and TiAP–water molecules.	143

Figure 5.17	Snapshot of liquid structure containing acidic water as the aqueous phase and TiAP/dodecane as the organic phase which reflects the interfacial structure at different simulation length. System: water/3M nitric acid - 30%TiAP in dodecane. Colour code: magenta - dodecane, blue - H_3O^+ , green - NO_3^- , orange - water, red – phosphoryl oxygen, grey –phosphorous atom.	144
Figure 5.18	Snapshot of biphasic liquid structure containing 30% TiAP/dodecane as organic phase and nitric acid solution as aqueous phase. The corresponding density profiles for each component at different molarity of nitric acid varies from 1M to 4M.	146
Figure 5.19	(a) Density profile of 30% TiAP/dodecane – water system at different acidity illustrating the shifting of interface towards organic phase and (b) Density profile of water at different aqueous phase acidity of 20% TiAP/dodecane – nitric acid system illustrating sharpness of water density.	147
Figure 5.20	(a) Density profile of 3M nitric acid–TiAP/dodecane system with various mole fraction of TiAP illustrating the interface thickness changing with mole fraction and (b) Density profile of 3M nitric acid - TiAP/dodecane system at different mole fraction of TiAP illustrating the water – dodecane solvent interface.	148
Figure 5.21	Interfacial thickness of 20% TiAP/dodecane–nitric acid system as a function of aqueous phase acidity which illustrates the effect of acidity on the interfacial thickness. The interfacial thickness shows a decreasing trend with the aqueous phase acidity.	149
Figure 5.22	Interfacial tension of TiAP/dodecane–neutral water biphasic system as a function of interface thickness illustrating the inverse relation between these two parameters.	151
Figure 5.23	(a) Interface thickness (w_C) due to capillary wave as a function of mole fraction of TiAP and (b) Square of interface thickness (w_C^2) as a function of interfacial tension.	153
Figure 5.24	Total interface thickness computed from both density curve and proposed equation as a function of (a) mole fraction of TiAP and (b) aqueous phase acidity.	154

Figure 5.25	Preferential orientation (P=O-P=O) of phosphoryl group of TiAP molecules obtained from simulations with different view.	159
Figure 5.26	Optimized structures of dimer of TiAP in different orientation of phosphoryl group of TiAP molecules at the B3LYP/TZVP level of theory using dispersion correction. (a) O=P-P=O (b) P=O-P=O and (c) P=O-O=P.	160
Figure 6.1	Schematic representation of H_3O^+ , UO_2^{2+} , NO_3^- and HNO_3 with respective partial charges on atom.	170
Figure 6.2	Uranyl nitrate solution prepared in 3M nitric acid at various uranyl nitrate concentrations. The respective systems are marked on the round bottom flux indicating the concentration of uranyl nitrate.	172
Figure 6.3	Liquid state structure of uranyl ion in water systems having different force field embedded with four types of partial atomic charges on uranium as well as on uranyl oxygen atom. Oxygen atom: Red, Uranium atom: Cyan, Light green, Yellow and Green and Water molecule: Pink.	173
Figure 6.4	(a) Pair correlation function of uranium and oxygen atoms ($U - O_w$) between two interacting uranyl ion and water and (b) Running coordination numbers.	177
Figure 6.5	Pair correlation functions obtained from simulation of uranyl ion in water: (a) Water hydrogen (H_w) around U atom ($U - H_w$), (b) water hydrogen (H_w) around uranyl oxygen ($O - H_w$), (c) water oxygen (O_w) around uranyl oxygen ($O - O_w$) and (d) configuration of uranyl ion and water molecule. Red: Oxygen, White: Hydrogen and Brown: Uranium atom.	180
Figure 6.6	Change of free energy of hydration ($\Delta G_{\text{Hydration}}$) versus coupling parameter (λ) evaluated using thermodynamic integration.	182
Figure 6.7	Hydrogen bond dynamics related to (a) hydrogen bond numbering with respect to simulation length and (b) hydrogen bond autocorrelation function for models – MG, ML, GW and MA. Number of donors: 1000 and number of acceptors: 1002.	183

Figure 6.8	(a) MSD profiles of uranyl ions and (b) MSD profiles of nitrate ions in 3M acidic solution as a function of uranyl nitrate concentrations in that solution. The uranyl nitrate concentrations are represented as the numbers of uranyl ions present in the aqueous phase and denoted by respective system. The snapshots of respective liquid phase are illustrating the gathering of uranyl nitrate in the solution with concentrations. Colour code: Green-Uranium, Red-Oxygen and Blue-Nitrogen.	187
Figure 6.9	Trend of self-diffusion coefficient of uranyl ion, nitrate ion and water calculated from MD simulations as a function of uranyl nitrate concentration.	189
Figure 6.10	Arrhenius plot of self-diffusivity of uranyl ion and water molecules computed from MD simulations against the inverse of temperature. 10-U system is used to study the temperature effect.	191
Figure 6.11	Pair correlation function between two interacting U atom and O_w atom	192
Figure 6.12	(a) First peak height calculated for U – O_w PCFs (b) Coordination number of water oxygen around uranium of uranyl ion and (c) Second peak height are plotted as a function of concentration of uranyl nitrate in 3M acid.	193
Figure 6.13	Pair correlation function between two interacting (a) Oxygen atom of uranyl ion and hydrogen atom of water molecule and (b) Oxygen atoms of uranyl ion and oxygen atom of water molecule at different uranyl nitrate concentration which represented by the numbers of uranyl ions present in 3M nitric acid.	194
Figure 6.14	Pair correlation function between two interacting atoms (a) Uranium (U) and oxygen atoms (O_N) (b) Uranium (U) and nitrogen atoms (N) of UO_2^{2+} ion and NO_3^- ion. Snap shot of liquid structure obtained from MD simulations study illustrating the bi-dentate and mono-dentate structure between uranyl ion and nitrate ion. Colour code: Red-Oxygen, Blue-Nitrogen and Pink-Uranium.	197

Figure 6.15	Pair correlation function between two interacting (a) Oxygen atom of nitrate ion and hydrogen atoms of water and (b) Oxygen atom of nitrate ion and oxygen atom water. Snap shot of orientation of water molecules around nitrate ions. Colour code: Red-Oxygen, Blue-Nitrogen and Yellow-Hydrogen.	199
Figure 6.16	Plot of orientational correlation function as a function of time (t).	200
Figure 6.17	Plot of density of various chemical species along X-direction.	203
Figure 6.18	Surface tension of uranyl nitrate solution in 3M nitric acid as a function of uranyl nitrate concentration. Experimental intensity of uranyl nitrate solution in 3M nitric acid for a wide range of uranyl nitrate concentration using DLS instrument.	205
Figure 6.19	Shear viscosity of uranyl nitrate solution in 3M nitric acid calculated from MD simulations illustrating an increasing trend with uranyl nitrate concentration.	207
Figure 6.20	Pair correlation function between two interacting (a) U atom and O_W (water oxygen) atom and (b) oxygen atom (O) of uranyl ion and O_W (water oxygen) atom.	210
Figure 6.21	Pair correlation function between two interacting atoms (a) U atom and O_N (oxygen atom of NO_3^-) atom and (b) oxygen atom (O) of uranyl ion and oxygen atom (O_N) of nitrate ion.	211
Figure 6.22	Pair correlation function between two interacting (a) U atom and O_A atom (oxygen atom of HNO_3), (b) U atom and nitrogen atom (N_A) of nitric acid, (c) uranyl oxygen (O) atom and oxygen atom (O_N) of nitric acid, (d) uranyl oxygen atom (O) and hydrogen atom (H_A) of HNO_3 . Inset: Snap shot representing the orientation of nitric acid around uranyl ion. Colour code: White-Hydrogen, Red-Oxygen, Pink-Uranium, and Blue-Nitrogen.	212
Figure 6.23	Pair correlation function between two interacting (a) Oxygen atom (ON) of nitrate ion and oxygen atom (OA) of HNO_3 (b) ON atom of nitrate ion and hydrogen atom (HA) of HNO_3 , (c) Nitrogen atoms of nitrate ion and HNO_3 , (d) Nitrogen atom (N) of nitrate ion and hydrogen atom (HA) of HNO_3 . Inset: Snap shot representing the orientation of nitrate ion around nitric acid. Colour code: Green-Hydrogen, Blue-Nitrogen, Red-Oxygen and Golden yellow-Nitrate ion.	213

Figure 6.24	Average free energy of uranyl nitrate in 3M nitric acid system as a function of (a) Uranyl nitrate concentration and (b) Nitric acid concentration	215
Figure 6.25	Plot of product of diffusivity and shear viscosity ($D\eta$) of (a) Aqueous phase containing uranyl nitrate in 3M nitric acid and (b) Organic phase containing TiAP in dodecane as a function of calculated density.	216

LIST OF TABLES

Table No.	Table Caption	Page No.
Table 2.1	Bonded force field Parameters	23
Table 2.2	Values of Ryckaert-Bellemans dihedral potential (kJ/mol)	24
Table 2.3	Non-bonded force field parameters	25
Table 3.1	Compositions of MD simulations systems: Box size and number of solvent molecules for pure liquid	50
Table 3.2	Compositions of MD simulations systems: Box size, number of solvent and solute molecules for hydration and solvation of TBP, TiAP and TEP	51
Table 3.3	Calculated density for different system of pure TBP using Mulliken partial charge model	54
Table 3.4	Calculated density (kg/m^3) of TBP and deviation from experimental data for different charge model	55
Table 3.5	Calculated density (kg/m^3) of TiAP and deviation from experimental data for different charge model	55
Table 3.6	Calculated density (kg/m^3) of TEP and deviation from experimental data for different charge model	56
Table 3.7	Diffusion coefficients of pure TBP, TiAP and TEP liquids for different charge models	67
Table 3.8	Computed values of $\Delta G_{\text{Hydration}}$ and $\Delta G_{\text{Solvation}}$ (kJ/mol) in water and dodecane respectively	69
Table 3.9	Calculated values of partition coefficient (logP) of the ligands in water-dodecane system	72
Table 3.10	The calculated chemical potential (kcal/mol) of solute in water and dodecane medium respectively at infinite dilution using QM/COSMO-RS theory	73
Table 3.11	The computed values of $\Delta G_{\text{Hydration}}$ and $\Delta G_{\text{Solvation}}$ (kcal/mol) in water and dodecane medium respectively using MD simulations	73
Table 3.12	Dipole moment (Debye) of ligand	75

Table 3.13	The values of heat of vaporization (ΔH_{vap} in kJ/mol) computed from MD simulations of pure liquid systems	76
Table 3.14	Calculated values of free energy of extraction (kcal/mol) with different ligands at the B3LYP/TZVP level of theory	79
Table 4.1	Summary of various binary systems – TiAP/dodecane and TBP/dodecane	85
Table 4.2	Calculated density (kg/m^3) of pure TiAP at various temperatures	91
Table 4.3	Diffusivity values of TiAP and dodecane in binary mixture	96
Table 4.4	Shear viscosity of pure TBP and TiAP	106
Table 5.1	Details of compositions of various aqueous-organic biphasic systems and the corresponding MD simulations box dimensions	122
Table 5.2	Calculated physical and dynamical properties of pure water using three different models as Mulliken partial charge model, SPC model and SPC/E model	124
Table 5.3	Calculated physical and dynamical properties of pure nitric acid and 3M nitric acid using Mulliken partial charge embedded force field.	126
Table 5.4	Coordination number calculated from PCF for pure as well as 3M nitric acid	128
Table 5.5	Interfacial tension of neutral water-TiAP/dodecane system at $T=300^0\text{K}$	140
Table 5.6	Calculated interfacial tension (mN/m) at various mole fraction of TiAP with different aqueous phase acidity	149
Table 5.7	Interfacial tensions and thicknesses (nm) of neutral biphasic system as a function of mole fraction of TiAP	155
Table 5.8	Interfacial tension and thicknesses (nm) of 10% TiAP/dodecane-water biphasic system as a function of aqueous phase acidity	156

Table 5.9	Calculated interface thicknesses (nm) including capillary, intrinsic and total thickness for a wide range of biphasic systems using Eqn. 5.2 and Eqn. 5.3 along with the earlier reported MD simulations results (parenthesis)	157
Table 5.10	Water extraction at water - TiAP/dodecane Interface	161
Table 6.1	Partial atomic charges on uranium (q_U) and oxygen (q_O) of uranyl ion	169
Table 6.2	Summary of Type-1, Type-2 and Type-3 simulation systems along with their composition belong to numbers of uranyl ion ($N_{UO_2^{2+}}$), numbers of nitrate ions ($N_{NO_3^-}$), numbers of water and acid molecules (N_{Water}/N_{Acid}) and the approximate concentration of uranyl nitrate [$C_{UO_2(NO_3)_2}$].	171
Table 6.3	Density of uranyl ion in water system for different models computed from MD simulations. The diffusion coefficient of uranyl ion in SPC/E water along with the diffusion coefficient of water has been computed and the experimental values as well as the reported computational values available in the literature are listed.	175
Table 6.4	Comparison of structural parameter obtained from U – O _w PCFs for all the models along with the reported experimental and calculated values computed from QM or MM or CPMD/AIMD calculations to understand the geometrical parameters obtained from the present study	178
Table 6.5	Free energy of hydration and the reported literature data	181
Table 6.6	Bulk density and average dipole moments for uranyl ions as well as for all ions (called as overall) present in 3M nitric acid medium at various concentrations of uranyl nitrate (GW force field)	186
Table 6.7	Self-diffusion coefficients of uranyl ion, nitrate ion and water molecule present in aqueous phase calculated from MD simulations for a wide range of uranyl nitrate concentrations	188
Table 6.8	Calculated tetrahedral order parameter (q) for various systems	201
Table 6.9	Surface tension of uranyl nitrate solution in 3M nitric acid medium at various uranyl nitrate concentrations calculated from MD simulations	203

Table 6.10	Shear viscosity calculated from NEMD simulation for all the systems with the effect of concentrations of uranyl nitrate	206
Table 6.11	Average density of uranyl nitrate solution at various acid concentrations and self-diffusivities of various ions present in uranyl nitrate solution as a function of acid concentration have been calculated. 85-U system with un-dissociated form of nitric acid has been used.	208
Table 6.12	Shear viscosity and surface tension computed from MD simulations with the effect of nitric acid molarities (associated form of HNO ₃)	209

Chapter 1

Introduction



CHAPTER ONE

Introduction

1.1 INDIAN NUCLEAR POWER PROGRAM & NUCLEAR FUEL CYCLE

Among the various sources of energy, nuclear energy shares ~15-20% of the total energy consumption worldwide. In view of the growing energy demand, fission-based nuclear power will play a vital role in meeting this need. To produce energy, nuclear power plants engender a controlled fission chain reaction of heavy elements - most commonly U-235 and Pu-239. Nuclear power provides power with virtually no greenhouse gas emissions.

India has a flourishing and indigenous nuclear power program guided by the unique three stage nuclear power program due to its small uranium inventory and large thorium reserves.¹

The first stage was employed for power generation in Pressurized Heavy Water Reactors (PHWRs) with the limited natural uranium resources along with the conversion of uranium to plutonium. Second stage utilizes the plutonium and depleted uranium produced in the first stage as fuel not only harness power but also to enhance the fissile inventory necessary by converting fertile Th-232 to fissile U-233 in the blanket of the 2nd stage reactor. The natural

Th-232 and U-233 will use as fuel for power generation in third stage thorium based power reactors.² A schematic of the three stage nuclear program is represented in **Figure 1.1**. The first stage has achieved a state of commercial maturity by operating of 18 PHWRs. In addition to that, many Pressurized Heavy Water Reactors (PHWRs) and Boiling Water Reactors (BWRs) are in under construction and planning stages. The second stage is in good shape with operation of a Fast Breeder Test Reactor (FBTR) since 1985 and with construction of a 500MWe Prototype Fast Breeder Reactor (PFBR). As far as, the third stage is concerned, an Advanced Heavy Water Reactor (AHWR) based on thorium fuel is being developed to propagate the thorium based technology in commercial-scale.³

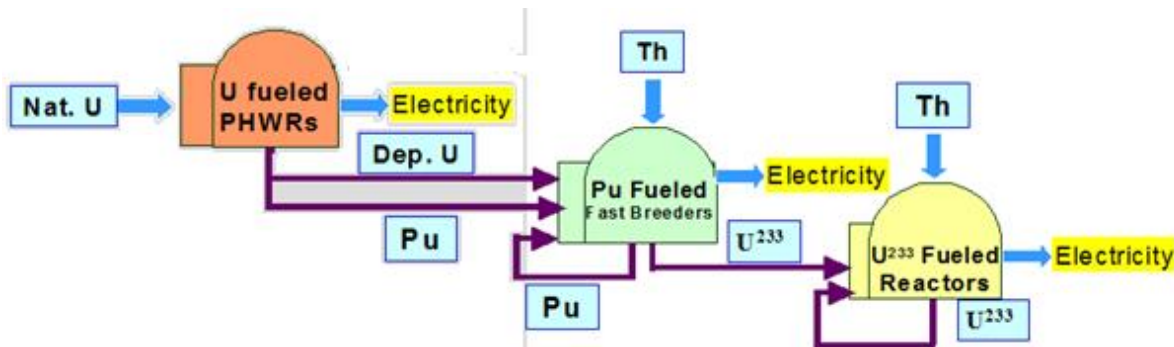


Figure 1.1: Schematic of the three stage Indian Nuclear Energy program

The nuclear fuel cycle deals with starting from the uranium exploration to the disposal of materials which have been used and generated during the cycle. It can be defined as the set of processes and operations required to produce nuclear fuel, its irradiation in nuclear reactors and storage, reprocessing, recycling or disposal. There are two types of fuel cycle (see **Figure 1.2**). One is open or once-through fuel cycle indicates without reuse of nuclear materials and another is closed fuel cycle, involves the reuse of nuclear materials extracted from irradiated fuel⁴. Both the options require robust and safe waste management technologies. India has opted for ‘closed’ option due to its limited uranium resources. In a closed nuclear fuel cycle

the un-burnt and bred fuel are recycled, recovered and reused as fresh fuel in nuclear reactor. Closed fuel cycle pursued in India by the pioneers envisaging sustainable source of power through nuclear energy.

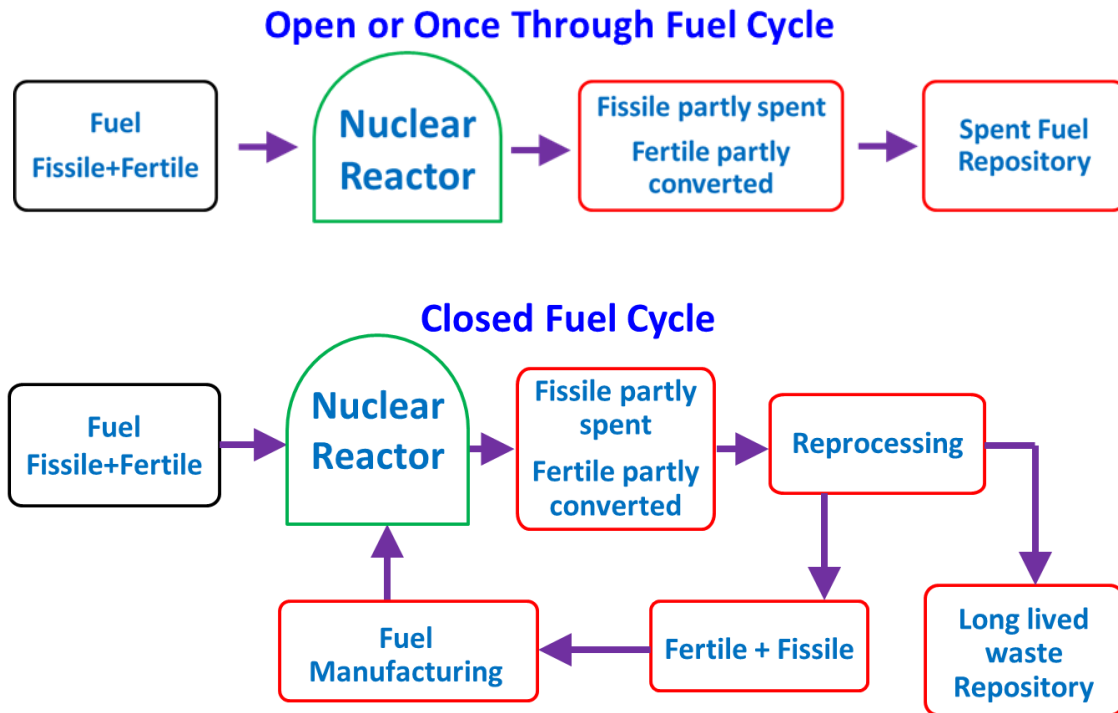


Figure 1.2: Flow diagram of Open Fuel Cycle and Closed Fuel Cycle

Not only the electricity generation using nuclear energy, other applications (see [Figure 1.3](#)) related to social and medical fields are also well established. All activities involving nuclear fuel in its various stages from mining of ore to final disposal of nuclear waste can be categorized in two ways. The activities before the fuel is placed in the nuclear reactor are commonly known as front end operation while the activities and the process after the fuel is used in the reactor are known as back end operation. Between front end and back end stage is the utilization stage of nuclear fuel cycle.

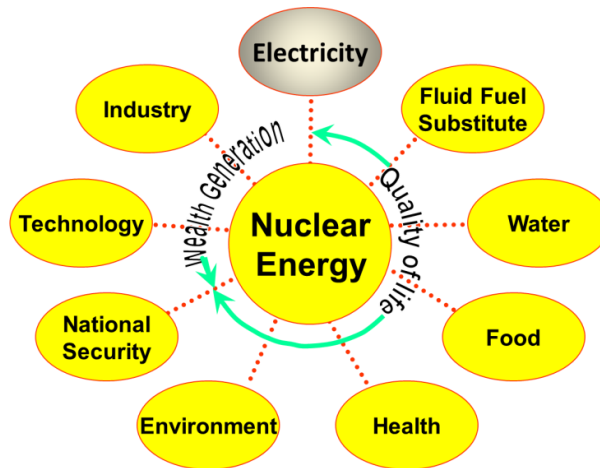


Figure 1.3: Flow chart for various applications of nuclear energy

1.2 NUCLEAR FUEL CYCLE

The nuclear power production technology is well established and has proven to be safe and reliable, although it will be essential to maintain the improvements that have been made in plant operational safety and efficiency over the past several decades. One aspect of nuclear power that still provides significant technical challenges is the management of irradiated nuclear fuel (fuel discharged from a nuclear reactor after its utilization).⁵ The management of continuously increasing used nuclear fuel in large volumes which contains un-burnt uranium, fissile plutonium, transuranic actinides and fission products (FP), necessitates the development of an effective and selective methodology to reuse fissile content by separating actinides and FP.^{6, 7} Reprocessing is the series of processes for separation of uranium and plutonium from the FP and transuranic actinides. This is the most important steps in back-end operation. The radionuclides present in spent fuel should be reprocessed for its safe disposal. The reprocessing of used nuclear fuel is of practical interest not only to reduce the high-active solid waste but also to produce the fresh fuel for 2nd generation nuclear reactor which can give dependable supply of fuel.⁶⁻¹⁰ The decay of radiotoxicity [see [Figure 1.4](#)] of the spent fuel needs several thousand years to reach its natural level.¹¹ Hence, spent fuel

reprocessing is also important to remove the radionuclide from the waste so that the time required to reach an acceptable activity level will be minimized.

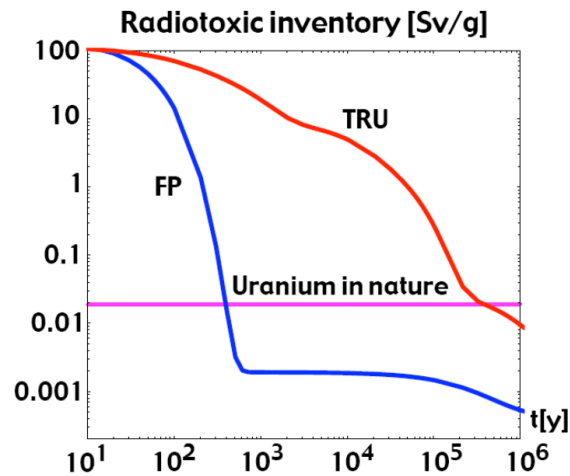
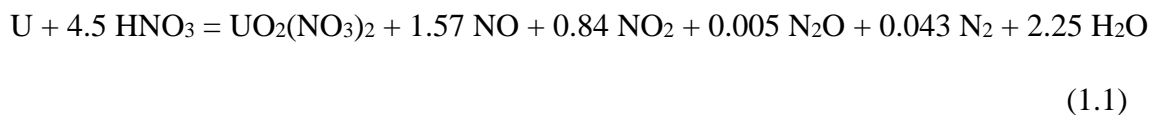


Figure 1.4: Decay of radiotoxicity of fission products (FP) and transuranic actinides with time

Various conventional separation processes are available such as distillation, absorption, adsorption, drying (Equilibrium governed) and osmosis, reverse osmosis, dialysis (Rate governed). These processes are quite common and the relevant technologies are well developed and well-studied. But they are not suitable due to high temperature and pressure, difficult to manage the generated waste and needs much effort to get product in desired form. Besides this, some non-conventional and non-traditional processes like Super Critical Fluid Extraction (SFE), Chromatographic Separation, Electric Field Assisted Separation, Membrane based Separation are also developed by resolving various issues present in the conventional processes. But again, they are not well established. So, the solvent extraction is the best choice for reprocessing.

The key role of the solvent extraction technologies is the selective transfer of valuables between aqueous and organic phases using liquid phase contractor.^{12, 13} Liquid – liquid extraction based technology is used to address the fuel reprocessing. The extent of

reprocessing depends on the efficiency of the liquid-liquid extraction processes which are widely used for separation and recovery of radionuclide from spent nuclear fuel. Further, the extraction method includes two immiscible liquids, mainly one aqueous phase which contains the metal ions and other is the organic phase consists of a mixture of a suitable ligand and a solvent. In this context, the most commonly practised extraction process is PUREX (Plutonium Uranium Recovery by Extraction) where the metal ions are extracted by organic ligand from acidic feed solution. Initially, the used nuclear fuel undergoes de-cladding and dissolution processes. The irradiated fuels containing fissile and fertile materials, have been chopped in small pieces and then dissolved in 12M boiling nitric acid to prepare the nitrates of Uranium (U) and Plutonium (Pu) which has been used as feed solution.¹⁴



The acidity of feed solution is maintained around 3 – 4M and then it is chemically processed to separate and purify the heavy metals of interest. The key extractant in PUREX process is tri-n-butyl phosphate (TBP) used with n-dodecane as an inert solvent and commonly used as diluent for TBP¹⁵. 30% TBP/n-dodecane ligand-solvent composition is used universally for recovery of uranium and plutonium from spent nuclear fuels.

The extent of purification or decontamination of uranium or plutonium achieved in each step is generally expressed by a term called Decontamination Factor or simply DF and is defined by the following expression:

$$\text{DF} = \frac{\text{Beta or Gamma activity/gm of U or Pu in feed}}{\text{Beta or gamma activity/gm of U or Pu in product}}$$

Again, the selectivity of any ligand or solvent under a particular set of conditions signifies the preferential extraction of that component by the ligand, is defined by separation factor as

$$\text{Separation Factor (F)} = \frac{K_A \text{ (Distribution Coefficient of A)}}{K_B \text{ (Distribution Coefficient of B)}}$$

Ligand with good selectivity or high separation factor towards Uranium (U) and Plutonium (Pu) will lead to a good DF during separation. TBP as a ligand used in PUREX process has good separation factor for U and Pu.

In PUREX process, the Uranium and Plutonium are extracted as metal-ligand complex $[\text{UO}_2(\text{NO}_3)_2 (\text{TBP})_2$ and $\text{Pu}(\text{NO}_3)_4 (\text{TBP})_2$] in organic-rich phase.^{16, 17}

The extraction mechanism of U (IV) into TBP is well established and the reaction at equilibrium is

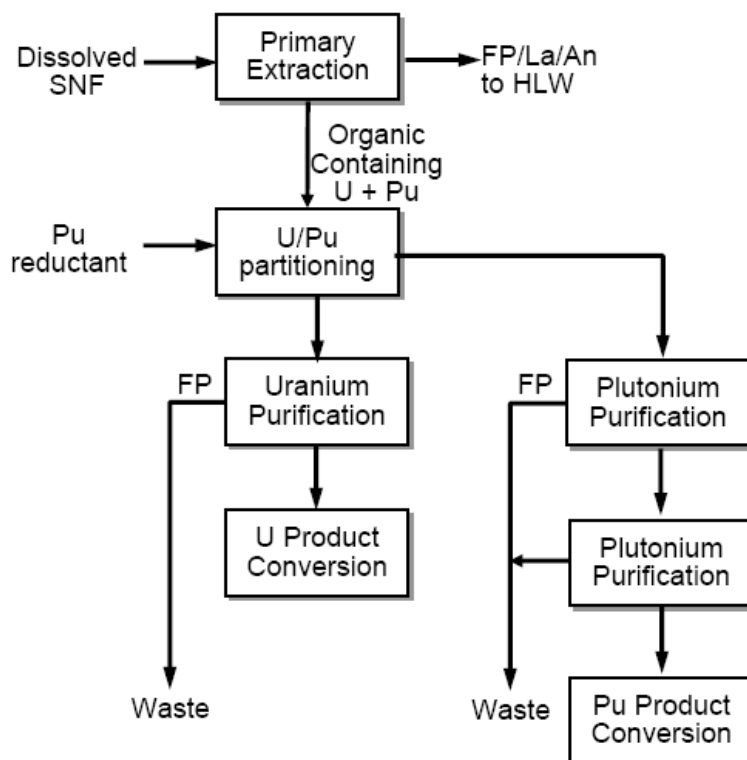
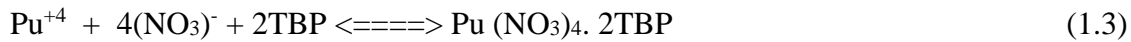


Figure 1.5: Block diagram of PUREX process. FP - Fission product, SNF – Spent nuclear fuel, La – Lanthanides and An – Actinides.

Similarly for plutonium the reaction is:



The block diagram of PUREX process is shown in **Figure 1.5** illustrating the stages of separation process. Initially, co-extraction of U and Pu followed by partitioning of them has been carried out and then the purification cycles for U and Pu have been performed to achieve the required purity.

1.3 TBP AS LIGAND IN REPROCESSING APPLICATION

This liquid – liquid extraction process is a multi-stage and multi-solute process which possesses several challenges for modelling the extraction phenomena and also for understanding the processes from molecular level. The most commonly used extractant molecules in solvent extraction process are organo-phosphorus ligands which bind the metal ions via their phosphoryl group. TBP (tri-n-butyl phosphate) is the most popular one and also thoroughly understood extracting agent among the organo-phosphorus ligands because of its pivotal role in various stages of nuclear fuel cycle.^{13, 15, 16} TBP has advantages of the (1) adequate extraction power for uranium and plutonium, (2) good selectivity for uranium and plutonium in comparison to the elements present in the fission products, (3) amenability to stripping with dilute nitric acid, and (4) good phase separation. TBP makes complexes selectively with Uranium and Plutonium.⁷⁻¹³ Although TBP is widely used in industrial scale, it has some inherent limitations also. For the reprocessing of fast reactor fuel involving Plutonium rich spent fuel with high level of radioactivity, TBP has the limitation of third phase formation at high metal loading.¹⁸ Also, the separation process is interfered by the formation of degradation products principally DBP (di-butyl phosphate) and MBP (mono-butyl phosphate) by radiological and chemical effects on TBP. These degradation products reduce the fission product decontamination efficiency by forming complex between fission

products and degradation products. Again, the degradation products also prevent the complete stripping of uranium and plutonium which results the losses of them into the raffinate (solvent wash waste). In addition to that the formation of low soluble metal (like Th, Zr, Pu) complexes of HDBP and H₂MBP sometimes was precipitated and interfered the operation¹⁸⁻²⁰. The fuel reprocessing is also affected by the significant aqueous solubility of TBP which creates problems in reduction process of Plutonium and makes the partitioning difficult. So, this is high time to think of alternative of TBP to pursue the reprocessing of fast reactor as well as thermal reactor fuel.

1.4 SELECTION OF NOVEL LIGAND OR ALTERNATIVE OF TBP

There is continuing search of an alternative novel ligand which has the merits of TBP and at the same time overcomes the above mentioned demerits of TBP. [Suresh et al](#) discussed the effect of elongation of alkyl chain and introduction of branching on alkyl group of phosphate ligand on extraction process.¹² Sometimes branching on first carbon atom significantly alters the extraction efficiency or the mutual solubility of water. Among many synthesized ligands, tri-iso-amyl phosphate (TiAP) has been shown to be quite promising. In recent past many researchers reported that TiAP, a homologous of TBP, is a potential ligand in many aspects: such as TiAP has the lesser tendency towards third phase formation for extraction of tetravalent actinides, lower aqueous solubility (0.019 kg/m³) compared to TBP (0.40 kg/m³), high extraction ability and better resistance to degradation.²¹ [Sreenivasulu and co-workers](#) carried out the radiolytic degradation studies on TiAP and they reported that the degradation behaviour of TiAP is similar to TBP and TiAP can be used as potential extractant because of its lower third phase formation tendency and lower aqueous solubility.²² Again, mixture settler experiments have been carried out by [Suresh and co-workers](#) with TiAP as an extractant for reprocessing applications and they reported that TiAP can be used as alternate extractant over TBP for both fast reactor and thermal reactor fuel reprocessing.²³ So, TiAP

might be a replacement of TBP and is being used for thermal reactor fuel reprocessing as well as fast reactor fuel reprocessing²⁴⁻²⁶. In addition to that the experimental studies also confirm the similar potentiality of TiAP in extraction, scrubbing and stripping and it mitigates the limitations.^{23, 24, 26-28} Moreover, TiAP has more thermal resistant compared to TBP when red oil formation is concerned. TiAP found to be safer under drastic temperature and concentrated acid condition in process evaporator. Again, Das and co-researcher also confirmed from the TGA test that the red oil prepared from TiAP is absence of exothermic reaction during heating from 30°C to 200°C which indicates TiAP is safer than TBP.²⁹ The extraction behaviour of U(VI) from nitric acid medium using 1.1M TiAP/n-dodecane as solvent along with scrubbing and stripping behaviour of U(VI) also have been investigated and found that both the TBP and TiAP ligands are comparable.²⁶ Again, the extraction behaviour of Th(IV) from nitric acid medium was also studied using TiAP – KO as extractant and a good separation factor $[D_{U(VI)}/D_{Th(IV)}]$ of 88.25 was reported at 6M HNO₃. The extraction of U(VI) by TiAP was an exothermic process whereas the extraction of Th(IV) was an endothermic process. It was also noted that the stripping of U(VI) from TiAP organic phase was comparatively easier than that of Th(IV) under identical conditions.²⁵ Further, the cost of TBP and TiAP are also very similar.^{30, 31} Hence, TiAP is shown to be comparatively better ligand over TBP in reprocessing applications.

1.5 NECESSITY OF SIMULATIONS

In order to predict and explain the behaviour of proposed ligands to develop an efficient extraction system, one can pursue either the experimental or theoretical route. From an experimental point of view, though one can get very accurate predictions but one should have laboratory infra-structure, radionuclide handling system and chemicals which are quite expensive and time consuming also. Even it sometimes can be completely impossible or dangerous also to measure what is desired. The complementary alternative to experiment is

the use of computational techniques like: molecular dynamics (MD) simulation and Quantum electronic structure calculation (QESC), which are principle tools for theoretical studies in biological as well as in chemical systems. This computational method calculates the time dependent behaviour of a molecular system based on Newton's laws of motion. Molecular dynamics simulations have evolved into a mature technique that can be used effectively to understand macromolecular structure-to-function relationships. These methods are now routinely used to investigate the microscopic structure, dynamics and thermodynamics of biological or chemical molecular systems and their complexes.

A wide range of chemical/physical processes can be modelled using MD simulations³² which help in planning the experiments and thus reduce the cost and time of experiments. So, elaborate molecular dynamic simulations studies are required to establish the liquid – liquid extraction processes with TiAP as an extractant for implementation in commercial scale. Therefore, a detailed investigation on the structural and thermo-physical properties of these ligands and the related dynamical and thermo-dynamic properties for the metal extraction is of utmost necessary for which molecular level studies are essential to predict structural and thermo-physical properties with an aim to have better understanding of the extraction process.^{17, 18, 21, 24, 25}

Therefore, MD simulations were conducted for pure TBP, TiAP, TEP and dodecane to determine the various structural, thermo-dynamical and dynamical properties^{33, 34}. The accuracy of physical and dynamical properties strongly depends on the performance of force field and it is very crucial to select the good one which can able to arrest all the properties. Though tri-ethyl phosphate (TEP) has not been reported in the literature for its use as metal ion extractant, few experimental values related to thermo-physical properties are available for TEP which are useful to calibrate the atomistic force field.

1.6 BACKGROUND & MOTIVATION OF THESIS

In recent past, MD simulations and QESC have been successfully applied to investigate the fundamental properties of various extraction systems.³⁴⁻³⁸ Recently, Cui et al have reported a comparative study between AMBER³⁹ (Assisted Model Building with Energy Refinement) and OPLS force field⁴⁰ by investigating two sets of partial charges calculation method for TBP model namely MNDO (Modified Neglect of Differential Overlap), a semi-empirical quantum chemistry calculation⁴¹ and DFT (ab initio Density Functional Theory) where atomic charges derived using the Restrained Electrostatic Potential charge fitting method⁴² for TBP model.⁴³ They have carried out scaling of atomic charges with respect to experimental dipole moment because the charges calculated by them using both the methods over-estimated the experimental value of dipole moment. Again, the predicted mass density was also improved with scaled charges. The self-diffusion coefficient was relatively better predicted by OPLS force field. The microscopic structure of pure TBP and TBP-alkanes is highly affected by the partial charge distribution and the magnitude of partial charges on TBP molecule.⁴⁴ Cui and co-workers have reported the structural and thermo-physical properties of TBP/n-dodecane mixture in entire mole fraction range with two sets of force fields for TBP where they have computed various properties of mixture in liquid phase such as mass density, excess volume of mixing, electric dipole moment and pair correlation function.⁴⁵ Junju Mu et al have computed various thermodynamic properties and microscopic structure of pure TBP liquid, TBP/n-alkane mixture and TBP/water mixture using various optimized model based on different atomic partial charge set calculated from DFT.⁴⁶ Different models have shown different limitations in predicting thermodynamic, kinetic, and structural properties. Recently, Siu and co-workers have refined the parameters of OPLS-AA force field for long hydrocarbons to reproduce the values of densities and heats of vaporization.⁴⁷ Haughney et al performed MD simulations of liquid methanol using different atomic partial charges on

carbon and oxygen atom and they reported two of them are in good agreement with available experimental values while the other two are less realistic.⁴⁸ Jamali and co-researchers investigated the thermodynamic and transport properties of several crown-ethers using force field-based molecular simulations introducing a new set of torsional potential parameters from DFT calculations and the computed thermodynamic and transport properties were found close to the experiments, suggesting the accuracy of the new force field which is also transferable to other cyclic-ether molecules in expense of parameterization.⁴⁹ Tsuzuki and co-workers carried out MD simulations of 13 ionic liquids using newly refined force field based on the ab initio molecular orbital calculations of the isolated ions and the experimental densities of a few ionic liquids and the calculated self-diffusion coefficients of ions followed the experimental trends but values are about 1 order smaller than the experimental ones.⁵⁰

1.7 OBJECTIVE OF THESIS

The parameterization of force fields based on some experimental thermo-physical data like dipole moment or density or potential energy have been carried out by researchers but still the refined force fields are not able to arrest all the physical and dynamical properties. Therefore, the primary aim should be to select the accurate force field for the pure ligands based on the calculation of physical and dynamical properties. For calibration of force field, four types of atomic charge models have been used. They are Mulliken, Löwdin, NPA (orbital population analysis methods) and ChelpG (a grid based method using electrostatic potential). Along with the calibration of force field, the screening of ligands has been done to find out an efficient ligand for liquid-liquid extraction process. To the best of our knowledge, the effect of partial charges on the structural and dynamic properties of ligands has not been touched upon. In addition, no literature is available for structural and dynamical properties of pure TiAP and TEP from MD simulation as well as the effects of different partial charges on pure TiAP and TEP. Therefore, the objective of the present study is to calibrate the OPLS-

AA force field by studying the structural, thermo-dynamical and dynamical properties for pure TBP, TiAP and TEP using different partial charges which finally help in the screening of ligands for the extraction applications. Subsequently, the calibrated force is to be tested for TiAP/dodecane binary mixture to see whether the single force field is able to capture all the physical and dynamical properties of binary mixture using MD simulations. Next, the compatibility of developed force field has been checked for water – TiAP/dodecane biphasic mixture by computing respective properties at liquid – liquid interface as third goal. In addition to that an attempt has been made for the calculation of total and intrinsic interface thickness for simple as well as complex biphasic mixture using the concepts of QM, MD and statistical mechanics. The versatility of single force field is the main attraction of the current studies. The forth objective is to find out the effect of partial charges on the structural and dynamical properties of actinides in water and then to calculate the various structural and dynamical properties of uranyl nitrate in acidic medium with wide range of uranyl nitrate as well as acid concentration. The MD simulation studies of aqueous feed solution at various uranyl nitrate concentration have been carried out to understand the limiting concentration of uranyl nitrate in feed solution used in PUREX process. Finally, the objective is accomplished with the study of uranyl nitrate – TiAP complex at the interface as well as at the organic and aqueous environment.

1.8 STRUCTURE OF THESIS

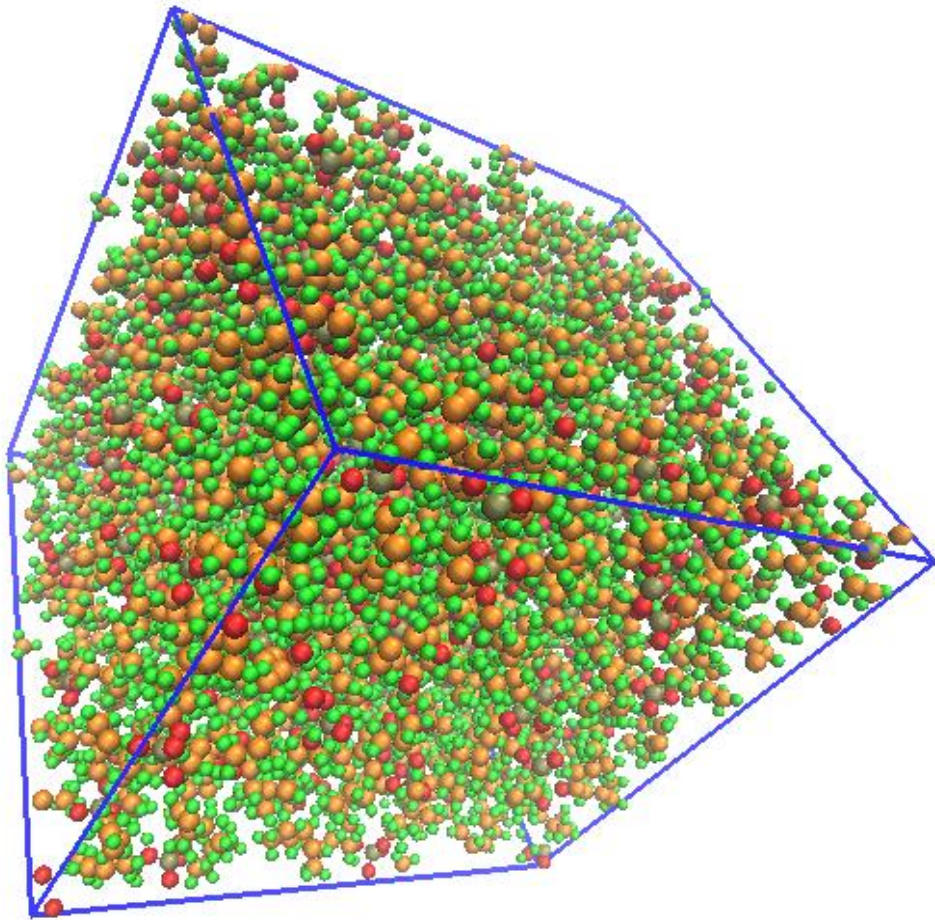
Chapter 2 deals with model and methodology used in the present work to perform the simulation studies and to calculate various physical, dynamical and thermo-dynamical properties of organic and aqueous solution. In **Chapter 3** of the thesis, the force field has been calibrated with the help of four different charge models. The atomic charges have been computed from Mulliken, Löwdin, NPA and ChelpG analysis method. The calibration has been done based on the calculated physical and dynamical properties to develop an accurate

force field. Then, the screening of pure ligand using the developed force field has been performed based on the free energy of hydration and solvation, free energy of extraction and partition coefficient. **Chapter 4** includes the test of developed force field in TiAP/dodecane binary mixture by calculating the physical and dynamical properties of binary mixture to see whether the single force field can arrest all the properties. TiAP/dodecane binary mixture with various composition ranging from 0 to 1 (with interval of 0.1) mole fraction of TiAP have been considered to study the effect of mole fraction on physical and dynamical properties. In addition to that the effective composition of binary mixture for liquid – liquid extraction is also decided based on the two important properties like self-diffusion coefficient and shear viscosity. Finally, the validation of Stokes-Einstein (SE) relation has been checked for this binary mixture. In **Chapter 5**, the present thesis deals with the biphasic system. The interfacial properties have been studied with the effect of composition of binary mixture ranging from 10% to 40% mole fraction of TiAP and the effect of aqueous phase acid molarity ranging from 0 to 4. The relation between interface thickness and interfacial tension has been established. The popular Capillary Wave Theory (CWT) relates the interface thickness and interfacial tension for two component system. Here, the CWT cannot be applied directly and it has been modified for three component system by introducing the weighted average of molecular length. The new model equation for three component system has been applied to the present biphasic system with the effect of mole fraction of TiAP and concentration of nitric acid. The validation of new model equation has also been checked for wide range of biphasic system reported in the literature. **Chapter 6** gives the wide range of information about the feed solution used in PUREX process. The concentration of uranyl nitrate in feed solution is essential for getting higher throughput. At the same time, the very high concentration will lead to create difficulties in extraction operation such as super saturation or crystallization. Therefore, various concentrations of uranyl nitrate ranging from

0.25M to 5.45M have been considered to analyse the structural, physical and dynamical properties as a function of uranyl nitrate concentration. The super-saturation effect is captured with respect to two important properties like surface tension and shear viscosity with a deviation from linear behaviour and it is also supported by conducting experiment using Dynamic Light Scattering (DLS) instrument. In addition to that the effect of acidity on feed solution is also investigated. Again, the validation of Stokes-Einstein (SE) relation has also been checked for aqueous mixture same as the binary mixture to find out its regime compared to the binary mixture. Finally, the work is briefly summarized in **Chapter 7** followed by the direction of extension of the present work in near future.

Chapter 2

Model & Methodology



CHAPTER TWO

Model & Methodology

2.1 INTRODUCTION TO MOLECULAR DYNAMICS SIMULATION

The understanding of various chemical and biological processes occurring in natural systems have direct pertinence to different fields of science and technology like chemistry⁵¹, biology⁵², environmental studies⁵³, chemical engineering⁵⁴, material science⁵⁵ etc. Condensed phase matters in everyday life usually exist in three phases namely gas, liquid and solid. Investigation of characteristics of liquid phases is more challenging compared to the other two phases. Because the many-body problem for gases and solids can be reduced to a few-body problem while for liquid phase, further simplification of the many-body problem is quite difficult. To understand the liquid state, the detailed information about inter-molecular interactions is required. Few experimental techniques are available to investigate the structural and dynamical properties of liquids such as X-ray⁵⁶ and neutron scattering⁵⁷, X-ray emission spectroscopy⁵⁸, X-ray absorption spectroscopy⁵⁹, Small-angle scattering⁶⁰, X-ray standing wave⁶¹ and Raman spectroscopy⁶². But the theoretical modelling and simulations are essential not only to interpret

the experimental results but also to acquire the information at atomistic level. Among the available simulation techniques, molecular dynamics (MD) simulations has the potential to replicate the chemical system.

Molecular dynamics (MD) is a computer simulation technique which involves in the time evolution of interacting atoms. It is a numerical method for studying many-body systems such as macroscopic systems like gases, liquids and solids, clusters. Molecular dynamics indicate the general process of describing complex chemical systems in terms of a realistic atomic model with the goal to understand and predict macroscopic properties based on detailed knowledge on an atomic scale. Classical MD belongs to the molecular interactions approximated by classical model potential while the Ab-initio MD deals with quantum calculation of electronic structure at every time step. Ab-initio MD provides higher accuracy compared to classical MD but has higher numerical effort. Finally, classical MD includes the temperature and pressure effects and able to treat large system for relatively long time. Classical MD simulation is a deterministic method which integrates Newton's equation of motion for the particles of the molecular system. According to the Newton's second law of motion,

$$F(r) = m \frac{d^2r}{dt^2} \quad (2.1)$$

where, m and r denote the mass of the atom and the positional coordinate respectively. F signifies the forces acting on atoms. At intervals of time steps, the forces between all pairs of atoms are calculated and accumulated, and then each atom is moved. The integration of the above equation of motion from an initial position and velocity provides the consecutive positions and velocities of next time frames separated by a small time interval Δt . The MD simulation is advantageous over Monte Carlo (MC) simulation⁶³ because MC considers random moves instead of using Newton's Law of Motion to move the atoms.

The inputs required to perform the MD simulations are described in **Figure 2.1**. The correct initial structure along with the topology is the essential part of modelling. Then the MD simulation requires a proper force field which leads the accurate prediction of properties using statistical mechanics. A force field refers to both an interatomic potential functional form and its related parameters. Interatomic potentials which are mathematical functions describe the potential energy of a statistical mechanical model, encapsulates both bonded (atoms linked by covalent bonds) and non-bonded (refer to long-range electrostatic and van der Waals forces).

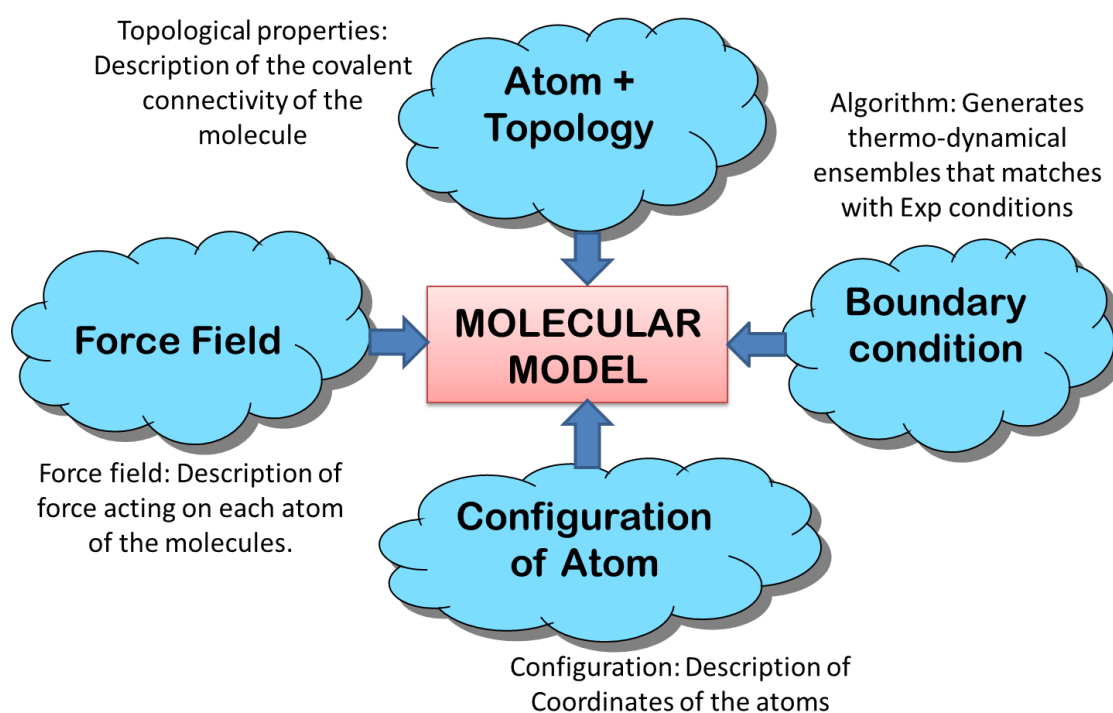


Figure 2.1: Inputs to molecular dynamics simulations

In MD simulations, the forces between molecules are calculated explicitly and the motion of the molecules is computed with a suitable numerical integration method using Newton's equations of motion for the constituent atoms. The initial boundary conditions are the positions of the atoms (taken from optimized structure) and their velocities. It is possible to calculate the positions and velocities of the atoms after certain time interval (a time step) using initial

boundary conditions. From the new positions the forces are recalculated and another step in time made. The cycle has to be repeated many times during course of simulation, usually for many thousands of time steps. It is worth noting that a single time step is usually of the order of 1 femtosecond. The steps of MD simulations are represented in the form of flow chart in

Figure 2.2.

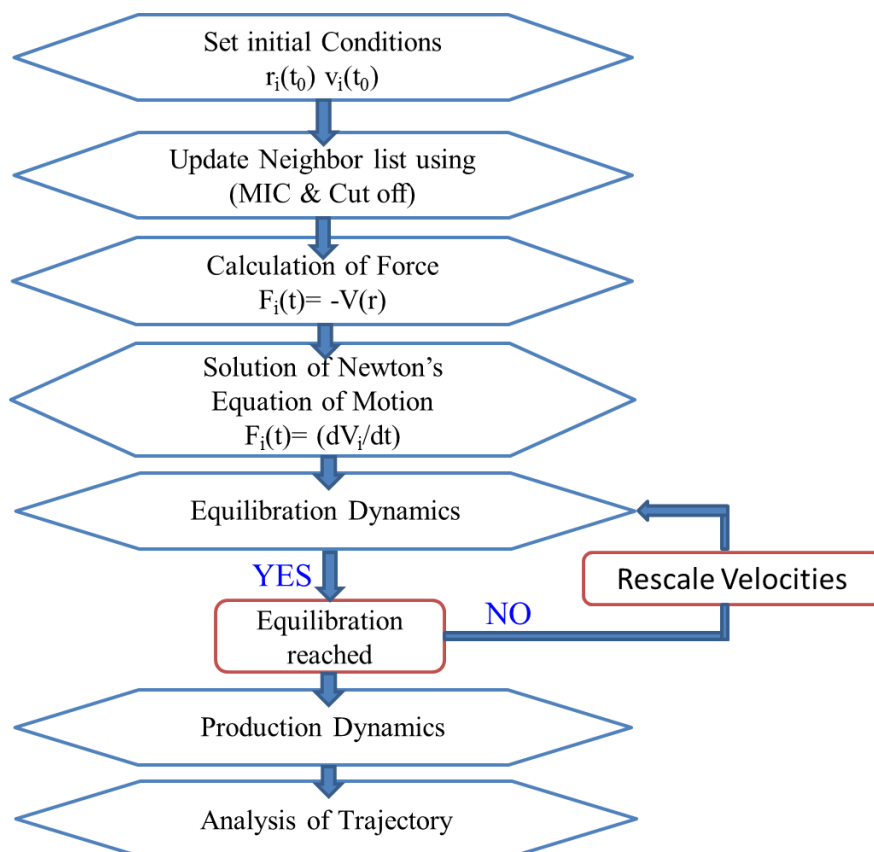


Figure 2.2: Flow chart for molecular dynamics simulations

Calculation of the atomic forces is usually the most expensive part in MD simulation. It is normally assumed that the forces act exclusively between pairs of atoms. Minimum Image Convention (MIC) and Periodic Boundary Condition (PBC) are used to replicate a large system with no surface effect. A cut-off is also applied at a certain distance beyond which the force is zero. This allows more efficiency in computing the forces because atom pairs at long distance

need not to be considered. During equilibration period the system is settled down towards the desired thermodynamic state point. After many of thousands of time steps, the trajectory of the molecules is accumulated for analysis which provides a statistically accurate description of the phenomenon of interest.

2.2 MODEL & METHODOLOGY

Molecular dynamic simulations have been carried out using GROMACS (GRONingen MAchine for Chemical Simulations)⁶⁴⁻⁶⁷ simulation package. The GROMACS package is a versatile and very well optimized package for molecular simulations. The potential energy function in MD simulations, commonly known as force field characterises the molecular system. In atomistic view, every atom present in the system and also some cases like lone pair of electrons associated with an atom is to be considered as an interaction site. Depending on the bonding nature in a molecule such a site-site interaction potential function is described in terms of bonded and non-bonded interactions. Total potential energy of any molecular system can be calculated by considering wise selection of potential functions for various intra-molecular and inter-molecular interactions among different sites in the molecular system. The energy belongs to bonded interaction involves 2-body, 3-body and 4 body interactions of covalently bonded atoms which includes the bond stretching, bond angle bending and the dihedral deformation respectively. The pair interaction between the non-bonded atoms includes the van der Walls (assumed to be pair wise additive in this 1 – 6 – 12 potential) and the electrostatic interactions which are computed using Lennard – Jones potential. The corresponding potential energy for both the interactions is given below.

Total potential energy for bonded interaction:

$$E = \sum_{bonds} K_r (r_{ij} - r_{eq})^2 + \sum_{angles} K_\theta (\theta_{ijk} - \theta_{eq})^2 + \sum_{dihedrals} \left[\frac{V_1}{2} (1 + \cos \Phi_{ijkl}) + \frac{V_2}{2} (1 + \cos 2\Phi_{ijkl}) + \frac{V_3}{2} (1 + \cos 3\Phi_{ijkl}) \right] \quad (2.2)$$

The first term appeared in the above equation is the potential energy due to bond vibration, called as bond energy and is modelled by using harmonic potential. The r_{ij} represents the bond length at any instant of time between atom i and atom j and r_{eq} is the equilibrium bond length and K_r is the force constant of the bond. The second term provides energy change due to bending motion of molecule is also modelled by harmonic potential. The K_θ represents the force constant, θ_{ijk} is the angles formed by three consecutive atoms i , j and k and θ_{eq} is the equilibrium value of that angles. The 3rd term represents the potential energy change due to dihedral or torsional motion where the angle Φ represents torsion angle. V_1 , V_2 and V_3 signifies the potential energy terms. Four consecutive atoms in a molecule form a dihedral angle and the dihedral angle potential describes the angular spring between the planes formed by i , j and k atoms and j , k and l atoms of a consecutively bonded. The cosine function in this term stands for the periodicity of this function.

The parameters of a force field are mainly acquired from experiments or quantum mechanical calculations. Transferability of force field parameters such as the parameters derived for a small fragment molecule of a large molecule can be used to study another large molecule without much complexity is a noteworthy advantage. For past several years, different types of force field have been developed which are extensively used in simulations for various systems of interests. All-atom optimized potentials for liquid simulations (OPLS-AA)^{40, 68} force field was used to model TBP, TiAP, TEP and dodecane in pure liquid phase. The primary requirement of MD simulations is to model the molecular system by choosing appropriate length scale and force field or total potential along with the subsequent creation of initial configuration for the same. The potential parameters are presented in **Table 2.1**, where the atoms of TiAP are represented in **Figure 2.3**. The atoms of TBP and TEP follow the similar atomic representation. The torsion parameters for the same are presented in **Table 2.2**.

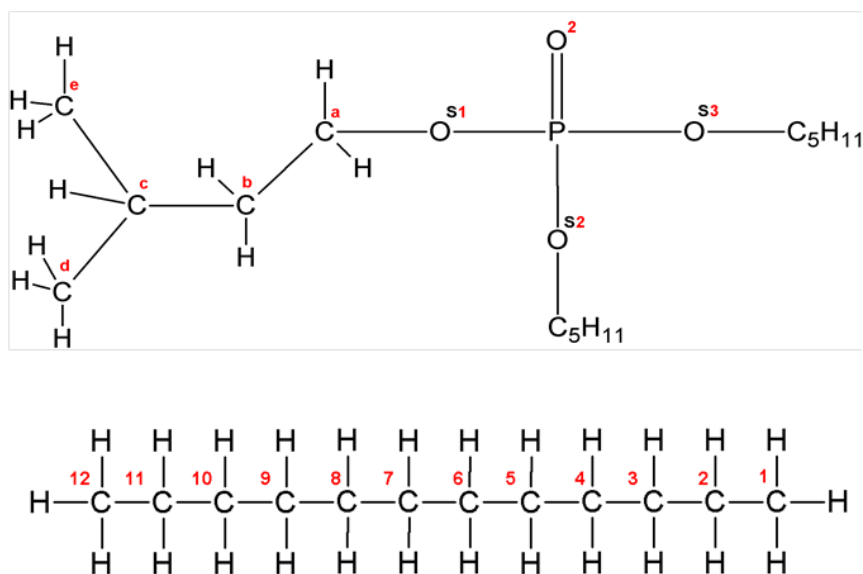


Figure 2.3: Schematic representation of TiAP and dodecane molecules with atom number

Table 2.1: Bonded force field parameters

Molecules	Bonds(i-j)	K_r (kJmol ⁻¹ nm ⁻¹)	r_{eq} (nm)
TEP/TBP/TiAP	O2-P	219660	0.148
	P-Os	96232	0.161
	Os-C	133888	0.144
	C-C	112131.2	0.153
	C-H	142256	0.110
Dodecane	C-C	112131.2	0.153
	C-H	142256	0.110
Molecules	Angles(i-j-k)	K_θ (kJmol ⁻¹ rad ⁻²)	θ_{eq} (degree)
TEP/TBP/TiAP	O2-P-Os	418.40	114.30
	P-Os-C	418.40	121.25
	Os-C-C	209.20	109.34
	Os-C-H	146.44	109.20

	Os-P-Os	188.28	102.72
	C-C-C	244.13	112.70
	C-C-H	156.90	110.70
	H-C-H	138.07	107.80
Dodecane	C-C-C	244.13	112.70
	C-C-H	156.90	110.70
	H-C-H	138.07	107.80

Table 2.2: Values of Ryckaert-Bellemans dihedral potential (kJ/mol)

Molecules	Dihedrals(i-j-k-l)	C0	C1	C2	C3	C4	C5
TBP/TiAP/TEP	C-Os-P-O2	1.17	3.52	0	-4.70	0	0
	C-Os-P-Os	1.04	3.13	10.04	-4.18	0	0
	H-C-Os-P	0.74	2.14	0	-2.98	0	0
	C-C-Os-P	12.51	0	-12.51	0	0	0
	Os-C-C-C	2.87	0.58	2.09	-5.54	0	0
	Os-C-C-H	0.97	2.93	0	-3.91	0	0
	C-C-C-C	2.92	-1.46	2.09	-1.67	0	0
	C-C-C-H	0.17	0.53	0	-0.71	0	0
	H-C-C-H	0.62	1.88	0	-2.51	0	0
Dodecane	C-C-C-C	2.92	-1.46	2.09	-1.67	0	0
	C-C-C-H	0.17	0.53	0	-0.71	0	0
	H-C-C-H	0.62	1.88	0	-2.51	0	0

Total potential energy for non-bonded interaction between the atoms is calculated by Lennard-Jones potential.

$$U(r_{ij}) = 4\varepsilon_{ij} \left[\left(\frac{\sigma_{ij}}{r_{ij}} \right)^{12} - \left(\frac{\sigma_{ij}}{r_{ij}} \right)^6 \right] + \frac{q_i q_j}{4\pi\varepsilon_0 r_{ij}} \quad (2.3)$$

Where, $U(r_{ij})$ is the total non-bonded interaction potential. The first term appeared in the potential function represents the van der Waals interaction between two atoms i and j with interatomic distance r_{ij} and the vdW force originates from the interplay of repulsive and attractive forces and yields an energy minimum at a particular interatomic separation. As atoms are brought closer from infinite separation, initially negative term ($1/r^6$) in the square bracket prevails and hence energy becomes gradually more negative. In case of distance closer to energy minimum the positive part ($1/r^{12}$) of the equation starts to dominate and energy becomes positive rapidly. The parameter ε_{ij} represents the depth of the potential well and σ_{ij} represents the collision diameter or the inter-atomic distance at which potential energy becomes zero. The values of these two parameters are basically guided by the nature of the interacting atoms. The second term provides the non-bonded electrostatic interaction between atoms i and j using the Coulomb's law due to point charges on different interaction sites of the system. The interacting atoms are separated by distance r_{ij} having partial charges q_i and q_j respectively.⁶⁴⁻⁷¹ The L-J parameters for all the liquids are represented in [Table 2.3](#).

Table 2.3: Non-bonded force field parameters

Molecules	Site	σ (nm)	ε (kJ/mol)
TBP/TiAP/TEP	O2	0.315	0.8368
	P	0.374	0.8368
	Os	0.290	0.5857
	C	0.350	0.2761

	H	0.250	0.1255
Dodecane	C	0.350	0.2761
	H	0.250	0.1255

The force field parameters for both the bonded and non-bonded potentials are taken from the all-atom optimized potentials for liquid simulations (OPLS-AA) but different charge models are used for electrostatic potential. The partial charges on the atoms were selected using different atomic population methods from the density functional theory (DFT). The partial charges from three different types of charged model (Mulliken, Löwdin and NPA) were obtained using TURBOMOLE package^{69, 72} and one (ChelpG) from GAMESS package⁷³. The initial molecular structures of TBP, TiAP, TEP and dodecane and the corresponding partial charges on the atoms were generated at the B3LYP/TZVP^{70, 71} level of theory using optimized structure at the B3LYP/SVP level of theory as implemented in TURBOMOLE^{69, 72} package which was then used in creating the topology. Initial velocities of each atom are to be dispensed by using Maxwell-Boltzmann equation by considering the average temperature of the system. A suitable boundary condition is employed to mimic the system of interest before starting the simulation. Periodic boundary condition (PBC) is one such condition which not only maintains the number of atoms/particles fixed in the simulation box but also creates bulk environment by removing the surface effects. The standard Lorentz – Berthelot mixing rules, $\sigma_{ij} = (\sigma_i + \sigma_j)/2$ and $\epsilon_{ij} = \sqrt{\epsilon_i \epsilon_j}$, are used for all the non-bonded pair interactions between different atoms with an atom based cut off of 12Å. During simulation, the long range electrostatic interactions are computed using particle mesh Ewald⁷⁴⁻⁷⁶ (PME) method with an order of 6 and with a cut off distance of 12Å. The equation of motion is integrated by applying finite difference methods. The basic criteria of any reliable integrator are 1) accuracy (it should follow the true trajectory) 2) stability (It should be energetically conserved) and 3) sturdy (it should allow larger time in propagation

of system in phase space). There are several proposed algorithms for the integrators in MD simulations. Throughout the study, we have used velocity Verlet⁷⁷ and leap-frog⁷⁸ algorithm for our molecular simulation purposes. To avoid larger computational requirement, usually the simulation of very fast motions due to bond or angle vibration is ignored by constraining these bonds or angles to its equilibrium value during the simulation. LINCS⁷⁹ has been used for constraining bonds.

After solving the Newtonian equations of motion, the trajectory generated corresponds to isothermal – isobaric or NVT ensemble. Various thermostats are employed to simulate systems in any other ensemble. Different temperature coupling like Berendsen⁸⁰, Velocity rescaling⁸¹, Nose-Hoover⁸² have been used to maintain the temperature of the proposed system and different pressure coupling such as Berendsen⁸⁰, Parrinello-Rahman⁸³ are used to control the pressure of the system. Again, some well-known ensembles have been employed in this thesis work are canonical or NVT ensemble where the total number of particles, temperature and volume of the system are fixed and isothermal-isobaric (NPT) ensemble which fixes the total number of particles, temperature and pressure of the system.⁸⁴ Some mathematical expressions relate a particular statistical ensemble and various thermodynamic properties of the system. The outputs of the MD simulations provide phase-space trajectory of the system which contains entire simulation length of evolution of the system regarding macroscopic quantities. So, the application of statistical mechanics⁸⁵ is involved here to extract the macroscopic properties of the system from the trajectory. In this context, the various aspects of statistical mechanics associated with the physical and dynamical properties of a many-particle finite-temperature system have been discussed.

2.3 STATISTICAL MECHANICS

The aim to introduce the statistical mechanics is to compute the observable properties of a many particle system from its microscopic description either as averages over a phase space

trajectory (the method of Boltzmann), or as averages over an ensemble of systems, each of which is a replica of the system of interest (the method of Gibbs).⁸⁵ Dynamics and thermodynamics properties of a system, with some exceptions, are expressible as averaged over a large number of particles or the time of the measurement of certain functions.⁸⁶

Conventional MD simulations deal with the positions and momenta of all the particles present in the system. These positions and momenta of the system are continuously changing with the passage of time and these position and momenta can be thought of as coordinates in a multidimensional space, called “phase space”. Certain thermodynamic properties of a physical system may be written as averages of functions of the coordinates and momenta of the constituent particles. These are called as “mechanical” properties, which include internal energy and pressure. Again, “thermal” properties such as entropy are not expressible in this way. In a state of thermal equilibrium these averages must be independent of time.⁸⁴⁻⁸⁶

Let us assume δ , a particular phase point in phase space, corresponds to N coordinates and N -momenta. Then, an instantaneous function $\Psi(\delta)$ corresponds to some macroscopic property C of the system and the instantaneous value of the property $\Psi(\delta)$ changes with δ . So any observable property can be obtained by averaging of all the $\Psi(\delta)$ and express as

$$C = \langle \Psi(r^N, p^N) \rangle \quad (2.4)$$

where the angular bracket represents the average value.

2.4 TIME AVERAGE (Method of Boltzmann)

Newtonian equation of motion has been solved in MD simulations and it generates phase space point Γ as a function of time. Therefore, it will be reasonable to assume that the experimentally measured value of the property, P is actually the time average of $\beta(\Gamma)$ taken over a long time interval such that

$$\langle \hat{\rho} \rangle_t = \lim_{\tau_{obs} \rightarrow \infty} \frac{1}{\tau} \int_0^{\tau_{obs}} \hat{\rho} \left[\overrightarrow{r^N}(t), \overrightarrow{p^N}(t) \right] dt \quad (2.5)$$

The concept of time averaging is proposed by Boltzmann. As in practice, the integration cannot be extended up to infinity and a discrete time is represented in MD simulations. Therefore it is convenient to express the above averaging procedure as a sum of N_t number of time steps of discrete step length = T_{obs} / N_t

$$P = \langle \hat{\rho} \rangle_t = \frac{1}{N_t} \sum_{\tau=1}^{N_t} \hat{\rho} (\Gamma(\tau)) \quad (2.6)$$

where $\Gamma(\tau)$ is the phase-space point corresponding to a particular set of N positions and N momenta (where N denotes number of particles in the system). The definition is correct when the system is “ergodic” which means that after a suitable time of observation the phase trajectory of the referred system will have passed equal number of times through every point in phase- space.

2.5 ENSEMBLE AVERAGE (Method of Gibbs):

The alternative to the time-averaging procedure described by [equation \(2.5\)](#) is to average over a suitably constructed ensemble, each of which is a replica of the original system of interest. This concept of ensemble averaging is proposed by Gibbs. A statistical - mechanical ensemble is an arbitrarily large collection of imaginary systems, all of which is a replica of the physical system of interest in so far as they are characterised by same macroscopic parameters like N , V , T , P , μ etc. The systems of ensemble differ from each other in the assignment of coordinates and momenta of the particles of the system. Ensemble is thus represented by a cloud of phase points distributed in space according to some probability density distribution. According to the Gibbs’ formulation of statistical mechanics the distribution of phase points of the ensemble is described by a phase-space probability density $f^{(N)}(\overrightarrow{r^N}, \overrightarrow{p^N}, t)$. The quantity $f^{(N)}(d\overrightarrow{r^N}, d\overrightarrow{p^N}, t)$ is the probability that at time t , the actual physical system is in a

microscopic state, represented by a phase point lying in the infinitesimal phase space element $\overrightarrow{dr^N}, \overrightarrow{dp^N}$. The equilibrium ensemble average implies that the integral of $f^{(N)}$ over all phase space and is denoted as $B = (\overrightarrow{r^N}, \overrightarrow{p^N})$ is given by

$$\langle A \rangle_e = \iint B (\overrightarrow{r^N}, \overrightarrow{p^N}) f_0^{(N)} (\overrightarrow{r^N}, \overrightarrow{p^N}) d\overrightarrow{r^N}, d\overrightarrow{p^N} \quad (2.7)$$

Where $f_0^{(N)}$ is the equilibrium probability density and is normalised in such that

$$\iint f_0^{(N)} (\overrightarrow{r^N}, \overrightarrow{p^N}) d\overrightarrow{r^N}, d\overrightarrow{p^N} = 1 \quad (2.8)$$

The explicit form of the equilibrium probability density depends on the macroscopic parameters that characterise the ensemble. This averaging procedure is used by various Monte Carlo methods in efficient way. The different types of ensembles are discussed here.

2.5.1 Canonical Ensemble (NVT):

In canonical ensemble the number of molecules (N), volume (V) and temperature (T) are held constant for a collection of systems. It is also called NVT-ensemble. The temperature is allowed to fluctuate and the canonical partition function is denoted Q (N, V, T). The system is in thermal contact with the surroundings so that they are all thermo-stated to the same temperature. There is no exchange of energy but heat can be transferred. The energy fluctuates about some mean value for each member of ensemble. The canonical equilibrium probability density for N identical point is

$$f_0^{(N)} (\overrightarrow{r^N}, \overrightarrow{p^N}) = \frac{1}{h^{3N} N!} \frac{\exp (-\beta \mathcal{H})}{Q_N} \quad (2.9)$$

where h is plank's constant, the factor N! ensures the in-distinguish ability of the particles and the Q_N is the normalization constant and it is also called canonical partition function, defined as

$$Q_N = \frac{1}{h^{3N} N!} \iint \exp (-\beta \mathcal{H}) d\overrightarrow{r^N} d\overrightarrow{p^N} \quad (2.10)$$

The factor $1/h^{3N}$ in the above definitions ensures that both $f_0^{(N)}$, dr^N , dp^N and Q_N are dimensionless.

The bridge between statistical mechanics and thermodynamics is established by means of the thermodynamic potential and the partition function:

$$F = -K_B T \ln Q_N(V, T) \quad (2.11)$$

where ‘F’ denotes the Helmholtz free energy. The thermal equilibrium corresponds to the minimum free energy at finite temperature. All equilibrium thermodynamic properties can be calculated by taking appropriate derivatives of the energy $F(N, V, T)$ with respect to the parameters. The thermodynamic potential becomes minimum when the equilibrium is reached for any system of fixed N , V , and T .

Such thermodynamic relations correspond to an equivalent relation in terms of partition function. The Hamiltonian can be separated into kinetics and potential terms as,

$$\mathcal{H}_N(\vec{r}^N, \vec{p}^N) = \frac{1}{2m} \sum_{i=1}^N |P_i|^2 + V_N(r_N) \quad (2.12)$$

Combination of [equation \(2.9\)](#) and [equation \(2.12\)](#) and integration over momenta N , yields a factor $(2\pi m K_B T)^{1/2}$ for each of the $3N$ degrees of freedom. The canonical partition function can be rewritten as

$$Q_N^{\text{id}}(V, T) = \frac{\Lambda^{-3N}}{N!} V^N \quad (2.13)$$

where, $\Lambda = \left(\frac{h^2}{2\pi m k_B T}\right)^{1/2}$ is known as thermal de Broglie wave length.

2.5.2 Isothermal-Isobaric (NPT) Ensemble:

In this ensemble pressure (rather than volume) is a fixed parameter. The thermodynamic potential of any system is characterised by fixed parameters of N , P and T and the Gibbs free energy (G) can be defined as

$$G = F + PV \quad (2.14)$$

Other state functions can be obtained by differentiation of G with respect to the independent variables and it is related to statistical mechanics through the relation

$$G = -K_B T \log \mathcal{D}_N(P, T) \quad (2.15)$$

where isothermal-isobaric partition function $\mathcal{D}_N(P, T)$ can be generally expressed as a Laplace transformation of the canonical partition function:

$$\mathcal{D}_N(P, T) = \frac{h^{-3N}}{N!} \iiint \exp[-\beta PV - \beta \mathcal{H}_N(\vec{r}^N, \vec{p}^N)] d\vec{r}^N, d\vec{p}^N dV \quad (2.16)$$

$$f_{0,NPT}^{(N)} = \frac{h^{-3N}}{N!} \frac{\exp[-\beta PV - \beta \mathcal{H}_N(\vec{r}^N, \vec{p}^N)]}{\mathcal{D}_N(P, T)} \quad (2.17)$$

2.6 SELECTION OF PARTIAL CHARGE MODEL

Assigning charges to atoms can be very useful as they can give a rough idea of the charge distribution in a molecule. The use of partial atomic charges to calculate the interactions in various MD simulations packages are presently an active area of application. The total electron density, $\rho(\mathbf{r})$ is expanded in terms of the MOs and then each orbital can be expanded in terms of atomic orbitals (the basis set):

$$\rho(\mathbf{r}) = \sum_i n_i \rho_i(\mathbf{r}) \quad (2.18)$$

It can be rewrite in the form of overlap and density matrix as

$$\rho(\mathbf{r}) = \sum_{\alpha\beta} D_{\alpha\beta} S_{\alpha\beta} \quad (2.19)$$

where, $S_{\alpha\beta} = \chi_\alpha \chi_\beta$ denoted the overlap matrix i.e. the product of two different AO functions where the electrons are shared between two atoms and $D_{\alpha\beta} = \sum_i n_i C_{\alpha i} C_{\beta i}$ denoted the density matrix includes square of single AO basis function as the electrons are belonging to the particular atom. $C_{\alpha i}$ and $C_{\beta i}$ denote the coefficients of basis function α and β in the MO i .

Population analysis methods shared the $D_{\alpha\beta}$ and $S_{\alpha\beta}$ to obtain numbers which provides the location of electron density in a system. Therefore, the partial atomic charges within the molecules of interest were determined using various Quantum partial charges generating techniques⁸⁷ such as Mulliken^{88, 89}, Löwdin^{90, 91}, NPA⁹² and ChelpG⁹³ for the present study. The first three are based on the linear combination of atomic orbital (LCAO) and therefore the wave function of the molecule. Mulliken population analysis is the most widely used method where the electron density is shared as 50:50. It is computationally cheap and provides reasonable charge magnitudes but it has one disadvantage because it depends on the size of the basis set. The improved version is the Löwdin population analysis where the atomic orbital basis function is transformed into an orthonormal set of basis function and hence is more stable compared to the Mulliken population analysis method but it is computationally more expensive. Finally, NPA, an alternative to conventional Mulliken population analysis is used to calculate the atomic charges⁹² which exhibits improved numerical stability and satisfactory description of molecule due to better electron distribution. NPA has a tendency to predict higher partial charges than other population analysis methods. The charges calculated with ChelpG (Charges from Electrostatic Potentials using a Grid based method) are more systematic and quite accurate than the methods based on the analysis of wave function. Here, the partial charges are derived from the calculated MEP (Molecular Electrostatic Potential) at all grid points. The limitation of ChelpG is that the calculated partial charges are not accurate for large systems because the inner atoms are located far away from the points at which the electrostatic potential is evaluated as MEP is a surface characteristic. Sometimes it generates noticeable asymmetric charge distribution over the symmetric atoms as observed for TBP. Since, we wanted to study the real effect of atomic partial charges obtained from different atomic charge generation scheme, the asymmetrical charge distribution was considered though it differs from the conventional approach.

The use of above four partial atomic charge generation schemes to calculate the partial charges on the atoms of ligands TBP, TiAP and TEP leading to four different OPLS-AA force field models. The respective partial charges calculated on atoms of TBP, TiAP, TEP and dodecane using Mulliken, Löwdin, NPA and ChelpG are exhibited that the partial charge on P and O atoms predicted by NPA method is comparatively higher than that of the other methods.⁹⁴

2.7 PAIR CORRELATION FUNCTION

It is very important and necessary to understand the microscopic structure of the molecular system. In this regards the pair correlation function (PCF) or radial distribution function (RDF) has been evaluated which is related to the probability of finding the centre of a particle from the centre of another particle at a given distance. It also provides the information of how the particles are packed together which describes how density varies as a function of distance from a reference particle. This proves to be an effective way of describing the average structure of disordered molecular system such as liquids. Thus the pair correlation functions (PCF) have been evaluated to examine the bulk and interfacial structures of various systems and is expressed^{34, 95, 96} as:

$$g_{ik}(r) = \frac{N}{\rho N_i N_k} \langle \sum_i^{N_i} \sum_{i \neq k}^{N_k} \delta(r - r_{ik}) \rangle \quad (2.20)$$

where $g(r)$ gives the probability of finding of molecule 'k' in a distance r from another molecule 'i'. N , r and ρ indicate total number of molecules, distance and number density respectively. N_i and N_k denotes the number of molecule i and molecule k respectively and r_{ik} is the distance between centre of masses of molecule i and k . The pair correlation function $g(r)$, accounts for these factors with normalization by the density. Thus at large values of r i.e. at large distance, it goes to 1 signifies uniform probability.

Potential of mean force (PMF)^{96, 97} is another important energy parameter which indicates the stability of a component in solvent and is determined using the formula given below:

$$W_{ik}(r) = -k_B T \ln[g_{ik}(r)] \quad (2.21)$$

Here, $W_{ik}(r)$ denotes potential of mean force, $g_{ik}(r)$ is pair correlation function belongs to the interaction between solute and solvent molecules, k_B is Boltzmann constant and T is temperature. The temperature is maintained at 300K.

The free energy (ΔG_R) related to the release of one water molecule from the solvation shell, has been calculated at the first minimum appeared in the potential mean force (PMF) plot. The PMF plot has been generated from the pair correlation function (PCF) using the following equation (2.21). The free energy of release, ΔG_R , which indicates the interaction between ions and water molecules can be also calculated using the above PMF equation.

2.8 SELF-DIFFUSION COEFFICIENT

Self-diffusion coefficient is a highly important dynamical quantity to build up an understanding of mobility of solute particles and is calculated from Einstein's equation using the mean square displacement (MSD) profile as:

$$\lim_{t \rightarrow \infty} \langle (r(t) - r(t_0))^2 \rangle = 6Dt \quad (2.22)$$

where, $r(t)$ and $r(0)$ are positions of atom at any time t and at $t=0$ respectively. D is the diffusion coefficient of molecule, $r(t)$ signifies centre of mass at time t and the angle brackets indicates ensemble averaging over all the molecules and time origins. The left part of the equation indicates the ensemble average of squared displacement i.e. MSD. The diffusivity can be estimated by dividing the gradient by 6 coming from a straight line to a plot of $(r(t) - r(t_0))^2$ against time 't'⁹⁸.

Molecular Dynamics (MD) simulations are a useful method in this respect as one can directly use the effect of molecular interactions to compute the transport properties of a many-body system on diffusion coefficients. It is important to distinguish the self-diffusion and transport (mutual) diffusion. Self-diffusion describes the motion of individual molecules whereas mutual

diffusion can be related to collective motion of the particles which is responsible for mass transport. Here, only self-diffusion coefficient has been calculated for the respective systems.

2.9 FREE ENERGY OF HYDRATION & SOLVATION OF LIGANDS

Free energy calculations have played an important role in computational chemistry for the last few decades. With the ever-increasing availability of computational power, the application of methods to calculate binding free energies in the field of drug discovery is coming within reach. However, in order to obtain the high accuracy required in this field, one has to use the more rigorous free energy methods, which are also the computationally more demanding ones, like free energy perturbation (FEP)^{99, 100} or thermodynamic integration (TI)¹⁰¹⁻¹⁰³ or adaptive biasing method^{104, 105}. The perturbation method utilizes the formally exact statistical mechanical relationship whereas the TI assumes that the Hamiltonian can be defined as a function of a continuously varying parameter, λ . The adaptive biasing method follows the concept of adding continuously updated biasing force in equation of motion which improves uniform sampling on a flat free energy surface, provides reliable free energy estimation.¹⁰⁴ The method of thermodynamic integration (TI) is a technique to calculate free energy differences that best corresponds to the general idea of how to measure the change in free energy of a system when some parameter specifying the thermodynamic state is slowly varied so that at each stage along the path the system is in equilibrium. It is an accurate and straightforward method that does not suffer from the high density and large system problems encountered in most other methods. TI is also known for its simplicity but usually also seen as a computationally demanding method¹⁰⁶.

The calculation of free energy difference or free energy transfer was performed using the thermodynamic integration scheme with the integrator for stochastic dynamics^{101, 107}. Free energy of solvation was computed by decoupling a solute molecule from the solvent using the identity:

$$\Delta G = \int_0^1 \left\langle \frac{dH(\lambda)}{d\lambda} \right\rangle d\lambda \quad (2.23)$$

where, H is the parameterized Hamiltonian. The coupled state ($\lambda = 1$) corresponds to a simulation with the solute fully interacting with the solvent and the uncoupled state ($\lambda = 0$) corresponds to a simulation considering the solute without interaction with the solvent.

Simulations conducted at different values of λ allow to plot a $\partial H / \partial \lambda$ curve, from which ΔG is derived. The value of λ was varied from 0 to 1 with interval of 0.1. The soft core Lennard-Jones potential parameters were taken as $\alpha = 0.5$, $p = 1.0$ and $\sigma = 0.3$.

2.10 PARTITION COEFFICIENT

Partition coefficient (P) or distribution coefficient describes the ratio of concentrations of a neutral solute molecule in a mixture of two immiscible phases at equilibrium. From practical point of view the value of partition coefficient of an extractant permits evaluation of its availability during solvent extraction. The partitioning (P) of a solute (L) between organic (O) and water (W) solvent phases can be described as



where P is expressed as the ratio of equilibrium concentrations of solute in both the solvent phases as

$$P = [L]_o / [L]_w \quad (2.25)$$

The solute present in both the solvents are typically reported as the logarithm of the concentration ratio ($\log P$) which is proportional to the transfer free energy between the two immiscible solvents and can be related to the solvation free energies. Solvation free energies can be used as benchmark to atomistic force fields.

Further, the partition coefficient of solute between water and dodecane phase was calculated using the following standard expression.¹⁰⁸

$$\log P = \frac{\Delta G_{hydration} - \Delta G_{solvation}}{2.303RT} \quad (2.26)$$

Here, $\Delta G_{hydration}$ and $\Delta G_{solvation}$ is the free energy of the solute in water and dodecane respectively. RT is the Universal gas constant time and temperature.

The partition coefficient of a solute between aqueous and organic solvent phase is calculated from change of free energy of transfer from one phase to another phase using COSMO-RS (conductor like screening model for realistic solvents) theory as implemented in COSMOtherm package^{109, 110}. COSMO-RS is an analytical model based on statistical thermodynamics and developed on the COSMO solvation model where a solute is placed in a cavity surrounded by continuum liquid solvent.

The partition coefficient of a solute j between two solvents (aqueous, w and organic, o) can be written as

$$\log P_j(O, W) = \log \left\{ \exp \left[(\mu_j^W - \mu_j^O) / RT \right] \frac{V_w}{V_o} \right\} \quad (2.27)$$

where V_w/V_o is volume quotient and can be evaluated either from experiment or COSMO-RS prediction¹¹⁰. The chemical potential of compound X_i in system S is given by

$$\mu_S^{X_i} = \mu_{C,S}^{X_i} + \int p^{X_i}(\sigma') \mu_S(\sigma') d\sigma \quad (2.28)$$

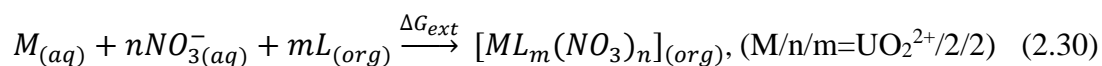
Here $\mu_{C,S}^{X_i}$ is a combinatorial contribution to the chemical potential¹¹¹. The probability distributions ($p^X(\sigma)$) of σ for any compound X_i is called σ profile and the corresponding chemical potential for a surface segment with SCD (screening charge density), σ is called σ -potential and can be described by

$$\mu_S(\sigma) = -RT \ln \left[\int p_S(\sigma') \exp \left\{ \mu_S(\sigma') - \frac{a_{eff} \exp(\sigma, \sigma')}{RT} \right\} d\sigma' \right] \quad (2.29)$$

where each surface segment of a solute is characterized by its area a_i and the screening charge density (SCD, it is the screening of the solute's charge by virtual conductor i.e. the surrounding environment along with the back polarization) is characterized by σ_i .¹¹²

2.11 FREE ENERGY OF EXTRACTION OF UO_2^{2+} ION IN WATER-DODECANE SYSTEM USING DFT/COSMO-RS APPROACH

Further, the extraction ability of a ligand (L) for a particular metal ion (M) can also be predicted by evaluating the free energy of extraction, ΔG_{ext} , using the following complexation reaction:



$$\Delta G_{ext} = E_{ML_m(NO_3)_n(org)} - (E_{M(aq)} + nE_{NO_3(aq)} + mE_{L(org)}) + \Delta nRT - T\Delta S \quad (2.31)$$

Here, L= TiAP, TBP or TEP. $E_{ML_m(NO_3)_n}$, E_M , E_{NO_3} and E_L represent the total electronic energy of the respective chemical species. Here, T is the temperature, which was taken as 298.15K and ΔS is the change in entropy due to complexation which was evaluated using earlier reported methods¹¹³⁻¹¹⁸. In order to evaluate the electronic energy, first the structure of free ligands and their complexes with uranyl nitrates were optimized at the B3LYP/SVP level⁷⁰,⁷¹ of theory using TURBOMOLE package^{69, 72} followed by single point energy at the B3LYP/TZVP level of theory. In the case of U atom, effective core potential (ECP) was used, where 60 electrons were kept in the core of U¹¹⁹.

2.12 DIPOLE MOMENT

The electric dipole moment of any molecule or complex can predict the behaviour of that molecule in any liquid system. Again, the shape of a molecule and the polarity of its bonds determine the overall polarity of that molecule. The polarity of a complex molecule like TBP or TIAP depends upon whether its overall centres of positive and negative charges overlap. When the centres lie at the same point in space, then the molecule has no overall polarity

otherwise it shows. So, the symmetric molecules exhibit no net dipole moment while the molecule can only be polar if the structure is not symmetric.

Dipole moment is measured in Debye units, which is equal to the distance between the charges multiplied by the charge. The dipole moment of a molecule can be calculated as

$$\vec{\mu} = \sum_i q_i \vec{r}_i \quad (2.32)$$

The dipole moment of asymmetric molecules can be computed by the equation:

$$P(r) = \sum_{i=1}^N q_i (r_i - r) \quad (2.33)$$

where, r locates the point of observation and each r_i is a vector from some reference point to the charge q_i .

Now, the dipole moment of liquid state was computed using the following expression:

$$P_n = \sum_i q_i (r_{ni} - r_n^{com}) \quad (2.34)$$

where, P_n is the instantaneous dipole moment vector of n -th molecule. The summation in the equation (2.33) runs through all atoms i in a molecule. The ensemble average of the magnitude of the dipole moment over all the ligand molecules in the system is obtained from the equation (2.34) and equation (2.35) represents the ensemble average.^{120, 121}

$$p_D = \left\langle \left(\frac{1}{N} \sum_{n=1}^N P_n^2 \right) \right\rangle \quad (2.35)$$

2.13 SHEAR VISCOSITY

The shear viscosity is an important property of a liquid, can be easily determined from experiments but also it is useful for parameterization or validation of force field, because it measures the kinetic property of liquids. Other properties might also be used for parameterization but they are of thermodynamic nature. It is not only important for pure liquids as it also influences the diffusion and the structural change of molecules solvated in a liquid and thus influences the mass transfer. The shear viscosity can be evaluated by several methods

either by pressure fluctuation or momentum fluctuation described in the literature. The accurate estimation of shear viscosity by transverse current auto correlation function (TCAF)¹²²⁻¹²⁴ from equilibrium molecular dynamics (EMD) calculations was found difficult due to heavy pressure fluctuation and also attaining convergence in this method is very slow. The periodic perturbation method from non-equilibrium molecular dynamics (NEMD) calculations determined the shear viscosity using momentum fluctuations. According to the various studies reported in the literature, the NEMD method is more efficient for the determination of viscosity compared to the EMD method.^{125, 126} Therefore, the shear viscosity has been computed using periodic perturbation method by performing NEMD calculations.

Periodic perturbation method

In periodic shear flow method, an external force is applied to the system instead of measuring intrinsic fluctuations of the system i.e. considered as a fixed magnitude. An external force ‘**a**’ which cause a velocity field ‘**u**’ in the liquid and it is easier to measure the viscosity than the internal fluctuation. According to the Navier–Stokes Equation, the velocity of the liquid in the x-direction where there is no pressure gradient in this direction, can be written as

$$\rho \frac{\partial u_x(z)}{\partial t} = \rho a_x(z) + \eta \frac{\partial^2 u_x(z)}{\partial z^2} \quad (2.36)$$

Steady state solution yields

$$a_x(z) + \frac{\eta}{\rho} \frac{\partial^2 u_x(z)}{\partial z^2} = 0 \quad (2.37)$$

As the periodic system is used in the simulations, the corresponding velocity and acceleration profiles should be periodic. A smooth velocity profile can be obtained with small local shear rates when the acceleration profile should be smooth. Thus, a simple function which satisfied the conditions is a cosine function as

$$a_x(z) = A \cos\left(\frac{2\pi z}{l_z}\right) \quad (2.38)$$

It is the function of z coordinate only as a_y and a_z are zero]; l_z is the height of the box and ρ is the density of the liquid. At $t=0$, $u_x(z) = 0$ and the velocity profile of the liquid is written as

$$u_x(z, t) = V \left(1 - e^{-\frac{\eta k^2 t}{\rho}} \right) \cos(kz) \quad (2.39)$$

$$V = A \frac{\rho}{\eta k^2} \quad (2.40)$$

$$k = \frac{2\pi}{l_z} \quad (2.41)$$

The Navier-Stokes equation is not valid for microscopic length scales, therefore the wavelength should be at least an order of magnitude larger than the size of a molecule.

In an MD-simulation acceleration can be added to each particle, according to the cosine equation (eq. 2.38). The average v can be measured and the viscosity can be calculated using the following formula:

$$\eta = \frac{A \rho}{V k^2} \quad (2.42)$$

The detail description for the calculation of V is available elsewhere.¹²⁵ The shear viscosity has been computed from NEMD simulations for pure liquids and liquid mixtures at constant external force or cosine acceleration of 0.10 nm/ps^2 in the x -direction with velocity – rescaling thermostat. The external force above 0.10 nm/ps^2 , causes a decrease in shear viscosity as it goes far away from equilibrium. The external force is chosen in such a manner so that there is nonlinearity in the fluid temperature as reported by Hess¹²⁵.

2.14 INTERFACIAL TENSION (IFT)

The oil – water interfaces are ubiquitous in nature, and also have important implications in a wide variety of chemical, physical and biological processes. Understanding of these processes relies on fundamental knowledge at the molecular level of the structural and dynamic characteristics of the interface itself. In this regards, interfacial tension is an essential physical

property which provides the detailed insight into liquid–liquid interfaces and plays a significant role in the extraction and stripping mechanism. It is calculated from the pressure tensor method. The surface tension is computed using diagonal terms of pressure tensor. The element of pressure tensor (P_{xy}) can be calculated from the particle's velocity, force and position as:

$$P_{xy} = \frac{1}{V} \left(\sum_{i=1}^N m_i v_{ix} v_{iy} + \sum_{i=1}^{N-1} \sum_{j=i+1}^N F_{ijx} r_{ijy} \right) \quad (2.43)$$

where, r_{ijy} refers to the y component of distance between the centres of molecule i and molecule j, F_{ijx} denotes the x component of total force acting on molecule i due to molecule j. Then, m_i is mass of particle 'i', v_{ix} and v_{iy} is the velocity of molecule 'i' in x and y direction.¹²⁷ Once, the pressure tensor is obtained, then the interfacial tension can be expressed when the interface is perpendicular to z axis as:

$$\gamma = \frac{L_z}{2} \left(P_{zz} - \frac{P_{xx} + P_{yy}}{2} \right) \quad (2.44)$$

where, P_{xx} , P_{yy} and P_{zz} are the diagonal terms of the pressure tensor while L_z represents the box length along the z direction.¹²⁷⁻¹²⁹

2.15 INTERFACE WIDTH OR THICKNESS (IFW)

The aim that waves on the liquid surface can be used to study the properties of this surface has been studied long back. The joint action of gravitational and capillary forces have been taken into account on the form of the surface wave yields the dispersion relation, which relates the spatio-temporal characteristics of the running wave with the liquid density and surface tension. Both mechanisms act to return the disturbed surface to the mechanical equilibrium state. The gravitational force is important in a long wave case (gravity waves), whereas the capillary force is dominated in short waves formation (capillary waves). In the interim case when the wavelength $\lambda \sim \pi a \sqrt{2}$ (a –capillary length), waves are the gravity-capillary waves.

Theoretically, the issue of how to define the interfaces microscopically and how to measure interface thickness, has encountered difficulties related to the fact that interfacial fluctuations are rough. The capillary wave method is a well-known classical technique to measure surface tension and surface rheological properties.¹³⁰ Despite the large number of theoretical works devoted to capillary waves, this technique has serious difficulties associated with its implementation, and therefore, it is not widely used by researchers.^{131, 132}

So, it is very critical to calculate the actual thickness of interface. The nature of the liquid/liquid interface described above has led to efforts aiming to describe it using capillary wave theory (CWT)^{133, 134}. A capillary wave is excited by pressure fluctuations generated locally at the interface. According to the CWT, a thermal motion generated from fluctuating interface produces a capillary wave at the molecular level and it is an account of how thermal fluctuations distort an interface. The surface tension contribution is relevant while the gravity and hydrodynamics part has negligible dependency. Most of these efforts rely on a relationship established by CWT between the width of the interface due to capillary wave fluctuations and the macroscopic interfacial tension.

The interfacial thickness using capillary wave theory (CWT)¹³³ is written as:

$$w_c^2 = \frac{k_B T}{2\pi\gamma} \ln\left(\frac{L_{II}}{L_b}\right) \quad (2.45)$$

where, w_c is the interface thickness due to capillary wave, k_B is Boltzmann constant, T is temperature, L_{II} is the box dimension along the x or y direction and L_b represents the bulk correlation length in terms of the molecular length.

2.16 SURFACE TENSION

Surface tension is a very useful physical property which plays an important role in liquid – liquid extraction and stripping operation in particular and various interfacial processes in general. The methodology is similar to the calculation of interfacial tension. Only change is

that here the system has only one phase so the space to be provided for vapour phase where some molecules of aqueous phase will escape from aqueous layer during simulation¹³⁵.

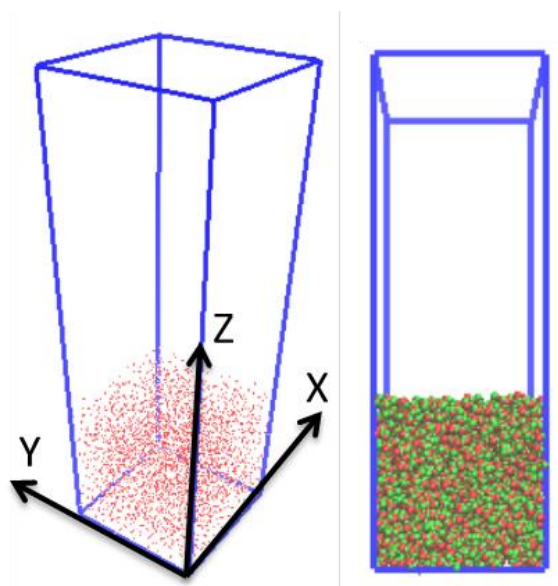


Figure 2.4: Typical diagram of rectangular simulation box extended towards *z*-direction used for calculation of surface tension of pure component.

For this reason the box is elongated along *z* direction but it can be done in any direction as various simulation box geometries can be considered for study of interfacial system. Note that here $L_x = L_y = 3 \cdot L_z$ is used for study where L_x , L_y and L_z are box length in *x*, *y* and *z* direction respectively as shown in **Figure 2.4**.

This rectangular box with vapour phase having two times of liquid volume is used as an input for surface tension calculation in GROMACS package.

2.17 WATER TRANSPORT IN ORGANIC PHASE

Further, the water solubility is an equally important parameter for aqueous-organic biphasic extraction system. The water solubility in the organic phase is estimated by computing the number of water molecules in the organic phase. Hence, the extraction of water molecules in

mole/lit is related to the number of water molecules in the organic phase and it is estimated as per the following relation

$$N_{Ex} = (n_m/N)/V \quad (2.46)$$

where, N_{Ex} represents the water extraction as solubility, n_m is the number of molecule extracted in each phase, N is total number of molecules and V denotes the volume of phase.

2.18 HYDROGEN BOND DYNAMICS

The understanding of network of hydrogen bond dynamics are very much important and are also play a key role in many physical, chemical and biological processes. The process of formation and breaking dynamics of H – bonds is very much significant in the dynamic behaviour of liquids. A microscopic understanding of water is essential to find out the static and dynamic behaviour of H – Bonds networks which characterises the properties.¹³⁶⁻¹³⁸ The tetrahedral structure of water and H – bond dynamics of water - water hydrogen bonds also take part in determining the thermo- physical and thermo-dynamical properties of molecular system in aqueous solutions.¹³⁸ Again, the study of interfacial H – bonds helps to develop an understanding interfacial aggregation and complex formation and it is challenging also. The H – bond life time is an important parameter to explain the geometry of liquids and it is also sensitive to temperature, pressure and chemical conditions. The average lifetime of H – bonds can be evaluated by calculating the time-dependent autocorrelation function.¹³⁹ MD simulations are the potential tools to characterize the dynamics of hydrogen bonds quantitatively for liquids in terms of different hydrogen bond time autocorrelation functions.

Definition of hydrogen bonding:

In computer simulation the potential of interactions between molecules have been introduced without distinguishing hydrogen bonding presence in it. So, some additional criteria have to be used to identify between which molecules this H – bonding occurs. The important criterion is

geometrical which differentiates between H – bonded and non H – bonded pairs of molecules. Let us assume the two molecules are to be hydrogen bonded if the following conditions are simultaneously satisfied,¹³⁶⁻¹⁴⁰

- I. The oxygen-oxygen distance (R_{OO}) does not exceed some boundary value and it is less than 3.6 Å.
- II. The distance between donor hydrogen and acceptor oxygen (R_{OH}) in neighbouring molecule also does not exceed some value and it is less than 2.4 Å.
- III. The angle θ_{HB} between the vector connecting the two oxygen atoms and the vector connecting the donor oxygen and acceptor hydrogen atom is less than 30°.

So, the dynamics of hydrogen bonds among molecules present in the medium is investigated by calculating the intermittent hydrogen bond auto-correlation function. The time autocorrelation function relates the probability of the H-bond existing at a given starting point $t = 0$ will also exist at the next instant t , regardless whether the H – bond was broken or not in the interval $[0$ to $t]$ and whether it will exist after the instant t .

$$C(t) = \frac{\langle h(0) h(t) \rangle}{\langle h(0) h(0) \rangle} \quad (2.47)$$

where, $h(t)$ measures the existence of H – bonds at any time t . The value of $h(t)$ becomes unity, if the particular tagged pair of water molecules is hydrogen bonded at time t , according to adopted geometry criteria for H bond relation or zero if the H – bond is absent. $C(t)$ represents the probability that H bond is intact at time t , given that it was intact at time 0, independent of possible breaking in the intervening time.

It will be really interesting to look into the local hydrogen bond topology¹⁴¹⁻¹⁴³ to enrich the present works. The tetrahedrality parameter following the prescription of Chau and Hardwick¹⁴⁴ was determined for pure solvent and uranyl solution.

The tetrahedral order parameter is composed of two parts. One is angular part (S_g) and other is distance part (S_k). Orientational tetrahedral order (q) is the widely used parameter where the q varies from 0 (belongs to ideal gas) to 1 (for regular tetrahedron).¹⁴⁵ The angular part can be expressed as¹⁴⁴

$$S_g = \frac{3}{8} \sum_{j=1}^3 \sum_{k=j+1}^4 \left(\cos \Psi_{jk} + \frac{1}{3} \right)^2 \quad (2.48)$$

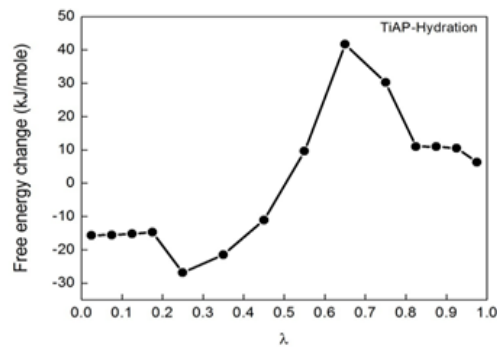
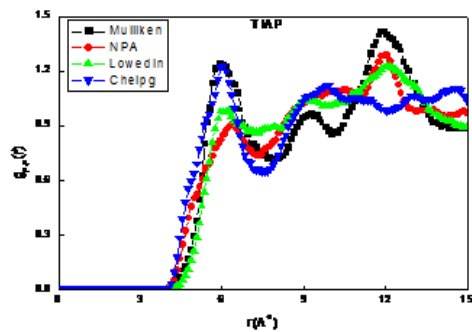
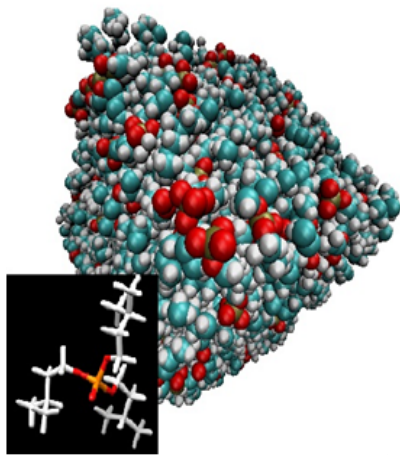
where, Ψ_{jk} denotes angle between the lines joining the oxygen atom of the water molecule and its nearest neighbour oxygen atoms j and k . Then the orientational tetrahedral order can be written as

$$q = 1 - S_g \quad (2.49)$$

where, q signifies the change in local structure of liquid water in the influence of solutes and surfaces. When the S_g increases, q decreases indicating deviation from regular tetrahedral structure of water.

Chapter 3

Calibration of Force Field & Screening of Ligand



CHAPTER THREE

Calibration of Force Field & Screening of Ligand

3.1 INTRODUCTION

In this chapter the screening has been done between the most popular ligand TBP and its higher homologous TiAP which may be an efficient ligand in the field of liquid – liquid extraction. In addition to that the TEP is studied to verify the force fields of interest. In this context, the screening has been performed based on their structural, physical, thermo-physical and dynamical properties. For investigation of molecular properties, the MD simulations have been carried out based on classical force field. The accuracy of physical and thermo dynamical properties strongly depend on the reliability of force field. The availability of good force field is pivotal for modelling the pure liquid systems which can arrest the intra-molecular and intermolecular interactions.

In earlier works, various groups of researchers developed force field for pure ligands. Many times force fields are parameterized to match the experimental data like dipole moment or density or heat of vaporization.⁴⁷ But this parameterization approach is not a good option as it

is slightly case sensitive. At the same time force fields are highly sensitive to the partial charges on atom. Hence, the selection of partial atomic charges is also crucial to obtain accurate properties of interest. Therefore, the selection of partial charges as well as the screening of ligands is discussed in the present chapter.

3.2 SIMULATION SYSTEMS

The present MD study was conducted with 200 numbers of molecules (500 for TEP) for 10ns simulation length to determine the suitable charge model. All the systems were first energy minimized using steepest decent method followed by equilibration for 10ns in isothermal-isobaric (NPT) ensemble at P=1 atm and T=300K with a time step of 1fs using standard periodic boundary condition in all directions. Berendsen⁸⁰ and Parrinello-Rahman⁸³ like weak coupling methods have been used to maintain the constant temperature and pressure respectively. The time constants for temperature coupling and pressure coupling were taken as 1.0 ps and 0.5 ps respectively. Finally, the production run was done with canonical (NVT) ensemble using 10ns simulation length. The detailed simulation compositions for different pure liquids as well as solvated ligand systems are given in [Table 3.1](#) and [Table 3.2](#). For water simple point charge (SPC) model potential was used.

Table 3.1: Compositions of MD simulations systems: Box size and number of molecules for pure liquid

System	Box Size (nm)	Molecules
TBP	4.54 x 4.54 x 4.54	200
TiAP	4.78 x 4.78 x 4.78	200
TEP	5.18 x 5.18 x 5.18	500
Dodecane	4.24 x 4.24 x 4.24	217

Table 3.2: Compositions of MD simulations systems: Box size, number of solvent and solute molecules for hydration and solvation of TBP, TiAP and TEP

System	Hydration		Solvation	
	Box Size (nm)	Water molecules	Box Size (nm)	Dodecane molecules
TBP	4.54 x 4.54 x 4.54	876	4.16x4.16x4.16	200
TiAP	4.78 x 4.78 x 4.78	875	4.16x4.16x4.16	200
TEP	5.18 x 5.18 x 5.18	882	4.27x4.27x4.27	200

3.3. RESULTS & DISCUSSIONS

3.3.1 Liquid state structure of the ligands and the solvents

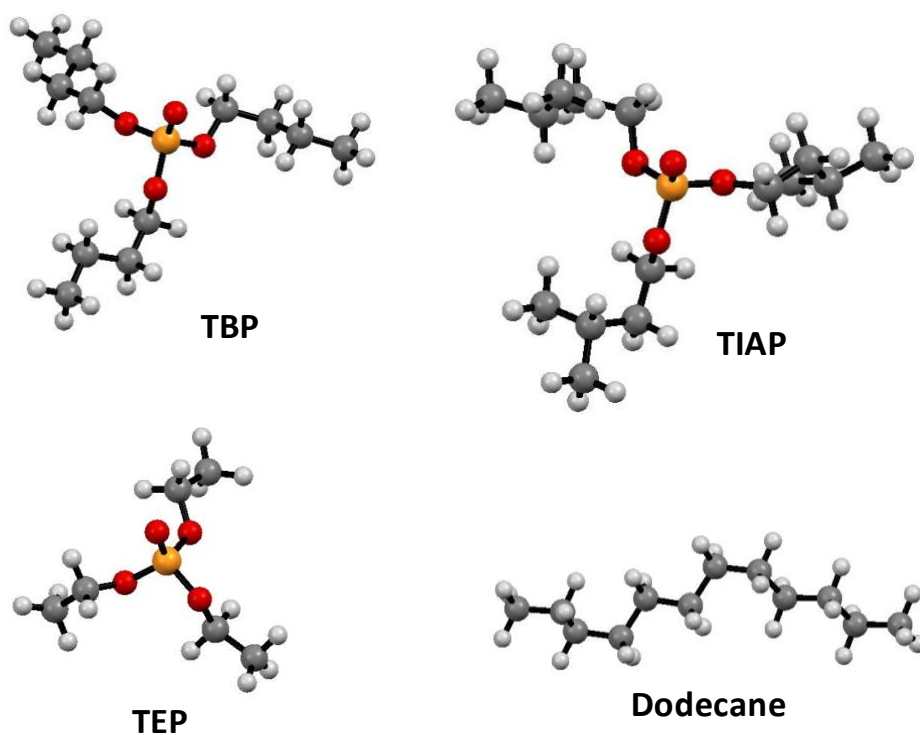


Figure 3.1: Optimized structures of ligand/solvent (red sphere: Oxygen atom; orange sphere: Phosphorous atom; grey sphere: Carbon atom and white sphere: Hydrogen atom)

Since it is of importance to use accurate structure for MD simulations, the ligands studied here were optimized and the structure (see [Figure 3.1](#)) was then used for generation of initial coordinates in the MD simulations.

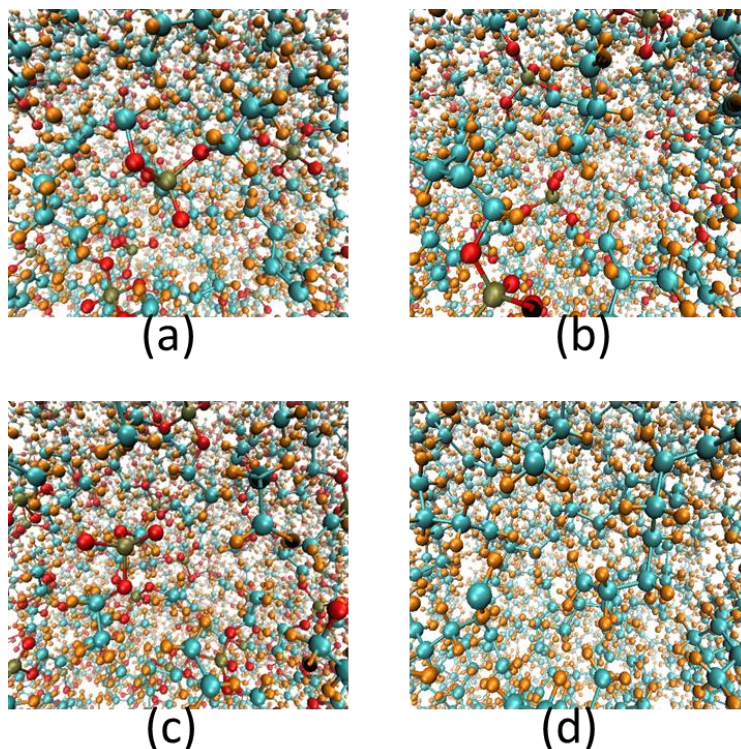


Figure 3.2: Snapshot of equilibrated structure of pure (a) TBP (b) TiAP (c) TEP (d) Dodecane after 10ns simulation run (Red: Oxygen atom; Olive green: Phosphorous atom; Cyan: Carbon atom and Orange: Hydrogen atom).

The MD simulations were conducted using 200 numbers of molecules for TBP and TiAP and 500 numbers of molecules for TEP ligand. The snapshots of liquid structure for the studied ligands and dodecane are presented in [Figure 3.2](#). From the snapshots, it is observed that the molecules of TBP, TiAP, TEP and dodecane stay spread homogeneously, demonstrating the liquid phase behaviour of TBP, TiAP, TEP and dodecane. It is worth to note that we did not observe any gel formation of dodecane as reported earlier⁴⁷ as evident from [Figure 3.2\(d\)](#).

3.3.2 Mass density of the pure ligands and solvents

Mass density is an important thermodynamic property which is strongly related to the intra-molecular and inter-molecular interactions between particles in a system. The pure liquid systems for TBP, TiAP and TEP without any partial charge were studied here for different simulation length like 10ns, 20ns, 30ns, 40ns and 50ns. Systems were then equilibrated using isothermal-isobaric (NPT) ensembles. The mass density of three ligands (TBP, TiAP and TEP) was computed against simulation length from 10ns to 50ns and it was seen that the density is independent of the simulation length after 10ns. Therefore, subsequently, all the equilibration runs were performed for 10ns simulation length.

Mass density profile of pure TBP, TiAP and TEP

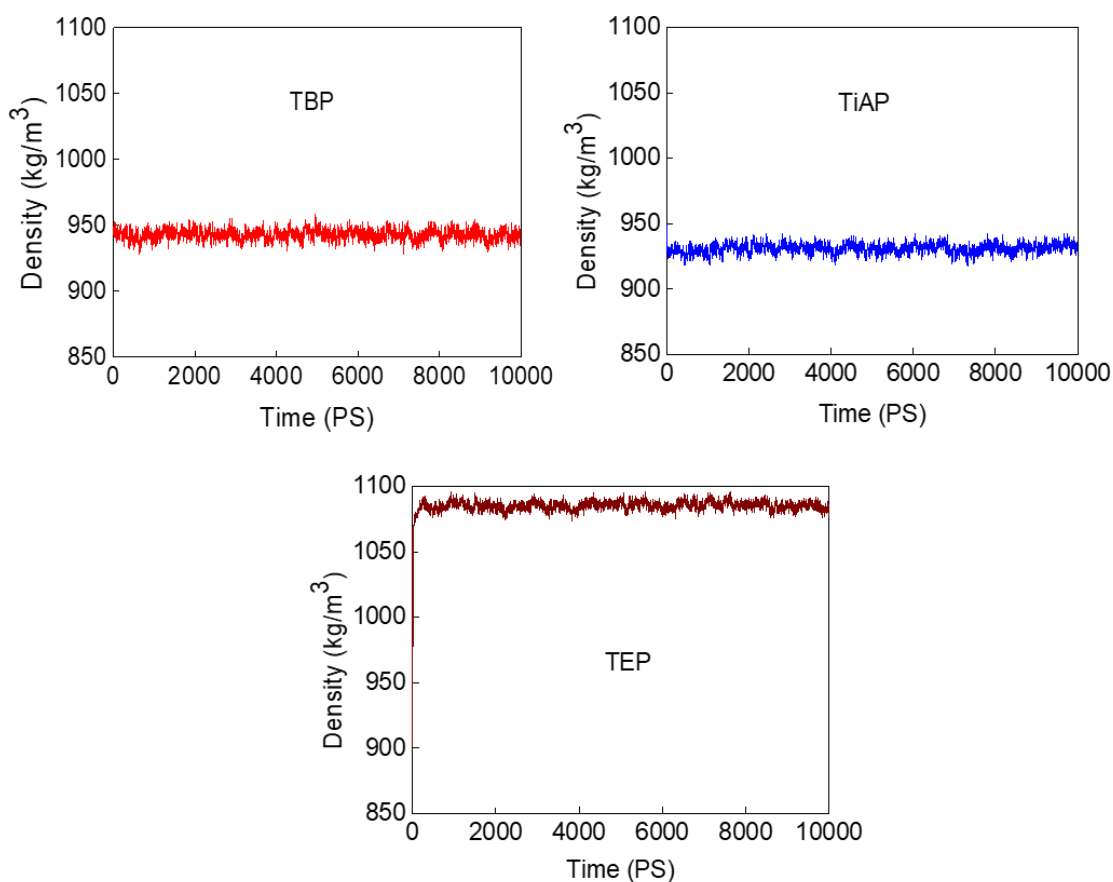


Figure 3.3: Density profile of pure TBP, TiAP and TEP with time

Furthermore, the density of all three liquid ligands was converged within few picoseconds and it was clearly established from the time profile of the density which is nearly constant indicating its equilibrium condition as shown in **Figure 3.3**.

Furthermore, in order to test the system size dependency, a system containing 500 numbers of TBP molecules was also equilibrated for 10ns simulation length and it was found that the density is almost same as with 200 TBP molecules (see **Table 3.3**). The % deviation from experimental data is same for both 200 and 500 molecules. Hence, all the calculations were performed using 200 molecules only.

Table 3.3: Calculated density for different system of pure TBP using Mulliken partial charge model*

No. of Molecules	Density (kg/m ³)	% Deviation
200	958.90±0.46	1.41
500	958.32±0.97	1.48

*Errors were estimated by standard block averaging

Mass density of pure TBP, TiAP and TEP using DFT derived partial charges:

In order to calibrate the OPLS-AA force field, four different population analysis methods as described in the methodology section were used to calculate the partial charges on the atom of the molecule. The density of various charge model for TBP, TiAP and TEP were determined from simulations using DFT derived charges and it was seen that the density is charge sensitive (see **Tables 3.4 – 3.6**). The calculated density of the pure TBP, TiAP and TEP and their reported experimental values are presented in **Table 3.4, 3.5** and **3.6** respectively.

Table 3.4: Calculated density (kg/m³) of TBP and deviation from experimental data for different charge model*

Model	Mulliken	Löwdin	NPA	ChelpG
MD	958.90±0.46	954.29±0.19	1003.26±2.0	991.40±1.2
Experiment	972.7	972.7	972.7	972.7
% Deviation	1.41	1.89	3.14	1.92

*Errors were estimated by standard block averaging. The reported densities of pure TBP in literature are 980.3 kg/m³ using scaled charge and 997.8 kg/m³ using un-scaled charge from OPLS/DFT model⁴⁶.

From [Table 3.4](#), it is seen that the density obtained from the partial charge calculated by Mulliken population analysis for TBP molecule is closer to the experimental value followed by Löwdin model. It is worth noting that density predicted by Mulliken and Löwdin underestimate the experimental density whereas NPA and ChelpG overestimate the experimental density.

Table 3.5: Calculated density (kg/m³) of TiAP and deviation from experimental data for different charge model*

Model	Mulliken	Löwdin	NPA	ChelpG
MD	950.39±1.3	937.67±0.76	973.29±1.9	998.97±1.7
Experiment	947	947	947	947
% Deviation	0.35	0.98	2.77	5.48

*Errors were estimated by standard block averaging

In case of TiAP the similar trend is obtained and the partial charge predicted by Mulliken population analysis method exhibits the best agreement with the experimental results (see **Table 3.5**). The % deviation of calculated densities from the experimental value for Mulliken, Löwdin, NPA and ChelpG are 0.35%, 0.98%, 2.77% and 5.48% respectively. From the above table it is seen that the Mulliken, NPA and ChelpG overestimate the experimental density whereas Löwdin underestimates the experimental density.

Table 3.6: Calculated density (kg/m³) of TEP and deviation from experimental data for different charge model*

Model	Mulliken	Löwdin	NPA	ChelpG
MD	1062.82±0.83	1027.71±0.77	1085.87±0.97	1069.01±0.82
Experiment	1072	1072	1072	1072
% Deviation	0.85	4.13	1.29	0.27

*Errors were estimated by standard block averaging. The reported density of pure TEP in literature⁸⁹ was 1082.1kg/m³.

From **Table 3.6**, it is observed that for TEP, the density obtained from the partial charge predicted by ChelpG method is though close to the experimental value, the density calculated from Mulliken charge is not far from (within 0.85%) the experimental value. The ChelpG model is shown to be quite efficient for the prediction of partial charges for small molecular system that might be the reason for good agreement with experimental results. From the above table, it is observed that the Mulliken, Löwdin and ChelpG underestimate the experimental density whereas NPA overestimates the experimental density.

The mass density of dodecane was also evaluated using Mulliken charge which was found to be 744.82 kg/m³ which is in excellent agreement with the experimental result of 745.80

kg/m³. Whereas the density of pure dodecane using OPLS-AA and refined L-OPLS-AA was reported⁴⁷ as 838.45 kg/m³ and 744.89 kg/m³ respectively. The density profile with simulation length for dodecane is displayed in **Figure 3.4**.

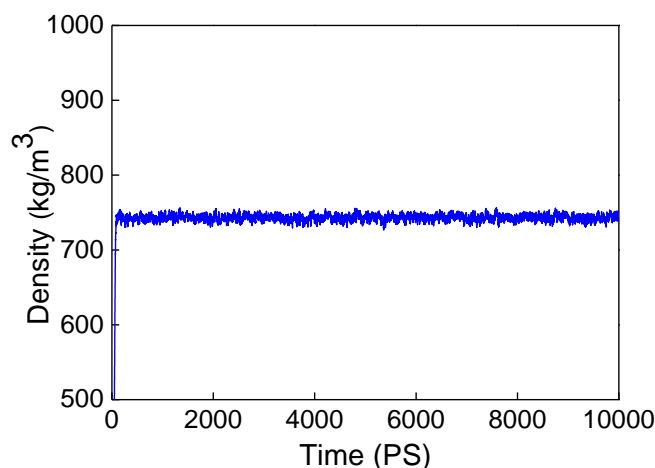


Figure 3.4: Density profile of pure dodecane

From overall density analysis for all the ligands using four different charge models, it can be stated that the OPLS-AA force field using Mulliken charge is the most suitable force field. It is worth mentioning here that earlier [Cui et al⁴³](#) and recently [Junju Mu et al⁴⁶](#) have arbitrarily scaled the charges used in the OPLS force field to match the mass density of TBP within 0.30% and 0.47% of the experimental value respectively for TBP, whereas, in the present study though Mulliken charge embedded OPLS-AA force field predicts the density little higher (within 1.41% of the experimental value) for TBP, it estimates the density of TiAP and TEP within 0.27% and 0.85% respectively and for dodecane within 0.13%. It is worth mentioning that the mass density of TBP predicted by [Cui et al⁴³](#) using unscaled charge was overestimated by 2.78% at the OPLS-DFT level of calculation whereas Mulliken charge embedded OPLS-AA force field predicts the density within 1.41%. Earlier, the calculated density for TEP was reported by [Caleman et al¹⁴⁶](#) was 1082.1±0.3kg/m³ which was

overestimated compared to experimental density of 1072kg/m^3 by 0.94% whereas in the present simulation the calculated density using Mulliken charge is 1062.82 kg/m^3 which underestimates the experimental density by 0.85% and thus further confirms the acceptability of Mulliken charge embedded OPLS-AA force field. Therefore, it might be stated that the Mulliken charge embedded OPLS-AA force field is the best calibrated OPLS-AA force field to simulate the try-alkyl phosphates and n-alkanes.

3.3.3. Pair correlation function (PCF) of pure liquid: TBP, TiAP and TEP

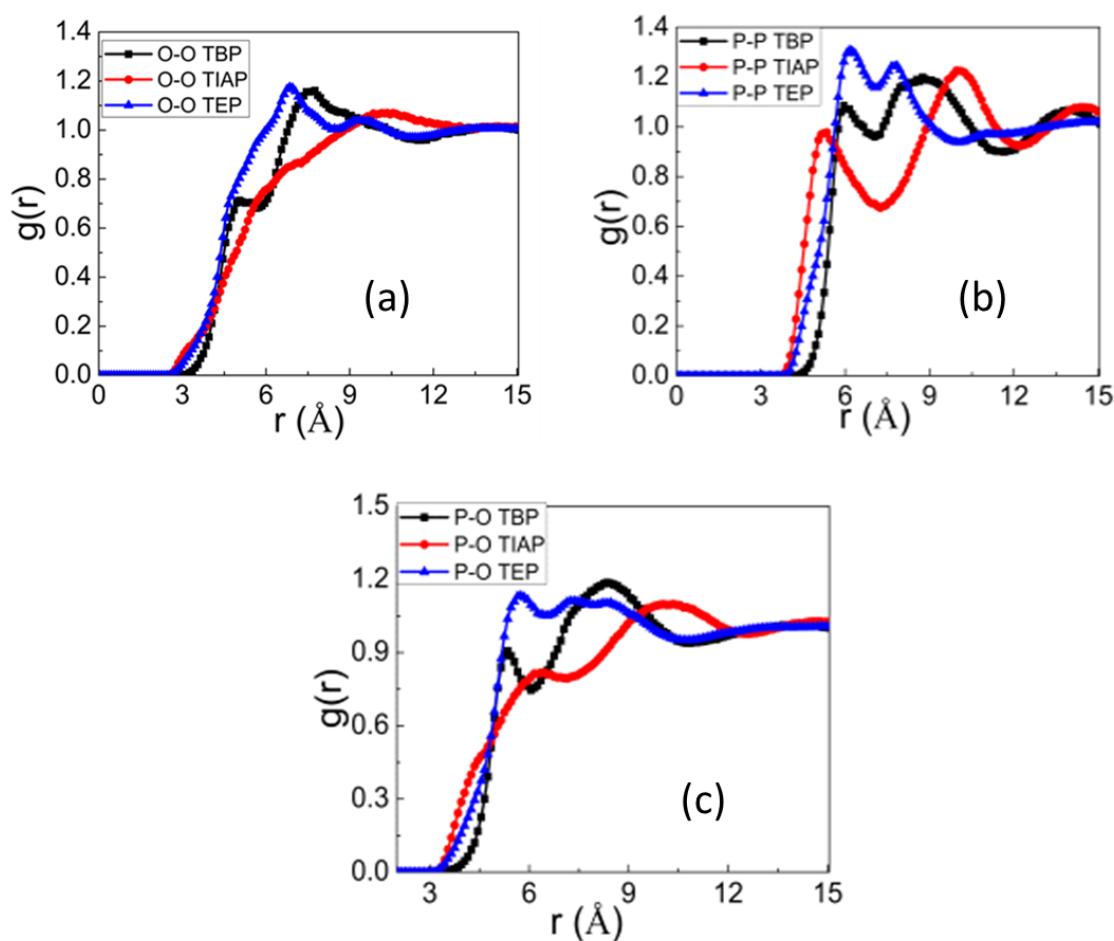


Figure 3.5: Intermolecular pair correlation functions between the pairs of atoms of P – P, P – O and O – O for pure TBP, TiAP and TEP ligands. (a) PCF's of O – O atoms (b) PCF's of P – P atoms (c) PCF's of P – O atoms.

It is similarly important to know the structural information of the pure liquids. The microstructure of liquids is well characterized from spatial pair correlation function which can also be determined from X-ray or neutron scattering. To the best of our knowledge we are unable to find any experimental data of PCF for the pure liquids studied here for comparison with computational results.

The theoretically computed PCFs not only provided the microscopic liquids state signatures but also help in understanding the macroscopic properties of the liquids as it accounts the interaction between molecules in bulk liquid phase. The strongest interaction between these tri-alkyl phosphate ligands involves through mainly the P and the O₂ atoms, hence, the discussion is mainly focused on the atoms of the phosphoryl group. The PCFs for P–P, P–O₂ and O₂–O₂ are analysed to determine the relative position between two interacting molecules which are shown in [Figure 3.5](#). Point to be noted here that the zero atomic charge was considered for these simulations. In [Figure 3.5](#), at a distance of 3Å in both the cases, there is no chance of finding any adjacent atom and hence the RDF is zero at very short distance due to the strong repulsive forces. The first minima in the P-P pair correlation function of TBP, TiAP and TEP appears at 7.05, 7.25 and 7.05Å respectively. In case of P-O pair correlation function, the first minima were noticed at 6.05, 7.05 and 7.95Å respectively. For O–O pair correlation function, the first minima were obtained at 5.85, 6.85 and 7.85Å respectively. The first peak height for P-P, P-O and O-O atom pairs was seen to be higher for TEP than that of TBP followed by TiAP. This is expected as neighbouring atom pairs come very close for TEP than TBP and TiAP due to smaller bulky tail (ethyl) compared to large bulky tail of butyl and iso-amyl for TBP and TiAP respectively.

A comparative study of PCFs for the different charge models are also discussed which will help in understanding the effect of atomic charge at the molecular level.

P–P Pair Correlation Function

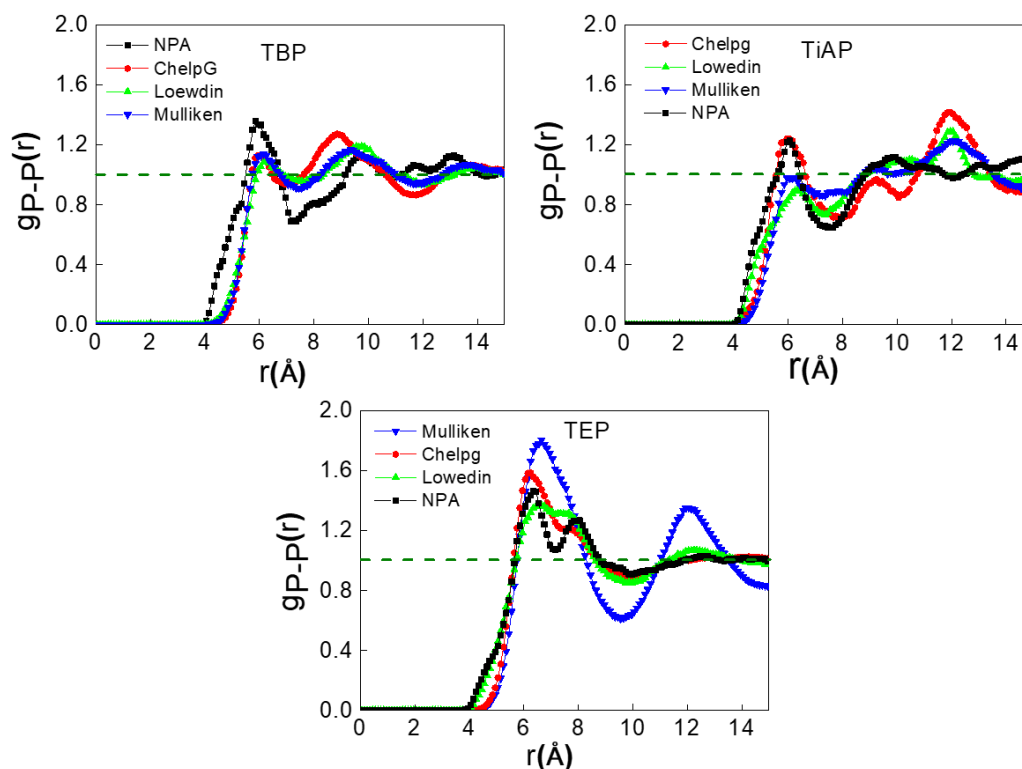


Figure 3.6: Intermolecular pair correlation functions between the pairs of atoms of P–P for different charged model of three ligands. (a) PCF's of P–P atoms of two TBP molecules (b) PCF's of P–P atoms of two TiAP molecules (c) PCF's of P–P atoms of two TEP molecules.

- TBP:** Figure 3.6(a) shows PCF's of P–P using the four different DFT charge models: Mulliken, Löwdin, NPA and ChelpG respectively for TBP molecule and they produce similar type of PCF's. The locations of first peak height for all the charge models are appeared at around 5.9 – 6.2 Å and the second peaks are at approximately 8.8 – 9.7 Å. The NPA charge model produces the higher peak may be due to the higher partial charges computed by NPA method. The first peak position using Mulliken charge appears at 6.05 Å which is very close to the value obtained by Cui et al⁴³.

- TiAP:** **Figure 3.6(b)** shows PCF's of P–P atoms for two interacting TiAP molecules with effect of different charge model. The peak heights are different for different charge model, the peak locations are somewhat at same distances: the first peak is appeared at around 5.9 – 6.3 Å. Mulliken charge model is giving a weak peak around 9.15 Å and a second peak at 12.15 Å. Löwdin model is giving a broad peak between 9.3 – 9.8 Å followed by a second peak at 11.9 Å. For NPA model, a broad peak is appeared at approximately 9.7–10.1 Å. For ChelpG model, there is a weak peak around 9.25 Å and a sharp second peak at around 11.95 Å.
- TEP:** **Figure 3.6(c)** represents the PCF's of P–P atoms for two TEP molecules with different charge model and the distance of first peak locations for all the charge model are at around 6.25 to 6.65 Å. The second peak is appeared approximately at 8 Å for NPA and for other charge model at around 12 – 12.75 Å. The stronger repulsion for the NPA charge model does not permit the closer approach between the phosphoryl groups.

P–O Pair Correlation Function

- TBP:** The PCF's of P – O atoms for two interacting TBP molecules with four different DFT charge models: Mulliken, Löwdin, NPA and ChelpG are shown in **Figure 3.7(a)**. The first peak is located at around 5.2 – 5.5 Å. The Second peaks for Mulliken and Löwdin charge model are appeared at 9.1 and 9.7 respectively. NPA charge model is giving a weak peak at 7.3 Å followed by a second peak at around 9.7 Å. For ChelpG charge model, there is a broad peak at around 8.1 Å. The first peak position using Mulliken charge appears at 5.35 Å which is very close to the value obtained by Cui et al⁴³.
- TiAP:** The PCF's of P – O atoms for two interacting TiAP molecules for different charge models are shown in **Figure 3.7(b)**. The first peak locations for Mulliken,

NPA and ChelpG charge model are appeared at around 5.9, 5.4 and 5.8 Å respectively. For Löwdin charge model, the first peak is pushed up to a larger distance at around 7.6 Å which results an overlap with the second peak and the second peak is appeared at 10.0 Å. The second peaks are located for Mulliken and ChelpG charge model at around 11.1 and 10.6 Å respectively. For NPA charge model, there is a broad peak at around 10.3 – 10.6 Å.

- **TEP:** The **Figure 3.7(c)** represents the PCF's of P – O atoms for two TEP molecules with different charge model and the locations of first peak all the cases are at around 5.5– 5.8Å. The second peak locations are appeared approximately at 7.0 – 7.7Å. Mulliken charge model is showing a third peak at a location of 12 Å.

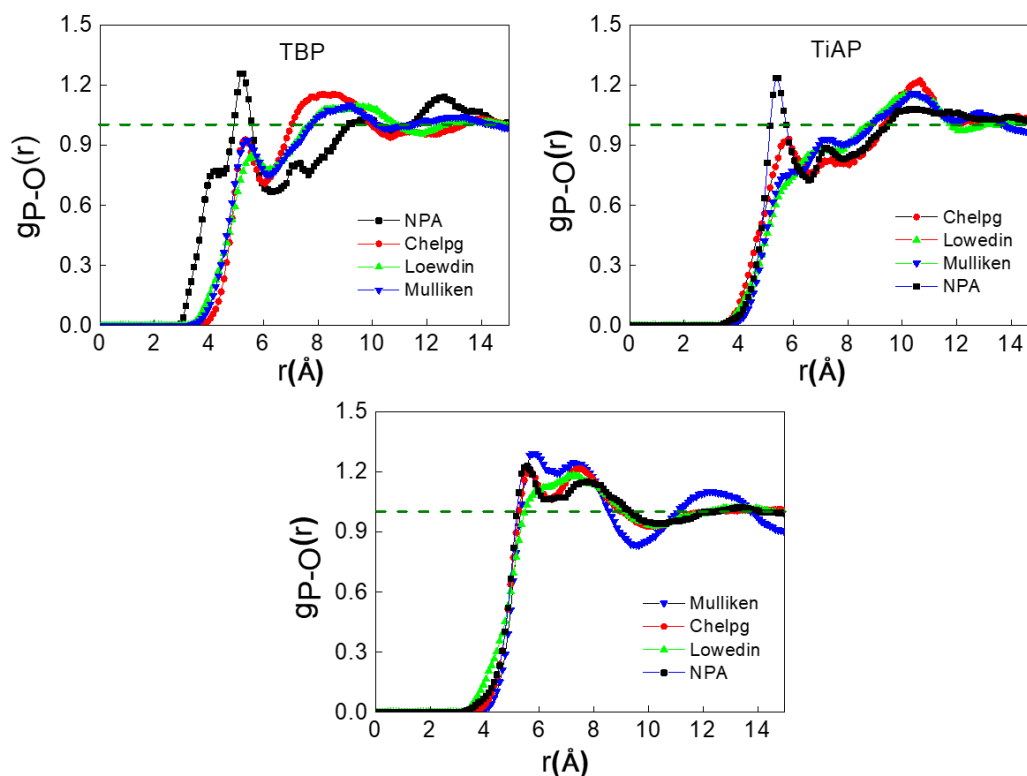


Figure 3.7: Intermolecular pair correlation functions between the pairs of atoms of P–O for different charged model of three ligands. (a) PCF's of P–O atoms of two TBP molecules (b) PCF's of P–O atoms of two TiAP molecules (c) PCF's of P–O atoms of two TEP molecules

O – O Pair Correlation Function

- TBP:** In [Figure 3.8\(a\)](#), PCF's of O–O using the four different DFT charge models: Mulliken, Löwdin, NPA and ChelpG for two TBP molecules are represented. The locations of the first peak for Mulliken, NPA and ChelpG are appeared at around 5.1, 4.9 and 5.1 Å respectively. The second peaks are located at approximately 6.5 – 7.7 Å. For Löwdin charge model, there is a first peak at 7.6 Å and a second peak at around 9.6 Å. The electrostatic repulsion between O–O atoms is important and the charges obtained from Löwdin may be pushed the peak at a longer distance in elimination of the first peak or overlap with the second peak. The first peak position using Mulliken charge appears at 5.15Å that is very similar to the value obtained by [Cui et al⁴³](#).

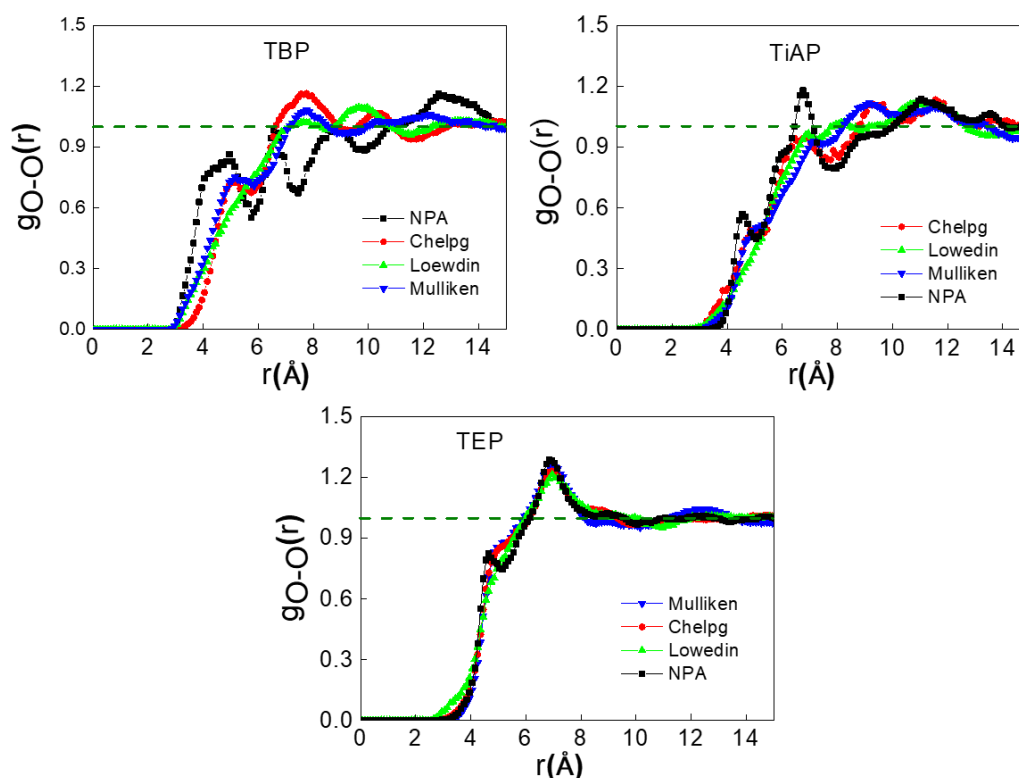


Figure 3.8: Intermolecular Pair Correlation functions between the pairs of atoms of O – O for different charged model of three ligands. (a) PCF's of O – O atoms of two TBP molecules

(b) PCF's of O – O atoms of two TiAP molecules (c) PCF's of O – O atoms of two TEP molecules.

- TiAP:** The PCF's of O–O atoms for two TiAP molecules with different charge models are shown in [Figure 3.8\(b\)](#). The first peaks for all the charge models are located at around 6.7 – 7.1 Å. The second peak for Mulliken and ChelpG charge models are located at around 9.2 Å. For Löwdin, a broad second peak is appeared at between 10.6 – 11.3 Å and for NPA charge model, there is also a second peak at 11.05 Å.
- TEP:** The PCF's of O–O atoms for two TEP molecules with different charge models are shown in [Figure 3.8\(c\)](#). The first peaks are located at around 6.85 – 6.95 Å indicates that a weaker repulsive force pushes the first peak to a little bit higher location. The second peaks are not appeared properly but fairly flat top located approximately at 12.20 – 12.55 Å.

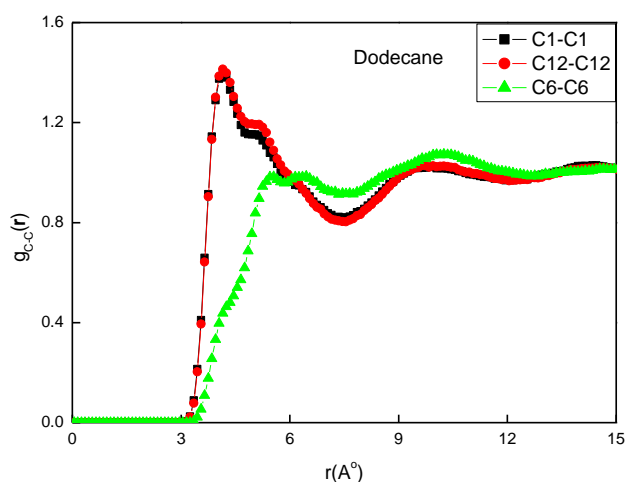


Figure 3.9: Plot of PCFs between the pairs of atoms of C–C of dodecane after 10ns production run in NVT

The calculated PCFs for liquid dodecane are displayed in **Figure 3.9**. From the figure it is seen that the PCFs for the terminal-terminal carbons (C1-C1) and (C12-C12) are identical whereas the PCF for middle-middle carbons (C6-C6) is different from the terminal-terminal PCFs of carbon atoms. The location of first peak height for terminal-terminal carbons is appeared at around 4.15Å and the second peak is at 9.65 Å respectively. In case of PCF for middle-middle carbons (C6-C6), the first peak height is appeared at around 6.45Å and the second peak is at 9.85 Å respectively.

3.3.4. Dynamical properties of liquid TBP, TiAP and TEP: Diffusion coefficient

Diffusion coefficient is an important parameter which helps in modelling the mass transfer in liquid-liquid extraction experiment. Therefore, diffusivity of the pure ligand system is calculated using the Einstein's relation from their respective mean square displacement (MSD) profile.

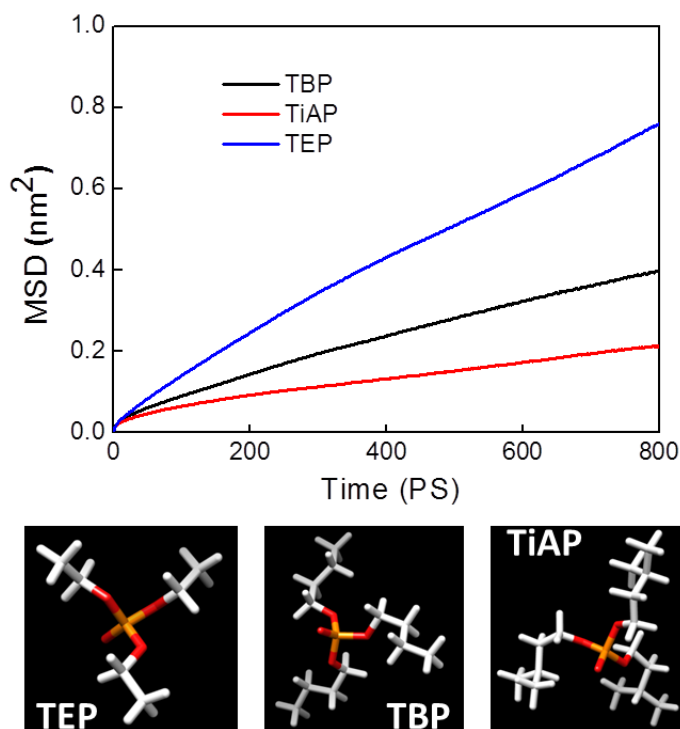


Figure 3.10: MSD profiles of Pure TBP, TiAP and TEP liquids and their respective molecular structures.

The MSD profiles for TBP, TiAP and TEP in pure phase are given in **Figure 3.10** and the results from NVT production run are consistent as per their molecular structure. TiAP has the lowest diffusion coefficient compared to the other two liquids and it is obvious because of its branched structure as shown in **Figure 3.10**. Furthermore, the diffusion dynamics for different charged models are also evaluated. The system was first equilibrated for 10ns followed by additional 10ns run. The MSD obtained for the ligands with four different charge models are shown in the graph below (**Figure 3.11**) and the values are given in **Table 3.7**.

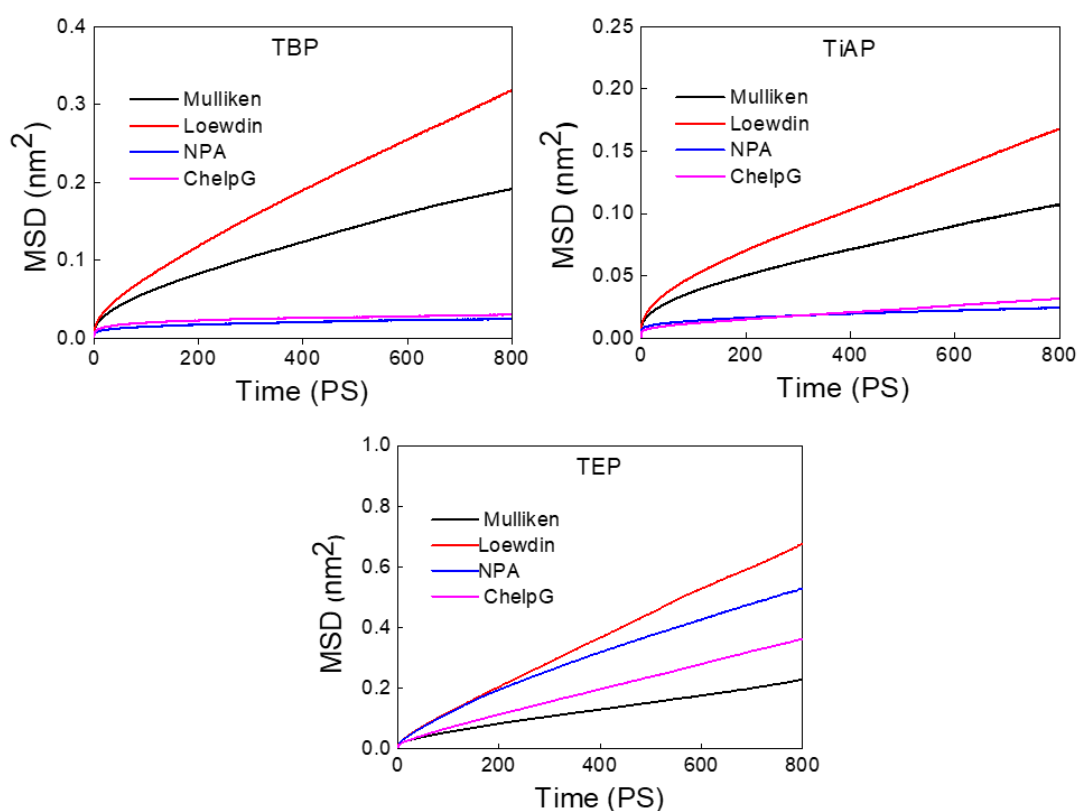


Figure 3.11: MSD profiles of TBP, TiAP and TEP for four different charge models illustrating the partial charges on atom has significant dependency on MSD

A linear fit to the MSD employing Einstein relation of [equation \(2.22\)](#) was performed to obtain the diffusion coefficient from the slope of the linear region of the MSD. From **Figure 3.11(a)**, it is seen that the slope is largest with Löwdin charge model and lowest with NPA

charge model leading to highest diffusivity in the former and lowest in the latter charge model. Results are shown in [Table 3.7](#).

Table 3.7: Diffusion coefficients of pure TBP, TiAP and TEP liquids for different charge models

System	Charge model	Diffusivity (cm ² /sec)
TBP	Mulliken	$(0.539 \pm 0.014) \times 10^{-6}$
	Löwdin	$(0.581 \pm 0.002) \times 10^{-6}$
	NPA	$(0.577 \pm 0.028) \times 10^{-7}$
	ChelpG	$(0.414 \pm 0.051) \times 10^{-7}$
TiAP	Mulliken	$(0.189 \pm 0.008) \times 10^{-6}$
	Löwdin	$(0.302 \pm 0.009) \times 10^{-6}$
	NPA	$(0.346 \pm 0.037) \times 10^{-7}$
	ChelpG	$(0.603 \pm 0.020) \times 10^{-7}$
TEP	Mulliken	$(0.629 \pm 0.143) \times 10^{-6}$
	Löwdin	$(1.463 \pm 0.117) \times 10^{-6}$
	NPA	$(1.581 \pm 0.017) \times 10^{-6}$
	ChelpG	$(0.770 \pm 0.018) \times 10^{-6}$

Experimental value of D for TBP is $(2.29 \pm 0.01) \times 10^{-6} \text{ cm}^2/\text{s}$ ^{147, 148}. The reported self-diffusion coefficients of TBP based on literature are $(0.404 \pm 0.060) \times 10^{-6} \text{ cm}^2/\text{s}$ from 90% DFT⁴⁶, $(0.499 \pm 0.59) \times 10^{-6} \text{ cm}^2/\text{s}$ from OPLS/DFT and $(0.509 \pm 0.24) \times 10^{-6} \text{ cm}^2/\text{s}$ from OPLS/MNDO⁴⁵, $0.21 \times 10^{-6} \text{ cm}^2/\text{s}$ ¹⁴⁹, $(0.311 \pm 0.30) \times 10^{-6} \text{ cm}^2/\text{s}$ with unscaled charges and $(0.499 \pm 0.59) \times 10^{-6} \text{ cm}^2/\text{s}$ after scaling⁴³. Similarly for dodecane, the reported self-diffusion $(4.883 \pm 0.208) \times 10^{-6} \text{ cm}^2/\text{s}$ ⁴⁶. The experimental value of diffusion coefficient for TiAP and TEP are not available.

For all the earlier equilibrium properties, it is seen that Mulliken charge incorporated OPLS-AA force field is the most suitable charge model. The diffusion constant predicted by Mulliken charge is $0.539 \times 10^{-6} \text{ cm}^2/\text{s}$, which is 4 times smaller than that of experimental value^{147, 148} but close to that of Cui et al⁴³ and 2 times smaller than that of Mu et al⁴⁶. Overall, our calculation also follows the same line of argument like Cui et al⁴³ and Mu et al that re-parameterization of OPLS-AA force field is perhaps necessary to reproduce the experimental diffusivity data for TBP.

Next, the diffusivity coefficient was determined for TiAP liquid using the four charge model in the OPLS-AA force field [Figure 3.11(b)]. As observed with TBP liquid, here also the slope of the MSD follows the trend: Löwdin>Mulliken>NPA>ChelpG. Results are shown in Table 3.7. The diffusivity of TiAP was found to be little slower than that of TBP as expected due to its higher molecular mass compared to TBP.

Like TBP and TiAP liquid, the diffusivity of TEP [Figure 11(c)] follows the same trend i.e.: Löwdin>NPA>Mulliken>ChelpG. Results are shown in Table 3.7. Overall, from the analysis of diffusivity it is seen that the diffusivity follows the inverse relation with molecular mass. The trend of diffusivity is: TEP>TBP>TiAP.

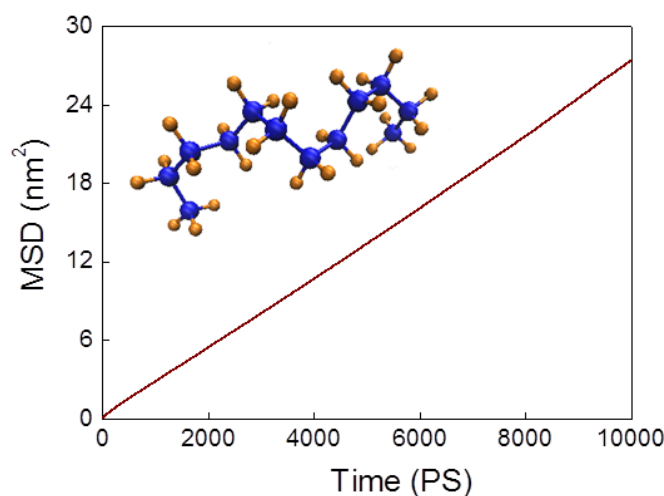


Figure 3.12: MSD profile of pure dodecane after 10ns production run in NVT

The diffusivity data for dodecane was also evaluated from the slope of MSD (see [Figure 3.12](#)) using Mulliken charge and was found to be $4.3 \times 10^{-6} \text{ cm}^2/\text{s}$ which is very close to the earlier literature value of $5.29 \times 10^{-6} \text{ cm}^2/\text{s}$ ⁴⁷ as well as experimental value of $8.71 \times 10^{-6} \text{ cm}^2/\text{s}$.

3.3.5 Free energy of solvation of TBP, TiAP and TEP in aqueous and organic environment

Free energy of hydration/solvation is another thermodynamical quantity which can also be used to test the predictive ability of the atomistic force field. In this study, the free energy of solvation of ligands in water as well as in dodecane is determined using thermodynamic integration (TI) method (see [eq. 2.23](#)) with atomic partial charge predicted by Mulliken. The free energy of hydration and the free energy of solvation of single TBP, TiAP and TEP molecule at infinite dilution in water and solvent respectively are calculated based on the Bennett's acceptance ratio (BAR) method under ambient condition. For free energy of hydration one ligand molecule is immersed within pool of water molecules in a cubic box of appropriate dimension as given in [Table 3.1](#). Similarly the free energy of solvation is also calculated by immersing one ligand molecule within pool of dodecane molecules in a cubic box for which the system description is presented in [Table 3.1](#).

Table 3.8: Computed values of $\Delta G_{\text{Hydration}}$ and $\Delta G_{\text{Solvation}}$ (kJ/mol) in water and dodecane respectively*

Ligand	$\Delta G_{\text{Hydration}}$	$\Delta G_{\text{Solvation}}$
TBP	-4.18 ± 0.85	-48.66 ± 3.93
TiAP	-0.75 ± 0.43	-80.10 ± 4.80
TEP	-33.99 ± 0.84	-31.29 ± 0.38

* The errors were estimated from the average variance over 5 blocks

The BAR method was carried out using 14 intermediate states, λ between 0 to 1 ($\lambda=0, 0.05, 0.1, 0.15, 0.2, 0.3, 0.4, 0.5, 0.6, 0.7, 0.8, 0.85, 0.9$ and 1.0). At, $\lambda=0$, there was no interaction between ligand and surrounding water or dodecane and at $\lambda=1$, they are fully interacted with each other. The system is equilibrated for 10ns and the results are obtained after production run of 2 ns. The free energy of hydration and the free energy of solvation for the ligands TBP, TiAP and TEP are calculated from thermodynamic integration are shown in [Table 3.8](#).

The calculated value of free energy of hydration for TiAP is seen to be less negative indicating less favourable process thus confirms the higher hydrophobic nature compared to the others. Hence, the solubility of TiAP in water is negligible which is very much desirable for biphasic extraction. Again the calculated value of free energy of solvation for TiAP is higher compared to TBP and TEP which suggests higher degree of partitioning of TiAP in organic phase. The larger the difference between hydration and solvation in case of TiAP signifies higher free energy of transfer leading to higher partitioning of solute between two phases.

The free energy of hydration and the free energy of solvation for the ligands TBP, TiAP and TEP are calculated from thermodynamic integration method are represented in [Figure 3.13](#).

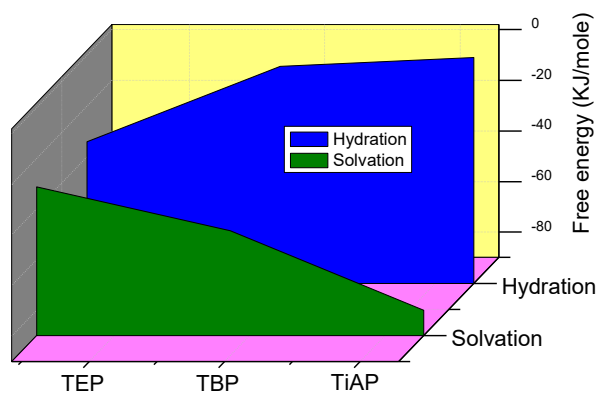


Figure 3.13: The calculated free energy of hydration and solvation in water and dodecane respectively for three ligands illustrating the energy gap between hydration and solvation.

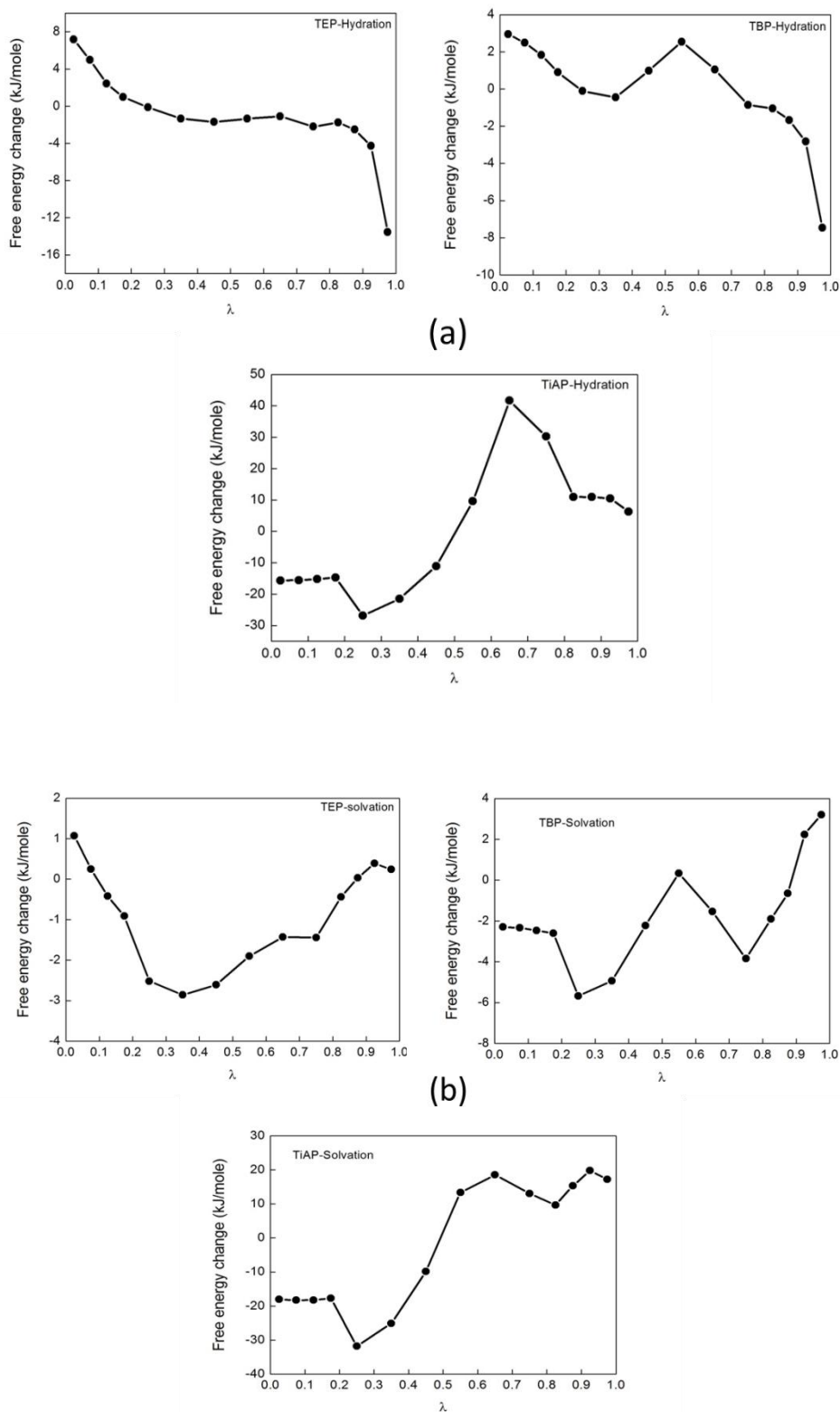


Figure 3.14: Free energy change (ΔG) for TiAP, TBP and TEP as a function of coupling parameter (λ) evaluated using thermodynamic integration in (a) water as free energy of hydration and (b) dodecane as free energy of solvation.

The $\Delta G_{\text{Hydration}}$ value obtained from model calculation is very much closer to the experimental value for TEP as -31.38 ± 0.84 kJ/mole (within 8.3% of experimental value¹⁵⁰) and for others values are not available in the literature for comparison. Nevertheless, the Mulliken charge model can be used for prediction of these thermodynamic properties. This further confirms the acceptability of the Mulliken charge embedded OPLS-AA force field. The remaining values of $\Delta G_{\text{Hydration}}$ and $\Delta G_{\text{Solvation}}$ need to be validated with experimental data which can be considered as future work.

The free energy of transfer for different solute in water and dodecane against the coupling constant λ using thermodynamic integration method was computed and the values are displayed in the **Figure 3.14**.

3.3.6. Partition coefficient (P) of TBP, TiAP and TEP in water-dodecane bi-phasic system

The partition coefficient (logP) of ligands is calculated from the MD simulation using [equation 2.26](#) and the values are reported in **Table 3.9**.

Table 3.9: Calculated values of partition coefficient (logP) of the ligands in water-dodecane system

System	log P		
	MD	QM/COSMO-RS	Experiment ¹⁵¹
TEP	-0.47	-0.89	-0.78
TBP	7.79	5.79	2.74
TIAP	13.90	6.07	-

The partition coefficient (logP) of TBP, TiAP and TEP from MD simulation in water-dodecane system follows the order: TiAP (13.907) > TBP (7.796) > TEP (-0.473). In absence of any experimental data, Quantum calculation using COSM-RS (Conductor like Screening

Model for Realistic Solvents) was performed in water-dodecane system to validate the results of MD simulation. DFT/COSMO-RS follows the same order as that of MD simulations i.e.: TiAP (6.07) > TBP (5.79) > TEP (-0.89) as shown in **Table 3.9**. Point to be noted that though the values of partition coefficient for smaller alkyl phosphates (TEP and TBP) calculated using QM/COSMO-RS and MD simulation are close, there is significant difference for TiAP. Further, in order to find out the origin of the systematic difference between the methods that results in lower logP values for the QM method over MD simulations, the chemical potential of ligands in water and dodecane was determined at infinite dilution using QM/COSMO-RS theory. The calculated values of chemical potential using COSMO-RS method and free energy of hydration using MD simulations are presented in **Table 3.10** and **Table 3.11**.

Table 3.10: The calculated chemical potential (kcal/mol) of solute in water and dodecane medium respectively at infinite dilution using QM/COSMO-RS theory

Ligand	μ_{water}	μ_{dodecane}	$\mu_{\text{water}} - \mu_{\text{dodecane}}$	$V_{\text{water}}/V_{\text{dodecane}}$
TEP	-1.55	-1.84	0.287	0.079
TBP	1.30	-8.12	9.421	0.079
TiAP	0.77	-9.03	9.800	0.079

Table 3.11: The computed values of $\Delta G_{\text{Hydration}}$ and $\Delta G_{\text{Solvation}}$ (kcal/mol) in water and dodecane medium respectively using MD simulations

Ligand	$\Delta G_{\text{Hydration}}$	$\Delta G_{\text{Solvation}}$	$\Delta G_{\text{Hydration}} - \Delta G_{\text{Solvation}}$
TEP	-8.13	-7.48	-0.64
TBP	-1.00	-11.64	10.64
TIAP	-0.18	-19.16	18.98

From the tables it is seen that the difference in chemical potential of a particular solute between water and dodecane is smaller than that of difference in free energy between water and dodecane obtained from MD simulation and the same is also reflected in the smaller value of logP for the QM/COSMO-RS method (using eq. 2.27) compared to MD simulations results (using eq. 2.23). The significant disagreement between the MD and QM methods for TiAP is attributed to the very high free energy of solvation of TiAP in dodecane compared to TBP for MD simulations whereas no such jump is noticed in the chemical potential for TiAP in dodecane compared to TBP for QM/COSMO-RS methods.

The study also confirmed that TiAP has the higher partitioning ability. The increasing value of partition coefficient of tri-alkyl phosphates with increasing alkyl groups in water-dodecane is attributed to the increasing hydrophobic alkyl group because the solubility of the tri-alkyl phosphates in water is decreased and increased in dodecane which in turn enhances the partitioning of the solute in dodecane. Furthermore, the calculated results of partition coefficient are found to be in qualitative agreement with the experimental results. Point to be noted that the experimental partition coefficient was determined in water-octane bi-phasic system, whereas the computed results were for water-dodecane system. It is expected that the experimental partition coefficient in water-dodecane system will be higher compare to water-octane system and hence the computed results can be considered to be reasonable and thus confirms the acceptability of the Mulliken charge based OPLS-AA force field. The experimental validation of the computational results is being planned as future work.

3.3.7. Liquid state dipole moment of TBP, TiAP and TEP

The dipole moment obtained from simulations for three ligands along with the effect of partial charges computed by various methods are shown in [Table 3.12](#).

Table 3.12: Dipole moment (Debye) of ligands

Model	TEP	TBP	TiAP
Mulliken	3.035 ± 0.0002	3.005 ± 0.0002	3.905 ± 0.0002
Löwdin	2.693 ± 0.002	2.977 ± 0.002	3.207 ± 0.0002
NPA	4.857 ± 0.002	4.902 ± 0.002	4.951 ± 0.003
ChelpG	3.457 ± 0.003	7.347 ± 0.005	3.908 ± 0.006

In case of TBP, the dipole moment predicted using Mulliken charge is though underestimated, still it is close to the experimental value of 3.32 D^{120, 121} compared to the other charge models. The next close value is predicted from Löwdin which is underestimated whereas both the NPA and ChelpG offer very high value of dipole moment. So, OPLS-AA model using Mulliken charge is the best force field model for predicting the dipole moment of TBP. The calculated dipole moment for TiAP ligand was found to be highest using NPA and lowest with Löwdin whereas Mulliken and ChelpG showed very close value. There are no experimental values reported for pure TiAP till date and hence cannot be compared with the experimental result. Next, for TEP, the magnitude of dipole moment computed from Mulliken, Löwdin, and ChelpG method is in a range from 2.69 to 3.45 and for NPA, it is slightly higher. The reported experimental value of dipole moment for pure TEP is 3.08D¹²¹ which is very close to the value determined using Mulliken charge based OPLS-AA force field. From overall analysis of dipole moment for different charge model, it can be confirmed that the Mulliken charge included OPLS-AA force field is the best choice for the simulation of the tri-alkyl phosphates liquids.

3.3.8 Heat of vaporisation

In order to further test the applicability of Mulliken charge, the heat of vaporization, ΔH_{vap} of the liquid system was determined as the difference in potential energy of a molecule in the gas phase, $E(\text{g})$ and the liquid phase, $E(\text{l})$ ⁴⁷:

$$H_{\text{vap}} = E(\text{g}) - E(\text{l}) + RT \quad (3.1)$$

The calculated values are presented in **Table 3.13** and it is seen that the calculated values of ΔH_{vap} for organophosphorus liquids using Mulliken charge are in fair agreement with the experimental results^{152, 153}. Even, the value of ΔH_{vap} for TEP using Mulliken charge is better than that of reported using OPLS-AA force field¹⁴⁶. The data of ΔH_{vap} for TBP and TIAP using OPLS-AA force field are not available for comparison. In case of dodecane, the value of ΔH_{vap} using Mulliken charge is in good agreement with the experimental results^{152, 153}.

Table 3.13: The values of heat of vaporization (ΔH_{vap} in kJ/mol) computed from MD simulations of pure liquid systems

Systems	ΔH_{vap} (Present study)	ΔH_{vap} (Experiment)	ΔH_{vap} (Literature)
TEP	67.54	55.73 ¹⁰¹ , 57.3 ¹⁰⁸	77.69 ⁸⁹
TBP	70.73	80.57 ¹⁰¹	-
TIAP	87.47	86.56 ¹⁰¹	-
Dodecane	65.90	62.60 ¹⁰¹ , 61.52 ¹⁰⁸	93.31 ⁴⁶ , 61.07 ⁴⁶

3.3.9. Application to nuclear fuel cycle

TBP has been and being extensively used in the reprocessing of spent nuclear fuels. Due to some inherent limitations of TBP, there is a search for an alternative of TBP. MD simulation

can be used to find out an alternative by comparing thermo physical, transport properties and microscopic structures among different ligands. The screening is required to choose the best one for reprocessing of thermal reactor fuel as well as fast reactor fuel. The results so far discussed will be analysed now in the light of how these are going to help in the screening of the ligands.

First, let us consider the case of density. The slightly lesser density of TiAP could help in the mass transfer. The minimum loss of solvents in water during extraction of radionuclide is one of the criteria for choosing the solvent. In view of that the solubility of TBP, TiAP and TEP was calculated using COSMOtherm package¹⁰⁹. The calculated solubility (gm/cc) order: TEP (2.0×10^{-1}) > TBP (1.07×10^{-6}) > TiAP (0.61×10^{-6}) suggests that TiAP is the best choice.

Further, ligand with higher partition coefficient means higher availability of the ligand in the organic phase which in turn has higher chance of complexation with the metal ions and thus might leads to comparatively high distribution constant. Here, TiAP with little bit higher partition coefficient than TBP shows slightly higher distribution constant compared to TBP for uranyl ion as observed in the solvent extraction experiment^{12, 13} supports the above findings.

Furthermore, the molecule with high dipole moment will have greater dipole-ion interaction which might be leading to higher complexation ability and distribution constant of the metal ions in the aqueous-organic bi-phasic extraction experiment. In the present study, TiAP with higher dipole moment over TBP has been found to have higher distribution constant over TBP for uranyl ion^{12, 13}. Though it is true for TiAP, it may not be true for other ligands as the distribution is controlled by many factors.

3.3.10. Free energy of extraction of UO_2^{2+} ion in water-dodecane system using DFT/COSMO-RS approach

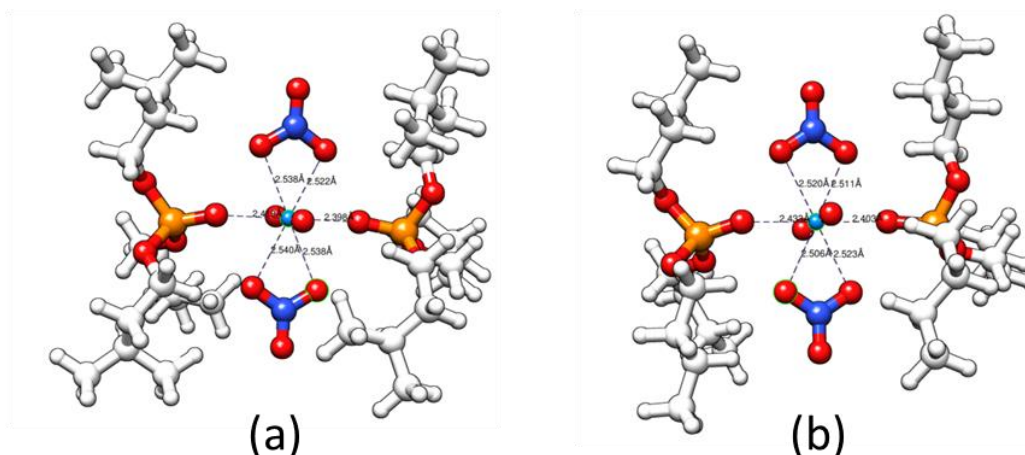


Figure 3.15: Optimized structures of complexes of (a) $\text{UO}_2(\text{NO}_3)_2(\text{TiAP})_2$ and (b) $\text{UO}_2(\text{NO}_3)_2(\text{TBP})_2$

In the preceding section, TiAP has been shown to be the probable screened extractant from the above studies of thermophysical and dynamical properties. It is now worthwhile to investigate the extraction ability of TiAP by evaluating the free energy of extraction, ΔG_{ext} , using eq. 2.31. The optimized structures of the complexes with uranyl ion are displayed in **Figure 3.15**. From the figure it is seen that the uranyl ion is coordinated to two phosphoryl O atoms of two ligands and two nitrate ions in bi-dentate mode leading to hexa coordinated complex for both TBP and TiAP ligands.

Then free energy of extraction has been calculated in the solution phase by evaluating the energy in solution employing conductor like screening model (COSMO)^{154, 155} where 2 and 80 were used as the dielectric constant of dodecane and water respectively. The calculated values of free energy of extraction, ΔG_{ext} are given in **Table 3.14**.

Table 3.14: Calculated values of free energy of extraction (kcal/mol) with different ligands at the B3LYP/TZVP level of theory

Complexation reaction	ΔG_{ext}
$\text{UO}_2^{2+}(\text{aq}) + 2\text{NO}_3^-(\text{aq}) + 2\text{TiAP}(\text{org}) = \text{UO}_2(\text{NO}_3)_2(\text{TiAP})_2(\text{org})$	-125.65
$\text{UO}_2^{2+}(\text{aq}) + 2\text{NO}_3^-(\text{aq}) + 2\text{TBP}(\text{org}) = \text{UO}_2(\text{NO}_3)_2(\text{TBP})_2(\text{org})$	-120.19

From the calculated values of free energy, it is observed that the TiAP shows the higher free energy of extraction than that of TBP which reflects the higher distribution constant of UO_2^{2+} ion with TiAP ($D_{\text{U(VI)}}=29.8$)^{12, 13} over TBP ($D_{\text{U(VI)}}=24.5$)^{12, 13} and hence the superiority of TiAP over TBP is confirmed and might be used as an alternative of TBP in nuclear fuel cycle.

3.4. SUMMARY

DFT derived partial charges on atoms were generated using population analysis methods of Mulliken, Löwdin, NPA and ChelpG and subsequently embedded in OPLS-AA force field to determine the mass density, pair correlation function, free energy of solvation, partition coefficients, diffusion coefficients and dipole moment using MD simulations in order to calibrate the suitable OPLS-AA force field for the tri-alkyl ligands and n-alkane liquids. From overall density analysis for all the ligands and diluent using four different charge models, it can be stated that the OPLS-AA force field using Mulliken charge might be the most suitable force field for determination of density which is within 0.35-1.41% of the experimental results. Further, the different partial charge on the phosphoryl group significantly affect the PCFs of liquid TBP, TiAP and TEP as envisaged from the peak height of PCFs.

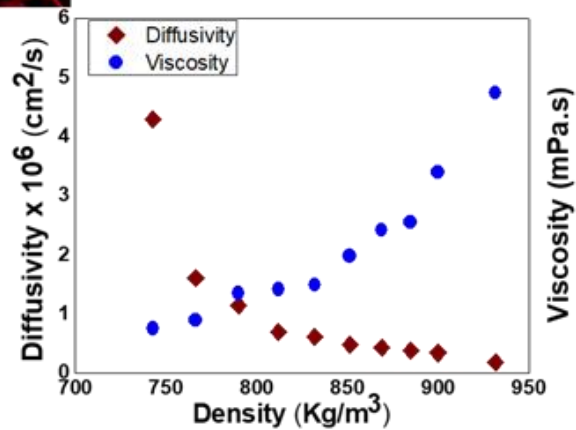
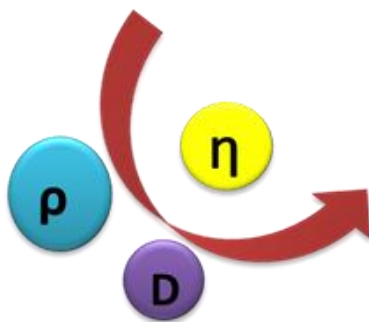
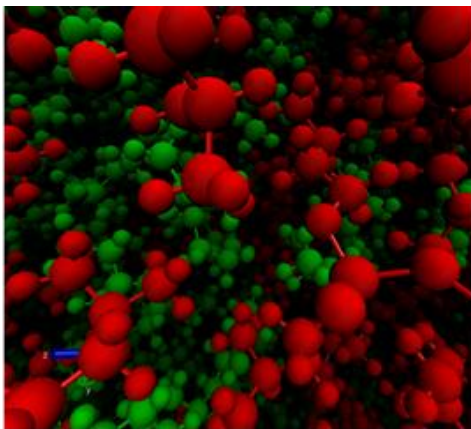
Though the predicted density with Mulliken charge is reasonable, the diffusion constant of TBP with Mulliken charge is found to be 4 times smaller than that of experimental value which suggests that re-parameterization of OPLS-AA force field might be necessary to produce the accurate diffusivity data as estimated by experiments. Overall, from the analysis of diffusivity it is seen that the diffusivity follows the inverse relation with molecular mass i.e.: TEP>TBP>TiAP.

The calculated value of $\Delta G_{\text{Hydration}}$ for using Mulliken partial charge is very close to the experimental value indicating that the Mulliken charge model might be useful for estimating the thermodynamic properties. In addition, the calculated partition coefficient of the ligands using MD simulations in water-dodecane system follows the order: TiAP> TBP>TEP which is further corroborated by QESC. Furthermore, the calculated results of partition coefficient are found to be in qualitative agreement with the experimental results. From overall analysis of dipole moment for different charge model, it can be confirmed that the Mulliken charge included OPLS-AA force field might be the suitable choice for the simulations of the present molecular system.

Further, the higher free energy of extraction for TiAP over TBP indicates higher distribution constant of UO_2^{2+} ion with TiAP ($D_{\text{U(VI)}} = 29.8$) over TBP ($D_{\text{U(VI)}} = 24.5$) and hence TiAP might be used as substitute of TBP in nuclear fuel cycle. Finally, after examining the thermophysical and dynamical properties of the pure liquids employing different Quantum partial charge, Mulliken charge embedded calibrated OPLS-AA force field is perhaps the most reliable one so far as it does not incorporate any arbitrary scaling in the force field or L-J parameters and thus can be used confidently to estimate the liquid state properties of alkyl phosphates and n-alkanes.

Chapter 4

Test of Calibrated Force Field in Binary Mixture



CHAPTER FOUR

Test of Calibrated Force Field in Binary Mixture

4.1. INTRODUCTION

In previous chapter, theoretical screening was done to select a suitable organo phosphorus ligand. Among TBP, TiAP and TEP, TiAP was established to be an alternative by analysing the structure, thermo-physical and dynamical quantities which matched quite well with the experimental results. TiAP like TBP also cannot be used in pure form due to its high viscosity and hence a diluent of appropriate composition is mixed to make it suitable for solvent extraction. Therefore, it is of great importance to explain the various structures, dynamical and thermophysical properties of TiAP-dodecane mixture. The extraction mechanism of metal-ligand complex and the phase separation in the TiAP-dodecane binary system involve various molecular level events which needs a clear understanding. Therefore, MD simulations have been employed to develop a structural understanding along with the dynamical and thermo-physical properties of the binary system.³² In recent past, molecular dynamics simulations have been employed to develop the understanding of the fundamental behaviour of extraction system

from molecular level.^{34-38, 40} Cui and co-workers carried out MD simulations on TBP/ n-dodecane mixture using DFT and MNDO charges on OPLS force field.⁴⁵ They showed that both the OPLS-DFT and the OPLS-MNDO models can well predict the properties like mass density (better than approximately 1%) and dipole moment. The density as a function of mole fraction for both the models was reported to be in good agreement with experimental values, but the dipole moments were moderately matched to the experimental value, about 5.3% for OPLS/DFT and 4.2% for OPLS/MNDO. They also discussed the excess volume of mixing and the calculated data from both the models were consistent with the experimental data. Again, it is reported that dipole moment of TBP is weakly affected by the mole fraction of TBP in binary mixture. They also suggested the probable orientation of TBP in the mixture.⁴⁵ Cui and co-workers reported the properties like mass density and dipole moment of TBP using four sets of force fields parameters but those force fields cannot predict the accurate self-diffusion coefficient.⁴³ Mu *et al* carried out a comparative molecular dynamics simulations studies on the five TBP models introducing a new partial charges calculated by DFT and they found that a single model cannot predict both the structural and thermodynamical properties. In case of dipole model, the OPLS-2005 model and the refined model showed good agreement with the experimental values. The self-diffusion and the shear viscosity were well predicted by OPLS-2005 model but the excess enthalpy of mixing was better explained by 60% MNDO and OPLS-2005 models.⁴⁶ Vo.*et al* worked for the refinement of LJ potential parameter of AMBER³⁹ force field for the TBP/n-dodecane mixture to achieve the most accurate model. They used their optimized parameter keeping the default scaling factors based on the experimental density and the heat of vaporization of each molecule. They reported the self-association study of TBP in TBP/n-dodecane mixture for low concentration.¹⁴⁹ Leay and co-workers have studied on the behaviour of TBP in different organic diluent with carbon number 6 – 12 and they stated that the bi-continuous structure is independent on composition, temperature and nature of organic

solvents. They have also reported that the self-association of TBP and the pathway of polar molecules from the aqueous phase to the organic phase through filament network.¹⁵⁶ Further, [Mu and co-worker](#) have studied shear viscosity of pure TBP from non-equilibrium molecular dynamics (NEMD) using periodic shear flow method with various models including refined model. The OPLS-2005 model though was predicted to be better compared to the other model, still it shows deviation of 14.7%.⁴⁶ [Sui et al](#) have computed viscosities of long hydrocarbons using optimized OPLS-AA (L-OPLS) and OPLS parameters. For dodecane, a very high viscosity was reported using OPLS force field because of gel-like phase formation whereas L-OPLS yields 1.668 mPa.s which is in good agreement with the experiment.⁴⁷ Again, [Allen et al](#) calculated the shear viscosity of branched and linear alkanes from NEMD and they have shown that AA-OPLS model parameterized with new σ_H can predict the viscosity quite quantitatively. Shear viscosity of n-dodecane using periodic perturbation method from NEMD has not been reported and also no simulations have been performed for the calculation of shear viscosity of pure TiAP as well as TiAP/dodecane mixture.¹⁵⁷ Therefore, it will be worthwhile to calculate the various structural, dynamical and thermodynamical properties of the TiAP/dodecane mixture for a wide range of temperature and composition using MD simulations. Further, the determination of shear viscosity of pure TiAP, TBP, dodecane and binary mixture using NEMD simulation with Mulliken partial charges will also be important for potential calibration. Therefore, the aim of the present study is to extend the recently tested force field to a binary fluid mixture which can explain both the structural and dynamical properties without any parameterization by performing MD simulations.

The all atoms optimized potential for liquid simulations (OPLS – AA) force field embedded with Mulliken partial charges on each atom is used in this study.^{68, 88} This Mulliken partial charge based potential is employed to investigate the structural and dynamical properties of TiAP and dodecane in TiAP/dodecane binary mixture. The theoretical data obtained from the

simulation is compared with the available experimental data. The simulation systems details are described in Section 4.2 followed by the Results and Discussion in Section 4.3 and finally the work is summarised in Section 4.4.

4.2. SIMULATION SYSTEMS

The force field parameters for both the bonded and non-bonded potentials are taken from the all-atom optimized potentials for liquid simulations (OPLS-AA). The initial molecular structures of TBP, TiAP and dodecane have been optimized at the B3LYP/TZVP⁷⁰ level of theory as implemented in TURBOMOLE⁶⁹ package which was then used in creating the topology. The partial charges on the each atom are computed from the density functional theory (DFT) using Mulliken population analysis method.

In the present study, the simulations of pure ligands (TiAP and TBP) as well as TiAP/dodecane mixture are performed with 500 numbers of molecules at 300K. The mixture of TiAP and n-dodecane contained total 500 number of molecule and various binary systems with different mole fraction of TiAP ranging from 0 to 1 are represented in [Table 4.1](#).

The energy minimization for all the pure and binary systems was carried out to relax the initial configuration using steepest decent method with a time step of 1fs. The systems are then equilibrated for 10ns simulation length in isothermal-isobaric (NPT) ensemble to equilibrate the volume with a time step of 2fs. Pressure of 1 atm is maintained using Berendsen like weak coupling methods and Velocity-rescaling thermostat is used to converge the temperature (T=300K). Three dimensional cubic periodic boundary conditions are employed for all the pure as well as binary systems. The Verlet velocity algorithm is used to integrate the equations of motion using a time step of 2fs. The coordinates obtained from the NPT run are used for the production run in NVT (constant volume and constant temperature) ensemble over 10ns. The

data obtained from production run was used for the calculation of various structural, dynamical and thermodynamical properties.

Table 4.1: Summary of various binary systems – TiAP/dodecane and TBP/dodecane

TiAP/dodecane binary mixture				
System (% of TiAP)	Mole fraction of TiAP	Nos. of TiAP molecules	Nos. of dodecane molecules	Box dimensions (nm)
100	1.0	500	0	6.44 x 6.44 x 6.44
90	0.9	450	50	6.38 x 6.38 x 6.38
80	0.8	400	100	6.33 x 6.33 x 6.33
70	0.7	350	150	6.26 x 6.26 x 6.26
60	0.6	300	200	6.19 x 6.19 x 6.19
50	0.5	250	250	6.11 x 6.11 x 6.11
40	0.4	200	300	6.05 x 6.05 x 6.05
30	0.3	150	350	5.96 x 5.96 x 5.96
20	0.2	100	400	5.90 x 5.90 x 5.90
10	0.1	50	450	5.83 x 5.83 x 5.83
0	0	0	500	5.75 x 5.75 x 5.75
TBP/dodecane binary mixture				
System (% of TBP)	Mole fraction of TBP	Nos. of TBP molecules	Nos. of dodecane molecules	Box dimensions (nm)
100	1.0	500	0	6.44 x 6.44 x 6.44
80	0.8	400	100	6.33 x 6.33 x 6.33
60	0.6	300	200	6.19 x 6.19 x 6.19

40	0.4	200	300	6.05 x 6.05 x 6.05
20	0.2	100	400	5.90 x 5.90 x 5.90
0	0	0	500	5.75 x 5.75 x 5.75

4.3. RESULTS & DISCUSSIONS

4.3.1. Structure of the pure liquids and mixtures

As the accurate structures of the liquids are very important for the MD simulations studies, the structures of the liquids are optimized using DFT at the B3LYP level of theory with the SVP basis set. The snapshot of the equilibrated structure of pure TiAP, pure n-dodecane and TiAP/dodecane mixture are displayed in [Figure 4.1](#). The random distributions of the molecules seems to be the attainment of the liquid state.

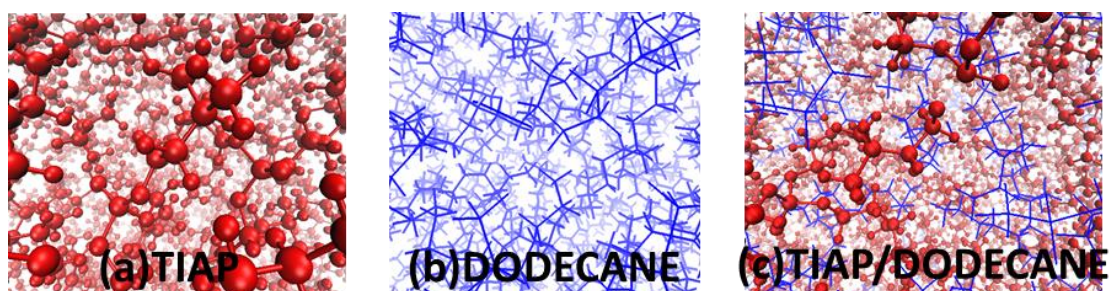


Figure 4.1: Snapshot of (a) pure TiAP, (b) pure dodecane and (c) 50% TiAP/dodecane mixture after the production run in NVT. Red: TiAP, Blue: Dodecane.

4.3.2 Dipole moment of TiAP/n-dodecane mixture

The calculated dipole moment of TiAP using [equation 2.34](#) and [equation 2.35](#) is displayed in [Figure 4.2](#) as a function of the mole fraction of TiAP. The plot exhibits a slow increasing trend of dipole moment which commensurate an independent nature of dipole moment with mole fraction or concentration of TiAP in the TiAP/dodecane binary mixture.

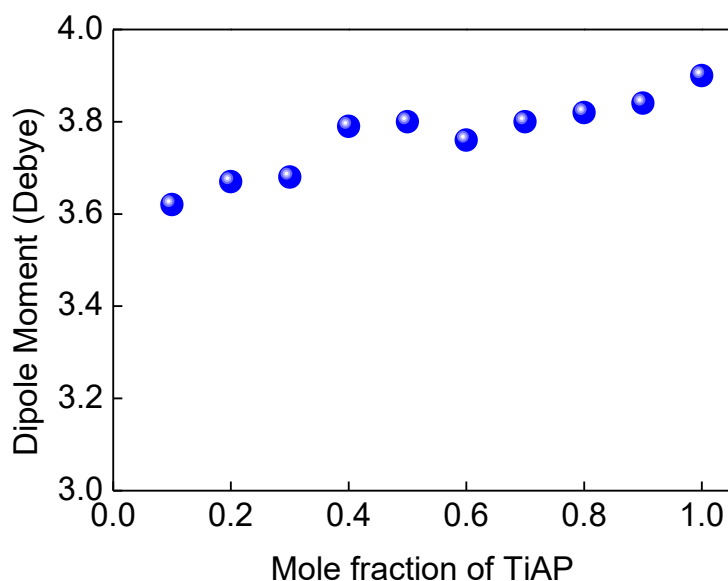


Figure 4.2: Dipole moment of TiAP as a function of the mole fraction

From the plot, it is seen that the variation of dipole moment is not so significant over the entire range of mole fraction and it lies between 3.62 to 3.90D. The calculated data cannot be verified because the experimental data on the TiAP/dodecane binary mixture is not available. The force field parameters used in this study has been verified with the experimental value of TBP and TiAP in our previous work⁹⁴. The calculated dipole moment of pure TBP using the same force field is 3.04D, which is in fair agreement to the reported experimental value of 3.32D. Since, TiAP is a higher homologue of TBP, therefore, the dipole moment of TiAP is expected to be close to that of TBP and the calculated values of TiAP in the mixture are in that range only and thus considered to be consistent. The above figure also suggested that the dipole moment of TiAP in TiAP/dodecane mixture largely unaffected by the variation of mole fraction of TiAP. This is because of the presence of nonpolar dodecane in the mixture does not significantly change the polarity of TiAP. The similar observation was reported earlier by *Cui et al* for TBP – dodecane mixture.⁴⁵

4.3.3 Mass density of TiAP/dodecane mixture

The mass density is an important property as both the intra-molecular and inter-molecular interactions are manifested in this quantity. The density of pure TiAP and pure dodecane with Mulliken atomic charges have been studied after NPT-equilibration for 10ns simulation length. The density has attained the equilibrium within few picoseconds as revealed from [Figure 4.3](#).

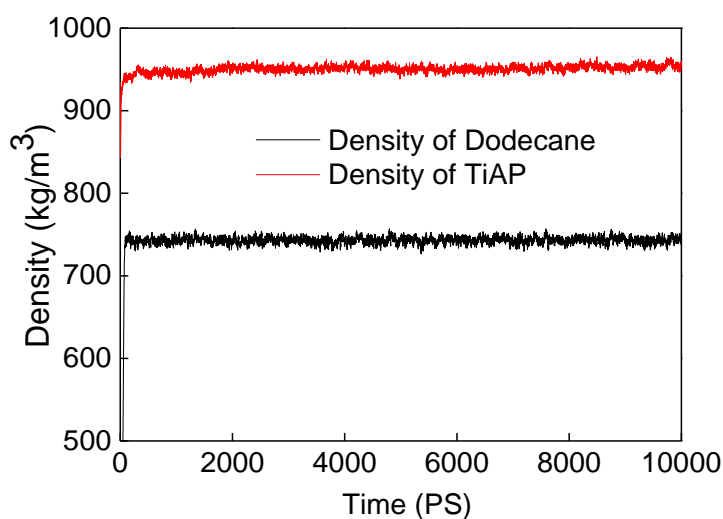


Figure 4.3: Density of TiAP and dodecane as a function of time

Mass density of mixture

The mass density of the pure liquids and the mixture are obtained from the converged volume after NPT run for 10ns simulation length. The density obtained from simulations and experiments are shown in [Figure 4.4](#) as a function of mole fraction of TiAP in the binary mixture. The calculated densities are in good agreement with the experimental values reported by [Singh and co-workers](#).²⁴ The calculated density of pure liquids like TiAP and dodecane are reproduced very well to the experimental results with a deviation of 0.36% and 0.42% respectively. The mixture densities from simulation are deviated from the experimental data

up to a maximum extent of 2.1 % at the 0.50 mole fraction of TiAP and the deviation is gradually decreasing at both end of the composition. This might be due to the disparate interaction between the TiAP and dodecane molecules. The dipole–dipole interaction between phosphoryl groups may be stronger as the number of TiAP molecule increases which results an increase in van der Waals interaction (forces of attraction). This phenomenon insists aggregations which in turns increase the mixture density.

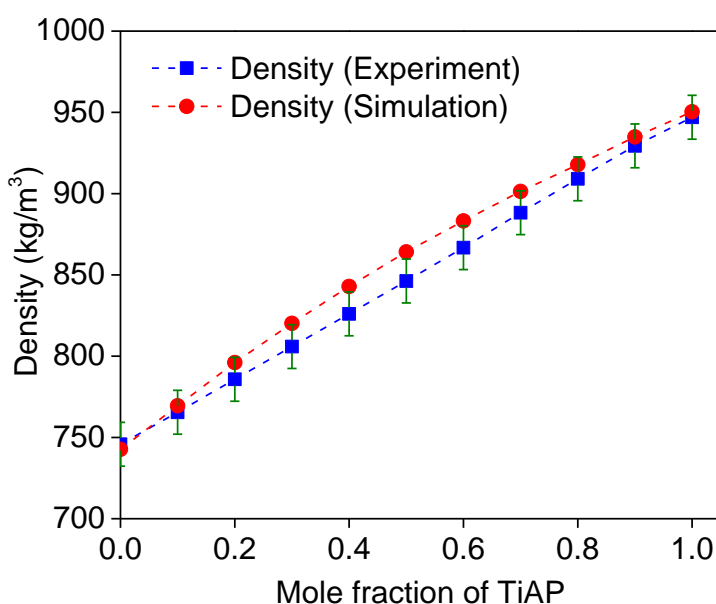


Figure 4.4: Density of binary mixture as a function of the mole fraction of TiAP

Again, at higher mole fraction, the dipole–dipole interaction becomes weak due to the steric effect of TiAP molecules which resists the phosphoryl groups to come closer thus reduces the van der Waals force of attraction leading to a small deviation from the experimental value.

Effect of temperature on the density of pure TiAP and the mixture

The effect of temperature on the density of TiAP has also been studied to compare the densities calculated from simulation with the available experimental values. The density of pure TiAP

and pure dodecane along with the density of TiAP/dodecane binary mixture at various mole fraction of TiAP are simulated at a constant pressure of 1 bar and at different temperatures ranging from 280K to 330K. Before going to the mixture of TiAP/dodecane, the effect of temperature on density for TiAP is studied to verify the force field parameters.

The calculated data obtained from simulations is compared with the available experimental data and is shown in **Figure 4.5**.

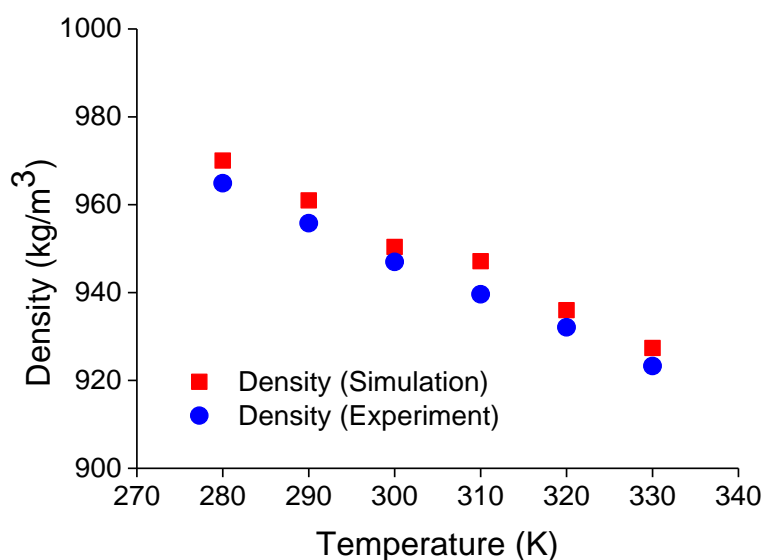


Figure 4.5: Calculated and experimental density of pure TiAP as a function of temperature

The **Figure 4.5** depicts that the calculated density for pure TiAP liquid follows the similar trend obtained from experiment and the density is a decreasing function of temperature. It also has been seen that the values from simulations correctly predicts the experimental values with a deviation of 0.35 to 0.80% (see **Table 4.2**) which indicates the simulation results are quite quantitative with experiment. This validates the accuracy of the force field as well as the simulations methods.

Table 4.2: Calculated density (kg/m^3) of pure TiAP at various temperatures

System	T280	T290	T300	T310	T320	T330
TiAP (Calculated)	970.0	960.9	950.3	947.1	935.9	927.3
TiAP (Experimental)	964.9	955.8	947	939.6	932.1	923.3
% Deviation	0.53	0.54	0.36	0.80	0.42	0.44

Furthermore, the density of TiAP/dodecane binary mixture as a function of temperature at different mole fractions of TiAP of 20%, 40%, 60% and 80% in dodecane along with the pure TiAP and dodecane are also evaluated. The effect of temperature on the density of mixture is presented in [Figure 4.6](#).

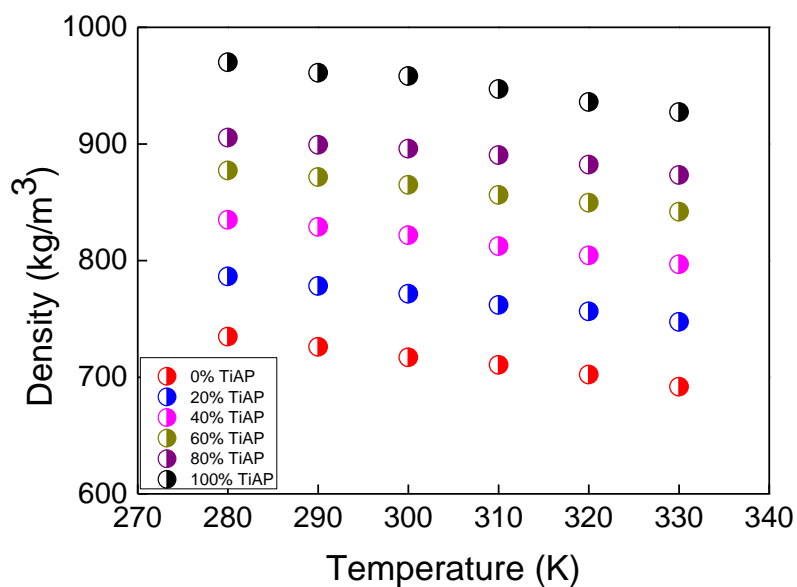


Figure 4.6: Effect of temperature on density of TiAP-dodecane mixture with various compositions

The simulated density for mixture follows the similar trend like pure liquids. The deviation from the experimental data is within 0.80% which further indicates the accuracy of simulations methods even for the TiAP/dodecane binary mixture.

From the above figure, it is observed that the density is decreasing with increase in temperature and also the density is increasing with increase in mole fraction of TiAP. As the mole fraction of TiAP increases, it increases the percentage of TiAP molecule in the dodecane medium which results in the increase of overall density.

4.3.4 Excess volume of mixing

In real liquid mixture, the volume after mixing may increase or decrease due to the type of molecular interactions between the components of mixture. The change in the volume of mixing either a positive or negative is a quantity of great interest because it provides the measure of molecular interactions. Furthermore, the prediction of excess molar volume is a good indicator for the accuracy of force field used in the MD simulations.

The volume of mixing is calculated by subtracting the molar volume of pure component from the molar volume of mixture, employing [equation 4.1](#)

$$V^E = \frac{x_1 M_1 + x_2 M_2}{\rho_{mix}} - \frac{x_1 M_1}{\rho_1} - \frac{x_2 M_2}{\rho_2} \quad (4.1)$$

where V^E is the excess molar volume of the liquid mixture, M_1 and M_2 are the molar masses, x_1 and x_2 are the mole fractions, ρ_1 and ρ_2 are the densities of component 1, 2 and ρ_{mix} is the density of mixture.^{45, 158, 159}

In the present study, the excess volume is computed based on the OPLS-DFT force field by considering the Mulliken partial charge on atoms. The excess molar volume of TiAP in dodecane binary mixture as a function of mole fraction of TiAP is displayed in [Figure 4.7](#).

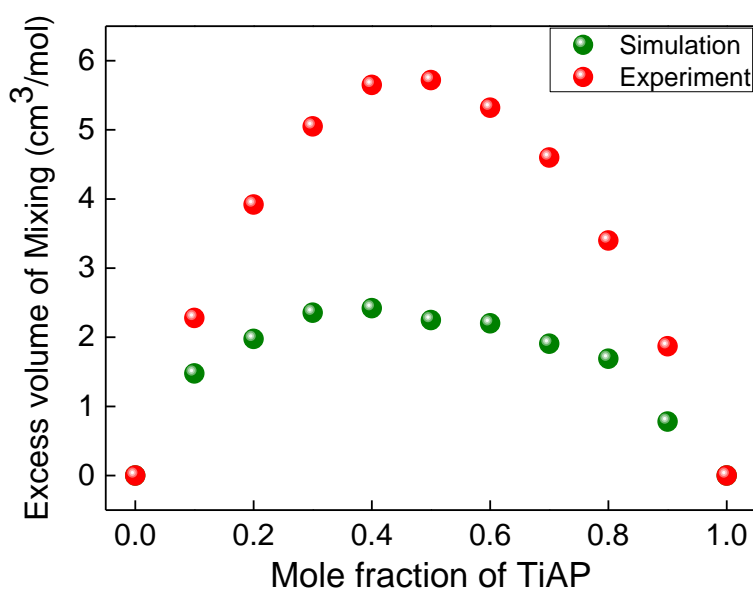


Figure 4.7: Excess volume of mixing of the TiAP/dodecane mixture as a function of mole fraction of TiAP

It is seen that the simulation results correctly predict the trend for excess volume of mixing with mole fraction of TiAP and the peak is appeared in between 0.3 to 0.5, as obtained experimentally²⁴ at around mole fraction of 0.5. It is also important to get the correct sign for the excess volume of mixing which proves the accuracy of the force field. The increase in (positive sign) excess volume obtained from simulation is in good agreement with the available experimental data as seen from the above figure and thus confirms the accuracy of the force field.

There is a rapid increasing trend of excess volume of mixing and then it is decreased slowly passing through a maximum. At low mole fraction of TiAP, the interaction between dodecane molecules dominate over the TiAP/dodecane interaction and at high mole fraction, the interactions between TiAP molecules is dominated which substantially reduces the effect of dodecane in the mixture. Both effects result to a lower value of excess volume of mixing. In

the intermediate range of mole fraction, the interaction between TiAP and dodecane is stronger which exhibits higher value in the excess volume of mixing. The initial rapid rising trend may be due to the strong disruptive effect of TiAP molecules in the mixture. The branched structure of TiAP exhibits higher interaction compared to the linear structure of dodecane. On increasing the mole fraction of TiAP, the numbers of TiAP molecules in dodecane medium are increasing which offers stronger interaction and thus results to an initial rapid rise in the excess volume of mixing. Similar trend was also obtained by Cui *et al* for the TBP/dodecane mixture.⁴⁵

4.3.5 Diffusion coefficient of binary mixture

The diffusion coefficients of TiAP and dodecane in the binary mixture are evaluated to study the effect of composition on the self-diffusion coefficients. The diffusion coefficient is a dynamic property which measures movement of individual molecules through the layer of molecules of the same substance (self-diffusion). Einstein's relation is used to calculate the diffusion coefficient from their respective mean square displacement (MSD) profile.

In case of binary mixture, the study of diffusion coefficient for both the TiAP and dodecane in TiAP/dodecane mixture is very crucial to determine the optimum composition for liquid – liquid extraction. The mean-square-displacement (MSD) of TiAP and dodecane in the binary mixture is shown in **Figure 4.8**. The diffusion coefficient of TiAP is decreasing with increase in mole fraction of TiAP and all the diffusion coefficients of TiAP for mole fraction ranging from 10% to 90% are appeared in between the diffusion coefficient of pure phases [see **Figure 4.8(a)**]. The MSD profiles of TiAP also reveal that the mobility of pure TiAP is enhanced in the presence of dodecane as solvent. The self-diffusivity values for TiAP and dodecane in TiAP/dodecane binary mixture are listed in **Table 4.3**.

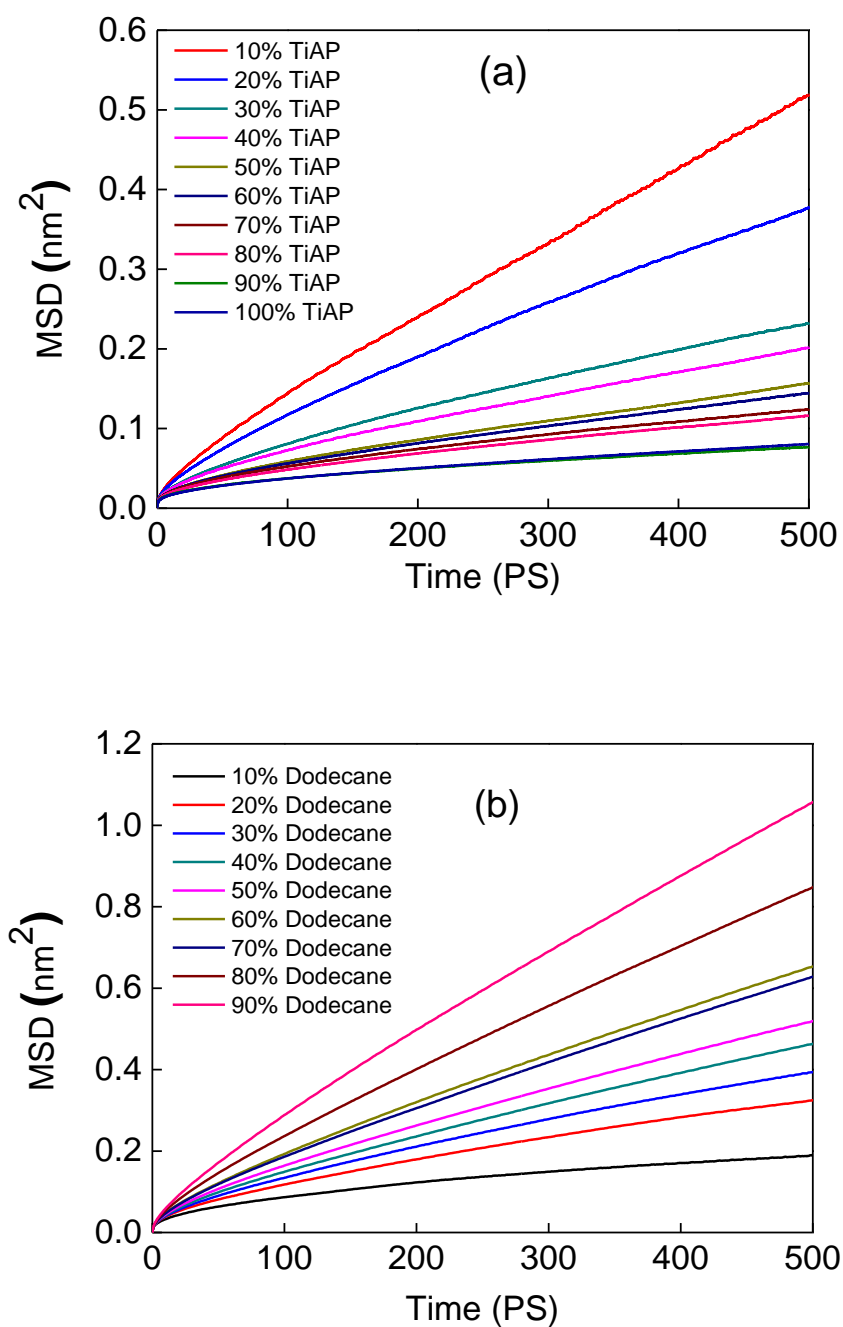


Figure 4.8: (a) MSD of TiAP and (b) MSD of dodecane in TiAP/dodecane binary mixture

Similarly, the self-diffusion coefficients of dodecane is increasing with increase in mole fraction of n-dodecane as seen from the MSD profiles of n-dodecane in [Figure 4.8\(b\)](#). It is also depicted that the diffusion coefficient of dodecane is reduced in presence of the TiAP molecule.

Table 4.3: Diffusivity values of TiAP and dodecane in binary mixture

Mole Fraction	Diffusivity of TiAP ($10^{-9} \text{ m}^2/\text{s}$)	Diffusivity of Dodecane ($10^{-9} \text{ m}^2/\text{s}$)
1.00	0.0189	0.43
0.90	0.0225	0.3033
0.80	0.0348	0.2383
0.70	0.0381	0.18
0.60	0.0441	0.1817
0.50	0.0487	0.1401
0.40	0.0625	0.1156
0.30	0.0708	0.1003
0.20	0.1146	0.0848
0.10	0.1619	0.0385
0.00	0.43	0.0189

Furthermore, the diffusion coefficients of ligand (TiAP) and solvent (dodecane) are studied as a function of mole fraction ranging from the 0 to 1.0 (10%, 20%, 30%, 40%, 50%, 60%, 70%, 80%, 90% and 100% of TiAP) to understand the effect of mole fraction on the diffusivity. The diffusivity of TiAP is a decreasing function of mole fraction of TiAP and for dodecane it is increasing function of mole fraction of dodecane [see [Table 4.3](#)]. The mass density of dodecane compared to TiAP is much lower which reflects a higher mobility of dodecane and finally it results higher diffusivity of dodecane compared to TiAP. The number of TiAP molecules in the dodecane medium is increasing with the mole fraction of TiAP. The van der Waals force of attraction between phosphoryl groups of TiAP molecules becomes dominate and leads to the aggregation of the TiAP molecules to form a cluster. It restricts the molecular movement,

indicating a reduction in diffusivity of TiAP. Also, the free volume is reduced with the increasing no of TiAP molecules at higher mole fraction of TiAP.

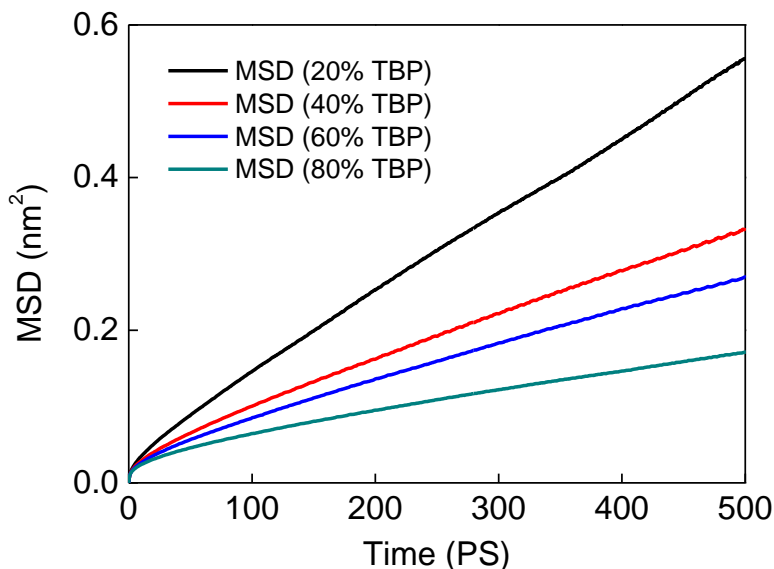


Figure 4.9: MSD of TBP in TBP/dodecane binary mixture

Similarly the self-diffusivities of TBP in TBP/dodecane binary mixture at various mole fraction of TBP are represented in [Figure 4.9](#). The diffusivity of TBP also follows the similar trend as TiAP like the diffusivity is a decreasing function of mole fraction of ligand.

4.3.6 Pair correlation functions (PCFs)

The pair correlation functions (PCF, $g(r)$) between atoms of two interacting molecule is studied to develop an understanding of the microstructure of TiAP in the liquid state. The phosphoryl group of TiAP indicates the polar core and the iso-amyl tail forms the non – polar core of the molecule. Earlier we have studied the PCFs of pure TiAP. The PCFs between P – P, P – O and O – O provide an understanding of the organization of TiAP molecule in the mixture. Furthermore, the PCFs between phosphorous – terminal carbon atom, phosphorous and two

different types of oxygen atoms are also determined to gain an insight of the microstructure of TiAP and dodecane in the mixture.

(a) P – P pair correlation function:

The pair correlation functions between P – P atoms of two interacting TiAP molecules with the variation of mole fraction of TiAP are displayed in **Figure 4.10(a)** and the trend of PCFs are seen to be similar for all the cases. The first peak for all the compositions are appeared approximately in the range of 6.05 – 6.55 Å and the second peak locations are at around 9.45 – 10.35 Å. Furthermore, the peak heights are different for different binary systems and it is decreasing with increase in the TiAP concentration of the TiAP/dodecane mixture. A similar trend is also reported by *Leay et al* in their study of TBP/dodecane mixture.¹⁵⁶

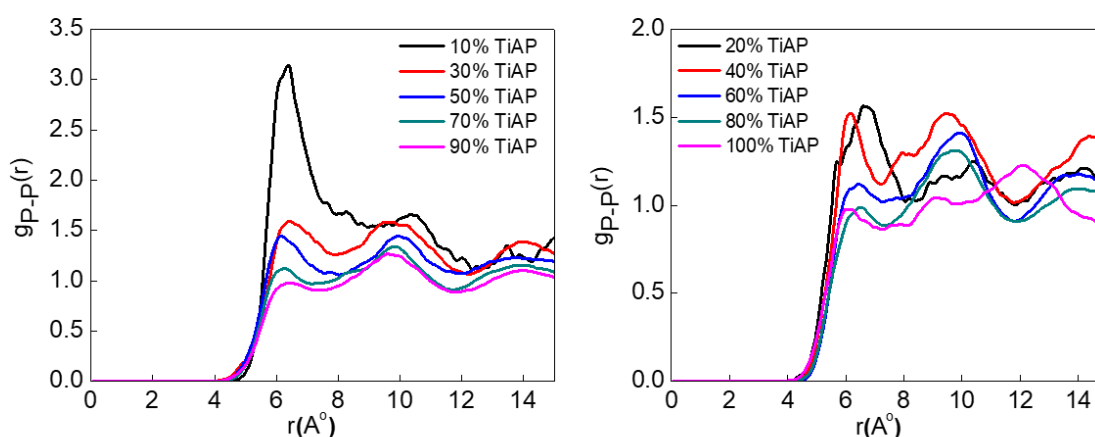


Figure 4.10(a): Pair correlation function of P – P atoms of two interacting TiAP molecules

The phosphorous atom of one TiAP molecule may be oriented in two possible ways with the neighbour phosphorous atom of another TiAP molecule (**Scheme-4.1**). First one is from the hydrophobic side of the two different TiAP molecules and it is difficult to approach each other due to the large isoamyl group and the second is from the phosphoryl group where the dipole – dipole interactions come into picture.



Scheme 4.1: Schematic representation of orientation of TiAP molecules

For 10% TiAP mole fraction, there is a sudden rise in the peak height. When TiAP is added in a nonpolar dodecane medium, the local density becomes much higher than the bulk density and the $g(r)$ reaches much greater than 1.0 which reflects in [Figure 4.10\(a\)](#). It might be due to the strong dipole – dipole interaction of localized TiAP molecules. Again, the peak heights are gradually decreasing with increase in the mole fraction, indicating that the $g(r)$ is decreasing as the repulsion between the DFT charges pushes the phosphorous atom apart from the first coordination shell.

(b) P – O pair correlation function:

The PCFs of P – O atoms for two interacting TiAP molecules are displayed in [Figure 4.10\(b\)](#). The PCFs of all the mixture with different compositions follow the similar trend as seen in the above figure. It is also stated that the second peak is comparatively higher than the first peak and the peak height is gradually decreasing with mole fraction of TiAP. For 10% and 20% TiAP mole fraction, a weak peak is appeared followed by the first peak and the first peak is shifted to a larger distance at around 7.35 Å which results an overlap with the second peak. The higher peak height for 10% TiAP mole fraction indicates very high local density.

The weak peaks become prominent at higher concentration of TiAP. The first peak for the rest of the compositions are located between 5.3 – 5.5 Å approximately and the second peaks are appeared somewhere between 8.8 – 9.3 Å.

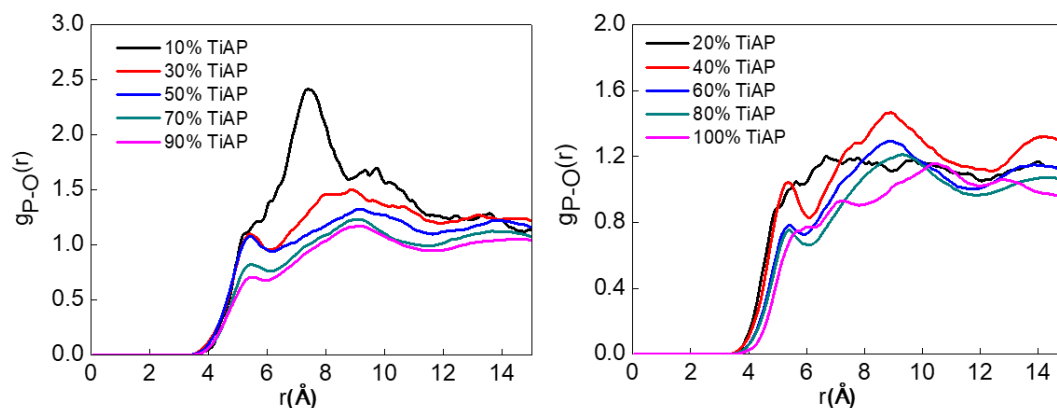


Figure 4.10(b): Pair correlation functions of $P - O$ atoms of two interacting TiAP molecules

(c) O – O pair correlation function:

The **Figure 4.10(c)** represents the intermolecular pair correlation function between the pairs of atom $O - O$ of two different TiAP molecules. The above figure is also displayed the PCFs for various mole fractions of TiAP and they are showing similar trend as above. A shoulder is appeared at about $5 - 5.5 \text{ \AA}$ and the first peak locations are approximately around $7 - 7.5 \text{ \AA}$ depending on the mole fraction. The shoulder is more prominent at mole fraction of 10% TiAP and it is reduced at the higher mole fraction.

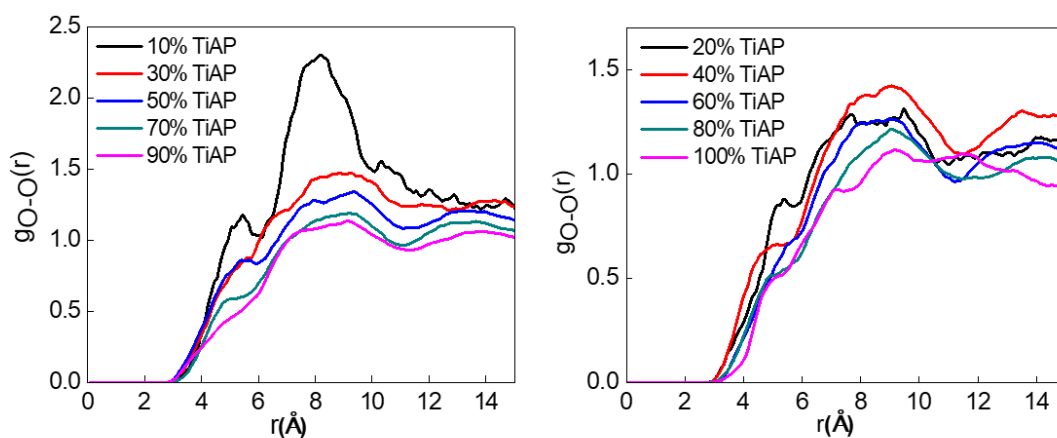


Figure 4.10(c): Pair correlation functions of $O - O$ atoms of two interacting TiAP molecules

The first peak height obtained from the PCFs of P–P atoms of two different TiAP molecules as a function of mole fraction of TiAP is displayed in **Figure 4.10(d)**. The trend is a decreasing function of mole fraction of TiAP. At 10% TiAP mole fraction, the contribution of TiAP is too small for self-association and the local density becomes very high. On increasing the mole fraction of TiAP, this effect decreases rapidly at the initial stage and then decreases gradually. The self-association of TiAP molecules becomes significant and they may create greater number of nodes. *Leay et al* have also reported similar observation in their studies on TBP and dodecane mixture.¹⁵⁶

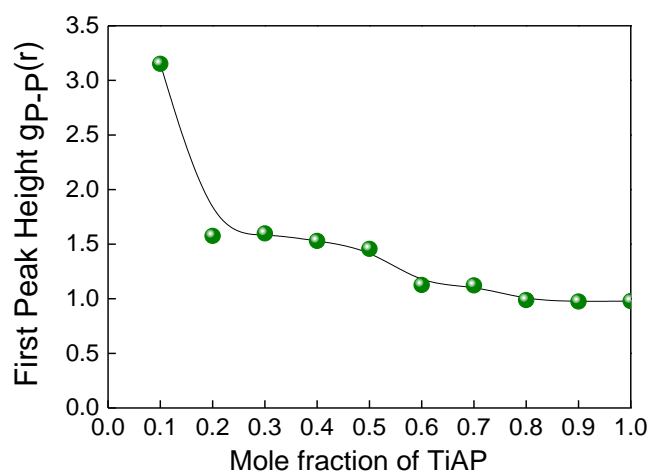


Figure 4.10(d): Trend of the first peak appeared in PCF of P–P atoms as a function of mole fraction of TiAP

(d) P–C and O–C pair correlation functions:

This pair correlation function involves the phosphorous atom of TiAP molecule and the last carbon atom (C12) of dodecane and it is shown in **Figure 4.11(a)**. The PCF has been plotted at different mole fraction of TiAP. The first peak for all the systems are appeared at around 4.75 – 4.95 Å and the peak height is decreasing with increasing mole fraction of TiAP up to a value of 60% TiAP mole fraction. Then it is increasing slowly. Initially the P atom of TiAP is

surrounded by dodecane and gradually the probability of finding of dodecane is decreasing with increasing mole fraction of TiAP and it results lower peak height.

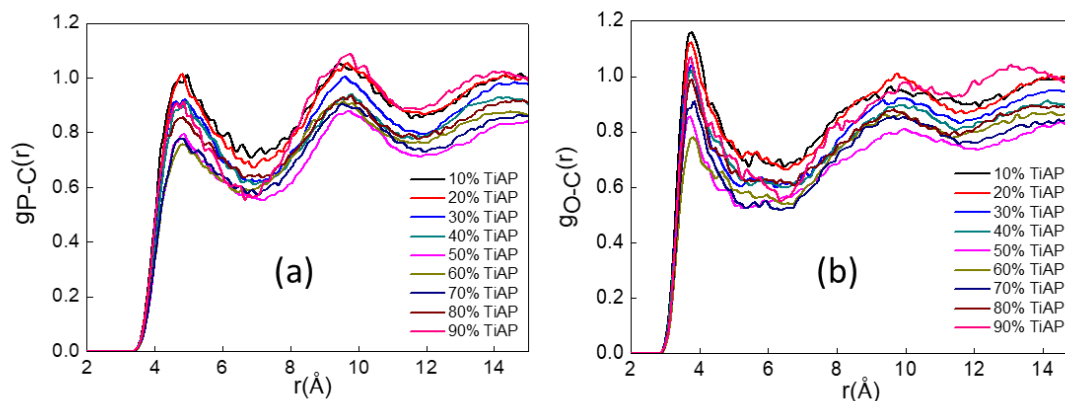


Figure 4.11: Pair correlation functions of (a) P – C atoms of two interacting TiAP and dodecane molecules and (b) O – C atoms of two interacting TiAP and dodecane molecules.

Again, at higher concentration of TiAP, the repulsion between TiAP molecules may be the dominating factor, which helps the dodecane molecules to get closer to TiAP and it increases the probability of finding dodecane molecules surrounding the phosphorous atom of TiAP and the same is reflected in the peak height. This phenomenon is also shown in [Figure 4.11\(b\)](#). The second peaks are appeared at approximately 9.45 – 9.75 Å. The above figure shows the pair correlation function between the oxygen atom of TiAP molecule and the last carbon atom (C12) of dodecane at various mole fraction of TiAP. The first peak locations are approximately between 3.65 – 3.75 Å.

Further, the peak height is decreasing first up to 60% TiAP mole fraction and then it is increasing as it is shown in [Figure 4.12](#). The second peaks are appeared at around 9.65 – 9.95 Å. Similar trend of PCF between O and C atoms is observed here like between P and C atom.

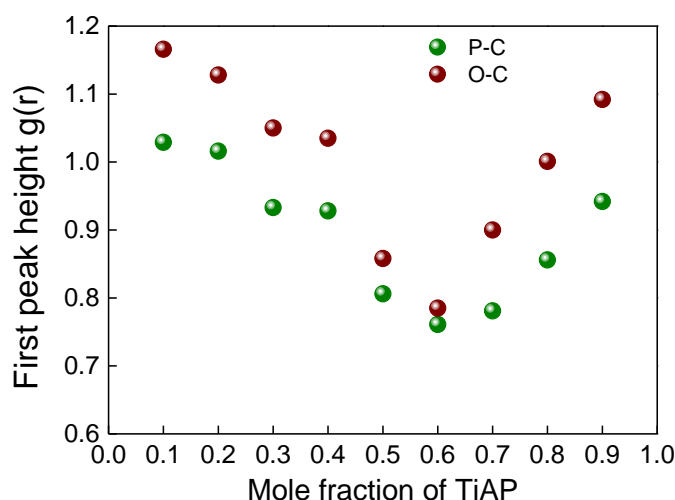


Figure 4.12: Behaviour of the first peak height in the PCF between P-C atoms and between O-C atoms as a function of mole fraction of TiAP

4.3.7 Excess enthalpy of mixing of TiAP/dodecane mixture

The excess enthalpy calculation for the binary mixture provides the thermodynamic activity of each component in the mixture. It is the consequence of the new interactions between TiAP and n-dodecane mixture. The excess enthalpy of mixing is computed by

$$\Delta H^{excess} = H_{mix} - x_1 H_1 - x_2 H_2 \quad (4.2)$$

where, H_{mix} is the enthalpy of mixture of TiAP/dodecane, x_1 and x_2 are the mole fraction of TiAP and mole fraction of dodecane, H_1 and H_2 are the enthalpies of pure TiAP and pure dodecane.⁴⁶

The simulation was performed for the TBP/dodecane and TiAP/dodecane mixture. The model predicts correctly the endothermic mixing of both cases as it was found experimentally. The **Figure 4.13(a)** depicts the calculated excess enthalpy of mixing of TBP/dodecane mixture with their experimental data^{148, 160} and it shows a moderate agreement with the experimental data

which again verifies the use of Mulliken charge embedded force field. *Mu et al* have studied the excess enthalpy of mixing for TBP/dodecane mixture using different models. Among them, 90% DFT model and the refined model are far away from the experimental values whereas OPLS–2005 and the simulation are in good agreement. The Mulliken charge embedded OPLS force field which does not have empirical scaling performs better than that earlier reported model.

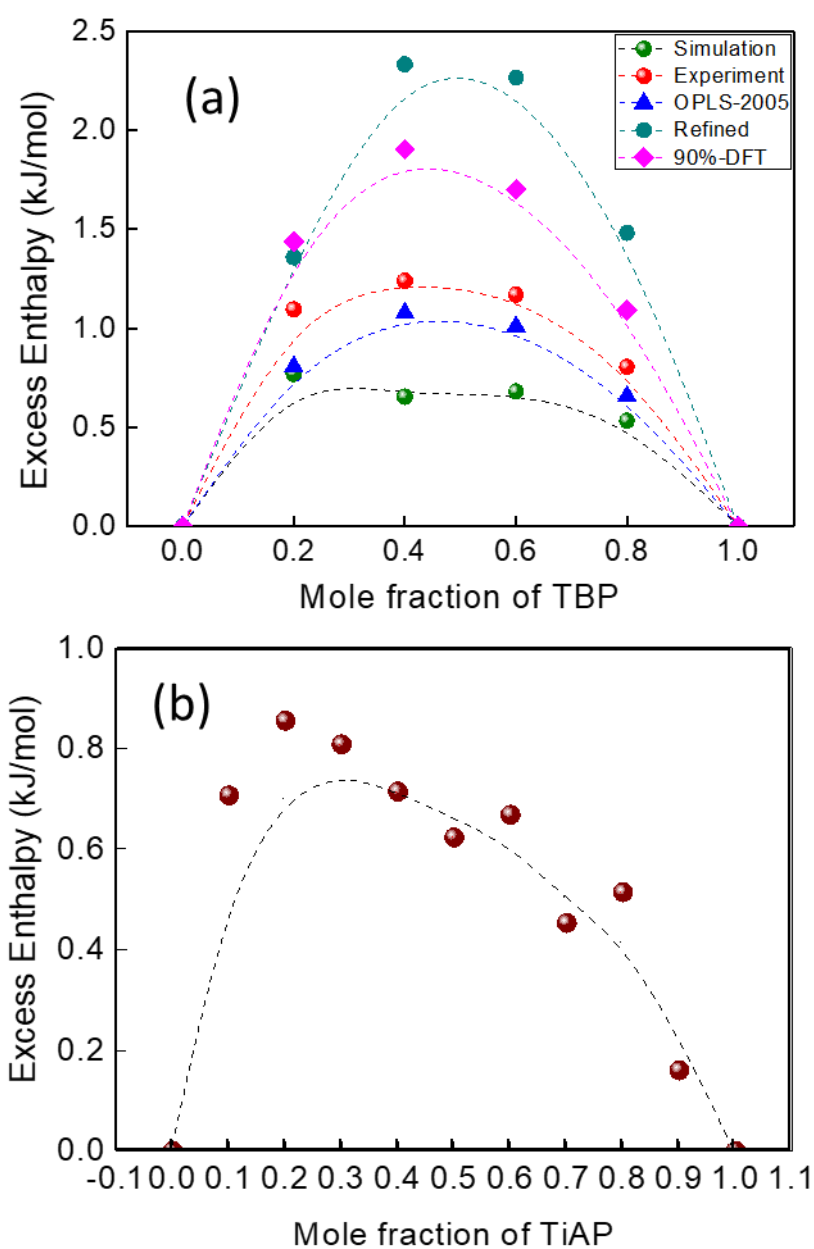


Figure 4.13: Excess enthalpy of mixing of (a) TBP/dodecane binary mixture and (b) TiAP/dodecane binary mixture

Next, the calculated excess enthalpy of TiAP/dodecane mixture is shown in [Figure 4.13\(b\)](#) and it follows the similar trend like TBP/dodecane mixture but since no experimental results are available for comparison, its level of accuracy cannot be validated.

4.3.8. Shear viscosity

The shear viscosity is an important dynamic characteristic of the liquid states. It has been seen that a single model cannot be able to explain the structural as well as dynamical properties of any system. It is very difficult to develop a force field without any parameterization which can describe equally both structural and dynamical properties. Here, earlier developed Mulliken embedded OPLS force field can explain structural and dynamical properties quite well. Hence, it is worthwhile to test this force field for calculation of shear viscosity. Therefore, shear viscosity is evaluated using periodic perturbation method from NEMD simulations for pure system as well as mixture [see [section 2.13](#)]. The determination of external force is crucial step for calculation of shear viscosity using NEMD method. So, the calculations have been at different values of external force which is reflected in [Figure 4.14](#).

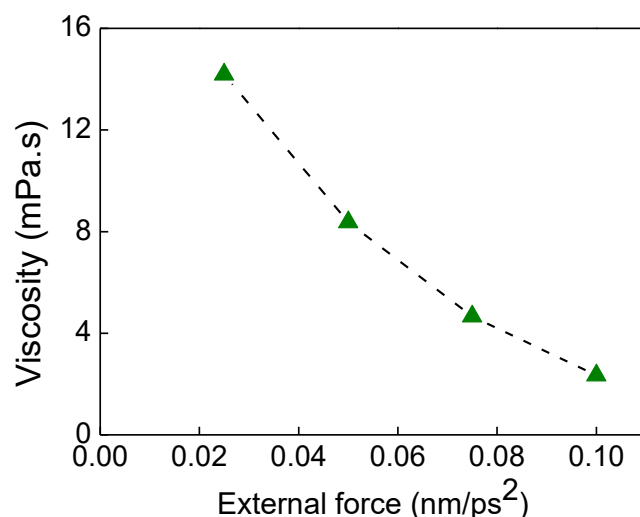


Figure 4.14: Shear viscosity of TBP as a function of external force in NEMD

The value of shear viscosity has been evaluated by extrapolation at $a = 0$. The shear viscosity obtained from this method is 19.99 mPa.s which is far away from the experimental value but similar value is also reported by *Mu et al* with 90% DFT model.⁴⁶ In case of TiAP, this method gives a value of shear viscosity which is much higher than the experimental value. The value of the external force will be small enough to ensure that the structure and dynamics should not be disturbed and it was found that normally it is taken in the range of 0.025 to 0.1 nm/ps² value. Again, the external force is chosen in such a manner that the calculated shear viscosity will be in good agreement with the experimental value of TBP. Then, the shear viscosity of pure TiAP as well as the binary mixture of TiAP/dodecane has been evaluated using that value of external force. Here considering all the issues, the external force has been chosen as 0.10 nm/ps².

Initially the Mulliken embedded force field is applied for pure TBP using a constant external force of 0.10 nm/ps².⁴³ The result shows that the calculated value is very close to the experimental value with a deviation of 0.25%, indicating a good accuracy of developed force field. Then, this method is used for computing shear viscosity of pure TiAP and it is found that the simulated value is little bit overestimating the experimental value but in good agreement. The calculated values and the experimental values of shear viscosity of pure liquids are represented in **Table 4.4**.

Table 4.4: Shear viscosity of pure TBP and TiAP

	TBP	TiAP	Dodecane
Experimental value (mPa.s)	3.24 ^a	4.27	1.29 ^a
Simulated value (mPa.s)	3.25 ± 0.02	4.74 ± 0.03	0.76 ± 0.08

^aThe experimental value for TBP was taken from Tian and Liu¹⁷ and experimental value of TiAP was from Singh.²⁴ The shear viscosity of TBP reported in the literature are 6.142 ± 0.043 mPa.s from refined model, 3.897 ± 0.029 mPa.s from OPLS-2005 model and

22.28 ± 1.78 mPa.s from 90% DFT⁴⁶. The reported shear viscosity of dodecane are 1.668 ± 0.038 mPa.s using optimized OPLS – AA (L – OPLS)¹⁵⁷, 1.22 mPa.s using OPLS – AA with parameterization⁶⁸.

The shear viscosity of dodecane is also calculated using this force field and the calculated value is little bit underestimating the experimental value. The excellent agreement of calculated shear viscosity for pure TBP and TiAP using calibrated OPLS force field further confirms the acceptance of the newly proposed OPLS force field.

Thereafter, the shear viscosity of TBP/dodecane binary mixture is also evaluated from this method and it is shown in **Figure 4.15(a)**.

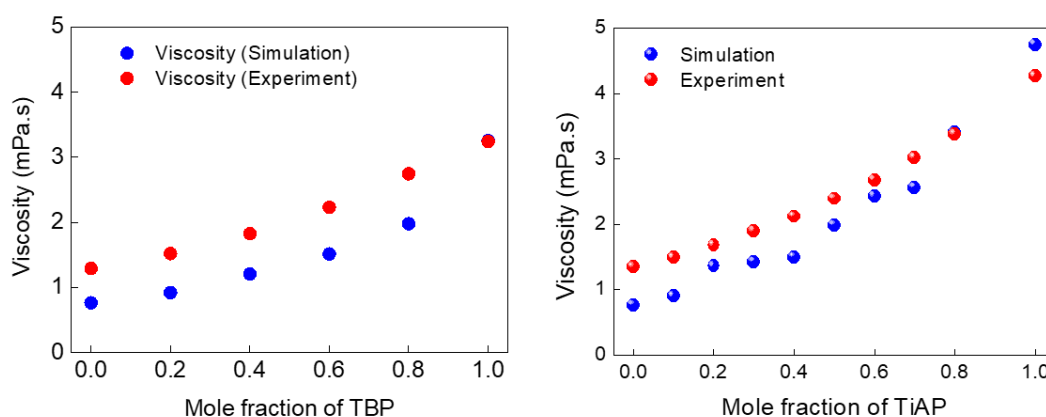


Figure 4.15: Shear viscosity of (a) TBP/dodecane binary mixture as a function of mole fraction of TBP in dodecane and (b) TiAP/dodecane mixture as a function of mole fraction of TiAP in dodecane.

The calculated values follow the similar increasing trend obtained from experiment. The shear viscosity value of pure TBP is quantitative to the experiment while the mixture is underestimating the experimental value. The deviation from experiment is decreasing with increasing TBP mole fraction which indicates the structural effect of TBP and dodecane play

an important role in the mixture. This study also ensures the validation of force field in the TBP/dodecane binary mixture.

Next, the shear viscosity of TiAP/dodecane binary mixture is also calculated from NEMD method. The calculated shear viscosity is plotted against the mole fraction of TiAP and it is shown in **Figure 4.15(b)**. The figure displays an increasing trend of shear viscosity with mole fraction. **Figure 4.15(b)** also reveals that the values calculated from simulations are in good agreement with the experimental values.²⁴

The rising trend of shear viscosity is similar to the experimental trend but a little bit higher rising rate of shear viscosity is observed after 0.70 mole fraction of TiAP. The calculated shear viscosity is underestimating the experimental value up to mole fraction of 0.70 and then it is overestimating. Such deviations can be explained from the aggregation of TiAP molecules which is dominating at higher concentration of TiAP, produce more frictional resistance. As the mole fraction increases, the contribution of TiAP molecule also increases. The structural effect of TiAP becomes weaker in the presence of dodecane. But when the contribution of dodecane is too low i.e. below 30% dodecane, the structural effect of TiAP become dominating in the mixture and sufficient shear velocity cannot be created by the external force. It introduces error in the measurement and thus results to a higher value of shear viscosity.

The shear viscosity obtained from simulations is also plotted as a function of calculated density of various compositions of TiAP/dodecane binary mixture and it is displayed in **Figure 4.16**. The graph states that the shear viscosity is an increasing function of mixture density and it follows the trend reported by **Singh and co-workers**.²⁴ Similar trend is also reported by **Tian and Liu**¹⁷ in their experimental study of TBP/dodecane binary mixture. This again proves the accuracy of newly developed force field.

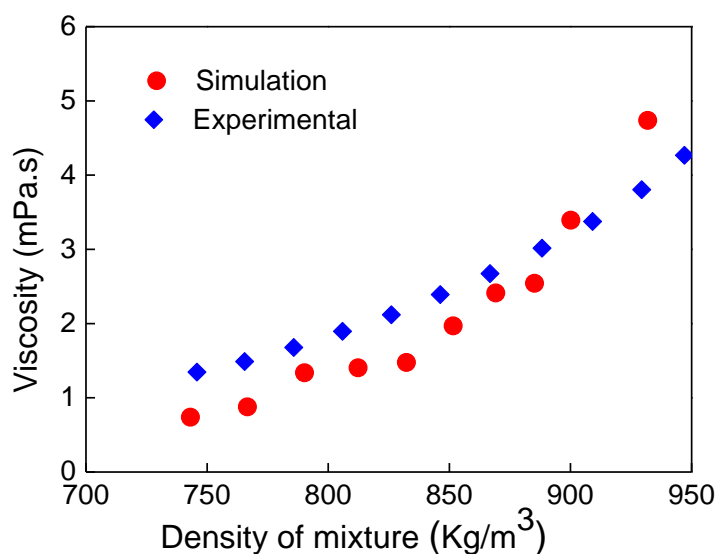


Figure 4.16: Shear viscosity of TiAP/dodecane binary mixture with corresponding density of the mixture.

4.3.9 Selection of composition for binary mixture of TiAP and dodecane

Dynamic properties of ligands or extractant play an important role in the extraction process. The mobility of the ligand is a determining factor for the formation of metal–ligand complex. In this context the dynamic properties are evaluated for various mole fraction of TiAP in TiAP/dodecane binary mixture and it is more crucial to select the useful composition of TiAP/dodecane mixture to develop efficient extraction system. The important parameters for the selection of composition are the diffusivity of TiAP in dodecane and the bulk viscosity of TiAP in the mixture. The low viscosity and high diffusivity are the major criteria for the selection of composition of any ligand–solvent system.

The mobility of pure TiAP is very slow compared to the n-dodecane as TiAP is heavier compared to dodecane. Hence, a diluent (dodecane) is added with pure TiAP to enhance the diffusivity and as well as the overall mass transfer of the extraction system. The optimum

composition of the ligand-solvent system is very important for a particular solvent extraction process. The most popular ligand and solvent used in the reprocessing of the spent nuclear fuel (SNF) are TBP and dodecane and the widely used composition for the well-known PUREX process is 30% TBP mole fraction. TiAP is a higher homologue of TBP and it is already established as a potential ligand over TBP in the reprocessing of the nuclear waste.

The optimum composition for the mixture might be decided by the intersecting point of the two curves and it is obtained at around 25% – 30% TiAP mole fraction (see [Figure 4.17](#)) which is much closer to the TBP/dodecane composition. Singh and co-worker have studied the removal of Cr (VI) using TiAP and they have shown that the removal was quantitative with 25% TiAP in 2M hydrochloric acid (HCl)²⁸, which may be mere happenstance and needs further investigation.

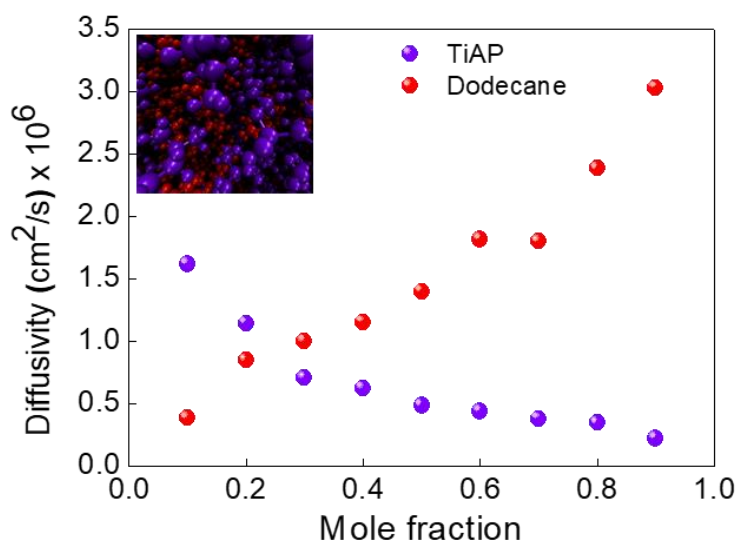


Figure 4.17: Diffusivity of binary mixture as a function of mole fraction

Furthermore, shear viscosity is shown to be an increasing function of mole fraction of TiAP whereas diffusivity of TiAP is a decreasing function. So, it is important to select an optimum

composition for developing an efficient mass transfer. From **Figure 4.18**, it is seen that optimum composition of mixture will be around 25–30% TiAP mole fraction where the curves are intersecting each other.

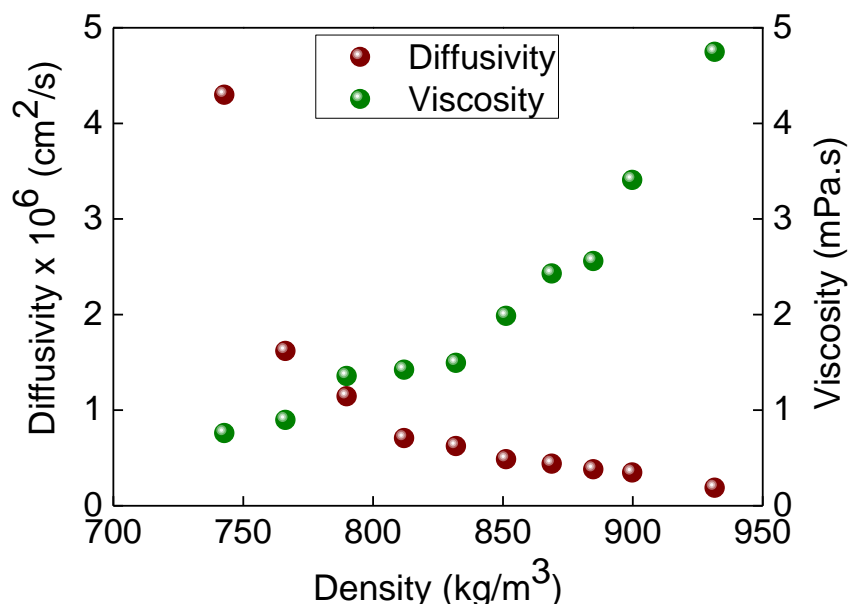


Figure 4.18: Diffusivity of TiAP and shear viscosity of TiAP-dodecane mixture as a function of density of the mixture

This composition of mixture exhibits a good value of diffusivity of TiAP and a low value of shear viscosity. One can choose a lower composition but there is another factor of TiAP concentration which should not be very low for extraction, otherwise metal loading in organic phase will be affected. Suresh and co-workers reported that 1.1 M TiAP/dodecane mixture which is in the range of 20–30% TiAP mole fraction, shows an excellent extraction efficiency for Th(IV) as well as U(VI) and even low extraction tendency of nitric acid.¹² Finally, this study indicates that 20–30% composition of TiAP/dodecane binary mixture is an effective composition for extraction. It needs further investigation using uranyl ion in bi-phasic extraction system.

4.3.10 Test of Stokes-Einstein relation in TiAP-dodecane mixture

In the preceding section, we have investigated the effect of mole fraction on the diffusivity and viscosity of a binary fluid mixture, where we have observed that shear viscosity is an increasing function of mole fraction of TiAP whereas diffusivity of TiAP is a decreasing function. Therefore it will be interesting to check the product of diffusion and viscosity against mole fraction. Fortunately, there is a very popular hydrodynamic relation known as Stokes-Einstein (SE) relation which connects the diffusivity and viscosity by the following expression:

$$D\eta = \frac{k_B T}{C\pi R} \quad (4.3)$$

where $C=4$ for slip and 6 for stick boundary condition and R is the radius of the solute^{85, 161-163}. The radius of TiAP solute has been estimated using volume obtained from COSMOtherm package¹⁰⁹. From the present MD simulations results, it is seen that SE relation is not satisfied at the molecular level as clearly revealed from the [Figure 4.19\(a\)](#).

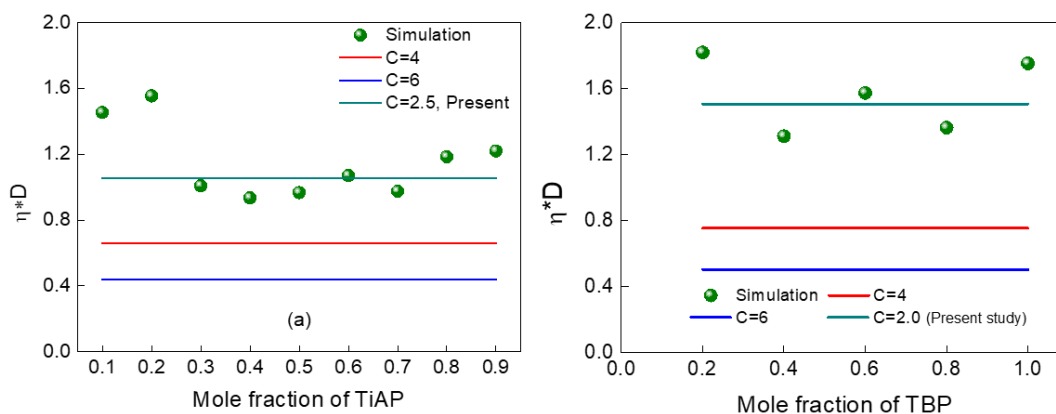


Figure 4.19: Plot of product of diffusivity and shear viscosity of (a) TiAP/dodecane mixture as a function of mole fraction and (b) TBP/dodecane mixture as a function of mole fraction of TBP in dodecane.

By changing the mole fractions of the components, the diffusivities and shear viscosities of the liquids can be changed but their product should remain fixed if SE relation would apply (see [equation 4.3](#)). But, the failure of S-E relation is expected as it was derived purely based on hydrodynamic theory, where a spherical solute moves with constant velocity in a fluid of shear viscosity. The [equation 4.3](#) does not contain any parameter which takes care of the mole fraction for finite concentration fluid mixture. The breakdown of SE relation has been reported earlier for molecular liquids at finite concentration¹⁶⁴⁻¹⁶⁷ and the same is reflected in our simulation results also. Further, SE relation for the present finite concentration system can be better expressed compared to stick or slip condition if the coefficient C in [equation 4.3](#) is taken as 2.5. Further, the validation of S-E relation has also been checked for TBP/dodecane binary mixture at different mole fraction and it is expressed in [Figure 4.19\(b\)](#).

The product of diffusivity and shear viscosity of TBP calculated from MD simulations is plotted against mole fraction of TBP in TBP/dodecane binary mixture and the ηD value located at far slipping boundary region. The corresponding value of numerical factor is 2 which is close to the TiAP/dodecane system and the TBP/dodecane mixture also follows the similar trend of TiAP/dodecane binary mixture. Earlier, the value of coefficient, $C=2$ has been used for Ar-Kr mixture at finite concentration¹⁶⁵.

4.4 SUMMARY

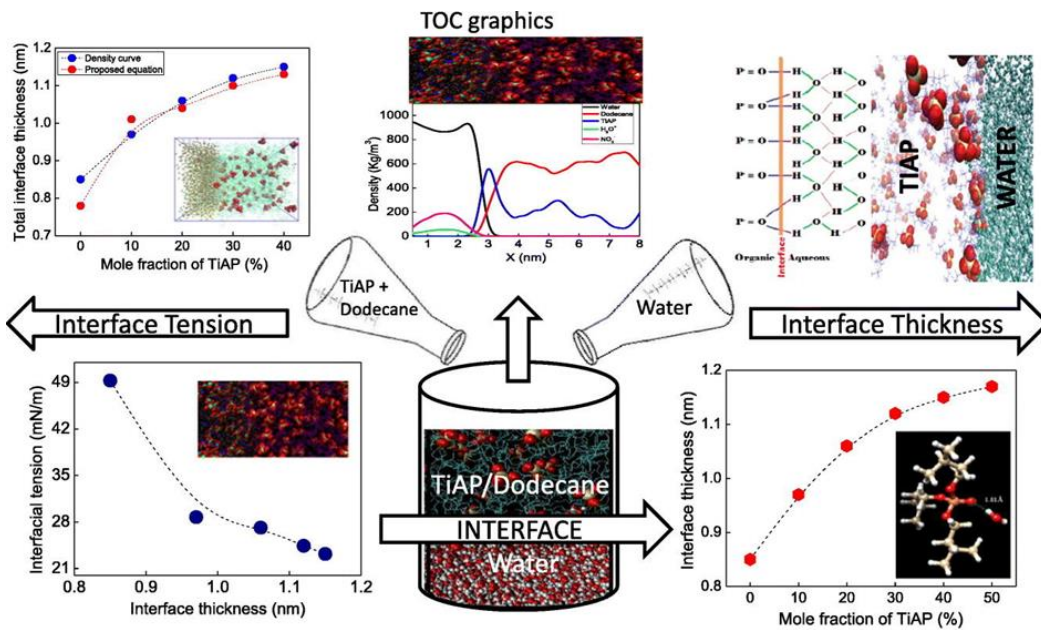
The structure, dynamics and thermodynamics of binary mixture of TiAP and dodecane have been determined and reported using the recently developed OPLS-AA potential by performing equilibrium and non-equilibrium MD simulations. The optimized OPLS potential embedding Mulliken partial charge was found to be quite successful in predicting the thermo physical and dynamical properties of pure liquids as well as of mixtures.

The calculated electric dipole moment of TiAP was seen to be mildly altered with TiAP concentration in the dodecane diluent in comparison to pure TiAP. The calculated liquid densities of TiAP/dodecane mixture were shown to be in excellent agreement with the experimental data over the entire range of the mole fraction. The mixture densities at different temperature are also studied which was found to be reduced with temperature as expected. The diffusivities of both TiAP and dodecane were computed and it was established that within the range of 25-30% TiAP in dodecane is perhaps the optimum composition to be used for conducting the solvent extraction experiment. Further, the excess volume of mixing for the TiAP/dodecane mixture was found to be positive over the entire range of mole fraction. In addition, the excess enthalpy of mixing was shown to be endothermic for TBP/dodecane mixture as observed experimentally and similar trend was also predicted for the TiAP/dodecane mixture. The characteristics of spatial pair correlation functions (PCFs) for TiAP/dodecane mixture was also captured over the entire range of the mole fraction. Furthermore, the calculated shear viscosity was in excellent agreement with the experimental values for both pure and mixture. Finally, this study indicates that 20–30% composition of TiAP/dodecane binary mixture is an effective composition for extraction. The newly calibrated OPLS force field was found to be working well even in the mixture and its predictability of experimental results for a wide range of temperature and mole fraction confirms the ability of the new OPLS force field. Further, the present MD simulations results demonstrate that SE relation breaks down at the molecular level.

The excellent matching of the computed results with the experimental results can be further extended to model the water-dodecane biphasic system which finally will be used for the extraction of uranyl ion as practiced in the PUREX process.

Chapter 5

Interfacial Phenomena of Biphasic Mixture



$$w_t^2 = \frac{(\sigma_{Water} + \sigma_{TiAP} + \sigma_{dodecane}) k_B T}{1.4 \sigma_{water} \gamma} \ln \left(\frac{L_{II}}{L_b} \right)$$

CHAPTER FIVE

Interfacial Phenomena of Biphasic Mixture

5.1 INTRODUCTION

The structural and dynamical properties of TiAP/dodecane binary mixture have been studied extensively in previous chapter using the calibrated force field to check its applicability in binary mixture and it was found that the developed force field is able to capture all the structural and dynamical properties of binary mixture as the simulation results were in good agreement with the experimental values which indicates the acceptance of the force field for binary mixture. Moreover, the earlier studies also predicted the composition of binary mixture for solvent extraction which was in the range of 20% – 30% of TiAP in dodecane based on the dynamic properties.

The interface between two immiscible liquids is one of the most interesting and important systems in physical chemistry, relevant to areas such as electrochemistry¹⁶⁸, chromatography¹⁶⁹, mass transfer catalysis¹⁷⁰ liquid-liquid extraction, drug delivery and many more. The buried nature of the interface makes the experimental probing of its structure and

dynamics at the molecular level very challenging. Theoretical studies are complicated by the strongly inhomogeneous environment and by the need to consider nontrivial intermolecular forces in order to reproduce the correct immiscibility, surface tension, etc., of the system. Thus, until recently, most experimental techniques studying the liquid-liquid (L-L) interface were based on macroscopic thermodynamic measurements such as the surface tension, and further most theoretical studies used continuum electrostatic and hydrodynamic model. These experimental and theoretical approaches, although have been used quite successfully in numerous applications, they are unable to provide a microscopic understanding of the L-L system. Thus, little is known about the microscopic structure and dynamics of the neat interface and, in particular, the behavior of solute molecules which are adsorbed (and possibly react) at the interface.

Moreover, the essential and crucial interfacial characteristics, interfacial tension (IFT) and interface width (IFW) can significantly affect the deformation of the interface and mass transfer and accordingly has a substantial effect on the industrial processes involving the oil–water interface. For example, a decrease of the dynamic interfacial tension with aging time provides signatures for protein clustering and crowding processes at the oil–water interface¹⁷¹ and IFT is also crucial to understand the oil–gas–water multiphase flow dynamics in porous media¹⁷², including the detachment of adhered oil from rock surfaces, the displacement of trapped oil and the crude oil emulsion stability. So, detailed knowledge of the structure and dynamics of the liquid/liquid interface is needed to solve many problems of considerable technological importance.

TiAP is almost insoluble in water compared to TBP and in acidic solution also. Hence, it is equally important to study the behaviour of TiAP/dodecane mixture in contact with aqueous phase in the presence of nitric acid in all aspect along with the performance of developed Mulliken embedded force field in TiAP–nitric acid–dodecane aqueous-organic biphasic

system. It is worthwhile to develop an understanding of structural and physical properties at the interface. Again, the interfacial properties in absence of acid are also required to make a comparative study and to establish a better understanding on the effect of aqueous phase acidity. As it is difficult to explore the molecular details of liquid–liquid interface by using advance experimental technique, limited experimental data is available which is not sufficient to develop an understanding of interfacial behaviour. This is mainly due to the fluidity of the interface and its buried nature, which precludes local experimental probing. Molecular dynamics (MD) simulations is an important tool which provides the microscopic view to predict the structure and dynamics of liquid–liquid interface.¹⁷³⁻¹⁷⁸ MD simulations can also explain the molecular level mechanism of capture and transfer of metal cation in liquid–liquid extraction process. Therefore, MD simulations offer an insight into the interface and provides quantitative explanation. The accuracy can be checked by comparing the calculated results with experimental data or other reported theoretical data. Therefore, MD simulations have been carried out on the equilibrium structure of interface as well as on the interfacial tension.

Though, in recent past, MD simulations were performed to investigate the interfacial properties of oil–water interfaces, progress in our fundamental understanding of interfacial properties has been relatively slow, perhaps due to the difficulty in defining the interface itself. So, the understanding of the interfacial properties is not clearly established. [Baaden and co-workers](#) have performed MD simulations to understand the microscopic picture at the interface with the effect of acidity and TBP concentration. They reported that the interface repelled the ionic species obtained from dissociated form of nitric acid in the absence of TBP while the neutral nitric acid behaves as surface active. They mainly focused on the mixing and de-mixing of aqueous–organic solution and their interfacial distribution, but did not calculate the interfacial tension and interface thickness.³⁶ [Sahu and co-worker](#) have studied uranyl extraction from water–dodecane system using TBP as an extractant and also reported that the water extraction

is much higher with un-dissociated HNO_3 compared to dissociated form of acid. They have reported the intrinsic thickness but the calculation of capillary thickness, total thickness and interfacial tension was untouched.¹⁷⁹ Wang and co-researchers have performed MD simulations on very simple immiscible (water + n-hexane) and partially miscible (water + 1-hexanol) systems and reported the interfacial tension and interface width. But they did not compute the total interface thickness as well as the effect of third component and acidity. They also reported that the interface is corrugated with small dynamic waves for immiscible system and highly corrugated with static waves for partially miscible system.¹⁸⁰ Jayasinghe and Beck have carried out MD simulations on liquid–liquid interfaces for developing interface structure and thermodynamics of solute transfer.³⁷ Furthermore, a considerable progress has been observed in the calculation of interfacial tension using MD simulations in recent past. Wen and co-workers evaluated decane–water interfacial tension induced by ionic hydration. They revealed the increment of interfacial tension at low ionic concentration as it enhances the ionic hydration at the interface. They also studied the effect of temperature and pressure on the interfacial tension but did not focus on the calculation of interface thickness.¹²⁸ Biswas and co-workers performed MD simulations for the extraction of cesium ion using macrocyclic ligands and ionic liquids and reported an enhancement of surface tension with the addition of metal salt.¹²⁹ It is really challenging to compute the interface thickness by means of experimental techniques because of the fluidity of interface. Earlier, advanced x-ray reflectivity studies¹⁸¹ and neutron reflectivity studies¹⁸² reported the interfacial width of the water/alkane interface. The long-standing query about the contribution of intrinsic thickness and broadening induced by capillary waves was partly resolved by the x-ray reflectivity studies.¹⁸¹ In order to compliment the experimental results, numerous MD simulations have been performed on the equilibrium structure of interface as well as on interfacial tension.^{173-178, 183} Among many, Jorge and co researchers performed MD simulations for water–nitrobenzene system to estimate the

total and intrinsic interface width by fitting density profiles where the proper prescription for calculation of total interface thickness is lacking and also has not been addressed the presence of third component and acidity.¹⁷³ Again, [Senapati and co-researchers](#) carried out MD simulations for computing the interface thickness and interfacial tension of carbon tetrachloride/water/carbon tetrachloride system. They calculated interfacial tension based on two different methods using pressure equation and capillary wave theory and computed the interfacial width by fitting the density curve¹⁸³ but didn't study the effect of third component for a wide range of concentration and acidity. From the above discussion it might be concluded that the exploration of water-oil interfaces is an awfully active, as well as contentious, field of research.

Further, earlier research works regarding interfacial studies, are related to mainly TBP/dodecane system and few of them have established the methodology of water transport to organic phase through TBP along with other interfacial properties but the understanding on structural and thermo-physical properties at the interface of water–TiAP/dodecane biphasic system is yet to be explored. Hence, it is worthwhile to address the problem by studying the structure and dynamics at the interface, interfacial properties and the solubility of water in TiAP because of its potential use in the field of nuclear fuel reprocessing. In addition to that there are lot of ambiguity in the calculation of total and intrinsic interface thickness and no one able to suggest any straightforward prescription for this purpose. Hence, an attempt has been made for the calculation of total and intrinsic interface thickness for simple as well as complex biphasic mixture using the concepts of QM, MD and statistical mechanics. Here, the discussion will be followed by simulation system, results and discussion and finally conclusion.

5.2 SIMULATION SYSTEMS

MD simulations have been performed to study the structure and dynamics of biphasic systems and the associated interfacial properties with the effect of aqueous phase acidity and mole fraction of TiAP. In the present study, the biphasic system includes an organic phase containing binary mixture of TiAP and dodecane and an aqueous phase containing nitric acid and they are in direct contact with each other. Not only the mole fraction of TiAP is varied from 10% to 40% but also the aqueous phase acidity has been changed from 0M to 4M to understand the effect on interfacial properties along with the structural and dynamical properties at the liquid–liquid interface of biphasic mixture. Water is represented by SPC/E model as it is more efficient compared to other models.¹⁸⁴ For TiAP and dodecane, we have used our recently developed Mulliken embedded^{94, 185} OPLS-AA (all–atom optimized potential for liquid simulations) force field.^{40, 68} The partial atomic charges on TiAP and dodecane were calculated from Quantum mechanical Mulliken population analysis.^{88, 89} The initial structures were optimized at the B3LYP level of theory using SVP basis set and then corresponding partial atomic charges were generated at the B3LYP/TZVP^{70, 71} level of theory using TURBOMOLE package⁶⁹. The partial charges of atoms for TiAP, dodecane, water and acid ions are taken from our earlier studies.

The starting simulation box is prepared by placing the TiAP molecules in dodecane molecules as the organic phase and water containing nitric acid molecules as the aqueous phase. Next, the volume of simulation box was made to be rectangular which is elongated in z direction with a cross sectional area of X x Y (X = Y) in x and y direction. A schematic biphasic simulation box containing 3000 water molecules and 500 TBP/dodecane molecules is shown in **Figure 5.1**. The dimension of simulation box is $L_x \times L_y \times L_z$ in x, y and z direction respectively where L_z is elongated. The interface is located at approximately one third of the box length starting from left corner and perpendicular to z-direction. Hence, one third of the total volume is occupied by the aqueous phase and rest by the organic phase.

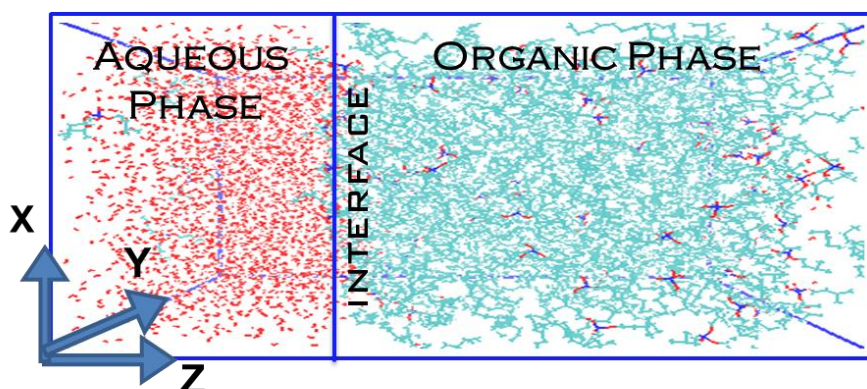


Figure 5.1: A typical biphasic simulation box containing TiAP in dodecane as organic phase and water as aqueous phase. The colour code and number of molecules for liquids are followed as red: water – 3000 molecules, blue and red: TiAP – 100 molecules and cyan: dodecane – 400 molecules.

For the present study, several biphasic systems have been prepared based on the mole fraction of TiAP in dodecane and on the acidity of the aqueous phase. Total 3500 number of molecules has been taken for all the systems where 500 molecules for the organic phase and 3000 molecules for the aqueous phase are kept constant. All the simulated systems are given in [Table 5.1](#) along with the molecules of respective phases and the corresponding dimensions of each simulation boxes.

Here, TiAP, dodecane, water and acid molecules are placed in a rectangular simulation box and then the system is relaxed by energy minimization using steepest descent algorithm in 5000 steps to adjust the atom coordinates and to avoid overlaps. Initially they formed a homogeneously mixed phase and then they started to separate out during equilibration in isothermal-isobaric (NPT) ensemble for 20ns simulation length with a time step of 2 fs.

Table 5.1: Details of compositions of various aqueous-organic biphasic systems and the corresponding MD simulations box dimensions

System	Mole fraction of TiAP	Acidity (M)	Box Size x, y, z (nm ³)	N _{TiAP}	N _{Dodecane}	N _{Water}	N _{H³O⁺} /N _{NO₃⁻}
D450-T50-W		0	5.760, 5.760, 8.687	50	450	3000	0
D450-T50-1M		1	5.769, 5.769, 8.677	50	450	2945	55
D450-T50-2M	10%	2	5.797, 5.797, 8.697	50	450	2895	105
D450-T50-3M		3	5.818, 5.818, 8.707	50	450	2845	155
D450-T50-4M		4	5.831, 5.831, 8.707	50	450	2800	200
D400-T100-W		0	5.835, 5.835, 8.753	100	400	3000	0
D400-T100-0.5M		0.5	5.838, 5.838, 8.745	100	400	2970	30
D400-T100-1M	20%	1	5.840, 5.840, 8.737	100	400	2945	55
D400-T100-2M		2	5.865, 5.865, 8.754	100	400	2895	105
D400-T100-3M		3	5.878, 5.878, 8.753	100	400	2845	155
D400-T100-4M		4	5.896, 5.896, 8.761	100	400	2800	200
D350-T150-W		0	5.885, 5.885, 8.783	150	350	3000	0
D350-T150-1M		1	5.902, 5.902, 8.787	150	350	2945	55
D350-T150-2M	30%	2	5.922, 5.922, 8.795	150	350	2895	105
D350-T150-3M		3	5.941, 5.941, 8.804	150	350	2845	155
D350-T150-4M		4	5.953, 5.953, 8.804	150	350	2800	200
D300-T200-W		0	5.949, 5.949, 8.834	200	300	3000	0
D300-T200-1M		1	5.959, 5.959, 8.827	200	300	2945	55
D300-T200-2M	40%	2	5.978, 5.978, 8.837	200	300	2895	105
D300-T200-3M		3	5.999, 5.999, 8.850	200	300	2845	155
D300-T200-4M		4	6.012, 6.012, 8.852	200	300	2800	200

The fluctuation in box dimension is allowed towards x direction as the box is elongated in that direction. At the end, the two phases were found to be immiscible. The periodic boundary conditions are applied in three directions to avoid surface effect. Further, the NPT coordinates are opted for production run in NVT (constant volume and constant temperature) ensemble over 10ns simulation length and the data obtained from this production run are used for the determination of various structural and dynamical properties.

5.3 RESULTS & DISCUSSION

Initially the MD simulations have been carried out for pure water followed by simple biphasic system like water/dodecane using our developed force field in order to ensure the validity of that force field prior to an application in a complex biphasic system like TiAP/dodecane in contact with aqueous phase having different nitric acid concentrations.

5.3.1 Water system

The water model was first tested using partial atomic charges calculated from Mulliken population analysis for its use in creating the aqueous-organic bi-phasic system. The calculated density and self-diffusivity were then compared with the available experimental results as shown in [Table 5.2](#) and noticed that there is marked deviation with the experimental results. In view of the deviation by Mulliken charge model, we evaluate the SPC^{186, 187} and SPC/E¹⁸⁴ water model for its simplicity and quantitative bulk properties compared to other models¹⁸⁴. The properties calculated from simulation using three different models are reported in [Table 5.2](#). It is seen that the physical and dynamical properties predicted by SPC/E model is quantitative with the reported experimental results whereas, the Mulliken charge model and SPC model show considerable deviation from the experiment. Further, the structural properties have been studied from PCFs: $g_{O-O}(r)$, $g_{O-H}(r)$, $g_{H-H}(r)$ to understand the liquid water structure and here all the models are almost similar as the first picks of $g_{O-O}(r)$ are located at around 2.75

Å. The first minimum obtained from PCF between O and H atoms is appeared at less than 2.45Å indicating the two water molecules are H – bonded. The position of first minimum of the O – O PCF is located at 3.45 Å which is used to find out the coordination number in the first solvation shell.

Table 5.2: Calculated physical and dynamical properties of pure water using three different models as Mulliken partial charge model, SPC model and SPC/E model

System	Density (kg/m ³)	Self-diffusion coefficient ($\times 10^{-9}$ m ² /s)	Dipole moment (Debye)	go-o(r) pick location (Å)
Water-Mulliken	976.54 ± 0.08	4.46 ± 0.07	2.27	2.75
Water-SPC	976.53 ± 0.15	4.04 ± 0.04	2.27	2.75
Water-SPC/E	999.03 ± 0.23	2.53 ± 0.09	2.35	2.75
Experimental	997 ¹⁸⁴	2.236 ± 0.004 ^a 2.12, 2.14 ^b , 2.30 ¹⁸⁴	1.85	2.73 ¹⁸⁴

The experimental value of self-diffusion coefficient of water was taken from ^aR. Mills¹⁸⁸ and ^bJ. H. Wang¹⁸⁹. The reported value of self-diffusion coefficient for SPC/E water model was $2.2 - 4.4 \times 10^{-9}$ m²/s. The reported literature data regarding the locations of first and second pick for SPC/E water model are as 2.75 & 4.50 Å [go-o(r)] and 1.77 & 3.25 Å [go-h(r)]¹⁸⁷ respectively.

Therefore, SPC/E water model was chosen for further aqueous-organic bi-phasic system simulation due to close agreement with the experimental results compared to other models. The density profile as a function of simulation length for SPC/E water model and its liquid structure are displayed in **Figure 5.2(a)** indicating the density of water has attained the equilibrium within few picoseconds.

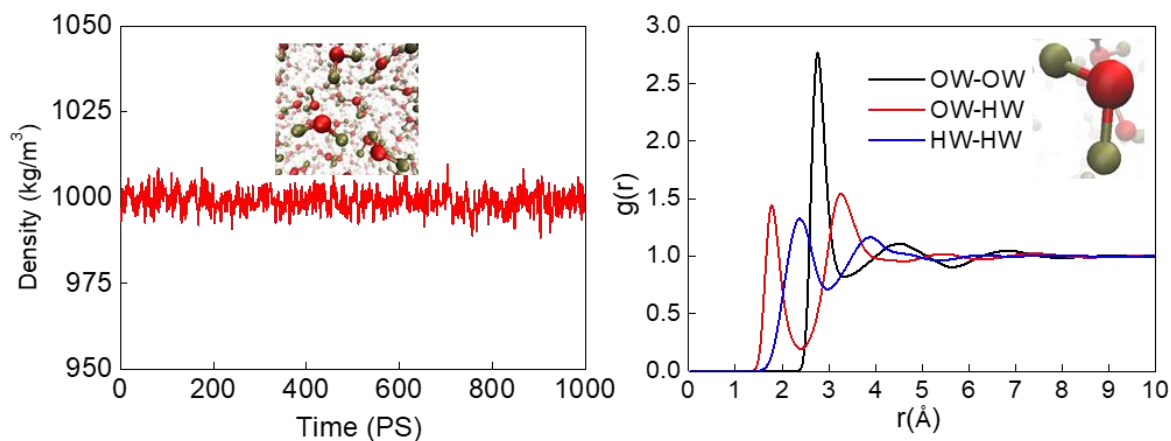


Figure 5.2: (a) Density profile and liquid structure of Water (SPC/E Model). Oxygen: Red balls and Hydrogen: Olive balls and (b) Plot of intermolecular pair correlation function between pairs of atoms of OW – OW, OW – HW, HW - HW of two water molecules.

Then, the pair correlation functions have been calculated between two interacting oxygen atoms, hydrogen atoms and oxygen and hydrogen atoms of two water molecules and it is shown in **Figure 5.2(b)**. The structure, dynamical and thermo-physical properties of pure TiAP and pure dodecane have been discussed in Chapter 3 and hence are not reported in the present chapter.

5.3.2 Pure nitric acid & 3M nitric acid system

After discussion of various properties of water, it is equally important to evaluate the physical and dynamical properties of pure nitric acid as well as 3M nitric acid to understand on molecular level. Here, nitric acid has been used in associated and dissociated form. For this study 1000 numbers of acid molecules have been taken in a square box and then the system was equilibrated followed by energy minimization. Finally, the production run has been carried out to compute the properties. So, the properties of both forms of acids have been compared to check whether there is any discrepancy or not. The structural and dynamical properties are listed in **Table 5.3**.

Table 5.3: Calculated physical and dynamical properties of pure nitric acid and 3M nitric acid using Mulliken partial charge embedded force field.

System	Density (kg/m ³)	Self-diffusion coefficient ($\times 10^{-9}$ m ² /s)	Dipole moment (Debye)
Pure nitric acid (Associate form)	1559.73 \pm 0.12	0.0035 \pm 0.02	3.45 \pm 0.50
Pure nitric acid (Dissociate form)	1634.77 \pm 0.30	0.00076 \pm 0.001 (H ₃ O ⁺) 0.0019 \pm 0.002 (NO ₃ ⁻)	1.05 \pm 0.69
3M Nitric acid	1059.44 \pm 0.25	0.825 \pm 0.02	2.41 \pm 0.26

The experimental values are taken from Lide, D.R., CRC Handbook of Chemistry and Physics 88TH Edition 2007-2008. CRC Press

The calculated density of pure nitric acid in associate form is quite close to the experimental value with a deviation of around 3% indicates the accuracy of Mulliken embedded force field. The dissociate form of nitric acid exhibits comparatively higher value of average density as 1634.77 kg/m³ because of close packing due to size effect and less dipole moment as shown in [Table 5.3](#). Again, the simulated density of 3M nitric acid is less than the pure nitric acid which is obvious and it is also in close agreement with the experimental values in the range of 4% deviation. The density of 3M nitric acid appears with in the densities of water and pure nitric acid which also validates the force field.

The density profile of pure nitric acid in associate and dissociate form along with 3M nitric acid as a function of simulation length and the respective liquid phase structures generated after equilibration are shown in [Figure 5.3](#) and [Figure 5.4\(a\)](#). The clustering of nitric acid in water medium for 3M nitric acid was observed.

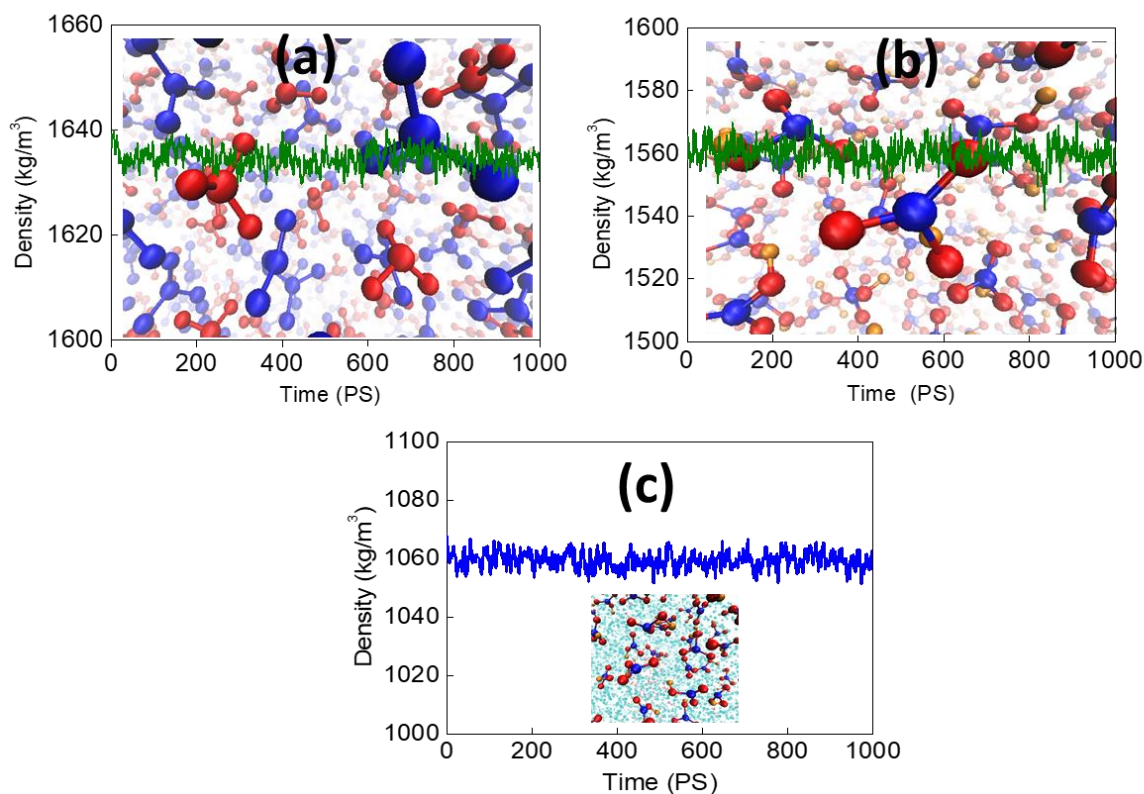


Figure 5.3: Density profile and liquid structure of (a) Dissociated form of pure nitric acid: H_3O^+ - Blue balls, NO_3^- - Red balls, (b) Associated form of pure nitric acid: O-Red balls, N-Blue balls and H-Orange balls and (c) 3M nitric acid. O: Red balls, N: Blue balls, H: Orange balls and Water: Cyan dots.

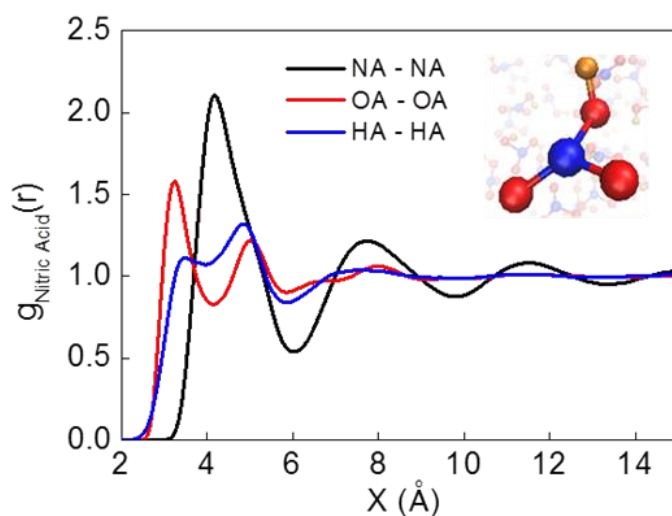


Figure 5.4: Plot of intermolecular pair correlation function between pairs of atoms of NA - NA, OA - OA, HA - HA of two nitric acid molecules of pure nitric acid.

The structure on molecular level can be expressed by pair correlation function (PCF) between two interacting atoms like nitrogen (NA), oxygen (OA) and hydrogen (HA) atoms of two interacting nitric acid molecules and it is shown in **Figure 5.4(b)**. The first peak of NA – NA PCF of nitric acid is appeared at 4.15Å with a peak height of 2.12 while the peak of OA – OA PCF of two interacting associated nitric acid molecules is located at 3.25Å which signifies the oxygen atoms of two nitric acids are comparatively closer than that of the two nitrogen atoms. The first peak location of two interacting hydrogen atoms (HA) of nitric acid is appeared at 4.85Å followed by a hump located at 3.45Å.

Again, the PCFs of NA – NA, OA – OA and HA – HA for 3M nitric acid is also computed to find out whether there are any changes in structural parameters of nitric acid and it is shown in **Figure 5.5(a)**. The first peak of NA – NA PCF is appeared at a location of 4.15Å and for OA – OA PCF, it is at 3.25Å which are exactly similar to the values obtained in pure nitric acid. The HA – HA PCF also gives the similar value. So, the structural parameters between two interacting nitric acids are not affected in presence of polar solvent like water. It is also observed that the peak heights are quite high for all the PCFs signifies the probability of finding nitric acids in first solvation shell is higher which indicates the aggregation of nitric acids in water medium. So, clustering effect of nitric acid in water medium is observed. It is also supported by the coordination number (CN) calculated for both the cases and listed in **Table 5.4**.

Table 5.4: Coordination number calculated from PCF for pure as well as 3M nitric acid

Atoms	CN (Pure nitric acid)	CN (3M nitric acid)
NA - NA	0.54	2.78
OA - OA	0.83	4.72
HA - HA	0.84	4.12

It is clearly seen that the coordination numbers for 3M nitric acid is higher than that of the pure acid which also supports the clustering effect.

Next, the PCFs have been evaluated for two nitric acid sites (OA and HA) with two water sites (OW and HW) and reported in **Figure 5.5(b)**. The first peaks of PCFs of oxygen atoms (OA – OW) and hydrogen atoms (HA – HW) are located at 3.35 Å and 3.05 Å respectively.

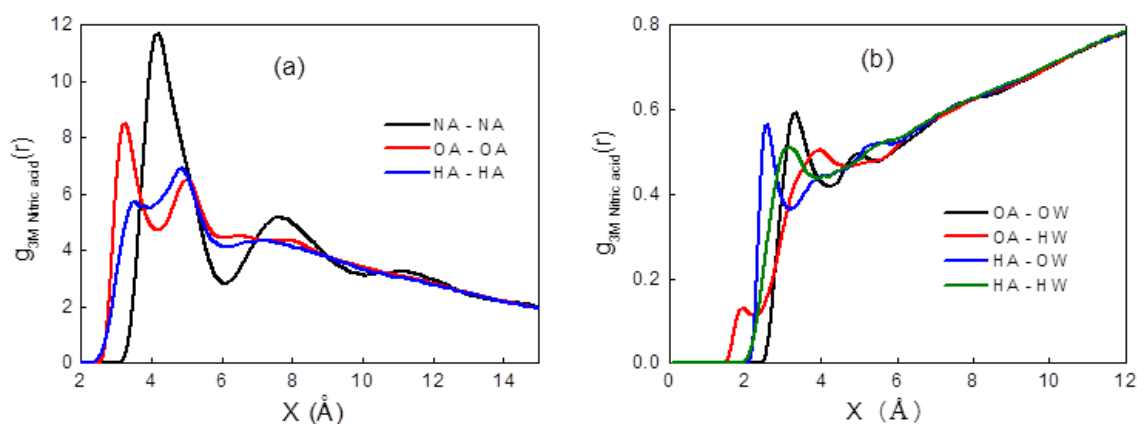


Figure 5.5: Plot of intermolecular pair correlation function for 3M nitric acid (a) PCFs between pairs of atoms of NA – NA, OA – OA, HA - HA of two nitric acid molecules and (b) PCFs between water and acid molecules of OA – OW, OA – HW, HA – OW and HA – HW pairs of atoms.

Thereafter, the formation of hydrogen bonds between oxygen of nitric acid and hydrogen of water molecule or the oxygen of water molecule and hydrogen of nitric acid can be seen from PCFs expressed in **Figure 5.5(b)**. The OA site of HNO₃ is involved in weak hydrogen bond with HW site of water as the first peak is located at 2.55 Å. Similar observation was also reported by *Shamay et al* as 2.24 Å¹⁹⁰. Again, the hydrogen bond of HA site of nitric acid to OW site of water emerges comparatively strong as the first peak is appeared at 1.95 Å which is close to the reported value of 1.87 Å¹⁹⁰.

5.3.3 Biphasic System

5.3.3a. Water–dodecane system

First, the performance of the developed force field needs to be verified in aqueous-organic biphasic system in the absence of ligand and acid before its implementation in more complex molecular system. Hence, it is worthwhile to develop first an understanding of water–dodecane biphasic system. The simulations were carried out with 2800 water molecules and 400 dodecane molecules. The structural and dynamical properties of water–dodecane system are discussed by considering 70:30 volume ratios between water and dodecane molecules. The density profile is shown in **Figure 5.6** which displays a sharp interface that separates the two liquid phases.

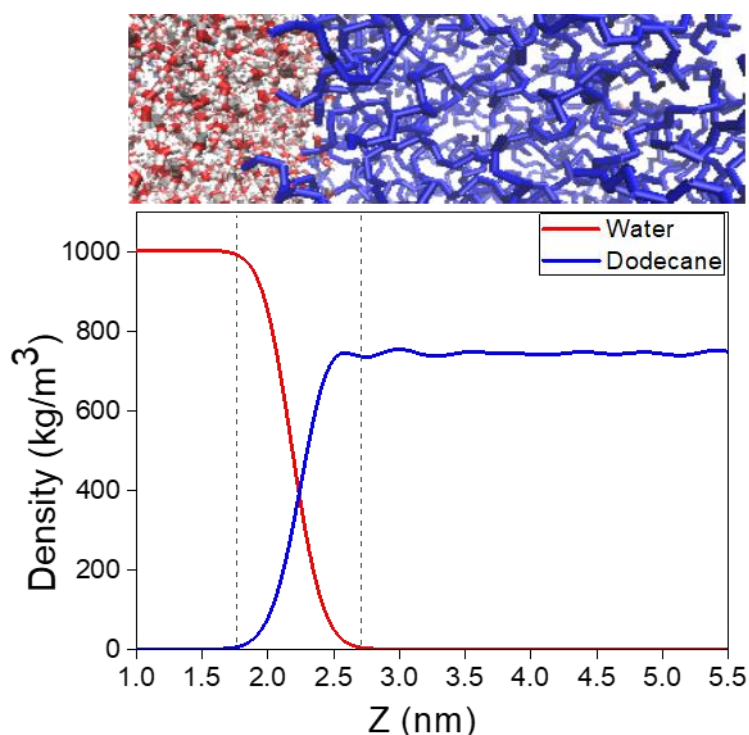


Figure 5.6: Density profile of water–dodecane system with snapshot representing the biphasic mixture of water (left side: red/white) and dodecane (right side: blue).

The computed average bulk density of water and dodecane away from the interface are about 1001 kg/m^3 and 744.61 kg/m^3 respectively which are in quite good agreement with the reported experimental values of 995^{184} kg/m^3 and $745.79^{17} \text{ kg/m}^3$ respectively. Further, the larger surface area at the interface as well as wider interface indicates large number of water molecules are in contact with the dodecane molecules as seen from the snapshot in **Figure 5.6**. Again, this can also be well understood from the snapshot captured from dodecane side of simulation box represented in **Figure 5.7**. It shows the interfacial roughness which is an indication of large surface area available at interface.

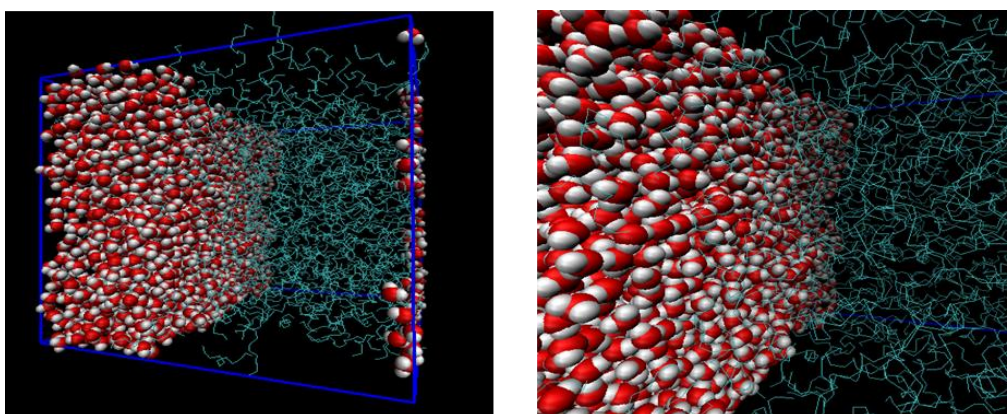


Figure 5.7: Snapshot of interfacial region of water – dodecane system illustrating surface roughness

The diffusivity of water and dodecane are also calculated in water–dodecane system and it was found that though the diffusion coefficient of dodecane remains unchanged as compared with our previous work⁹⁴, but in presence of dodecane, the diffusivity of water has been reduced from 2.53×10^{-5} to $1.65 \times 10^{-5} \text{ cm}^2/\text{s}$ as shown in **Figure 5.8** which may be due to the influence of the dodecane phase on the water phase. Further, the interfacial tension also has been computed at the water–dodecane interface using the pressure tensor method and the value obtained from simulation is 49.27 mN/m which is in quite good agreement with the reported experimental data of $52.8 \text{ mN/m}^{191, 192}$.

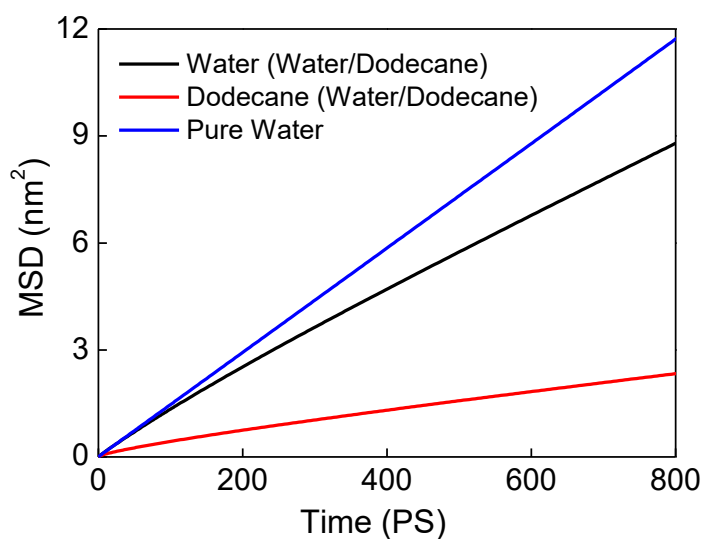


Figure 5.8: MSD of water and dodecane for water–dodecane biphasic system along with MSD of pure water.

5.3.3b. Neutral water/ (TiAP + dodecane) system

In the preceding section, the developed force field was tested for biphasic system like water – dodecane system and the performance was quite good. Now, TiAP has significant influence on the structural and dynamical properties of the interface. Therefore, next, the effect of TiAP on the interfacial properties of TiAP/dodecane–water biphasic system was studied along with the validation of the newly developed force field. From our previous studies the effective composition of binary mixture was concluded to be between 20–30% mole fractions of TiAP.¹⁸⁵ Hence, the compositions selected for this present study are within 10–40% to generate sufficient data for a quantitative understanding. The description of the simulated system is provided in [Table 5.1](#).

Liquid state structure of water/ (dodecane + TiAP) system

Generation of appropriate liquid state structure is a primary requisite in performing the MD simulations and subsequent property calculation. During creation of the simulation box with

two phases, initially both phases are seen to be randomly mixed even after energy minimization. Then, the phases are started to be separated out during equilibration in NPT ensemble. The snapshots of liquid structures at different simulation length of equilibration process are depicted in **Figure 5.9(a)** to understand the separation of phases. The transport mechanism of water has been already reported by *Ye et al* in their studies on MD simulation of water extraction into a TBP/dodecane solution¹⁹³, therefore it is not repeated here again. In the present work, we are interested to discuss about interface thickness and interfacial tension at TiAP/dodecane-water interface and the effect of packing of TiAP at the interface as well as the mole fraction of TiAP on the interfacial properties.

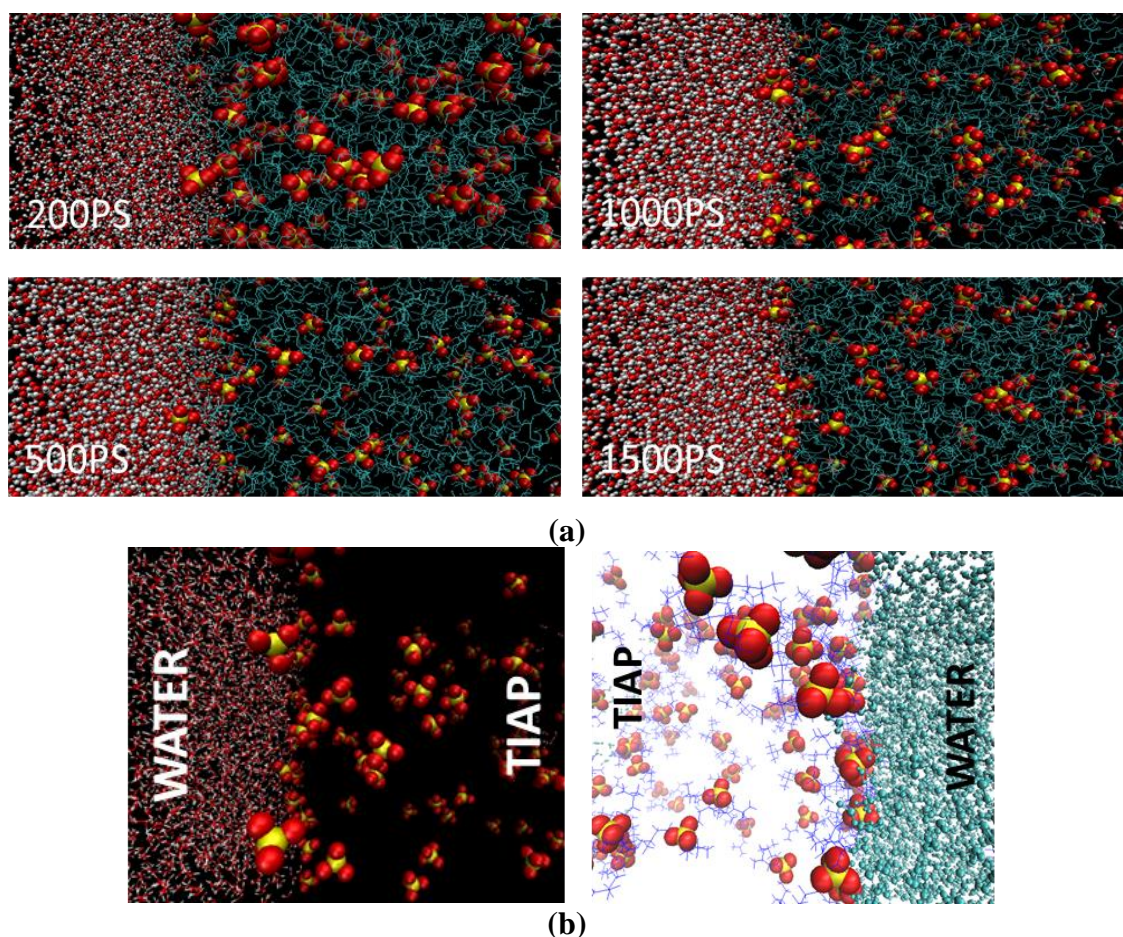


Figure 5.9: (a) Snapshot of water/(TiAP + dodecane) system at different simulation length representing the TiAP accumulation at neutral interface. System: water-20%TiAP in dodecane. Colour code: red-O, yellow-phosphorous, white-H, cyan-dodecane and (b) orientation of phosphoryl group of TiAP molecules at neutral interface

As seen from the above snapshots, the interface becomes sharper with time progression of the simulation length indicating the phases are started to separate out and it is observed that after 1500ps, they are separated with a sharp interface. At the same time, the accumulation of TiAP at neutral interface is increased with increasing simulation length. The TiAP molecules are migrated towards the interface from bulk dodecane phase. Further, it gradually increases the surface roughness as well as the interfacial area. The TiAP molecules are oriented in such a manner that the phosphoryl group of TiAP molecules are pointed towards water molecules at the interface as shown in [Figure 5.9\(b\)](#).

Density profile for neutral water / TiAP + dodecane

Density profile of neutral water–TiAP/dodecane biphasic systems for all the systems have been evaluated along the z-direction of simulation box with the effect of mole fraction of TiAP in dodecane. Concentration of TiAP has an important implication on the interface. It affects the interface structure and the interfacial properties also. Again, the packing of TiAP at the interface and the concentration of TiAP at the bulk phase is also influenced by mole fraction of TiAP in dodecane. The above effects can be observed from the snapshot of liquid structure taken at the liquid–liquid interface (see [Figure 5.10](#)) and the corresponding density profile of various mole fractions considering 10% to 40% mole fraction of TiAP.

The density profile of dodecane is passing through a maxima appearing at some distance from interface as shown in [Figure 5.10](#) which indicates that the interface is not so sharp and the packing is propagated more intensely into the bulk dodecane phase. Again, as illustrated in the above snapshots of TiAP/dodecane – neutral water system, TiAP is accumulated at the interface with increasing mole fraction of TiAP from 10% to 40%. The increasing peak height of TiAP at the interface as shown in density profile also proves the same phenomena.

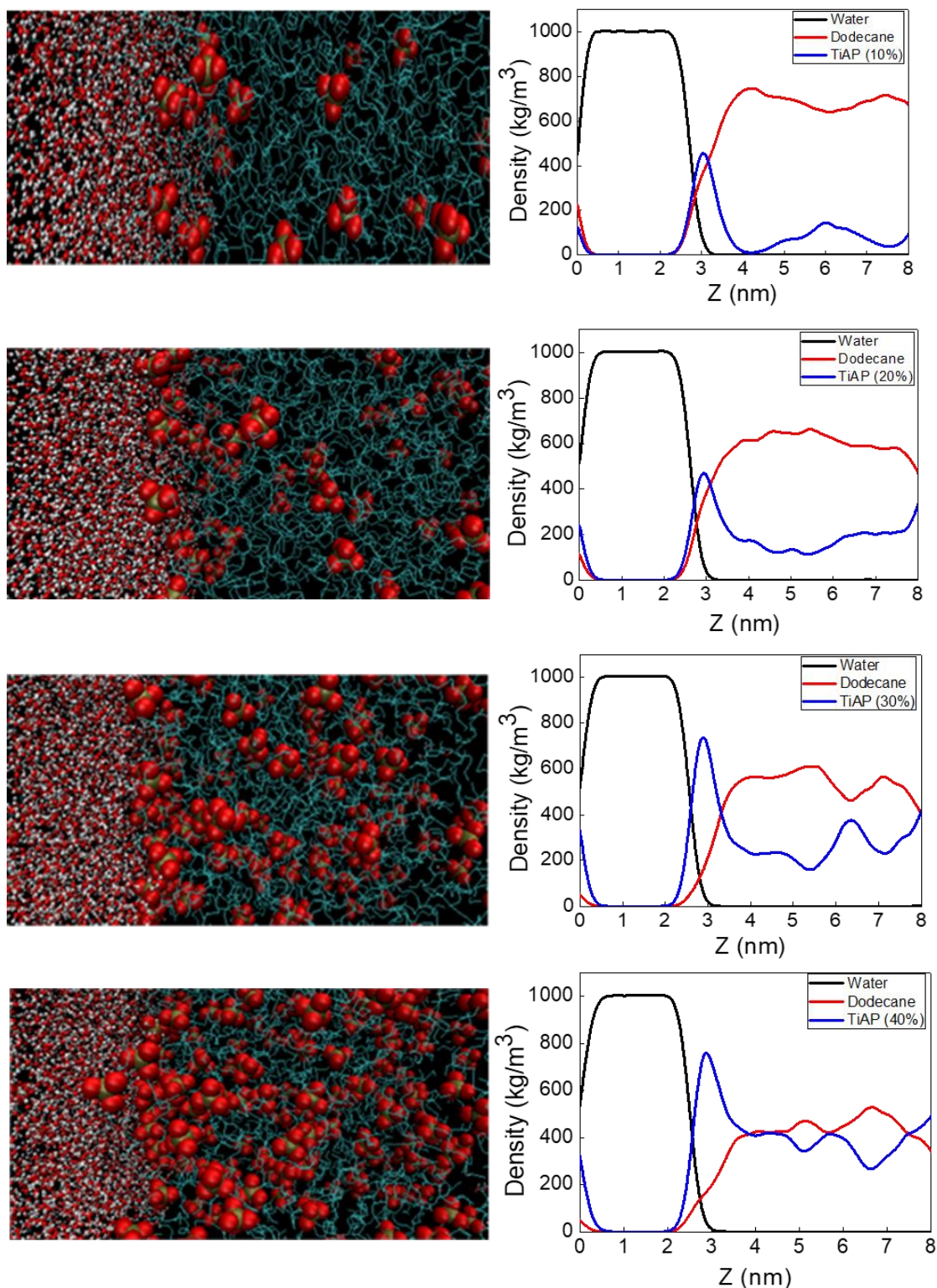


Figure 5.10: Snapshot of liquid structure and its corresponding density profiles for 10%, 20%, 30% and 40% mole fraction of TiAP/dodecane-water biphasic system. Cyan: dodecane, red & white: water, red & grey: phosphoryl group of TiAP.

In addition to that, the TiAP molecules form chain like structure along the interface at higher concentration. For a particular TiAP mole fraction, TiAP is aggregated at the interface diluting the bulk dodecane phase but with increasing mole fraction, the average TiAP concentration is raised up in bulk dodecane phase as seen from snapshots and also from density profile in [Figure 5.10](#).

Again, it can also be concluded that the higher TiAP accumulation at interface leads to higher interfacial roughness and thus a wider effective interfacial area where larger number of water molecules are exposed to the organic phase. Therefore, higher roughness will promote the water molecule to enter into the organic phase by breaking the fewer hydrogen bonds which connects the water molecules in the aqueous phase. Hence, surface roughness has significant role on water extraction to the organic phase. The increasing interfacial area with mole fraction of TiAP is depicted in [Figure 5.11](#).

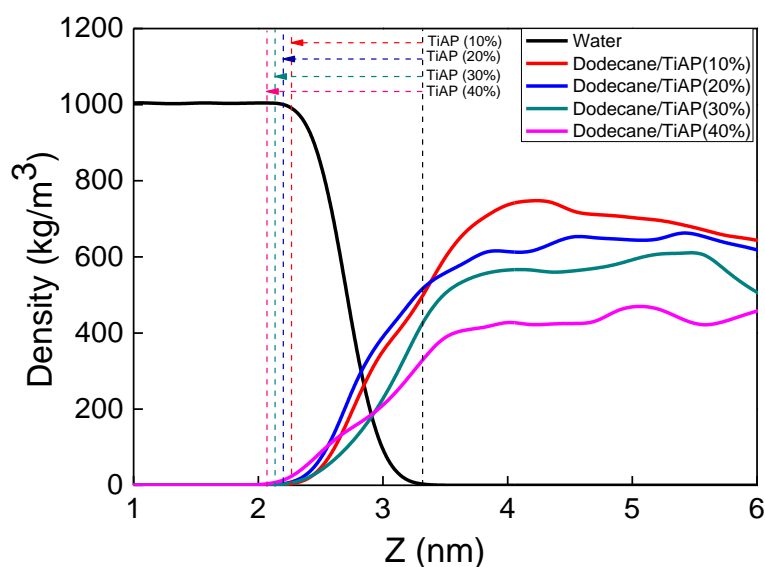


Figure 5.11: Schematic density profile for various mole fraction of TiAP from 10 % to 40%, representing the interface thickness which increases with mole fraction of TiAP.

Figure 5.11 illustrates a typical representation of the density profile of water and dodecane for various mole fraction of TiAP from 10% to 40% to discuss the effect of mole fraction of TiAP on the interface thickness. In this context, the corresponding water–dodecane interface thickness has been calculated using each water-dodecane profile obtained from individual systems. The position of organic molecules at the aqueous edge and the water molecules at the organic edge are represented by the vertical lines and the distance between two vertical lines indicating the interface thickness (shown by dashed lines in **Figure 5.6**). Point to be noted that quite similar methodology was earlier adopted for determining the total interface thickness¹⁷³ for water-nitrobenzene system. It is clearly seen that the interface thickness is broadened with increasing mole fraction of TiAP. Therefore, the choice of mole fraction of TiAP for liquid–liquid extraction system is very crucial and higher mole fraction leads to higher water extraction in the organic phase which is not desirable. Again, lower mole fraction provides lower interfacial area which affects the rate of mass transfer and it is also not desirable. So, we have to optimize a composition to develop an efficient extraction system which is discussed in the succeeding sections.

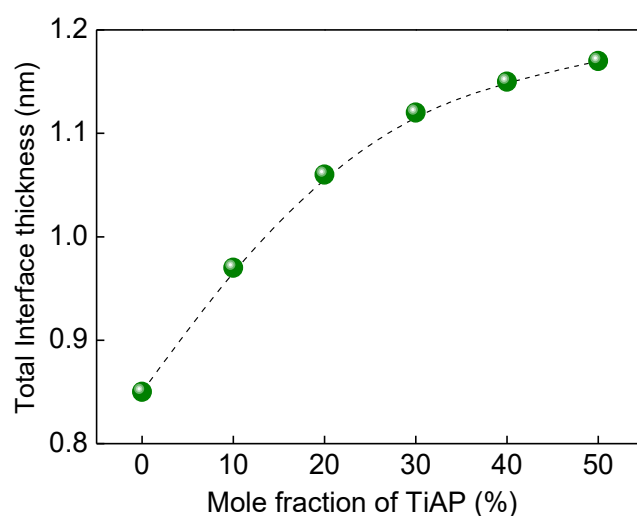


Figure 5.12: Total interface thickness as a function of mole fraction of TiAP representing an increasing trend of interface thickness.

The interface thickness plays an important role in mass transfer. At higher interface thickness, mass transfer rate is high and the roughness is also high which greatly influences the mass transfer. In **Figure 5.12**, the interfacial thickness is expressed as a function of mole fraction of TiAP and it shows an increasing trend. The interface thickness is calculated from respective density profile using the distance between the die out point of each phase. Initially, the growth of interface thickness is high but finally it reaches to near saturation. Hence, the interface thickness is affected only up to a certain mole fraction of TiAP (here 50%) and after that it is not worth to increase the mole fraction of TiAP in dodecane as it will not of much help in the mass transfer further.

In this aspect, the microstructures of these biphasic liquid mixtures also have been characterized from pair correlation function (PCF) to understand the interfacial structure. Here, PCFs, mainly accounting the interaction between phosphoryl group and water molecules are only discussed. The PCFs between phosphorous atoms (P – P) and phosphorous and oxygen atoms (P – O) of two TiAP molecules were already analysed in Chapter 4 (see **Figure 4.10**). So, PCFs between O – HW and O – OW of interacting TiAP – water molecules are evaluated to understand the relative positions of phosphoryl group and water molecules in the mixture. The PCFs of O – HW and O – OW are presented in **Figure 5.13(a)** and **Figure 5.13(b)**. The higher peak height at lower TiAP mole fraction is due to high local density and then it is decreasing with increasing mole fraction of TiAP as discussed in our previous chapter. Again, the PCFs between oxygen atom of TiAP molecule and hydrogen atom of water molecule along with the oxygen atom of TiAP and oxygen atom of water are also shown in **Figure 5.13(a)** to understand the availability of TiAP molecules at the water surface.

The first peaks of O–HW for all compositions of TiAP are appeared at same location, 1.95Å indicating that the interfacial positional distribution of TiAP and water molecules is independent of mole fraction of TiAP. In addition to that, the peak height is decreasing at higher

mole fraction of TiAP interpreting the availability of water molecules surrounding the TiAP molecules is reduced. At higher mole fraction, larger numbers of TiAP molecules are accumulated at the interface and it reduces the probability of founding water molecule around TiAP molecules. It is also rendered the formation of hydrogen bond between oxygen of phosphoryl group and hydrogen of water. Similar trend is also observed for PCFs between O–OW of two interacting TiAP and water molecules in [Figure 5.13\(b\)](#) where the first peaks are appeared at around 2.85\AA .

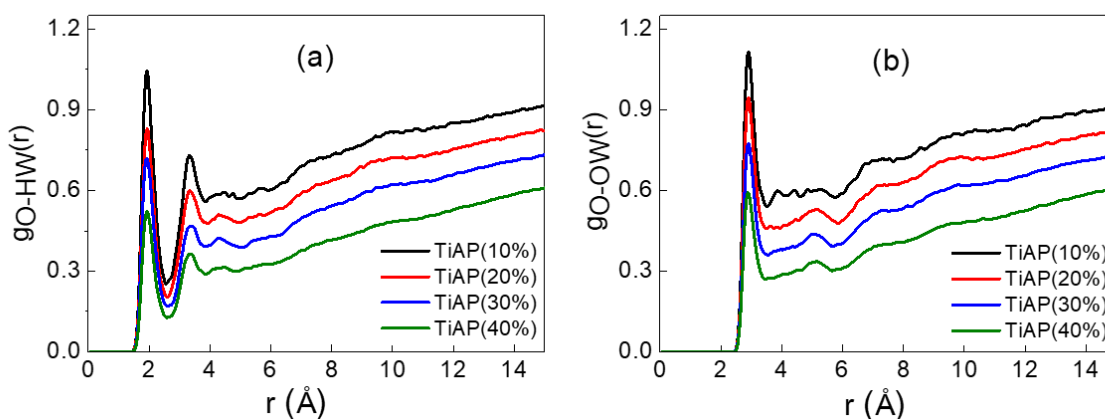


Figure 5.13: Pair correlation function (a) between O – HW atoms and (b) between O – OW atoms of two interacting TiAP and water molecules.

Further, the interfacial tension is the most important interfacial property. It has strong influence on the characteristics of liquid – liquid interface and also a guiding parameter for dispersion of one phase into other. The interfacial tension has been calculated for neutral water–TiAP/dodecane biphasic system using pressure tensor method. The output obtained from production run is used for further semi-isentropic run followed by surface tension run. The values of interfacial tension obtained from simulation along with reported experimental data are presented in [Table 5.5](#).

Table 5.5: Interfacial tension of neutral water-TiAP/dodecane system at T=300^oK

Mole fraction of TiAP in %	Interfacial tension (mN/m)	
	Simulation	Experiment ²⁴
0	49.3± 1.6	52.6
10	28.7± 2	35.3
20	27.1± 2.3	25.5
30	24.4± 2.9	20.5
40	23.2± 2.1	18

From the table, it is seen that the interfacial tension is decreasing with increasing mole fraction of TiAP. Interfacial tension is maximum in absence of TiAP molecules and then it is decreasing gradually indicating TiAP acts as a surface active agent which can be nicely explained from the concept of interfacial roughness. As it is seen from the above snapshot and density profile in [Figure 5.10](#), the system with higher mole fraction of TiAP induces the TiAP molecules to accumulate at the interface and large numbers of water molecules are in contact with them resulting to larger interfacial roughness which facilitates the breaking of hydrogen bonds between water molecules and of making hydrogen bond between phosphoryl group of TiAP and water molecules as shown in [Figure 5.14](#). Thus, the interaction between water molecules is reduced in presence of TiAP. The breakage of hydrogen bond among water molecules reduces the surface tension of water and it may help to increase the mingling of water and organic phases. Therefore, at higher TiAP concentration the packing of TiAP at the interface is increased which accelerates the hydration of TiAP and thus leads to more reduction of the interfacial tension. Similar observation was also reported by [Zhang et al.](#)¹⁹⁴

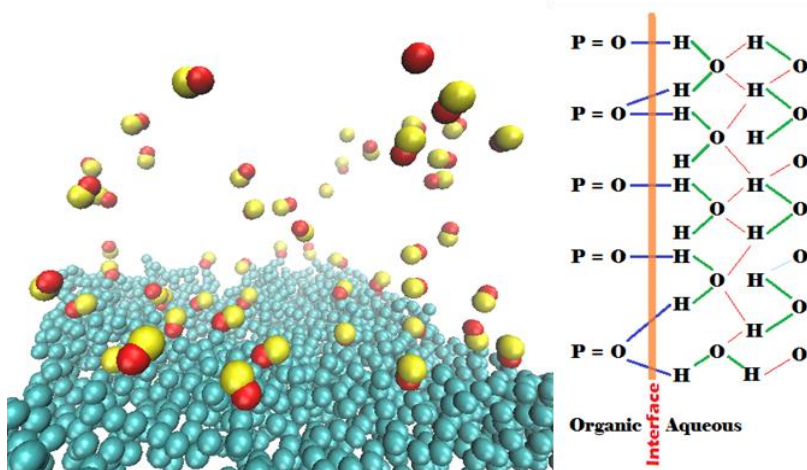


Figure 5.14: Snapshot of phosphoryl group of TiAP and water molecules at interface representing the orientation of phosphoryl group towards water surface and a schematic diagram of that phenomenon. Yellow: P, red: O, cyan: water.

Interaction of water with TiAP at the interface

In view of the increased interfacial roughness, it is worthwhile to investigate the interaction of water molecules with TiAP at the interface. In that connection, TiAP-H₂O complex was optimized at the B3LYP/TZVP level of theory using Grimme's dispersion correction¹⁹⁵ and the optimized structure is depicted in **Figure 5.15**. For comparison, the water dimer structure is also presented in **Figure 5.15**. The O---H bond length (1.81Å) in TiAP-H₂O complex (O of P=O and H of water molecule) is found to be quite smaller than that of O---H bond length (2.16Å) in water dimer (shown in Figure) which indicates that the TiAP-H₂O interaction is stronger than that of H₂O-H₂O interaction as reflected in the interaction energy. The interaction energy for TiAP-H₂O interaction (-10.74kcal/mol) is found to be higher than that of H₂O-H₂O interaction (-4.63kcal/mol) at the B3LYP/TZVP level of theory with dispersion correction¹⁹⁵. The O---H bond length in TiAP-H₂O complex (O of P=O and H of water molecule) from MD simulation was found to be 1.55Å whereas O---H bond length in water was found to be 1.95Å,

which might be considered to be reasonable due to different physical state of the molecular system in MD and QM.

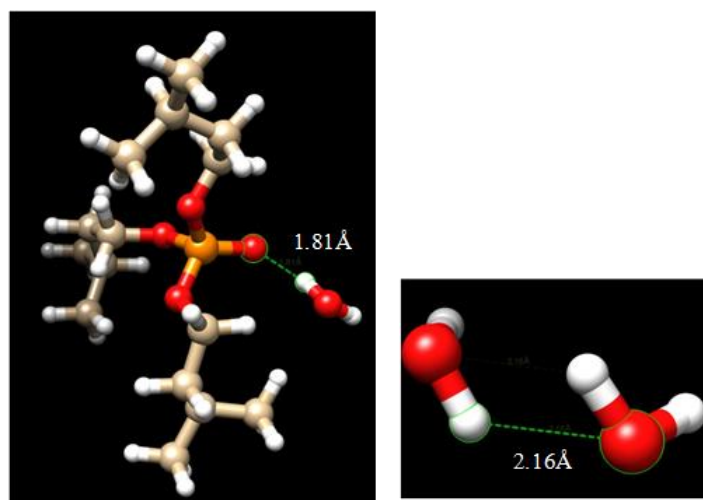


Figure 5.15: Optimized structure of TiAP-H₂O and H₂O-H₂O at the B3LYP/SVP level of theory to exhibit the hydrogen bond.

Furthermore, the potential of mean force (PMF) has been studied along reaction coordinate to understand the free energy profile of ligand and water. PMF is a highly reliable method to calculate the free energies and hence has been adopted for TiAP/dodecane and TiAP/dodecane/water system. The PCF of P–P atoms and P–O atoms between two TiAP molecules have been computed in our previous studies and the PMF is then calculated from the PCF using the [equation 4](#) as shown in [Figure 5.16\(a\)](#) and [Figure 5.16\(b\)](#) respectively.

The figure depicts free energy between two TiAP molecules separated at a distance as reaction coordinate. The figures also exhibit that profile of 10% and 30% mole fraction of TiAP pass through more minimum indicating stable probable composition. Again, the PMFs are also evaluated between TiAP–water as O–W and O–W and it is represented in [Figure 5.16\(c\)](#) and [Figure 5.16\(d\)](#) respectively. In presence of the aqueous phase which is in contact with the organic phase, the more minima are observed at lower mole fraction of TiAP. In addition to

that a shallow secondary minimum has been observed for all the mole fraction of TiAP in **Figure 5.16(c)** indicating the presence of second solvation shell. So, it may be considered as a strong interaction due to the presence of hydrogen bonding between phosphoryl oxygen and water hydrogen.

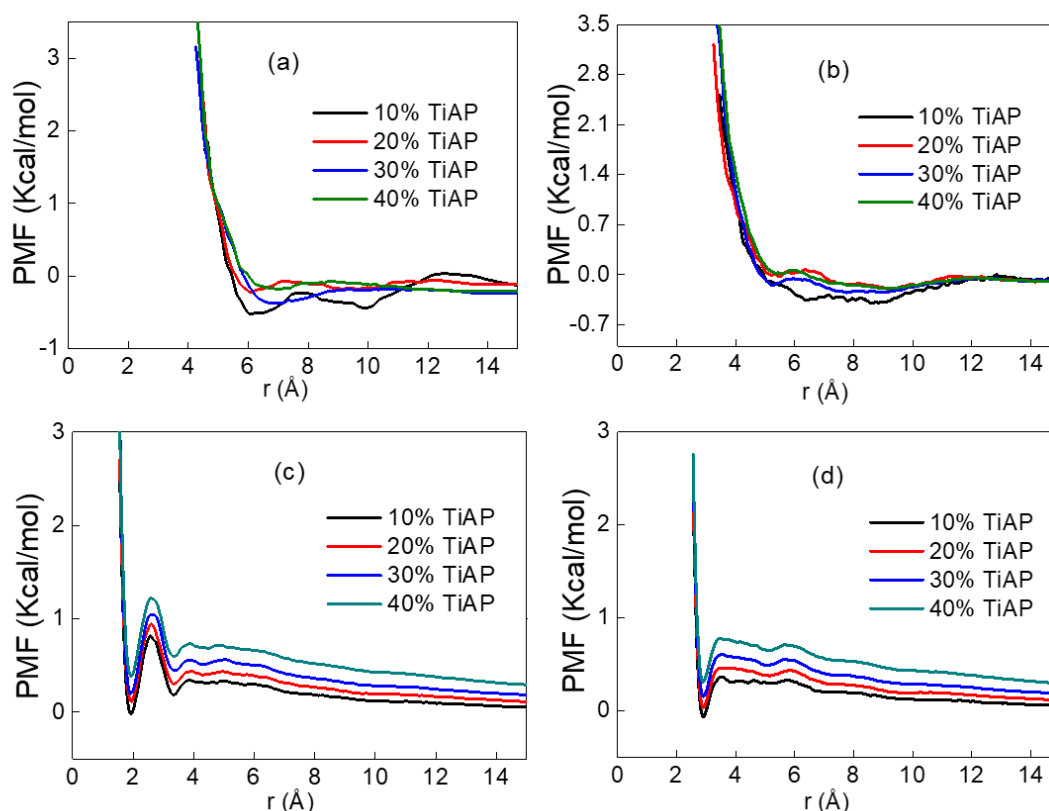


Figure 5.16: PMF along the coordinates of (a) $P-P$ atoms, (b) $P-O$ atoms, (c) $O-HW$ atoms and (d) $O-OW$ atoms between two interacting $TiAP-TiAP$ and $TiAP-water$ molecules.

5.3.3c. Acidic water/ (TiAP + dodecane) system

In addition to the influence of mole fraction of TiAP in dodecane at the interface, the acidity of the aqueous phase also has significant effect on the structural and dynamical properties of interface. In the next section, we have discussed the effect of acidity in terms of acid molarity

in aqueous phase by varying the concentration of nitric acid from 1M to 4M. The compositions of acidic systems are tabulated in [Table 5.1](#).

Liquid state structure of acidic water/(TiAP + dodecane) system

The liquid state structure at the acidic interface is of great significance for interpreting the interfacial properties. The snapshots of liquid structure for step wise progress of simulation length in the separation of two phases during equilibration run are shown in [Figure 5.17](#).

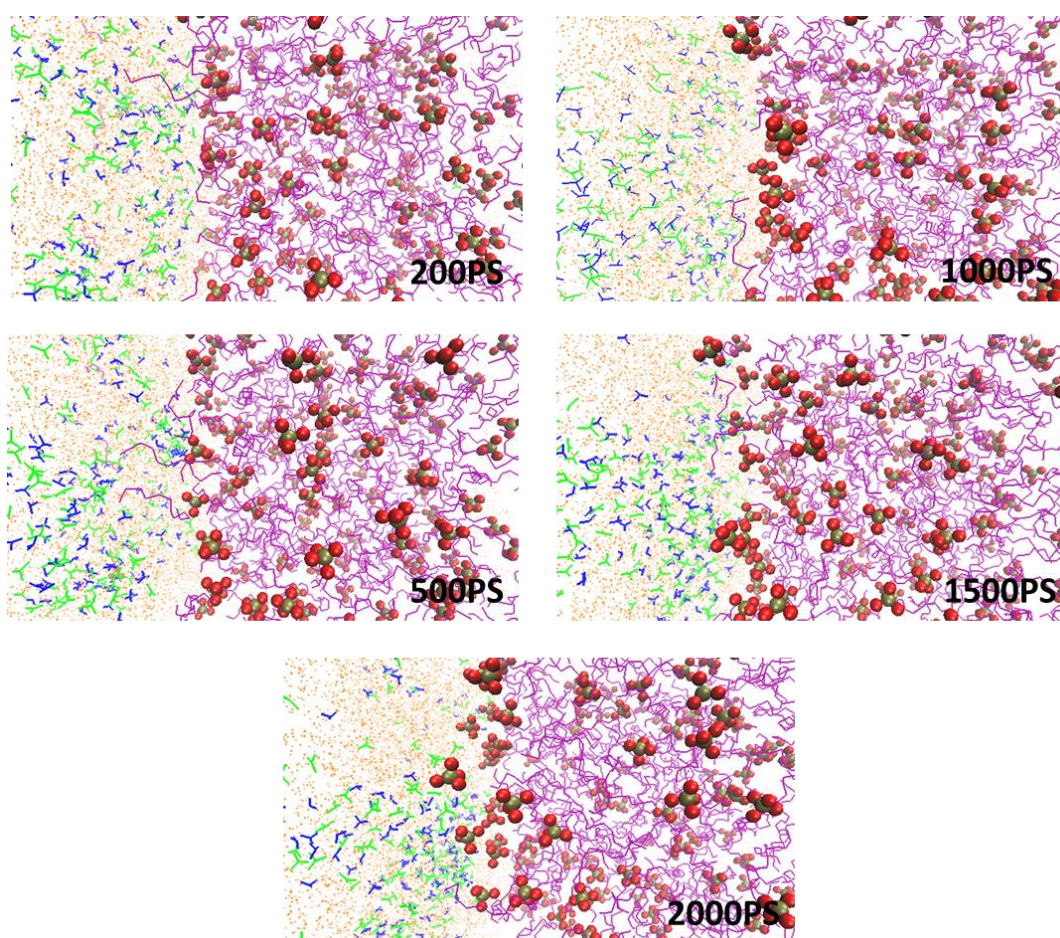


Figure 5.17: Snapshot of liquid structure containing acidic water as the aqueous phase and TiAP/dodecane as the organic phase which reflects the interfacial structure at different simulation length. System: water/3M nitric acid - 30%TiAP in dodecane. Colour code: magenta - dodecane, blue - H_3O^+ , green - NO_3^- , orange - water, red – phosphoryl oxygen, grey – phosphorous atom.

The similar phenomena like earlier neutral interface system are also observed here. As shown from the snapshot, the phase separation process is carried out on progression of simulation length and finally the phases are separated out with formation of sharp interface. Here, the phase separation is comparatively faster means it is achieved in shorter time interval compared to the absence of acid in the aqueous phase. This can be explained even better with density profile of biphasic system. The H_3O^+ and NO_3^- ions are initially well dispersed in the bulk aqueous phase but they form cluster in the bulk phase with the progress of simulation length.

Density profile for acidic water / TiAP + dodecane system

Density profile at the acidic interface between acidic water and TiAP/dodecane mixture has been discussed along with the effect of aqueous phase acidity. Here, the interfacial properties have been evaluated under the acidic environment and the nitric acid is used in fully dissociated form instead of neutral nitric acid. The systems are first energy minimized and then equilibrated in NPT followed by production run in NVT. The final snapshot of these acidic biphasic mixtures considering 30% mole fraction of TiAP in dodecane contacted with aqueous phase having different acidity and the density profile of all the components of corresponding acidic systems are presented in **Figure 5.18**.

From the figure it is shown that the density of dodecane passes through a maximum just after the interface indicating that the dodecane is deeply packed which leads to a sharp interface. Again, the density of TiAP is maximum at the interface and then it is diluted in the bulk dodecane phase. The concentration of H_3O^+ and NO_3^- in the aqueous phase passes through maxima and they are accumulated in the bulk aqueous phase as shown from the above snapshot and density profile. It is already reported in previous literature that the nitric acid in dissociated form preferred to be in bulk phase and to lesser extent at the interface. The dip in density profile of water is obtained because the number of molecules in aqueous phase has been kept constant for all the systems.

In addition to that the concentration of TiAP at the interface indicated by the peak height is gradually decreasing with increasing aqueous phase acidity as seen from **Figure 5.18**.

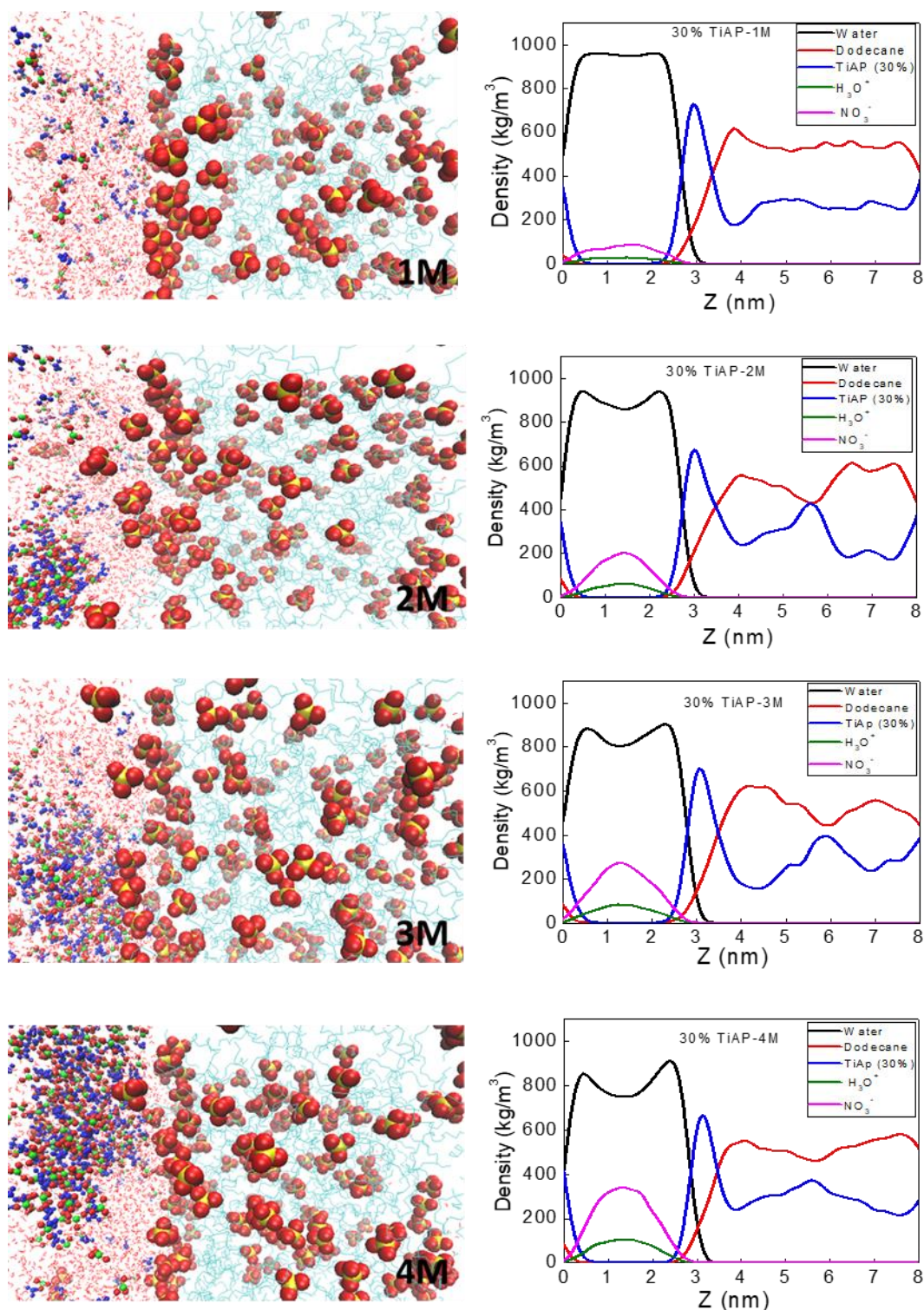


Figure 5.18: Snapshot of biphasic liquid structure containing 30% TiAP/dodecane as organic phase and nitric acid solution as aqueous phase. The corresponding density profiles for each component at different molarity of nitric acid varies from 1M to 4M.

It can be assumed that the accumulation of TiAP at the interface is less in presence of hydronium and nitrate ions. At high aqueous phase acidity, the ionic concentration at the interface is also high and it reduces the TiAP hydration at the interface. Hence, the packing of TiAP at the interface becomes weaker as represented in **Figure 5.19(a)**.

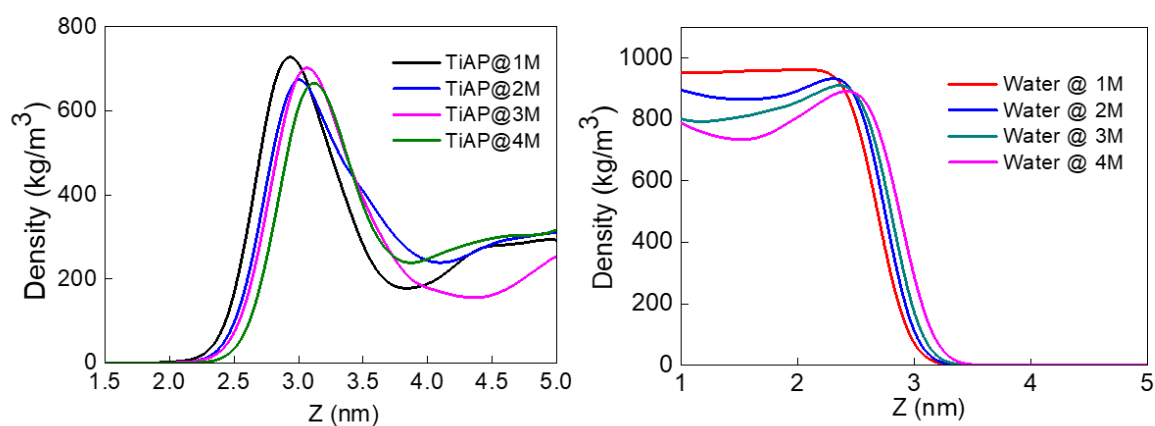


Figure 5.19: (a) Density profile of 30% TiAP/dodecane – water system at different acidity illustrating the shifting of interface towards organic phase and (b) Density profile of water at different aqueous phase acidity of 20% TiAP/dodecane – nitric acid system illustrating sharpness of water density.

It is also observed that the density profile of water becomes much steeper at the higher acidity showing a sharp fall of water density at the interface with increasing acidity as shown in **Figure 5.19(b)**. So, it indicates that the water located at the interface participated in hydration, is gradually shifted to the bulk aqueous phase which leads to a reduction of the interfacial thickness.

Furthermore, the concentration of TiAP at the interface is increasing with increase in mole fraction of TiAP having aqueous phase acidity of 3M as shown in **Figure 5.20(a)**.

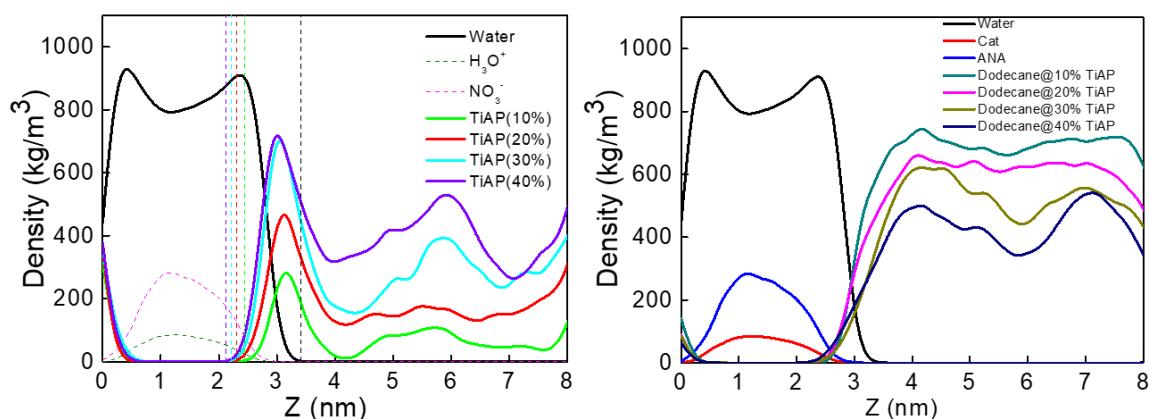


Figure 5.20: (a) Density profile of 3M nitric acid–TiAP/dodecane system with various mole fraction of TiAP illustrating the interface thickness changing with mole fraction and (b) Density profile of 3M nitric acid - TiAP/dodecane system at different mole fraction of TiAP illustrating the water – dodecane solvent interface.

It has been already shown in the preceding section for neutral interface that higher accumulation of TiAP is observed at the interface at a higher mole fraction of TiAP. Similar behaviour is also observed here in the presence of acid. It is obvious that the peak height of TiAP at the interface will be lowered in the presence of acid compared to the neutral interface. The water – dodecane interface for 3M acid system is shown in supplementary material as **Figure 5.20(b)**.

In addition, an interesting observation can be drawn at higher acidity. The interface thickness becomes narrow with increasing aqueous phase acidity as depicted in **Figure 5.21**. Initially the interface is thinning rapidly followed by a gradual reduction of it. It may be due to the replacement of interfacial water by acid ions at higher acidity. It leads to the reduction of hydration of TiAP which helps to separate out both the phases.

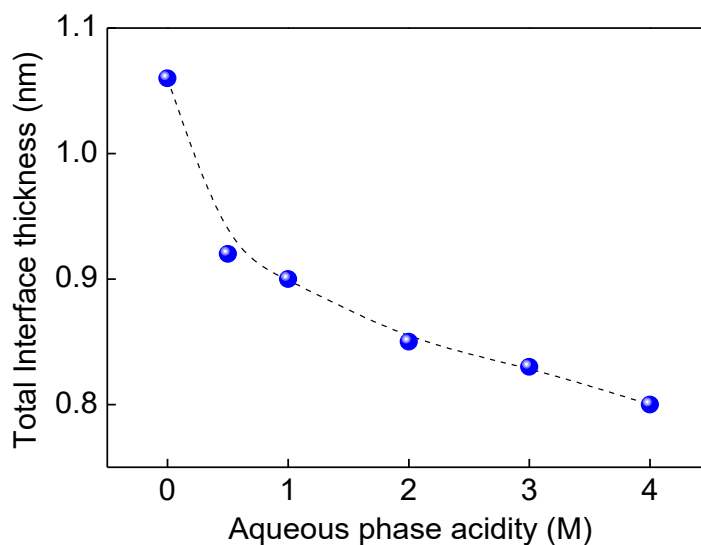


Figure 5.21: Interfacial thickness of 20% TiAP/dodecane–nitric acid system as a function of aqueous phase acidity which illustrates the effect of acidity on the interfacial thickness. The interfacial thickness shows a decreasing trend with the aqueous phase acidity.

This behaviour can be explained by analysing interfacial tension at the interface. The interfacial tension of different systems based on the mole fraction of TiAP is presented in [Table 5.6](#) as a function of acidity.

Table 5.6: Calculated interfacial tension (mN/m) at various mole fraction of TiAP with different aqueous phase acidity

Aqueous phase acidity (M)	10% TiAP/dodecane	30% TiAP/dodecane	40% TiAP/dodecane
0	28.7± 2.0	24.4± 2.9	23.2± 2.1
1	--	25.6± 1.9	25.4± 4.9
3	32.1± 3.1	26.1± 2.7	--
4	33.4± 1.9	--	27.8± 3.2

The interfacial tension values obtained from simulation display an increasing trend. At the same time, at higher interfacial tension, the interface width is reduced and due to the lesser packing of TiAP at the interface, the interfacial roughness is also reduced. Hence, the two phases prefer to remain separated like de-mixing situation resulting to a clear interface.

5.3.4. Relation between interface thickness and interfacial tension

The liquid–liquid interface can be well characterized by two thermodynamic quantities such as interface thickness and interfacial tension. The interfacial tension can be calculated in different ways using pressure tensor method, capillary wave theory and free energy calculation. In recent past, lots of efforts have been put to calculate the interfacial tension as well as interface thickness for different biphasic systems like carbon tetrachloride/water¹⁸³, isooctane/water¹⁷³, hexane/water¹⁸⁰ and octane/water¹⁹⁶. But the interfacial tension for complex systems like TBP/dodecane/water or TiAP/dodecane/water has not been investigated. Again, few researchers applied the capillary wave theory to provide a relation between interface thickness and interfacial tension for simple system. They have calculated interface thickness from capillary wave where thermal fluctuation at the interface is considered. *Senapati et al* have computed the intrinsic width and the width obtained from thermal fluctuation by fitting with density curves for liquids¹⁸³. Then, the interfacial tension was calculated from CWT using these width and the values obtained from both the calculations are in good agreement. But all these calculations have been done for simple system like two component system. Again, they were not prescribed any straightforward equation for the calculation of total thickness. The presence of ligand in organic phase and ions in aqueous phase alter the physical and dynamical properties as well as these two thermodynamic quantities also. As it is seen from the above study, presence of acid increases the interfacial tension and presence of TiAP decrease the interfacial tension. Therefore, it is necessary to check the applicability of CWT in complex three component molecular systems. In addition to that, it is equally important to establish a method for

calculation of total and intrinsic interface thickness. Hence, it is worthwhile to develop a simple relation between them so that one can calculate the interfacial properties for complex system.

The calculated values of interfacial tension is plotted against interface thickness in **Figure 5.22** and it is found that they follow an inverse quadratic relation which is very much similar to the relation obtained from CWT.

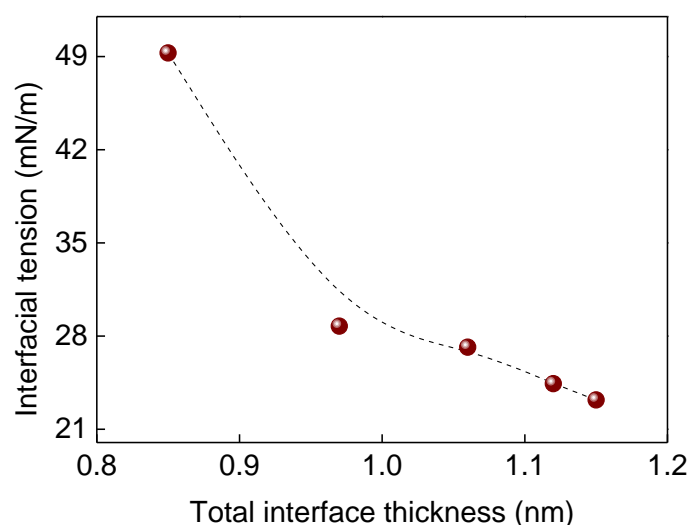


Figure 5.22: Interfacial tension of TiAP/dodecane–neutral water biphasic system as a function of interface thickness illustrating the inverse relation between these two parameters.

Therefore, the CWT has been applied to calculate the interface thickness due to thermal fluctuation for three component system.

Furthermore, the interface thickness due to thermal fluctuation (w_c) [see [equation 2.45](#)] is computed for two component system before dealing with three component system. Then, the CWT is applied to calculate the w_c for water–dodecane system which is found to be (0.202 nm) in good agreement with the reported experimental results¹⁸¹. Earlier, the reported thickness for water–carbon tetrachloride system was 0.158 nm¹⁸¹, which is very close to our value. It is obvious to have higher value compared to water–carbon tetrachloride system as the larger size

of dodecane increases the molecular length. So, the thickness obtained from water–dodecane system is in close proximity with the reported data which indicates the validation of CWT. Thereafter, the CWT has also been applied to three component system where TiAP is present in dodecane. Here, the calculation of bulk correlation length is really a concern because of the presence of TiAP as third component at the interface. Hence, it will be inappropriate to calculate the molecular length considering only water and dodecane or water and TiAP. Hence, we have formulated a simple prescription, where, the weighted average of the molecular length of TiAP and dodecane has been considered as given by the following expression:

$$L_b = L_{W-T} * x_{TiAP} + L_{W-D} * x_{Dodecane} \quad (5.1)$$

Where, L_{W-T} and L_{W-D} are the average molecular lengths considering water–TiAP interface and water–dodecane interface respectively. x_{TiAP} and $x_{dodecane}$ are the mole fraction of TiAP and dodecane respectively. Now, the question arises how to find the molecular size theoretically. The molecular diameter of the solute of interest was evaluated from the volume of the solute by assuming spherical shape of the molecule. The volume (V_{COSMO}) of the water, dodecane and TiAP was determined by COSMOtherm program¹⁰⁹ using charged surface of the solute obtained from single point energy using conductor like screening model for realistic solvents (COSMO-RS)¹¹¹ at the BP/TZVP level of theory as implemented in TURBOMOLE suite of program⁶⁹. The calculated diameter (σ) of water, dodecane and TiAP using the respective COSMO volume was found to be 0.36, 0.81 and 0.93 nm respectively. The interface thickness due to thermal fluctuation using CWT is calculated for three component system like water–TiAP/dodecane using three methods for calculation of bulk correlation length which is displayed in **Figure 5.23(a)** and **Figure 5.23(b)** as a function of mole fraction of TiAP and function of interfacial tension respectively.

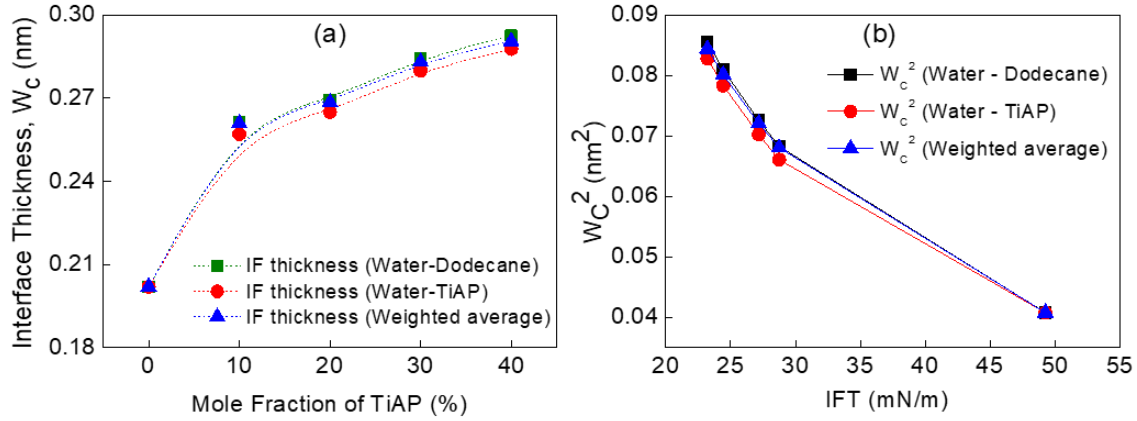


Figure 5.23: (a) Interface thickness (w_c) due to capillary wave as a function of mole fraction of TiAP and (b) Square of interface thickness (w_c^2) as a function of interfacial tension.

The figure illustrates that the interface thickness (w_c) due to capillary wave is an increasing function of mole fraction of TiAP and the square of interface thickness (w_c^2) is a decreasing function of interfacial tension. Moreover, the interface thickness due to capillary wave obtained from the calculation of molecular length by considering water–dodecane at the interface is very close to that of the calculation by weighted average method and the weighted average method for calculation of w_c is comparatively better among the others. Again, the w_c values for all cases are in close proximity which concludes that the methodology for two component system can also be applicable for three component system. Thus, the simulations results are seen to be almost insensitive to the molecular length. Further, the total interface thickness (w_t) can be nicely fitted to an equation as follows:

$$w_t^2 = C \frac{k_B T}{\gamma} \ln \left(\frac{L_{II}}{L_b} \right) \quad (5.2)$$

$$C = \frac{(\sigma_{Water} + \sigma_{TiAP} + \sigma_{dodecane})}{1.4 \sigma_{water}} \quad (5.3)$$

Here, σ represents the diameter of TiAP, dodecane and water respectively.

Further, the model equations (equation 5.2 and equation 5.3) are applied to the present system to calculate the total interface thickness by using the molecular length (L_b) calculated from the weighted average method and compared with the total interface thickness obtained from the density curve in Figure 5.24.

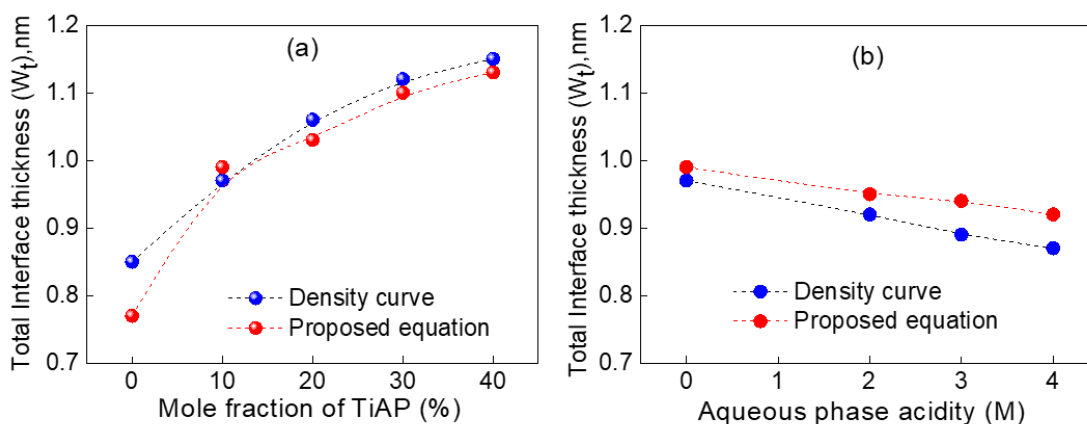


Figure 5.24: Total interface thickness computed from both density curve and proposed equation as a function of (a) mole fraction of TiAP and (b) aqueous phase acidity.

The above figure depicts that the results calculated from proposed equation are in excellent agreement with the values obtained from density curve. For two components bi-phasic system, though it underestimates the total thickness, for three component bi-phasic system it performs quite well for a wide range of composition, whereas the calculated results for w_t using the proposed equation slightly overestimates the results obtained from the density curve over a varied acidity. The proposed equation is found to be useful to determine the w_t for a wide range of bi-phasic system. Now, the interface thickness obtained from the density profile and thermal fluctuation is quite different. The interface thickness calculated from the density profile is substantially high compared to the value obtained using capillary wave (w_c) indicating that w_c is not the sole contributor, hence, it is inappropriate to intend w_c as the genuine interface

thickness. The contribution from intrinsic thickness (w_i) can now be obtained using a reported relation as¹⁸¹:

$$w_i^2 = w_t^2 - w_c^2 \quad (5.4)$$

The calculated value of w_i for water-dodecane system using [equation 5.2](#), [equation 5.3](#) and [equation 5.4](#) was found to be 0.74nm which is very close to the reported MD simulation value of 0.51nm¹⁹⁷ and thus confirms the acceptance of the present model equation ([equation 5.2](#)). In concern with the above studies regarding interface thickness, the capillary thickness, total interface thickness and the intrinsic thickness calculated from the [equation 5.2](#), [equation 5.3](#) and [equation 5.4](#) are tabulated for various compositions of TiAP and aqueous phase acidity in [Table 5.7](#) and [Table 5.8](#) respectively.

Table 5.7: Interfacial tensions and thicknesses (nm) of neutral biphasic system as a function of mole fraction of TiAP

Biphasic System	IFT (mN/m)	w_c	w_t	w_i
dodecane-water	49.3 ± 1.6	0.202	0.767	0.740
10% TiAP/dodecane-water	28.7 ± 2	0.261	0.996	0.961
20% TiAP/dodecane-water	27.2 ± 2.3	0.268	1.03	0.994
30% TiAP/dodecane-water	24.4 ± 2.9	0.283	1.091	1.054
40% TiAP/dodecane-water	23.2 ± 2.1	0.291	1.126	1.088

It is worth mentioning that the computed value of w_t using [equation 5.2](#) and [equation 5.3](#) for water-dodecane system is 0.767 nm which is in reasonable conformity with the reported experimental result of 0.49nm¹⁸¹. Furthermore, the proposed equation ([equation 5.2](#)) has been applied for other reported systems also to test the predictability and its wide applicability. We

have taken the interfacial tension values for various biphasic systems along with the respective box dimensions reported in the literature and then the capillary thickness, w_c has been calculated using the bulk correlation length computed from COSMOtherm program from [equation 5.1](#). We extend the study to compute the total interface thickness, w_t using our proposed equation and further we calculate the intrinsic thickness, w_i from total thickness using [equation 5.4](#).

Table 5.8: Interfacial tension and thicknesses (nm) of 10% TiAP/dodecane-water biphasic system as a function of aqueous phase acidity

Aqueous phase acidity	IFT (mN/m)	w_c	w_t	w_i
0M	28.7 ± 2	0.261	0.996	0.961
2M	31.2 ± 2.5	0.251	0.957	0.923
3M	32.1 ± 3.1	0.247	0.944	0.911
4M	33.4 ± 1.9	0.242	0.926	0.894

The intrinsic thickness has the major contribution on total interface thickness. It has been observed from [Table 5.7](#) that the intrinsic thickness is increased around 0.127 nm whereas the capillary thickness is around 0.03 nm. Similar observation is also noted from [Table 5.8](#) where the w_i is decreased by 0.067 nm and w_c is 0.019 nm. So, the w_c is less affected by the mole fraction of TiAP and nitric acid concentrations compared to the w_i . Again, the intrinsic thickness is dramatically affected by the mole fraction of TiAP in organic phase compared to the concentration of nitric acid in aqueous phase. Hence, the organic phase has dominating effect on interface thickness compared to the aqueous phase.

The calculated various interface thicknesses for a wide range of biphasic systems using the [equation 2.45](#), [equation 5.2](#), [equation 5.3](#) and [equation 5.4](#) as well as from the earlier reported MD results are presented in [Table 5.9](#).

Table 5.9: Calculated interface thicknesses (nm) including capillary, intrinsic and total thickness for a wide range of biphasic systems using Eqn. 5.2 and Eqn. 5.3 along with the earlier reported MD simulations results (parenthesis)

System	IFT (mN/m)	w_c	w_t	w_i
Water-dodecane (2800 + 700)	49.3 ± 1.6	0.202 (0.338) ¹⁸¹	0.767 (0.5) ¹⁸¹	0.74 (0.37) ¹⁸¹ (0.51) ¹⁹⁷
water-hexane (875+125)	56 ± 6 ¹⁸⁰	0.168	0.594	0.570
Water-octane (560+62)	61.5 ± 1.9 ¹⁹⁸	0.155 (0.14) ¹⁹⁸	0.565	0.544
water-isooctane (794+168)	58.8 ¹⁹⁹	0.158 (0.12) ¹⁹⁹	0.575	0.553
Water-nonane (500+108)	42.5 ²⁰⁰	0.184 (0.15) ²⁰⁰	0.680	0.654
water-decane (389 + 50)	48.2 ¹²⁷	0.172	0.643	0.620
water-CCl4 (2465 + 1134)	53.13 ¹⁸³	0.192 (0.17) ¹⁸³	0.671	0.64 (0.07) ¹⁸³
Water-nitrobenzene	39.7 ± 3.3 ¹⁷³	0.209 (0.178) ¹⁷³	0.736 (0.19) ¹⁷³ (0.45) ²⁰¹	0.706 (0.05) ¹⁷³
Water- Ionic liquid (2657+219)	8.77 ± 2 ¹²⁹	0.445	1.773	1.716
Water-octanol (500 + 108)	12 ± 3 ²⁰²	0.348	1.27	1.23
Water-heptanone (794 + 168)	12.9 ± 0.1 ¹⁷⁷	0.339	1.221	1.173
water-benzene (504 + 144)	55 ± 45 ²⁰³	0.168 (0.17) ²⁰³	0.578 (1.0) ²⁰³	0.553

The reported value of w_i for water–dodecane¹⁹⁷ system using MD simulations was 0.51 nm. The calculated w_c for water–CCl₄ is much closer to the reported value of 0.171 nm where the reported w_i is significantly less compared to our calculation.¹⁸³ Similar observations are also found in water–nitrobenzene¹⁷³ system where the present calculated w_c is in close proximity to the reported value but reported w_t and w_i are significantly low compared to our results. It is worth mentioning that the experimentally²⁰¹ measured value of 0.45nm for w_t is in far better agreement with our calculated value of 0.736nm compared to the earlier reported value of 0.19nm using MD simulations. For water–benzene system, the calculated w_c is much closer to the reported value, but high value for w_t is reported as 1 nm where the total interface thickness was determined to be of 2-3 molecular diameters.²⁰³ The calculated values of w_c using [equation 2.45](#) are found to be in good agreement with the reported MD simulations results^{173, 183, 198-200, 203} and experimental results¹⁸¹ for a wide varieties of oil-water bi-phasic system. Similarly, the calculated values of w_t using [equation 5.2](#) and [equation 5.3](#) for water-dodecane and water-nitrobenzene are in good agreement with the experimental results^{181, 201} and for water-benzene with the earlier reported MD simulations results²⁰³. Further, the calculated value of w_i using [equation 5.4](#) for water-dodecane is in good agreement with the experimental¹⁸¹ and reported MD simulations results¹⁹⁷. It is worth mentioning that the computed value of the intrinsic thickness, w_i is always greater than that of capillary thickness, w_c as revealed by the experiments¹⁸¹ as well as the present study, whereas, earlier MD simulations studies on water-CCl₄¹⁸³ and water-nitrobenzene¹⁷³ systems predicts the reverse trend where w_c was shown to be much greater than that of w_i . Note, the accurate intrinsic width can also be obtained by fitting the density profile to a hyperbolic tangent provided the density profile is very smooth¹⁸³. Therefore, further experimental and computational studies are needed to arrive at a reasonable conclusion.

5.3.5. Preferential orientation of TiAP at the interface

The structure of the interface using pair correlation function has been already described in earlier section. The molecular orientation also provides structural information for understanding the interaction at the interface. Therefore, we have attempted to capture the molecular orientation at the aqueous-organic interface. The interface has quite negligible effect on the orientation of water molecule because they do not need any special orientation for making hydrogen bond¹⁷⁶. The ordering of water molecules is seen to be high as the liquids are in more demixing condition which leads to a sharp interface. But the orientation of the organic molecules has been changed markedly in the presence of interface compared to that in pure state. Interface has a great influence on the ordering of TiAP molecules. So the knowledge of preferential orientation of TiAP at the interface is required to develop a detail understanding of molecular transport. From the snapshot it was seen that the phosphoryl oxygen from one TiAP unit is facing the back of the P of P=O of the neighbouring TiAP unit (see [Figure 5.25](#)).

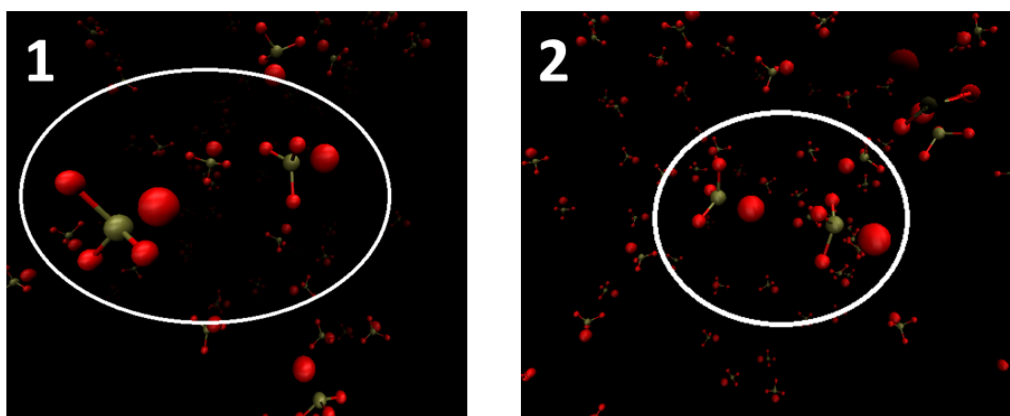


Figure 5.25: Preferential orientation ($P=O-P=O$) of phosphoryl group of TiAP molecules obtained from simulations with different view.

Further, in order to confirm the probable populated conformers, dispersion corrected DFT calculation was performed by considering three kind of probable orientation between dimers of TiAP. The optimized structures are displayed in [Figure 5.26](#). The stability of the dimer with

different orientation was established by computing the dimerization energy. The interaction energy for dimer with orientation of $O=P-P=O$, $P=O-P=O$ and $P=O-O=P$ was found to be -12.98, -14.97 and -10.81 kcal/mole respectively indicating that dimer with orientation of $P=O-P=O$ is the most stable which was also captured in the MD simulations.

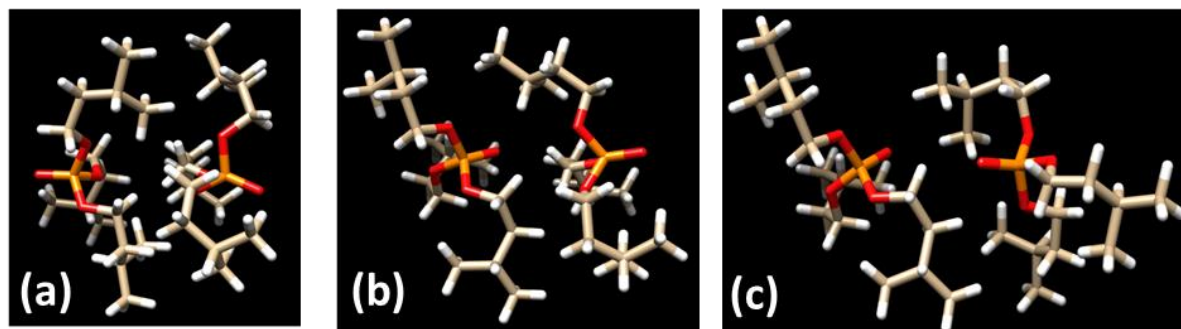


Figure 5.26: Optimized structures of dimer of TiAP in different orientation of phosphoryl group of TiAP molecules at the B3LYP/TZVP level of theory using dispersion correction. (a) $O=P-P=O$ (b) $P=O-P=O$ and (c) $P=O-O=P$.

5.3.6. Water Solubility in TiAP/dodecane System

The water solubility in the organic phase containing TiAP in dodecane phase has also been computed in the present study. It is one of the very important criteria for selection of a ligand which in turn control the economy of the process. The water extracted by the organic phase having different mole fraction of TiAP is reported in [Table 5.10](#).

From the table, it is noticed that the water extraction is enhanced at a higher mole fraction of TiAP. It is obvious because the interface thickness is increased at higher composition of TiAP which induced the water transport to the organic phase. Again, the calculated values reveal that the water extractability is decreased with increasing aqueous phase acidity as the interface thickness is reduced at a higher acidity. Therefore, the interface thickness plays an important role in the mass transfer and it may control the transfer processes by choosing the appropriate composition of a biphasic mixture.

Table 5.10: Water extraction at water - TiAP/dodecane Interface

Neutral biphasic system (TiAP/dodecane–water)		Acidic biphasic system (30% TiAP/dodecane–water)	
System	Amount of water extraction (mol/lit)	Aqueous phase acidity (M)	Amount of water extraction (mol/lit)
dodecane-water	--	2	3.49
10% TiAP/dodecane	1.00	3	3.01
40% TiAP/dodecane	4.71	4	2.44

In our previous work, the effort was devoted to evaluate the probable composition of TiAP/dodecane binary system based on the dynamic properties like diffusivity and viscosity and 20–30% TiAP/dodecane mixture obtained from the intersection of diffusivity and viscosity profile was predicted to be an optimum composition.¹⁸⁵ The interface thickness and interfacial tension both can significantly affect the mass transfer and these physical properties of interface get affected in the presence of acid also. In the present study, it has been seen that these two physical properties are inversely related. At higher interfacial tension, the interface thickness is reduced indicating the two phases are more prone to be separated. Moreover, the interface thickness is increasing with mole fraction of TiAP in the dodecane phase and is decreasing with aqueous phase acidity. Similarly, the interfacial tension is decreasing with mole fraction of TiAP in the dodecane phase and is increasing with the aqueous phase acidity. So, it is very crucial to choose an optimum composition of TiAP/dodecane–nitric acid system which is suitable for the effective mass transfer having less interfacial tension and wider interface thickness. Again, the interface thickness and interfacial tension both are affected in the presence of acid in the aqueous phase. The interfacial tension increases whereas the interface thickness decreases with the aqueous phase acidity. So, the aqueous phase acidity can also be

chosen in similar fashion. But there are some other parameters which also depend on the aqueous phase acidity and they also play a significant role. The most important point among them is the distribution coefficient (K_D) of heavy metals which depends strongly on the aqueous phase acidity. In PUREX process, the recovery of heavy metals has the priority over the purification as it can be achieved later on. In addition to that, the decontamination factor (DF) and the recovery of acids are also affected by the aqueous phase acidity. So, the acidity can be selected based on the above factors not only based on the physical properties. Hence, it is very challenging task to select the appropriate aqueous phase acidity at which the heavy metal recovery will be satisfactory and it can be performed in the presence of heavy metal ions which we are intended to explore in our future study.

5.4. SUMMARY

In the present study, MD simulations have been performed for the aqueous-organic biphasic system using a newly developed force field to test its applicability in two phase consisting of four chemical species. The calculated structural and dynamical properties of pure water and water–dodecane like biphasic system using MD simulations are in excellent agreement with the reported experimental values which establishes the validation of Mulliken embedded force field. Again, the study was extended to determine the interfacial properties with the effect of mole fraction of third component (here TiAP) and the acidity of aqueous phase for aqueous-organic biphasic system. It was found that the packing of TiAP as well as the interface thickness is an increasing function of mole fraction of TiAP but after 50% mole fraction there is no significant effect of it. The interfacial tension is a decreasing function of mole fraction of TiAP and the computed values are shown to be in excellent agreement with the reported experimental results. Interfacial tension was found to be maximum in the absence of TiAP molecules and then it decreases gradually indicating TiAP acts as a surface active agent. The system with higher mole fraction of TiAP induces the TiAP molecules to accumulate at the interface and

large numbers of water molecules are in contact with them resulting to a large interfacial roughness which facilitates the breaking of hydrogen bonds between water molecules and of making hydrogen bond between phosphoryl group of TiAP and water molecules. Thus, the interaction between water molecules is reduced in the presence of TiAP. The breakage of hydrogen bond among water molecules reduces the surface tension of water and it may help to increase the miscibility of water and organic phases. At higher TiAP concentration, the packing of TiAP at the interface is increased which accelerates the hydration of TiAP thus leads to more reduction of interfacial tension. Further, TiAP-H₂O complex was optimized at the B3LYP/TZVP level of theory using Grimme's dispersion correction. The O---H bond length (1.81Å) in TiAP-H₂O complex (O of P=O and H of water molecule) was found to be quite smaller than that of O---H bond length (2.16Å) in water dimer which indicates that the TiAP-H₂O interaction is stronger than that of H₂O-H₂O interaction as reflected in the interaction energy for TiAP-H₂O interaction (-10.74kcal/mol) and H₂O-H₂O interaction (-4.63kcal/mol). The O---H bond length in TiAP-H₂O complex (O of P=O and H of water molecule) from MD simulation was found to be 1.55Å whereas O---H bond length in water was found to be 1.95Å, thus compliments the results of QM calculation about H-bond.

The interfacial tension is an increasing function of aqueous phase acidity. In addition to that the interface thickness has been calculated using a model equation and a simple scheme has been suggested for the determination of bulk correlation length. Finally, the interface thickness is correlated with interfacial tension, molecular diameter and bulk correlation length as per the newly proposed scheme. It is worth mentioning that the computed value of the intrinsic thickness is always greater than that of capillary thickness.

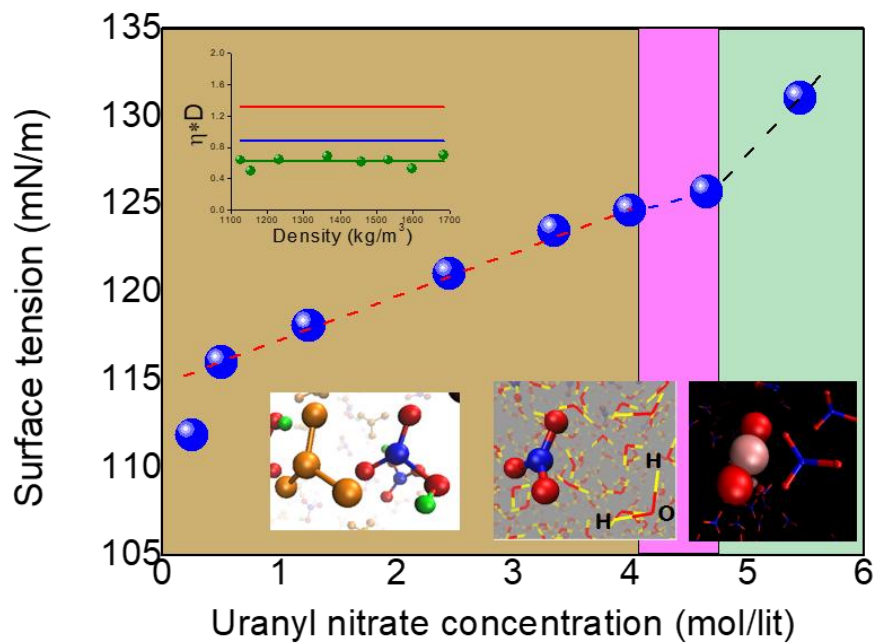
Additionally, the stability of the dimer of TiAP with different orientation was established by computing the dimerization energy using DFT. The interaction energy for dimer with orientation of O=P-P=O, P=O-P=O and P=O-O=P was found to be -12.98, -14.97 and -10.81

kcal/mol respectively indicating that dimer with orientation of $P=O-P=O$ is the most stable which was also captured in the MD simulations. Further, the present MD simulations data shows that the water extraction is enhanced at higher mole fraction of TiAP because of wider interface thickness at higher composition of TiAP which induced the water transport to the organic phase. Again, the calculated values reveal that the water extractability is decreased with increasing aqueous phase acidity as the interface thickness is reduced at higher acidity. Therefore, the interface thickness plays an important role in mass transfer and it may control the transfer processes by choosing the appropriate composition of biphasic mixture.

We anticipate that the present results will assist to illuminate a few dazzling issues on the structure of water-oil interfaces, in particular, the role of interfacial thickness in the kinetics of self-assembly of hydrophobic materials and biomolecules in contact with acidic water. The present MD simulation studies will thus further invite the experimental verification of the calculated results of interfacial tension and interface thickness at a wide variation of composition of third component and acidity. Additionally, it will be worthwhile and challenging to test this force field for ion transfer across the interface. Work in this direction is in progress in our computational molecular engineering laboratory.

Chapter 6

Structure & Dynamics of Uranyl Nitrate Solution



CHAPTER SIX

Structure & Dynamics of Uranyl Nitrate Solution

6.1 INTRODUCTION

The management of continuously increasing used nuclear fuel in large volumes necessitates the development of an effective and selective methodology for reuse by separation of actinides.^{6, 7, 204} The radioactive actinides like uranium majorly present in used nuclear fuel, has always been of paramount interest because of its key role in the civil as well in military field. The actinides are extracted from aqueous nitric acid solution and the raffinate containing fission products with lean actinides was disposed as nuclear waste.^{8, 10} So, the interest has been accelerated to develop an understanding of their importance in environmental chemistry and also to flourish a methodology for better management of nuclear waste. Hence, the separation of actinides from aqueous solution and the associated transport properties are very crucial in view of performance assessments like not only for the design of effective separation process but also for an understanding of the prevalence of actinides in the environment.²⁰⁵

Therefore, it is very worthy to understand the chemistry of actinides in aqueous solution which demands variety of experiments. The radio-toxicity of actinides put restrictions in carrying out the experiments. Again, some difficulties arise due to their variable oxidation states and coordination numbers in aqueous solution which determine the characterization of actinides as well as the performance of separation process. Hence, a theoretical investigation on thermo-physical and dynamical behaviour of aqueous actinides is required. Quantum and classical Molecular dynamics (MD) simulations are the best alternatives to calculate the structural and dynamical properties of actinides²⁰⁶ as it has the basic ability to model molecular system.

MD simulations have been carried out based on classical force field to investigate the molecular properties. The accuracy of physical and thermo dynamical properties strongly depend on the reliability of force field. The availability of good force field is pivotal for modelling the actinide system which can arrest the intra-molecular and intermolecular interactions. Earlier, various research groups developed force field for uranyl cation. Many times force fields are parameterized to match the experimental data like free energy or residence times²⁰⁷⁻²⁰⁹. But this parameterization approach is not a good option as it is slightly case sensitive. Another approach for developing force field is to carry out Quantum Mechanical (QM) calculation.²¹⁰⁻²¹² Earlier, several research groups have developed force field to model uranyl ion based on QM calculations and classical molecular dynamics simulations. They have calculated the partial atomic charges on atom and tested the force field by evaluating radial distribution function (RDF) and free energy of hydration. [Guilbaud](#) and [Wipff](#) presented a theoretical study of uranyl ion (UO_2^{2+}) in water using a non-covalent 1-6-12 representation to determine the coordinating environment in solvent.^{209, 210} [Kerisit *et al*](#) carried out MD simulations of uranyl ion in water using GW and two other force fields which have comparatively higher partial charges on uranium atom namely model 1 and model 2. They have shown that not a single model able to predict the uranium–water oxygen distance or water binding energy or hydration

free energy. Water exchange rate and hydration free energy were well predicted by model 1 whereas uranium–water oxygen distance was by model 2. The self-diffusion coefficient and relative diffusion coefficient both calculated from GW model were better compared to the new parameterized model but in close proximity with each other. They have not calculated viscosity and surface tension which are important liquid state properties to design various extraction processes.²⁰⁸ Rai and co-researchers developed a force field using QM calculations and shown the importance of using many body solvation effects for development of force field.²⁰⁷ Pomogaev *et al* incorporated a new force field to predict accurately the interactions of actinyl ions with water where the intra-molecular interactions was considered as a combination of implicit and explicit methods and the intermolecular interactions were shaped with a pair wise Lennard – Jones along with coulomb potential. The computed An=O and An·····O_w bond lengths and water coordination numbers were in good agreement with experimental results. They have not dealt the dynamic properties²¹³, whereas Tiwari *et al* studied the dynamics of actinyl ions in water.²¹⁴

In past, several works have been carried out for the development of a force field of uranyl cation which can predict the structural properties, water exchange rate, water binding energy, and hydration free energy with suitable accuracy.²⁰⁷⁻²²⁰ It is true that the development of accurate force field is necessary and the same time very challenging also. For this purpose different atomic partial charges have been used to parameterize the force field in the last few decades. One of the primary concerns is whether the different charge models are really required to understand the uranyl ion in water system or whether the partial charges have an important implication on the physical and dynamical properties and finally what will be the right choice. In addition to that, it is equally important to ensure whether the developed force field is able to model the biphasic system in contact with organic solvent or it can predict the thermophysical and dynamical properties along with the solute transfer to organic phase. In view of the above

questions, our primary objective is to find out the effect of partial charges on the structural and dynamical properties of actinides in water. Among actinide ions, uranyl (UO_2^{2+}) ion is the most widely characterized actinides by both computational and experimental studies because it is the major actinide present in the used fuel as well as in the waste stream. Though, several studies have been carried out to determine the thermo-physical and dynamical properties of uranyl ion²¹⁰⁻²²⁰, here we have focused to explore the effect of partial charges by incorporating the partial charges on atom calculated from Mulliken population analysis method^{88, 89}. So, a comparative MD simulations studies have been carried out for uranyl ion in water with modified force field and some reported force field which are based on Mulliken charges in the gas and liquid phase on uranyl ion²²¹ along with the most commonly used force field parameters developed by [Guilbaud](#) and [Wipff](#)²⁰⁹.

Again, the literature review also depicted that the earlier studies on uranyl ion were carried out in water only.²¹⁰⁻²²⁰ But according to the PUREX process, the feed solution which will come in contact with the ligand is commonly prepared in 3 to 4 molar nitric acids. The aqueous phase acidity can change the structural and dynamical properties. Hence, it has equal implications to carry out the studies in the presence of acid. Therefore, the second objective of this work is to perform MD simulations and to calculate the various structural and dynamical properties of uranyl nitrate in acidic medium with wide range of uranyl nitrate as well as acid concentration. The fundamental understanding developed from the present studies will guide us to choose the appropriate force field for uranyl ion water system to conduct the simulations in nitric acid to model the PUREX process more realistically.

The simulation details in this work are presented in section 6.2. The results and discussion are described in section 6.3. Within this section, selection of force field for uranyl ion based on physical and thermo-dynamical properties, extension of that force field to study the effect of

uranyl nitrate concentration in 3M nitric acid medium are discussed. Finally, the work is summarised in section 6.4.

6.2. SIMULATION SYSTEMS

The partial charges on each atom of uranyl cation is computed from quantum mechanical calculation using Mulliken population analysis method^{88, 89} after the initial structure was optimized at the B3LYP level of theory using TZVP^{70, 71} basis set in TURBOMOLE⁶⁹ package. This new Mulliken embedded OPLS-AA force field is termed as model-MA. The partial charge on uranyl ion calculated by Gulibaud and Wipff²⁰⁹ is called as Model-GW. Mulliken charges for uranyl ion in the gas and liquid phase are reported in literature²²¹ and these are also considered here namely as Model-MG and Model-ML respectively. The partial atomic charges on each atom of uranyl ion for the above said models are reported in [Table 6.1](#).

Table 6.1: Partial atomic charges on uranium (q_U) and oxygen (q_O) of uranyl ion

Model	q_U (e)	q_O (e)
Model-MA	2.719	-0.3595
Model-GW	2.500	-0.2500
Model-ML	2.198	-0.0992
Model-MG	2.033	-0.0164

The nitric acids used here are in associated as well as in dissociated form and the partial charges are calculated from Mulliken population analysis. The initial structure is optimized at the same level of theory as mentioned earlier. The atoms of UO_2^{2+} , H_3O^+ , NO_3^- and HNO_3 along with atomic charges are represented in [Figure 6.1](#).

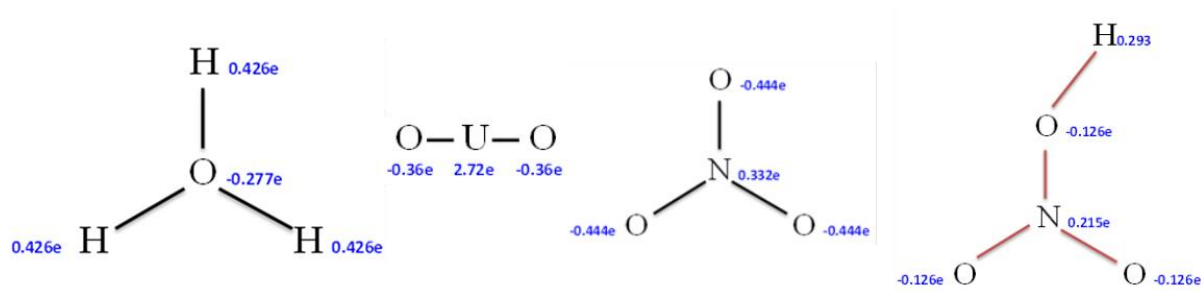


Figure 6.1: Schematic representation of H_3O^+ , UO_2^{2+} , NO_3^- and HNO_3 with respective partial charges on atom.

In the present work, majorly three types of simulation systems are specified. For first type, the systems are represented by one uranyl ion in 1000 water molecules in a cubic box having a length of 3.11 nm. The second type belongs to uranyl ions in 3M nitric acid. Total number of molecules is maintained as 3000 with water and acid for each system. A wide range of uranyl nitrate concentrations are considered here ranging from around 0.25 to 5.45 moles/litres. Uranyl nitrate concentration around 4.0 mol/litres in various nitric acid concentrations ranging from 1M to 4M are considered as type-3 systems. SPC/E model is used for water because it performs better compared to the other available water models.¹⁸⁴ The details of composition of simulation systems are provided in **Table 6.2**.

All systems are relaxed by energy minimization step using steepest decent method with a time step of 2fs. Then the equilibration in isothermal-isobaric (NPT) was carried out for 10 ns simulation length maintaining the pressure at 1 atm and temperature at 300K using Berendsen like weak coupling methods and Velocity-rescaling. Standard periodic boundary conditions are appointed in all three directions. The equation of motion is integrated by Verlet velocity algorithm with a time step of 2fs. The trajectories obtained from equilibration run are used further for production run in NVT for 5 ns simulation length. The structural and dynamical properties have been calculated using the data obtained from production run.

Table 6.2: Summary of Type-1, Type-2 and Type-3 simulation systems along with their composition belong to numbers of uranyl ion ($N_{\text{UO}_2^{2+}}$), numbers of nitrate ions ($N_{\text{NO}_3^-}$), numbers of water and acid molecules ($N_{\text{Water}}/N_{\text{Acid}}$) and the approximate concentration of uranyl nitrate [$\text{C}_{\text{UO}_2(\text{NO}_3)_2}$].

System	Model	Cubic Box length (nm)	$N_{\text{UO}_2^{2+}}$	$N_{\text{NO}_3^-}$	$N_{\text{Water}}/N_{\text{Acid}}$	$\text{C}_{\text{UO}_2(\text{NO}_3)_2}$ (mole/litre)
Water	SPC/E	3.112	--	--	1000	
Type-1	Model – MA	3.105	1	--	1000	0.05
	Model – GW	3.113	1	--	1000	0.05
	Model – MG	3.108	1	--	1000	0.05
	Model – ML	3.108	1	--	1000	0.05
Type-2	5 – U	4.592	5	10	2845/155	0.25
	10 – U	4.594	10	20	2845/155	0.50
	25 – U	4.634	25	50	2845/155	1.25
	50 – U	4.673	50	100	2845/155	2.45
	70 – U	4.701	70	140	2845/155	3.35
	85 – U	4.727	85	170	2845/155	4.00
	100 – U	4.744	100	200	2845/155	4.65
Type-3	120 – U	4.783	120	240	2845/155	5.45
	85U – 1M	4.674	85	170	3000/55	4.00
	85U – 2M	4.724	85	170	3000/110	4.00
	85U – 3M	4.770	85	170	3000/160	4.00
	85U – 4M	4.827	85	170	3000/216	4.00

6.3. EXPERIMENTAL PROCEDURE

6.3.1 Solution preparation

Uranyl nitrate solutions at various concentrations ranging from 0.25 to 5.45 moles/litter have been prepared in 3M nitric acid solution to replicate the feed solution used in PUREX process and each solution is labelled properly as mentioned in [Table 6.2](#). The [Figure 6.2](#) displayed the prepared uranyl nitrate solution and a variation in colour has been observed from low concentration to high concentration of uranyl nitrate solution.



Figure 6.2: Uranyl nitrate solution prepared in 3M nitric acid at various uranyl nitrate concentrations. The respective systems are marked on the round bottom flask indicating the concentration of uranyl nitrate.

6.3.2. Density measuring principle

The density of prepared uranyl nitrate solution has been calculated by using DMA 5000 M, Anton Paar. The sample is introduced into a U – shaped borosilicate glass tube that is being excited to variable at its characteristics frequency using DMA 5000 M, Anton Paar. The characteristics frequency changes depending on the density of the sample. Through the precise determination of the characteristic frequency and a mathematical conversion, the density of the sample can be measured. The density is calculated from the quotient of the period of

oscillations of the U – tube and the reference oscillator. Then the measuring cell is filled with sample before ensuring the measuring cell was clean properly and dry also. Finally the output values are collected from the data memory.

6.3.3. Dynamic light scattering (DLS) experiments

In order to support the simulation findings, dynamic light scattering (DLS) experiment was also conducted to explore the behaviour of uranyl nitrate solution using a Malvern 4800 Autosizer employing a 7132 digital correlator. The dynamic light scattering technique exhibited the size distribution of particles or molecules which are dissolved or dispersed in solution in nanometer range. The particles or molecules are in suspension scattered the laser light at different intensities due to Brownian motion. The scattering results are noted for analysis.

6.4. RESULT AND DISCUSSION

6.4.1. Type – 1: Uranyl ion in water

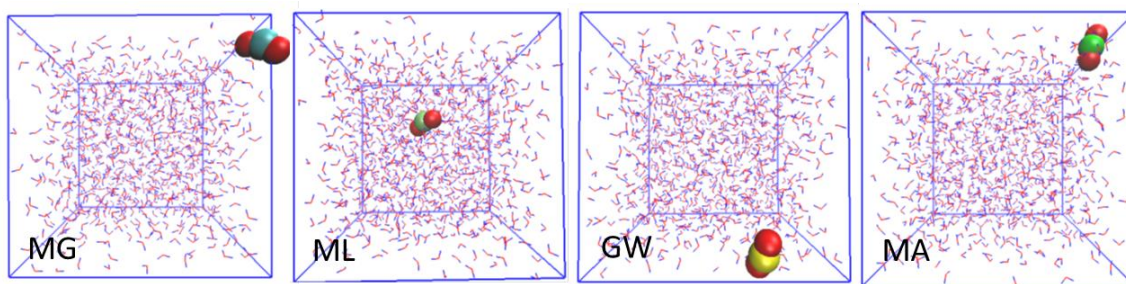


Figure 6.3: Liquid state structure of uranyl ion in water systems having different force field embedded with four types of partial atomic charges on uranium as well as on uranyl oxygen atom. Oxygen atom: Red, Uranium atom: Cyan, Light green, Yellow and Green and Water molecule: Pink.

The primary objective of the present study was to test the performance of the new charge Model–MA with respect to the other models. For this purpose, we have used the type 1 systems

containing one uranyl ion in 1000 water molecules. The liquid structures of all the models are presented in **Figure 6.3**.

Density and self-diffusion coefficient:

The density of uranyl ion in water system for all the models are computed and it was found that there are no significant difference in densities as reported in **Table 6.3**. The partial charges have negligible effect on density. There is no reported data to check the calculated values. But the density of pure water for SPC/E model was already reported in previous chapter as 999.3 kg/m³. Therefore, the density of single uranyl ion in pure water should be higher than that of the pure water and our results followed that trend. Thus, the qualitative validation of the model has been established.

Thereafter, the diffusion coefficient of uranyl ion in water has been calculated from the slope of mean square displacement (MSD) by using Einstein relation ([equation 2.22](#)) and the calculated values are given in **Table 6.3**.

The diffusion coefficients computed for Model – MA and Model – GW are quite overestimating the experimental value while the diffusion coefficients obtained from reported Mulliken charge models (Model – MG and Model – ML) are appeared in between 0.426 to 0.759 x 10⁻⁹ m²/s which was obtained from experiment through ionic conductivity and ionic mobility of UO₂²⁺ ion.²¹⁴ The simulations results from reported Mulliken charge models are quite converging to the experimental value with a deviation of 8.5% and 3.2% respectively. During investigation of such pattern, it is found that the diffusivity is increasing at higher partial charges on uranium atom. The two reported Mulliken charge models have nearly close atomic charges on U which are ranging approximately 2e – 2.2e whereas the other two models have around 2.5e to 2.7e. The change in partial charge on atom alters the dipole moment as well as the dielectric constant of the medium. Higher the partial charge on atom, higher will be the

effect on dielectric constant and it will significantly increase the dielectric field. The dielectric field is responsible for ionic movement in the medium. So, the higher dielectric field make the system more random which increases the mobility of the ions. In addition, the calculated diffusion coefficient when compared among the Mulliken charges, it is seen that the diffusivity is increasing with atomic charges on U atom from model–MG to model–MA. The reported diffusion coefficients in literature are also provided in **Table 6.3**. Though the calculated diffusivity of GW model is higher compared to the experimental value but it is close to the reported value of $0.94 \pm 0.03 \times 10^{-9} \text{ m}^2/\text{s}$.²⁰⁸

Table 6.3: Density of uranyl ion in water system for different models computed from MD simulations. The diffusion coefficient of uranyl ion in SPC/E water along with the diffusion coefficient of water has been computed and the experimental values as well as the reported computational values available in the literature are listed.

System	Density(kg/m ³)	Diffusion coefficient (10 ⁻⁹ m ² /s)	
		UO ₂ ²⁺	Water
Model – MG	1013.05 ± 0.38	0.738 ± 0.05	2.154 ± 0.01
Model – ML	1013.40 ± 0.12	0.702 ± 0.03	2.283 ± 0.09
Model – GW	1013.44 ± 0.14	1.052 ± 0.38	2.432 ± 0.09
Model – MA	1013.10 ± 0.13	1.070 ± 0.02	2.312 ± 0.11

Experimental value for diffusion coefficient of uranyl ion was taken from $0.68 \times 10^{-9} \text{ m}^2/\text{s}$ as direct while 0.426 to $0.759 \times 10^{-9} \text{ m}^2/\text{s}$ as indirect²¹⁴. The diffusion coefficients reported in the literature are $0.61 \pm 0.09 \times 10^{-9} \text{ m}^2/\text{s}$, $0.94 \pm 0.03 \times 10^{-9} \text{ m}^2/\text{s}$ (using GW), $0.85 \pm 0.04 \times 10^{-9} \text{ m}^2/\text{s}$ (using model-1) and $0.88 \pm 0.03 \times 10^{-9} \text{ m}^2/\text{s}$ (using model-2)²⁰⁸. The reported diffusivity of water is $2.52 \pm 0.01 \times 10^{-5} \text{ cm}^2/\text{s}$.²²²

The diffusion coefficients of water have also been calculated and it can be seen that not only the values are reduced from pure water but also they are different from model to model. Primarily, the values are suppressed from the pure water which was reported in previous chapter as $2.53 \pm 0.09 \times 10^{-9} \text{ m}^2/\text{s}$ ²²³ and the reported value was $2.52 \pm 0.01 \times 10^{-9} \text{ m}^2/\text{s}$ ²²². The experimental values are found between $2.38 \times 10^{-9} \text{ m}^2/\text{s}$ to $2.52 \times 10^{-9} \text{ m}^2/\text{s}$ ²²⁴. In presence of uranyl ion, the water molecules are associated with UO_2^{2+} ion via exchange mechanism which affects the mobility of water molecules. Secondly, the diffusivity of water is increased with the atomic partial charges on uranyl ions. It can be further clarified from hydrogen bond life time (see section H-Bond dynamics). At higher partial charges, more positive environment is created and more water molecules will come to compensate this which accelerates the rate of exchange of water between hydrated water and the bulk water, resulting comparatively higher diffusivity of water at higher partial charges. Overall, the diffusivity studies for uranyl ions and water molecules indicated that the change in partial charges on uranyl ions has significant but not dramatic effect on the diffusivity.

Pair correlation function:

The understanding of structural aspects of the uranyl/water system can be analysed from pair correlation function (PCF). Here, the PCFs of two uranyl sites (U and O) with respect to two water sites (O_w and H_w) have been calculated to find out the structural arrangements. The PCFs of uranium atom and the oxygen atom ($\text{U} \cdots \text{O}_w$) between two interacting uranyl ion and water for four different types of models are shown in **Figure 6.4(a)** and the nature of PCFs are found to be similar for all the studied models.

The first peaks are located at around 2.45 \AA to 2.55 \AA for all the models where the peak is shifted towards central U atom around 0.10 \AA at higher partial atomic charges. The distance becomes shorter at higher a partial charge which was also reported by **Guilbaud and co-worker**²¹⁰.

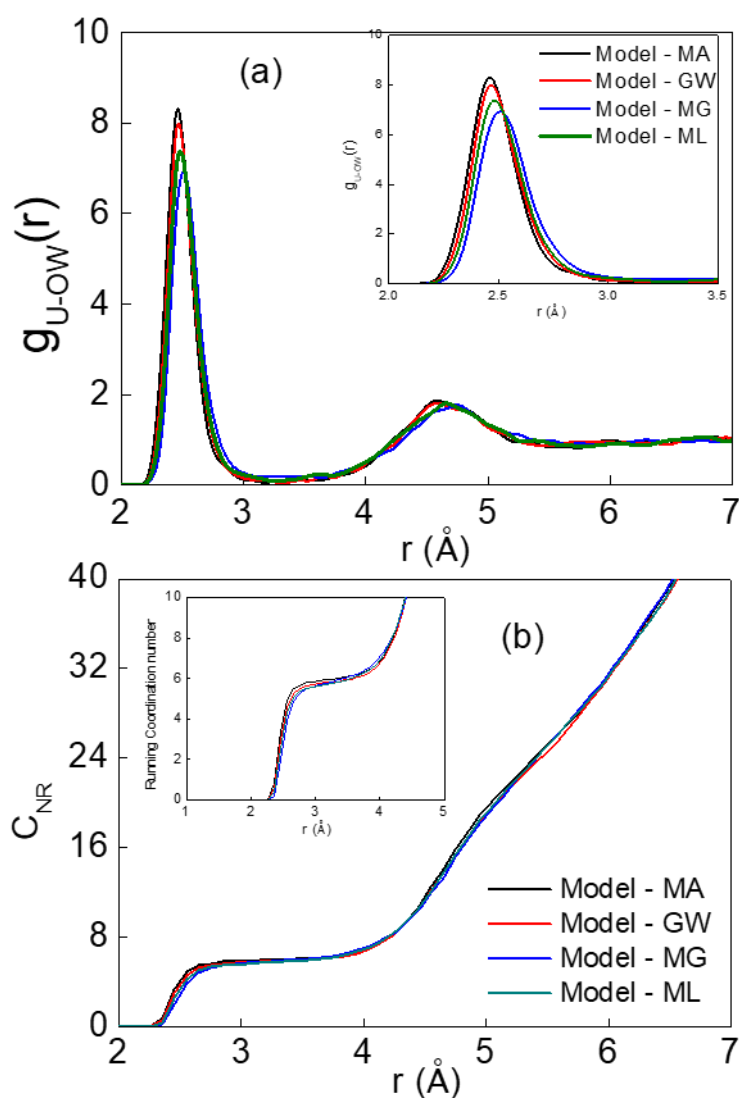


Figure 6.4: (a) Pair correlation function of uranium and oxygen atoms ($U - O_w$) between two interacting uranyl ion and water and (b) Running coordination numbers.

The first peak locations and their corresponding peak heights for present studies and the other computational studies reported in literature are listed in [Table 6.4](#). Though the predicted values are slightly higher compared to the experimental values but they are agreed with other reported computational results. An interesting phenomenon has been found from the above PCFs that the peak height is increasing with partial charges on atoms of uranyl ion while the location of first peak nearly insensitive to the atomic charges as seen in the inset of [Figure 6.4\(a\)](#). The

Model – MA has the highest partial atomic charges whereas the Model – MG has the lowest and the other two models are lying in between. The higher atomic charges on uranium atom strongly associates with the water oxygen and the corresponding local density is increased which leads to the higher peak height.

Table 6.4: Comparison of structural parameter obtained from U – O_w PCFs for all the models along with the reported experimental and calculated values computed from QM or MM or CPMD/AIMD calculations to understand the geometrical parameters obtained from the present study

System	1 st peak location (Å)	1 st peak height	1 st Hydration shell radius (Å)	Coordination number
Model – MG	2.55	7.24	3.15	5.75
Model – ML	2.45	8.49	3.25	5.75
Model – GW	2.45	9.71	3.25	5.85
Model – MA	2.45	10.09	3.15	5.92

The experimental mean values for U – O_w distance of aqueous uranyl are 2.41 Å²²⁵⁻²²⁷ from X-ray absorption fine structure spectroscopy (XAFS) measurement and 2.42 Å^{228, 229} from X-ray scattering data. The experimental values of coordination numbers varies from 4.5 to 5.3 obtained from XAFS data^{226-228, 230, 231} and 4.5, 5 and 6 from EXAFS (extended X-ray absorption fine structure spectroscopy)²³².

Model	U····O _w (Å)	Model	U····O _w (Å)
GW, Model 1, Model 2	2.49, 2.36, 2.40 ²⁰⁸	CPMD	2.47 ²¹⁵
QMCF – MD	2.49 ²¹¹	MM - MD	2.42 ²¹⁰
MM – MD	2.40 ²²⁰	B3LYP	2.37 – 2.42 ²³³
MD	2.46 ²¹³	CPMD	2.48 ²¹⁷
MD	2.44 ²²²	MM – MD	2.40 ²⁰⁹
CPMD	2.44 – 2.46 ²³⁴	AIMD	2.47 ²¹⁵ , 2.48 ²¹⁷

The radius of first solvation shell as defined by the first minimum for distribution of water oxygen around U obtained from MD simulations of different models are close to each other and the values are ranging from 3.15Å to 3.25Å which is comparable with the reported value around 3Å²²². Then, the coordination number (CN), that consists the number of water molecules present in the first solvation shell, have been calculated from the first minima for all the models and it lies in the range of 5.75 to 5.92 as reported in **Table 6.4**. The CN values are slightly higher compared to the experimental values but the CN of 6 was also reported by *Antonio et al*²³². The running coordination numbers of the respective systems are also represented in **Figure 6.4(b)**.

The second peaks corresponding to the second hydration shell are rather wide and trends are similar for all the models as seen from **Figure 6.4(a)**. The location of second peaks are appeared at around approximately 4.55Å to 4.75Å which are close to the reported computational values of 4.3Å to 4.7Å^{210, 217, 220, 233} and experimental values of 4.5Å by high-energy X-ray scattering (HEXS)²³⁵ and 4.4Å by X-ray diffraction²³⁶.

The PCFs of U – H_w for all the models are represented in **Figure 6.5(a)** and the first peaks of H_w around U, are approximately appeared at 3.15Å which match well with the reported computational estimation of 3.12Å²²² and 3.01Å to 3.05Å²⁰⁷. So, the water oxygen atom is comparatively closer to the uranium atom of UO₂²⁺ than the water hydrogen atom (H_w) which signifies such an orientation of water molecules around the UO₂²⁺ ion that the hydrogen atom will be pointed away from the uranium atom as seen in **Figure 6.5(d)**.

Similarly the PCFs of two water sites (H_w and O_w) around uranyl oxygen are calculated from simulations. The distribution of uranyl oxygen – water hydrogen (O – H_w) for all the models are shown in **Figure 6.5(b)** and the first peaks are split into two peaks where the dominant peaks are appeared at around 3.15Å to 3.55Å which are in good agreement with the reported computational results at 3.7Å²⁰⁷ and 3.2Å to 3.7Å²²². The splitting of peak may be regarded as

the formation of disordered structures which indicates several configurations may be there and the current PCFs represent the statistical average of most probable orientations. Then, **Figure 6.5(c)** depicts that the first peak of uranyl oxygen – water oxygen (O – O_w) PCFs are located at approximately 2.75Å for all the models which is in close proximity to the values obtained by Kerisit and co-worker²⁰⁸ as 3.08Å, 2.98Å, 3.01Å and 2.96 Å from GW, model-1, model-2 and AIMD respectively. Similar values for the position of maximum at around 3.0Å were also reported by other researchers^{207, 222}. Here, the water oxygen is close to the uranyl oxygen than that to the water hydrogen which supports the above predicted orientation. Overall, the atomic partial charges have negligible effect on the structural parameters as well as on the orientations.

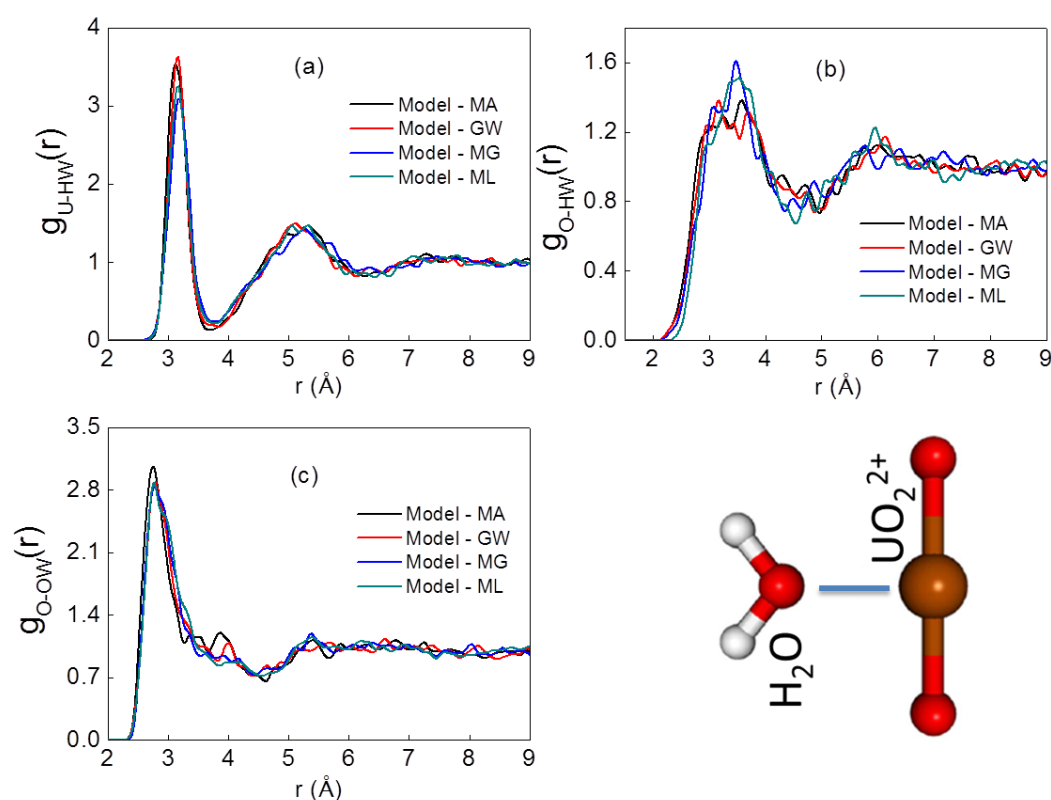


Figure 6.5: Pair correlation functions obtained from simulation of uranyl ion in water: (a) Water hydrogen (H_w) around U atom ($U - H_w$), (b) water hydrogen (H_w) around uranyl oxygen ($O - H_w$), (c) water oxygen (O_w) around uranyl oxygen ($O - O_w$) and (d) configuration of uranyl ion and water molecule. Red: Oxygen, White: Hydrogen and Brown: Uranium atom.

Free energy of hydration:

Gibbs free energy is an essential thermodynamic property that decides the feasibility of any chemical reaction. The hydration free energy ($\Delta G_{\text{Hydration}}$) also ensures the validity of force field. The calculation of free energy was performed using the thermodynamic integration scheme with the integrator for stochastic dynamics^{101, 107} as reported in our previous studies related to the selection of ligands⁹⁴. Free energy of hydration was calculated by decoupling a solute molecule from the solvent. The coupled state ($\lambda = 1$) corresponds to simulations with the solute fully interacting with the solvent and the uncoupled state ($\lambda = 0$) corresponds to simulations considering the solute without interaction with the solvent.

The free energy of hydration is calculated based on the Bennett's acceptance ratio (BAR) method for all the models where a single uranyl ion present in water at infinite dilution under ambient condition. The values of $\Delta G_{\text{Hydration}}$ calculated for various models are presented in **Table 6.5** along with the reported literature values and the plot of free energy with coupling parameter for all the models are shown in **Figure 6.6**.

Table 6.5: Free energy of hydration and the reported literature data

System	$\Delta G_{\text{Hydration}}$ (kcal/mol)	Reported literature value (kcal/mol)
Model - MA	-332.71 ± 0.74	-325.36 ± 5.7 (Experiment) ²³⁷
Model - GW	-319.66 ± 1.33	-398.32 ± 15.5 (Experiment) ^{238, 239}
Model - ML	-301.61 ± 0.67	-332.54 ²¹³
Model - MG	-292.28 ± 0.51	-304 (GW), -371 (model-1), -377 (model-2) ²⁰⁸ -369.62 ± 15.5 ²⁴⁰

The uncertainties in computation are around ± 0.24 kcal/mol.

The $\Delta G_{\text{Hydration}}$ of UO_2^{2+} obtained from model-MG underestimates the experimental value by 10.2% while the model-ML around 7.3%. The prediction of $\Delta G_{\text{Hydration}}$ for model-MA and model-GW are in good agreement with the experimental value reported by Marcus²³⁷ as 325.359 kcal/mole and the deviations are 1.75% and 2.25% respectively. The upper and lower bound of hydration free energy can be considered as 325.36 kcal/mol²³⁷ and 398.32 kcal/mol^{238, 239} respectively. Our calculated free energy values are appeared in the experimental range. Though the structure of water molecules around uranyl ion is hardly altered by the effect of atomic partial charge distribution on the U and O (uranyl oxygen) atom of uranyl ions, it has noticeable effect on the free energy of hydration. The higher partial charge increases the polarity of U – O bond which results higher interactions with water molecules. So, the free energy value becomes more negative which is also reflected in the $\Delta G_{\text{Hydration}}$ values reported in Table 6.5.

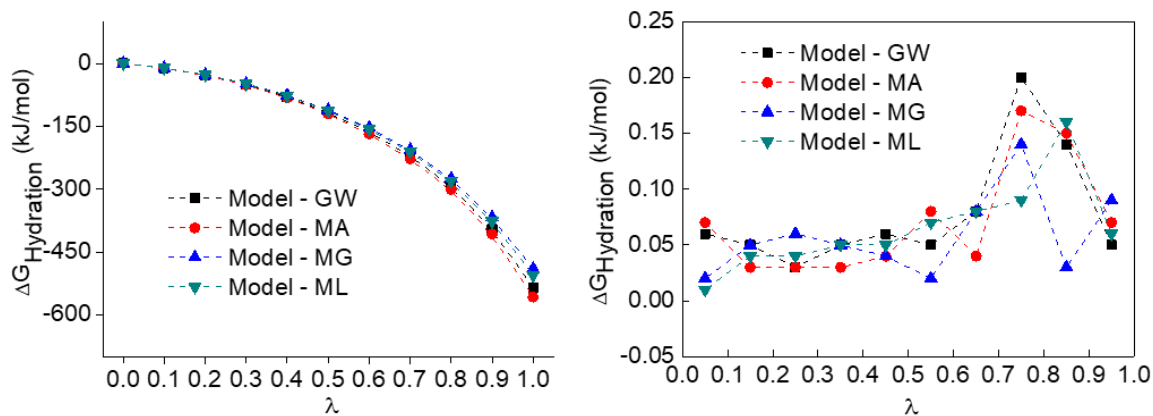


Figure 6.6: Change of free energy of hydration ($\Delta G_{\text{Hydration}}$) versus coupling parameter (λ) evaluated using thermodynamic integration.

Hydrogen bond dynamics (HBD):

The dynamics of hydrogen bond is very significant for any aqueous or biphasic systems. HBD signifies the hydrogen bond network of aqueous phase and the various physical and dynamical

properties can be characterized by using HBD. Here, hydrogen bond analysis has been carried out for 1ns simulation length after the production run of 10ns. The numbers of hydrogen bonds determined for each models are shown in **Figure 6.7(a)**.

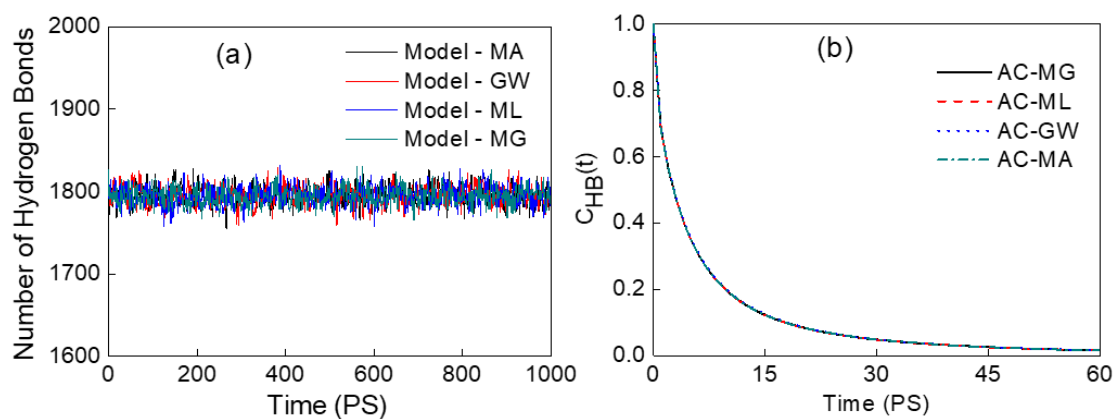


Figure 6.7: Hydrogen bond dynamics related to (a) hydrogen bond numbering with respect to simulation length and (b) hydrogen bond autocorrelation function for models – MG, ML, GW and MA. Number of donors: 1000 and number of acceptors: 1002.

The calculated HB numbers are plotted against the simulation length and focused on the number of hydrogen bond presents at that instant. It has been found that the values are remained fairly constant throughout the progress of simulation. The number of hydrogen donors and acceptors in the system between which the hydrogen bond is formed, depends on the molecular orientation and packing. Generally, they are oriented in such a fashion which maximizes the number of hydrogen bonds. Here, there is hardly any difference in the number of hydrogen bonds for all the systems, indicates that the partial atomic charges do not have significant effect on the orientation of the ions or molecules.

Additionally, the hydrogen bond autocorrelation function also has been evaluated for all models and shown in **Figure 6.7(b)**. The correlation between uranyl ions and water molecules is determined from HB correlation function, where the two molecules are to be hydrogen bonded.

The decay pattern is shown in the **Figure 6.7(b)** and they are exactly similar which signifies the effect of partial charges on atom as well as the effect of force field has negligible effect on hydrogen bond autocorrelation function. In addition to that, the orientation of molecules can be supported by hydrogen bond lifetime which is guided by the mobility and packing of molecules. The hydrogen bond lifetime has been computed for SPC/E water model from simulation and it gives the value of 2.60 ps. It is very difficult to determine the proper HB lifetime based on the HB broken and reform dynamics. HB lifetime for various water models was reported earlier^{136-140, 241} and the lifetime computed from auto correlation function (ACF) lies between 3.0 – 3.5 ps. So, the simulation result for water is in close proximity to the reported values. Then, the hydrogen bond lifetime for all models has also been calculated and it is varied between 2.72 to 2.77 ps which is comparatively higher than that of the pure water. It indicates that the presence of uranyl ion makes the hydrogen bond more stable compared to the pure water in the first solvation shell. Hence, the hydrogen bond lifetime also assures the similar kind of molecular orientation and packing present in all the models.

Again, the reduction in self-diffusivity of water molecules which are already reported in **Table 6.3** can be justified by hydrogen bond life time. The hydrated water spends some time with uranium in the solvation shell and they usually get exchanged with the bulk water molecules. The exchange mechanism of water may follow the associative or dissociative path. So, the hydrated water molecules are relatively less mobile compared to the bulk and this event is influenced by the hydrogen bond lifetime. The higher lifetime means more residence time of the hydrated water which indirectly slowed down the mobility of bulk water and thus the self-diffusivity of water molecules is reduced in presence of uranyl ion. Again, the self-diffusivity of water is also increased at higher partial charge on uranium atom because the interaction between the water oxygen and uranium atom is comparatively stronger which basically

accelerates the water exchange rate with the bulk water and increases the self-diffusivity of water.

The force fields with various partial atomic charges on uranium as well as on uranyl oxygen atoms were used to model uranyl ion in water system and the various properties have been calculated. There are hardly any differences found in the properties like physical, structural and dynamical except the free energy of hydration where the partial charges have significant effect on it. Overall, the variation in atomic charges does not have much significant effect on the force field. So, any one of these force fields of uranyl ion can be used for further studies in acidic medium. Here, the model – GW has been chosen for studies the uranyl ions in acidic medium based on the free energy of hydration which captures the interaction more accurately.

6.4.2. Type – 2: Uranyl nitrate in 3M nitric acid

Hence, we are going to discuss the structural and dynamical properties of uranyl nitrate in presence of acid. Point to be noted, this issue has not yet been explored that how these models will behave in the acidic medium or against the organic phase during the replication of PUREX process. Therefore, in type – 2 systems, we have attempted to address these issues along with the effect of uranyl nitrate concentration in 3M nitric acid medium. The details of simulation systems are reported in [Table 6.2](#).

Density and dipole moment:

All the simulated systems have been equilibrated for 20 ns simulation length followed by production run for 10 ns. The bulk densities of each system have been calculated and we have found an increasing function of uranyl nitrate concentrations as seen in [Table 6.6](#).

In assurance of simulation data, the experiments have been carried out to estimate the density of uranyl nitrate solution using an oscillating U-tube density meter (DMA 5000 M, Anton Paar). The experimental results exhibit an excellent agreement with the densities [shown as

(*)] obtained from MD simulations. The maximum deviation from experimental density is observed to be 7% which ensures the accuracy of force field parameters used in the MD simulations.

The corresponding average dipole moments obtained from the contribution of uranyl ions as well as from the contribution of all ions present in the medium for all systems are also shown in [Table 6.6](#). The calculated average dipole moments acquired from all ions present in the aqueous phase are also reported in the table as an average dipole moment of the system.

Table 6.6: Bulk density and average dipole moments for uranyl ions as well as for all ions (called as overall) present in 3M nitric acid medium at various concentrations of uranyl nitrate (GW force field)

System	Bulk density (kg/m ³)	Dipole moment (Debye)	
		UO ₂ ²⁺	Overall
5-U	1126.04 ± 0.18 (1114.7*)	0.979 ± 0.003	2.215
10-U	1153.67 ± 0.17 (1134.4*)	0.997 ± 0.003	2.208
25-U	1232.35 ± 0.26 (1195.7*)	0.975 ± 0.002	2.184
50-U	1364.19 ± 0.22 (1298.1*)	0.972 ± 0.001	2.150
70-U	1459.32 ± 0.20	0.949 ± 0.001	2.122
85-U	1531.89 ± 0.22 (1423.0*)	0.949 ± 0.001	2.102
100-U	1597.88 ± 0.40 (1490.8*)	0.930 ± 0.001	2.082
120-U	1685.85 ± 0.12	0.920 ± 0.001	2.057

The effect of uranyl nitrate concentrations in 3M nitric acid on the average dipole moment exhibited that both the average dipole moments are decreasing with concentrations. The dipole

moment value changes from 0.997 to 0.920 Debye throughout the systems which is quite insignificant. Probably the U=O is responsible for both Van der Waals force of attraction and dipole – dipole interaction. Higher concentration of uranyl nitrate in this acidic medium may weaken the dipole – dipole interaction between U=O groups which is reflected in the computed dipole moment. The overall dipole moment changes from 2.215 to 2.057 and the values are higher compared to that of uranyl ions. It can be concluded that the uranyl ion is the major contributor to the overall dipole moment.

Self – diffusion coefficient:

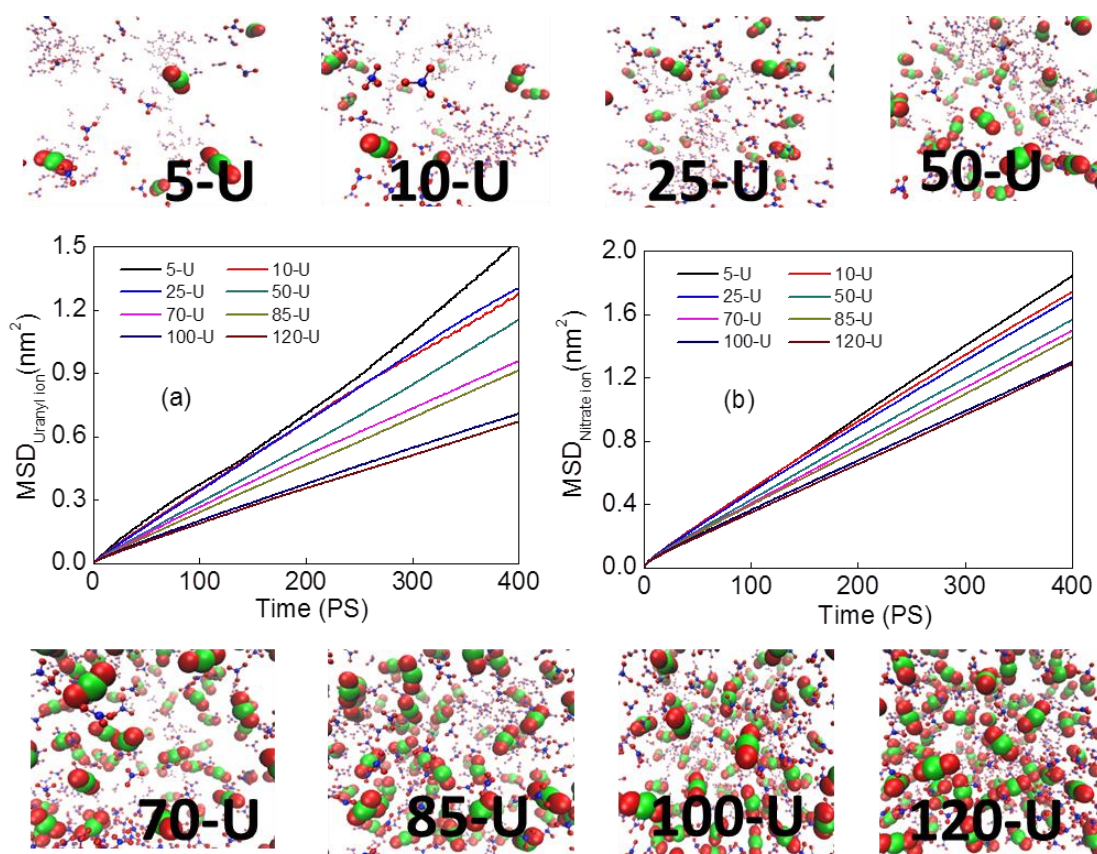


Figure 6.8: (a) MSD profiles of uranyl ions and (b) MSD profiles of nitrate ions in 3M acidic solution as a function of uranyl nitrate concentrations in that solution. The uranyl nitrate concentrations are represented as the numbers of uranyl ions present in the aqueous phase and denoted by respective system. The snapshots of respective liquid phase are illustrating the gathering of uranyl nitrate in the solution with concentrations. Colour code: Green-Uranium, Red-Oxygen and Blue-Nitrogen.

The self-diffusion coefficient describes the translational mobility of molecules or ions in a medium. The process, diffusion in a mixture can be expressed as self-diffusion or mutual diffusion. The self-diffusion signifies the movement of individual molecules or ions whereas the mutual diffusion, a collective property, describes the mixing of two or more components and how fast they mix with each other. As they are not connected by straightforward relation, only self-diffusion is studied here for all systems using Einstein relation.

The MSD profiles are represented in **Figure 6.8(a)** as a function of concentration of uranyl nitrate and it follows a decreasing trend with UO_2^{2+} concentrations. Further, the MSD profiles of NO_3^- ions are also shown in **Figure 6.8(b)** and it follows the similar trend. The self-diffusion coefficients have been computed from the slope of MSD profiles and are reported in **Table 6.7**.

Table 6.7: Self-diffusion coefficients of uranyl ion, nitrate ion and water molecule present in aqueous phase calculated from MD simulations for a wide range of uranyl nitrate concentrations

System	Self-diffusion coefficient ($10^{-9} \text{ m}^2/\text{s}$)		
	UO_2^{2+}	NO_3^-	H_2O
5-U	0.677 ± 0.09	0.676 ± 0.09	2.306 ± 0.01
10-U	0.557 ± 0.14	0.662 ± 0.08	2.239 ± 0.02
25-U	0.527 ± 0.11	0.656 ± 0.08	2.031 ± 0.04
50-U	0.457 ± 0.06	0.649 ± 0.04	1.748 ± 0.07
70-U	0.368 ± 0.05	0.588 ± 0.05	1.564 ± 0.05
85-U	0.333 ± 0.04	0.570 ± 0.03	1.466 ± 0.02
100-U	0.265 ± 0.01	0.548 ± 0.03	1.287 ± 0.02
120-U	0.260 ± 0.01	0.511 ± 0.04	1.168 ± 0.03

As seen from the above table and **Figure 6.9**, the self-diffusion coefficients of UO_2^{2+} ions are decreasing with uranyl nitrate concentration. The concentrated uranyl nitrate in 3M acid restricts the mobility of uranyl ion in the medium. Due to non-availability of reported MD or experimental data, the validation of simulation results can be done only with respect to the uranyl ion in water system. It is obvious that the diffusivity calculated in higher uranyl nitrate concentration has to be demoted by surrounding uranyl or nitrate ions that is absent in single uranyl ion in water system. Similar effect of concentration on self-diffusivity of uranyl ions is also reported by **Chopra et al²⁴²**, where the diffusivity was reduced from U1 to U10 system. But, their reported diffusivity values were higher compared to the present studies because of the absent of 3M nitric acid.

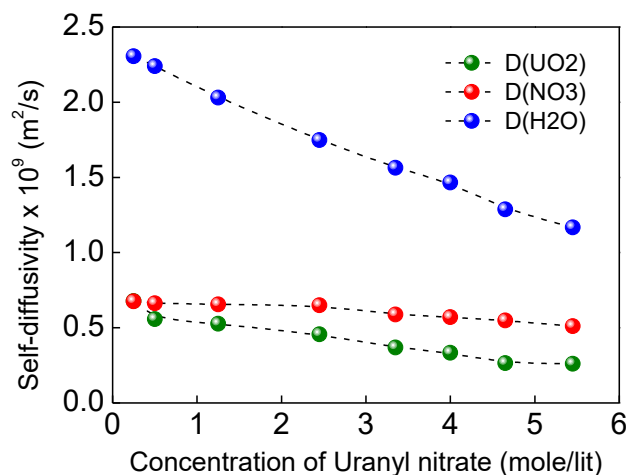


Figure 6.9: Trend of self-diffusion coefficient of uranyl ion, nitrate ion and water calculated from MD simulations as a function of uranyl nitrate concentration.

Hence, the present study follows the decreasing trend i.e. the diffusivity is decreased when UO_2^{2+} ion concentration is increased. The calculated self-diffusivities of NO_3^- ions also follow the similar trend i.e. it is reduced to $0.511 \times 10^{-9} \text{m}^2/\text{s}$ from $0.676 \times 10^{-9} \text{m}^2/\text{s}$ but not so significant compared to the self-diffusivities of UO_2^{2+} ions. In addition to that, the self-

diffusivities of water have been evaluated for all the systems and it was found changing with uranyl nitrate concentrations rather it is decreasing as observed earlier²⁴². Such reduction in self-diffusion is not only due to the influence of UO_2^{2+} ions but also due to NO_3^- ions present in the system. When the hydrated ions form complexes, it decreases water shielding resulting in reduction of water exchange rate due to structure breaking and forming which is responsible for the development of shielding. So, a reduction in shielding decreases the solvent diffusivity. Here, the presence of uranyl nitrate complexes reduces the water shielding which is reflected in the self-diffusivities values of water. We have compared the self-diffusivity of water between type-1 and type-2 systems and a dramatic effect has been observed in type-2 system due to the presence of uranyl complex while a negligible effect was found in type-1 system. Therefore, it can be concluded that both the effect may alter the water diffusivity but in different magnitude. The reported self-diffusivity of water for 5U system ($2.26 \times 10^{-9} \text{ m}^2/\text{s}$)²⁴² is in quantitative agreement with the present simulations results.

In addition to the concentration effect of uranyl ions, the temperature dependency on self-diffusivity has also been studied to acquire more insight about the activation energy of diffusion. The self-diffusivity (D) at various temperatures (T) was determined and the activation energy (E_a) is computed by using the Arrhenius equation^{243, 244},

$$\ln D = \ln D_0 - \frac{E_a}{RT} \quad (6.1)$$

Where, D_0 is pre-exponential factor and k_B is Boltzmann constant. Here, MD simulations have been performed for 10 ns simulation length in the range of temperature from 290K to 340K and the self-diffusivities are computed from the slope of MSD using equation S2.

The logarithmic value of self-diffusivities for uranyl ion and water molecules are plotted against inverse of temperature and the dependency is found to be linear throughout the range of temperature as shown in **Figure 6.10**.

The computed activation energy (E_a) for diffusion of uranyl ion is found to be higher than that of the water molecules which indicates that more energy is required for the diffusion of uranyl ions compared to the water molecules. So, low activation energy of diffusion for water molecules supports faster transport in the aqueous medium and it is in accordance with the calculated self-diffusivity values as reported in [Table 6.7](#).

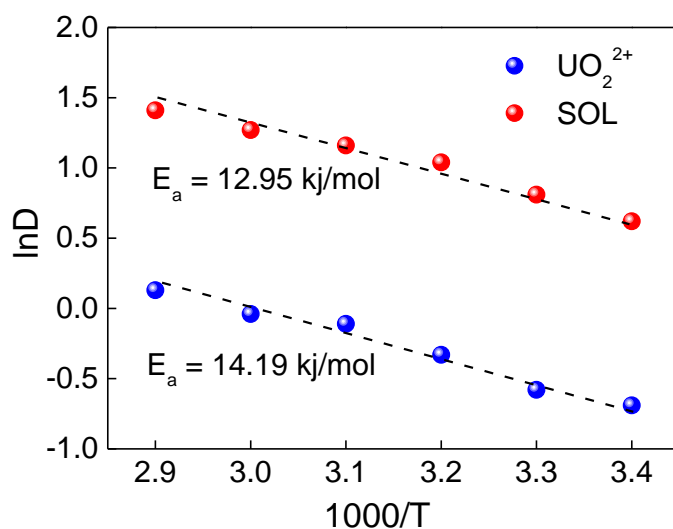


Figure 6.10: Arrhenius plot of self-diffusivity of uranyl ion and water molecules computed from MD simulations against the inverse of temperature. 10-U system is used to study the temperature effect.

Pair correlation function:

The understanding of structural properties can be developed from pair correlation function (PCF). The PCFs are evaluated for two uranyl sites (U and O) interacting with two water sites (H_w and O_w) along with the U – U. In addition to that, the two nitrate sites (N and O_N) interaction with U, O_w and H_w also have been evaluated to relate the orientation of nitrate ions around UO₂²⁺ ions or water molecules.

U – O_w pair correlation function:

The PCFs between two interacting U atom and water oxygen atom (U – O_w) have been evaluated for all the systems and it is displayed in **Figure 6.11**.

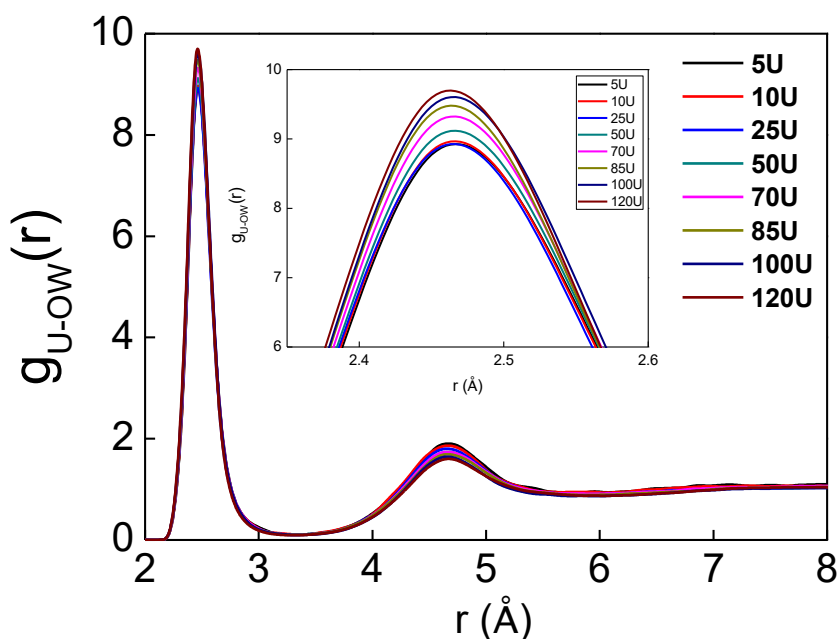


Figure 6.11: Pair correlation function between two interacting U atom and O_w atom

As seen from the above figure, all the PCFs displays similar pattern. The first peaks are located at same distance approximately 2.45Å but the peak heights are different for all the cases (see inset of **Figure 6.11**). The first peak heights are plotted against the concentration of uranyl nitrate which shows an increasing function in **Figure 6.12(a)** indicating that the local density i.e. the probability of finding of water molecules locally is increased with availability of uranyl ions. Note, the U····O_w distance remains unchanged with the gradual increase of water molecules surrounding the uranium atom of UO₂²⁺ ion. At higher concentration of UO₂²⁺ ions, more numbers of water molecules are attracted towards UO₂²⁺ ions as reflected in the peak height.

Next, the first minima are appeared at a distance around 3.35\AA . The corresponding coordination numbers (CN) for all the systems have been computed and a decreasing trend has been observed in accordance with the concentration of uranyl ion as shown in **Figure 6.12(b)**. The CN is found to be varied from 5.88 to 5.39. Similar reduction in CN with increasing concentration of uranyl ion was also reported by [Chopra et al²⁴²](#). But the change in CN is not very significant and can be concluded that the CN of U – Ow PCFs is independent of uranyl ion concentration and system composition.

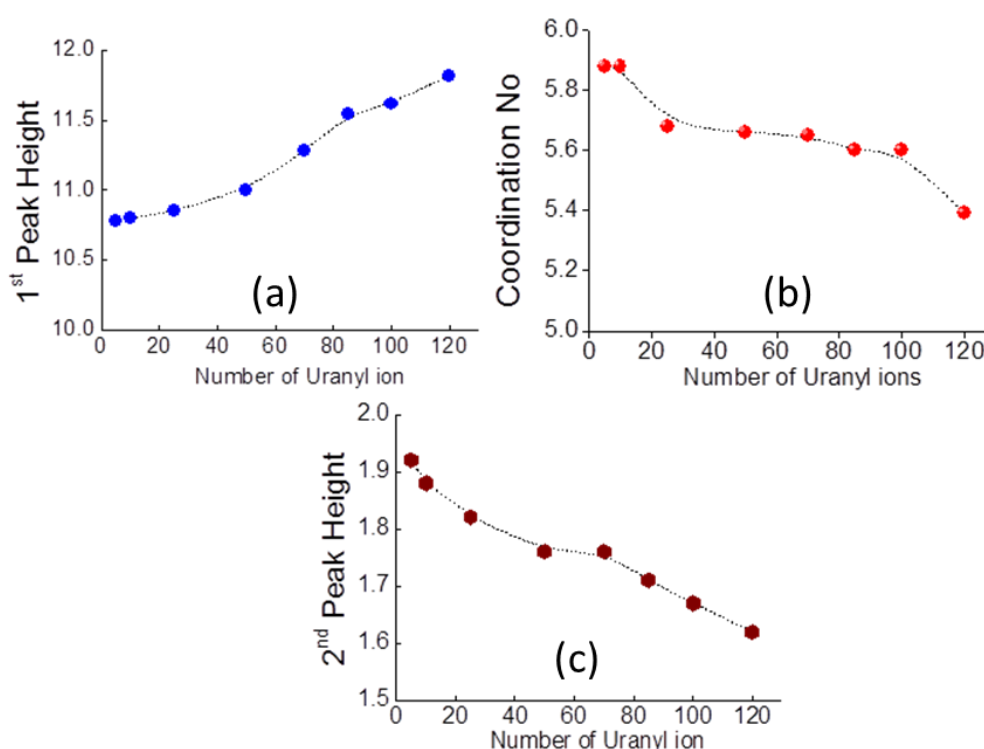


Figure 6.12: (a) First peak height calculated for U – Ow PCFs (b) Coordination number of water oxygen around uranium of uranyl ion and (c) Second peak height are plotted as a function of concentration of uranyl nitrate in 3M acid.

Thereafter, on further away from the uranium atom, the second peaks for all the systems are appeared at a distance of $\sim 4.65\text{\AA}$ similar to the first peak. But when the peak heights are plotted, it was found to be a decreasing function of uranyl ion concentrations as seen from **Figure**

6.12(c). Such opposite effect of peak heights may be due to the dense packing of uranyl and nitrate ions at higher concentration which reduce the availability of water molecules surrounding the uranyl ions.

O – H_w and O – O_w pair correlation function:

The PCFs of two water sites (H_w and O_w) with respect to the uranyl oxygen (O) atom for all the simulation systems are depicted in **Figure 6.13(a)** and **Figure 6.13(b)** respectively.

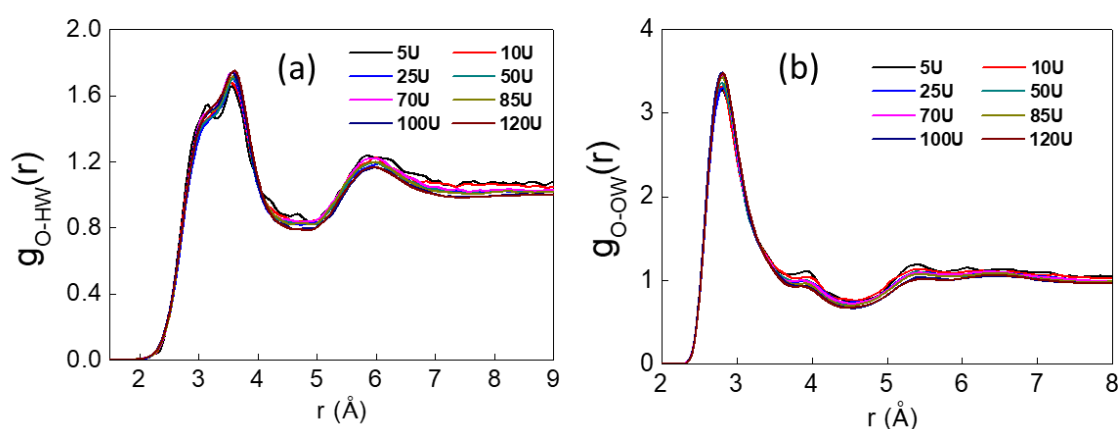


Figure 6.13: Pair correlation function between two interacting (a) Oxygen atom of uranyl ion and hydrogen atom of water molecule and (b) Oxygen atoms of uranyl ion and oxygen atom of water molecule at different uranyl nitrate concentration which represented by the numbers of uranyl ions present in 3M nitric acid.

All O – H_w PCFs follow the similar trend and the first peaks are appeared at a location of 3.55 Å with a small hump as seen from **Figure 6.13(a)**. The peak height is varied from 1.69 Å to 1.77 Å. The nature of first peaks of O – H_w PCFs in presence of acid are quite similar to the PCF obtained in absence of acid except the peaks are split into two peaks in the later case. Here, the split peaks are converted to single peak with a small hump. So, the nitric acid which is present in dissociated form as H₃O⁺ and NO₃⁻ has significant influence on the O – H_w PCFs. The first minima is appeared at a range of 4.65 Å to 4.95 Å and the calculated CN are reduced to 13.9-

12.2 from 15.70 which was obtained for uranyl ion in water system. Such reduction is obvious as both the UO_2^{2+} and NO_3^- ions are present in the medium. The second peaks are located at approximately in the range of 5.85Å to 5.95Å which is quite similar to the calculated results of uranyl ion in water system.

The O – O_w PCFs for all the systems also exhibit similar trend as shown in **Figure 6.13(b)** and the first peaks are located at around 2.75Å to 2.85Å. The peak heights are in a range of 3.31 to 3.52. Here, we also found the similar observation that the nature of PCFs in acidic medium has negligible difference from that of the water medium. The first minima are observed at around 4.45Å to 4.55Å and the CN is varied from 13.2 to 10.7 indicating a decreasing trend. The CNs obtained in type-1 systems are higher compared to the acidic system. This may be due to the gradual reduction of the availability of water around the uranyl oxygen at higher uranyl nitrate concentration. The second peaks are broad and flattened in nature and are appeared at approximately 5.45Å.

U – O_N and U – N pair correlation function:

The pair correlation functions of two sites (O_N and N) of nitrate ion around the uranium (U) atom have been evaluated to understand the orientation of nitrate ions around U atom with the competition of water molecules in acidic medium. The PCFs of oxygen atom (O_N) of nitrate ions with respect to U atom at variable concentration of uranyl nitrate are represented in **Figure 6.14(a)**.

The first peaks of U – O_N PCFs are located at approximately 2.55Å except for 5U and 10U where the first peaks are appeared at a location around 4.65Å and 4.55Å respectively. The sharp first peak at 2.50Å was also reported by *Ye et al* with 18 numbers uranyl ions.³⁸ The U – O_N distances are found to be almost same to that of the U – O_w for all concentrations, which confirms the presence of both water molecules and nitrate ions in the solvation shell. Similar

observation was also reported by [Chopra et al](#)²⁴² for U10 system. Again, in case of 5U and 10U, the first peaks are associated with second peaks and only one peak is appeared which is located near the second peaks of the rest of the systems and was absent in their studies²⁴². The unusual characteristics appear due to the presence of 3M acid in the medium. So, it can be concluded that the acid medium may alter the orientation in the solvation shell. [Bhul et al](#) also reported the U – O_N distance in the range of 2.49Å to 2.59Å calculated from CPMD, ZORA and LANL whereas 2.53Å from X-ray diffraction analysis²¹⁷. From the calculated CNs for all the systems, it has been found that the orientation of uranium atom allows the CN of 2.84 and 2.56 for 5U and 10U systems respectively. It indicates that the uranium is attached to two oxygen atoms of nitrate ions. For the rest of the systems, the CN keeps on increasing from 0.32 to 0.55 which also indicates the association of single oxygen atom of nitrate ions with uranium atom. So, the bi-dentate structure is formed at lower concentration of uranyl ions and it converted to mono-dentate at higher concentration. Because more number of uranyl ions reduces the availability of nitrate ions around UO₂²⁺ ions and also a competition between water and nitrate ion to occupy the space in solvation shell. This might be the reason for changing the CN from 2.84 to 0.32. Similar observation in CN was also reported by [Chopra et al](#)²⁴². The predominant mono-dentate binding mode was observed in aqueous environment using Raman spectroscopy by [Brooker et al](#)²⁴⁵ and [Nguyenttung et al](#)²⁴⁶. Again, [Chiarizia et al](#) also established the mono-dentate structure in water-rich medium using EXAFS measurements.¹⁸ According to the work of [Bhul et al](#), the solvent effect facilitated the transition from bi-dentate to mono-dentate and the nitrate ions are rather involved in inter-molecular hydrogen bonds with solvent instead of intra-molecular hydrogen bonds with uranyl water²¹⁷. Hence, it can be concluded that the coordination properties can be affected by the solvation as well as by the solute concentrations. Therefore, it can also be seen that the CN of O_N atom is increased with uranyl nitrate concentration while that of O_w is decreased. Along with the concentration of

uranyl nitrate, one more factor is responsible for the CN which is the number of water molecules present in the medium. Higher numbers of water molecules reduces the U – O_N coordination numbers as also seen from the study of Chopra *et al*²⁴⁷. Our study with 2845 numbers of water molecules exhibits the CN in between their studied system containing water molecules around 2400 and 3920 numbers. The second peaks are appeared at around 4.55 – 4.65Å except 5U and 10U systems where the second peaks are small and located further away approximately at a location of 6.05 – 6.25Å. The second peaks of rest of the systems are higher compared to the first peaks which indicate more nitrate ions are available within the 2nd solvation shell.

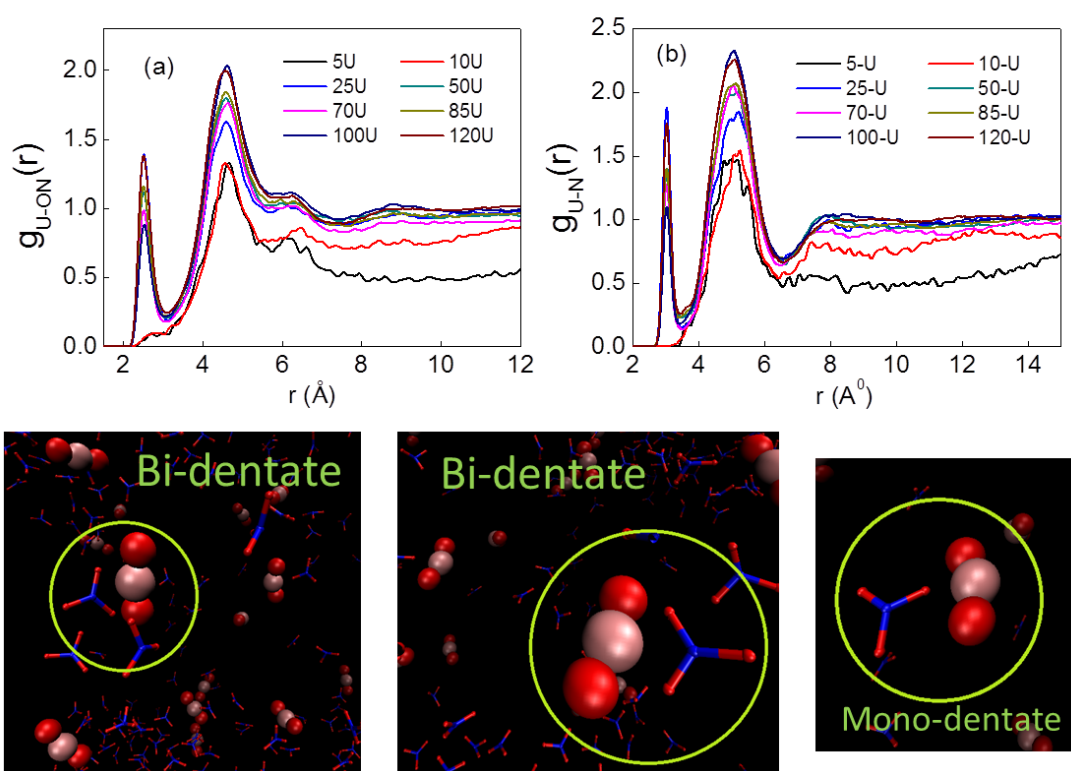


Figure 6.14: Pair correlation function between two interacting atoms (a) Uranium (U) and oxygen atoms (O_N) (b) Uranium (U) and nitrogen atoms (N) of UO₂²⁺ ion and NO₃⁻ ion. Snapshot of liquid structure obtained from MD simulations study illustrating the bi-dentate and mono-dentate structure between uranyl ion and nitrate ion. Colour code: Red-Oxygen, Blue-Nitrogen and Pink-Uranium.

The PCFs between two interacting U and N atoms are also calculated and they are shown in **Figure 6.14(b)**. The profile of these PCFs is similar to that of the U – O_N PCFs. A single broad peak is observed for both the 5-U and 10-U systems whereas two peaks are there for rest of the systems. The first peaks are located at around in the range of 4.75 – 5.15 Å and 5.05 – 5.25 Å for 5-U and 10-U systems respectively. For other systems, it is located at approximately at 3.05 Å. The orientation of nitrate ions around uranium atom can be described from the above PCFs study and it has been seen that the O_N atom is much closer compared to the N atom with respect to U atom. So, they may be oriented as shown in snap shot in **Figure 6.14**.

The first minima is appeared at 6.45 – 6.55 Å for 5-U and 10-U systems while at 3.35 – 3.45 Å for rest of the systems. The CN is also reduced from 1.55 to 0.14 which indicates the less availability of nitrate ions around U atom. The second peaks are appeared at around 5.05 – 5.25 Å except 5-U and 10-U where it was absent.

O_N – H_W and O_N – O_W pair correlation function:

The PCFs of two water sites (H_W and O_W) around the oxygen atom (O_N) of nitrate ions have been computed to understand the interaction as well as the orientation of water molecules with respect to nitrate ions in the acidic medium. The O_N – H_W PCFs for all the systems are evaluated and the PCFs are gradually increasing with uranyl nitrate concentration and they exhibit similar feature as shown in **Figure 6.15(a)**.

The first peaks are located at around 1.75 Å with an increasing peak height ranging from 1.01 to 1.53. *Buhl et al* also obtained the first peak at similar location using CPMD (Car-Parrinello molecular dynamics) but the profile was noisy due to short simulation time²¹⁷. Here, the profiles are sufficiently sharper and smoother compared to their PCFs because of longer simulation run. Again, they have reported a board peak which is not observed in the present

study. The hydrogen atom of water molecule is located within the hydrogen bonding distance ensures that the nitrate ions are significantly solvated in water.

The first minima are appeared at approximately 2.45 Å for all the systems and the corresponding CNs are obtained in the range of 0.81 to 1.07. The coordination number is gradually increasing with the nitrate ion concentration which indicates more number of water molecules is aggregated around the nitrate ion. A sudden jump is noticed from 50U to 70U which is also reflected in peak height, first minima and coordination number. The second peaks are appeared at approximately 2.75 Å and the peak heights are gradually increasing from 0.74 to 1.07.

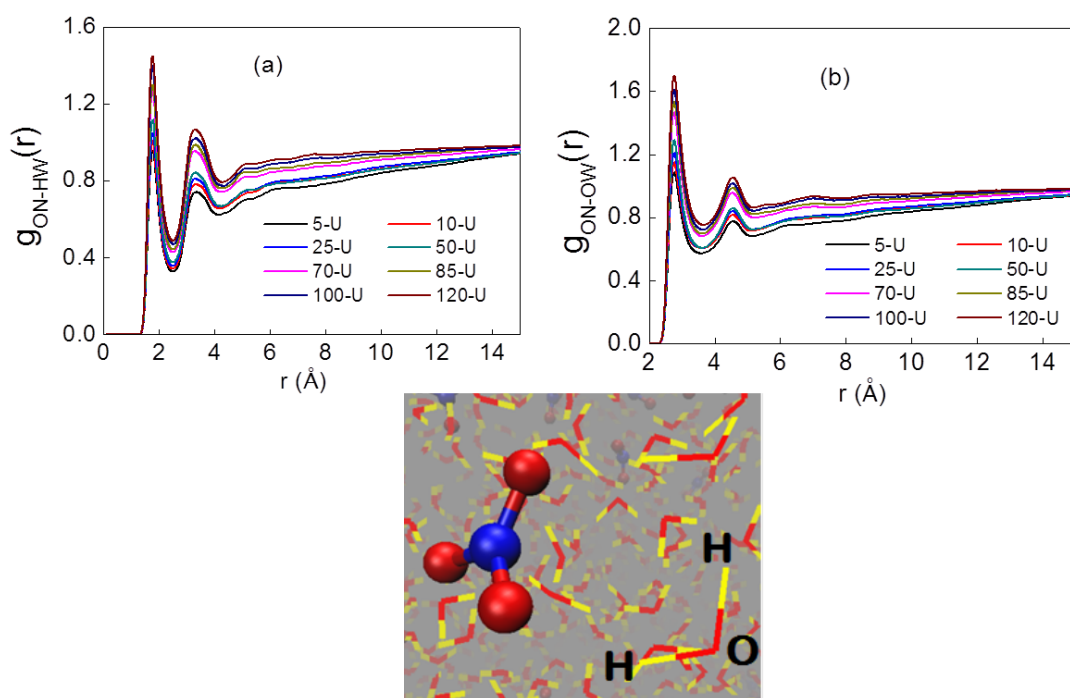


Figure 6.15: Pair correlation function between two interacting (a) oxygen atom of nitrate ion and hydrogen atoms of water and (b) oxygen atom of nitrate ion and oxygen atom water. Snapshot of orientation of water molecules around nitrate ions. Colour code: Red-Oxygen, Blue-Nitrogen and Yellow-Hydrogen.

The $O_N - O_W$ PCFs for all the systems are also computed and represented in **Figure 6.15(b)**. All the PCFs followed the similar trend and the first peaks are located at around 2.75\AA which is also similar to that of the work done by *Bhul et al.*²¹⁷ But again the profiles are different from the results of the present study. The water hydrogen (H_W) is much closer to the oxygen atom of nitrate ion which provides an idea regarding the orientation of water molecules around the nitrate ions and the probable orientation may be like the one as shown in snap shot in **Figure 6.15**.

The first peak heights are gradually increasing as seen from the **Figure 6.15(b)** and the values are ranging from 1.13 to 1.77. Then, the PCFs passed through minima at a distance of $\sim 3.55 - 3.65\text{\AA}$ and the corresponding calculated CN lies between 2.75 to 3.91. Thereafter, the second peaks are appeared at approximately 4.55\AA along with increasing peak height.

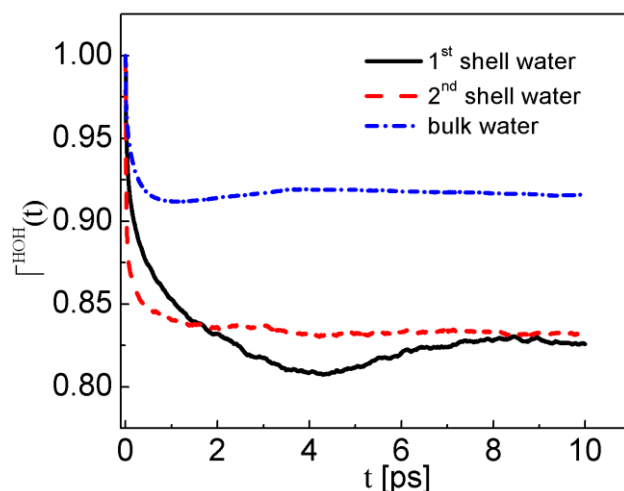


Figure 6.16: Plot of orientational correlation function as a function of time (t).

Further, it will be interesting to investigate the orientational correlation function of water molecules in the solution in presence of uranyl ions. The orientational correlation function ($\Gamma^{\text{HOH}}(t) = \langle \theta(t)\theta(0) \rangle / \langle \theta(0)\theta(0) \rangle$) has been calculated by considering the angle ($\langle \text{HOH} \rangle$) of water

molecule for bulk water and in presence of uranyl ion (5-UO₂ system). The presence of uranyl ion affects the angular orientation of surrounding water molecules as revealed from the plot of orientation correlation function (see the **Figure 6.16**). The orientation correlation function decays faster in presence of uranyl ion. Further, the decay is slowed down as one move from first solvation shell to second solvation shell.

The tetrahedrality parameter ($q=1-S_g$) pure solvent (here water) as well as uranyl nitrate solution in 3M nitric acid have been calculated to understand the deviation from tetrahedrality from pure water in presence of uranyl nitrate and also the effect of concentration on tetrahedrality. The calculated results are presented in **Table 6.8**. From the results, it is seen that the tetrahedral order parameter (q) is reduced with increasing concentration of uranyl ions indicating the disruption of hydrogen bond.

Table 6.8: Calculated tetrahedral order parameter (q) for various systems

System	S_g	Orientation Tetrahedral order ($q = 1 - S_g$)
SOL	0.0923	0.9077
5-UO ₂	0.1097	0.8903
10-UO ₂	0.1104	0.8896
25-UO ₂	0.1189	0.8811
50-UO ₂	0.1203	0.8797
70-UO ₂	0.1232	0.8768
85-UO ₂	0.1278	0.8722
100-UO ₂	0.1297	0.8703
120-UO ₂	0.1348	0.8652

Surface tension:

Surface tension is a very useful physical property which plays an important role in liquid – liquid extraction and stripping operation in particular and various interfacial processes in general. In our previous studies, we have calculated the interfacial tension at TiAP/dodecane – water interface²²³. Now, it is important to calculate the surface tension of aqueous phase which is generally treated as feed in well-known PUREX process. The methodology is similar to our previous work²²³. Only change is that here the system has only one phase so the space to be provided for vapour phase where some molecules of aqueous phase will escape from aqueous layer during simulation¹³⁵. For this reason the box is elongated along z direction. Note that here $L_x = L_y = 3*L_z$ is used for study where L_x , L_y and L_z are box dimensions in x, y and z direction respectively.

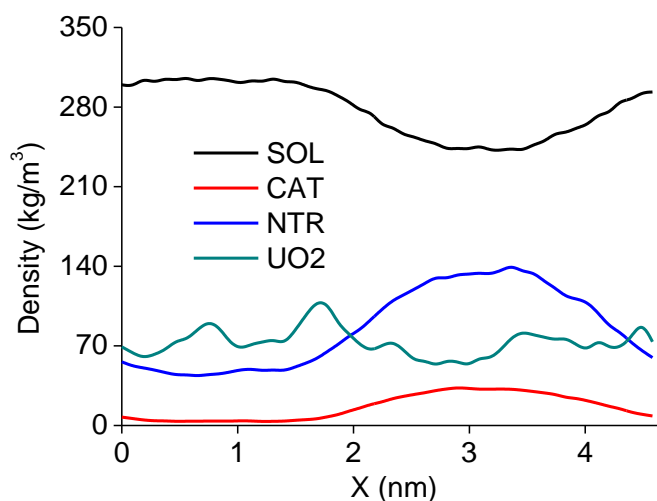
MD simulations have been performed for 1 ns simulation length with rectangular box to evaluate the surface tension. Initially, the surface tension of SPC/E water is computed and was found to be 85.15 mN/m which is close to the reported experimental value 90 mN/m²⁴⁸, indicating confirmation of simulation accuracy. Other reported surface tension using SPC/E water model are 55.4mN/m²⁴⁹, 61.3 mN/m²⁵⁰, 70 mN/m^{251, 252}. Thereafter, the surface tensions of uranyl nitrate in 3M acid systems have been evaluated to understand the trend during variation in concentrations of uranyl nitrate. The simulation result indicates that the surface tension is an increasing function of concentration as shown in **Table 6.9**.

In presence of uranyl ions, the surface tension is raised from 85.15 mN/m in case of pure water to 111.87 mN/m. After that the surface tension value reaches up to 131.03 mN/m with 120 numbers of uranyl ions. It is obvious that the surface tension should be higher in presence of uranyl nitrate compared to the pure water because the uranyl ions are responsible to pull down the liquid surface due to the strong interaction between UO_2^{2+} and medium.

Table 6.9: Surface tension of uranyl nitrate solution in 3M nitric acid medium at various uranyl nitrate concentrations calculated from MD simulations

System	Surface tension (mN/m)	System	Surface tension (mN/m)
5-U	111.87 ± 3.5	70-U	123.50 ± 3.6
10-U	115.99 ± 1.8	85-U	124.65 ± 3.3
25-U	118.08 ± 4.1	100-U	125.71 ± 4.1
50-U	121.04 ± 3.4	120-U	131.03 ± 1.9

In order to check whether uranyl ions are accumulated at the surface, the density profile of various chemical species present in uranyl nitrate in 3M nitric acid along x-direction of the simulation box was estimated and is displayed in the [Figure 6.17](#).

**Figure 6.17:** Plot of density of various chemical species along X-direction.

From the plot, it has been seen that there is a slight accumulation of density at the surface. Again, uranyl ions behave as impurities in the system which creates barrier to the vaporisation

of water molecules to the associated vacuum space created above the aqueous phase and then increases the surface interaction towards the liquid phase. Similar observation was also reported by *Garnt et al*²⁵³ but the values are close to that of the pure water. Again, *Wang et al*²⁵⁴ also have performed MD simulations to calculate surface tensions of NaCl solution which increases with concentration.

The computed surface tensions were found to be increased linearly with concentrations of uranyl nitrate up to certain concentration as shown in **Figure 6.18**. The nonlinearity starts appearing at higher concentration ~ 4.65 mole/liters where a deviation in surface tension is noted from monotonic linear increase. This phenomenon perhaps indicating the super saturation of uranyl nitrate at very high concentration which drives the formation of crystal. It affect the surface tension considerably as both the surface excess enthalpy and entropy contribute to elevate the surface tension as reported by *Wang et al*²⁵⁴. In support to that, the distance between two interacting U atom is also calculated from structural property and it is reduced to approximately 7.25\AA from $9 - 10\text{\AA}$. So, it can be concluded that the simple linear function may not be valid when the concentrations become high. Hence, the present MD simulation studies are able to imitate the increment of surface tension along with the oversaturation phenomena from pure water to the various concentration of uranyl nitrate in 3M nitric acid solution.

In order to support the simulation findings, dynamic light scattering (DLS) experiment was conducted to explore the behaviour of aqueous mixture. The scattering results (shown in **Figure 6.18**) depict that homogeneity of the aqueous mixture is maintained up to 4.0 moles/lit and after that the mixture becomes heterogeneous as the light fails to pass through the solution. It is worthwhile to mention that the nonlinearity in surface tension is appeared at the same location where the nonlinearity in the dynamic light scattering (DLS) intensity (see **Figure 6.18**) was observed.

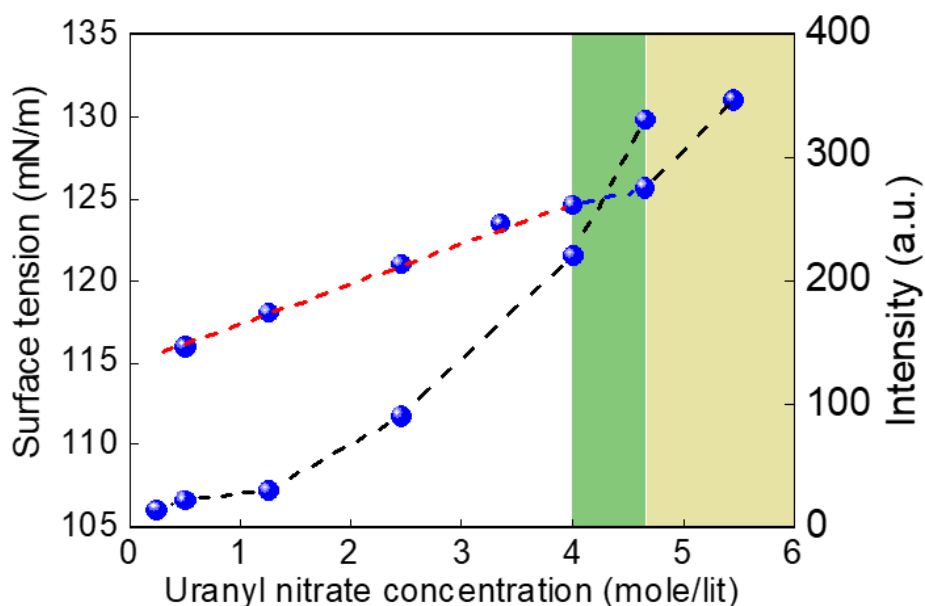


Figure 6.18: Surface tension of uranyl nitrate solution in 3M nitric acid as a function of uranyl nitrate concentration. Experimental intensity of uranyl nitrate solution in 3M nitric acid for a wide range of uranyl nitrate concentration using DLS instrument.

Shear viscosity:

The shear viscosity is very important dynamic property for any aqueous or organic system to develop an understanding of material transfer in biphasic system. Here, the shear viscosity is calculated from non-equilibrium molecular dynamics (NEMD) simulation using periodic perturbation method¹²⁵. An external force is applied to the system which causes a velocity field. The steps of this perturbation method are reported in our previous work¹⁸⁵. The only changes have been done in the magnitude of external force. In previous chapter, the shear viscosity was computed for organic liquids as pure or mixture form where the magnitude of external force was 0.10 nm/ps^2 .¹⁸⁵ The calculated value of shear viscosity for water with this magnitude of external force was quite small. As we know for non-equilibrium MD simulation, the shear viscosity will be low when the shear flow is too high. So, the magnitude of the external force

should not be higher than 0.01 nm/ps^2 in case of aqueous system. An appropriate value of external force was fixed by calculating the shear viscosity for a range of external force which is very much similar to the work of Song and Dai¹⁸⁴. They obtained quantitative value of shear viscosity for both the acceleration amplitude of 0.0025 and 0.005 nm/ps^2 . In our present study, we have used the acceleration amplitude of 0.0025 nm/ps^2 to calculate the shear viscosity.

The shear viscosity of water is calculated before going to the uranyl system. It is very challenging to calculate the accurate shear viscosity of water. Many researchers have computed the shear viscosity for different water models from MD simulation. Here, the shear viscosity obtained from our simulations for SPC/E water model is $0.87 \pm 0.003 \text{ mPa.s}$ which is very much closer to the reported experimental value of 0.854 mPa.s ²⁵⁵ with a deviation of only 1.87%. The shear viscosity reported by Song and Dai from NEMD simulation was $0.722 \pm 0.006 \text{ mPa.s}$ ¹⁸⁴ which underestimates the experimental value by 15%. The other reported values of shear viscosity calculated from MD simulations are 0.63 mPa.s ¹²⁶ and $0.642 \pm 0.008 \text{ mPa.s}$ ²⁵⁶ which also underestimate the experimental value. The similar acceleration amplitude is also applied to calculate the shear viscosity of uranyl nitrate in 3M nitric acid system from NEMD simulation and the values obtained from simulation are reported in Table 6.10.

Table 6.10: Shear viscosity calculated from NEMD simulation for all the systems with the effect of concentrations of uranyl nitrate

System	Shear Viscosity (mPa.s)	System	Shear Viscosity (mPa.s)
5-U	0.940	70-U	1.662
10-U	0.896	85-U	1.971
25-U	1.229	100-U	1.912
50-U	1.498	120-U	2.692

The calculated shear viscosity was seen to be increased with increasing concentration of uranyl nitrate due to higher intermolecular interactions with increasing concentration. The calculated shear viscosity displays a linear relation with the concentrations as shown in [Figure 6.19](#) and a nonlinearity starts appearing at higher concentration similar to that of the surface tension where the monotonic linear behaviour was deviated and a sharp rise in shear viscosity is observed from 100-U to 120-U indicating a possible super saturation phenomena. At the stage of super saturation the shear viscosity becomes very high due to high molecular friction and large hydrodynamic forces.

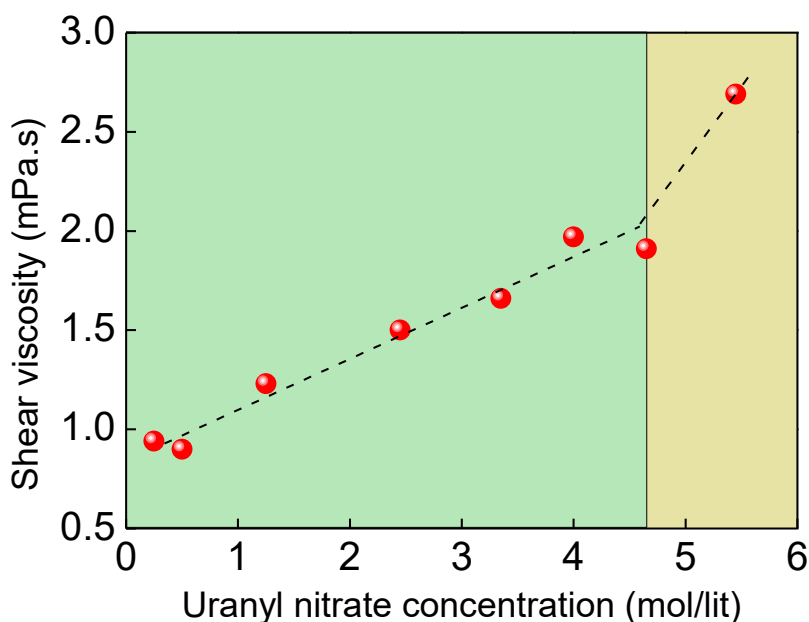


Figure 6.19: Shear viscosity of uranyl nitrate solution in 3M nitric acid calculated from MD simulations illustrating an increasing trend with uranyl nitrate concentration.

6.4.3. Type 3: Uranyl nitrate in varying nitric acid concentrations

In addition to the preceding discussion, the effect of acid concentration or acid molarity on the aqueous feed solution is equally important to develop an understanding of extraction of solutes. Aqueous phase acidity has a key role in liquid –liquid extraction to achieve a better

decontamination factor (DF). Here, the range of acid concentrations have been considered from 1M to 4M as per the actual PUREX process where the feed acidity has been maintained around 3–4M. Hence, the physical and dynamical properties have been calculated to understand the effect of acid concentrations.

The above studies have been performed with 85 numbers of uranyl ions and its associated nitrate ions of 170 numbers. The nitric acid has been used in un-dissociated form and the respective numbers are reported in [Table 6.2](#). Every system is relaxed through energy minimization step followed by equilibration for 10ns simulation length. After that, the production run for next 10 ns simulation length has been carried out followed by 1 ns to determine the physical and dynamical properties. The densities and self-diffusivities for each system have been reported in [Table 6.11](#).

Table 6.11: Average density of uranyl nitrate solution at various acid concentrations and self-diffusivities of various ions present in uranyl nitrate solution as a function of acid concentration have been calculated. 85-U system with un-dissociated form of nitric acid has been used.

System	Density (kg/m ³)	Self-diffusion Coefficient (10 ⁻⁹ m ² /s)			
		UO ₂ ²⁺	NO ₃ ⁻	H ₂ O	HNO ₃
85U-1M	1485.65 ± 0.23	0.611 ± 0.02	1.167 ± 0.09	1.697 ± 0.01	1.087 ± 0.06
85U-2M	1489.55 ± 0.13	0.464 ± 0.02	1.105 ± 0.02	1.622 ± 0.04	1.006 ± 0.03
85U-3M	1491.43 ± 0.21	0.421 ± 0.12	0.984 ± 0.06	1.599 ± 0.08	0.740 ± 0.05
85U-4M	1494.27 ± 0.28	0.395 ± 0.03	0.893 ± 0.05	1.546 ± 0.02	0.628 ± 0.11

The calculated densities were found to be followed an increasing path with acid concentration as expected. The self-diffusivities of uranyl and nitrate ions were found to be decreased with

acid molarity because the un-dissociated nitric acid imposed restriction into the medium which slows down the mobility of UO_2^{2+} and NO_3^- ions. The self-diffusivity of uranyl ion for 85-U in 3M nitric acid system was determined using two different forms of nitric acid. The dissociated form gives the value of $0.333 \pm 0.04 \times 10^{-9} \text{ m}^2/\text{s}$ while the un-dissociated form of acid predicts $0.421 \pm 0.12 \times 10^{-9} \text{ m}^2/\text{s}$. The movement of free ions are faster compared to that when they are in associated form and the mobility of free ions has been interrupted by each other. It may affect the self-diffusivity of ions in the medium. The self-diffusivities of water and nitric acid also have been evaluated and they have followed the similar decreasing trend.

In addition to that, another important dynamic property to understand the extraction process is shear viscosity which has been computed at various acid concentrations. The calculated viscosity values are reported in [Table 6.12](#).

Table 6.12: Shear viscosity and surface tension computed from MD simulations with the effect of nitric acid molarities (associated form of HNO_3)

System	Shear Viscosity (mPa s)	Surface Tension (mN/m)
85U-1M	1.319 ± 0.01	115.31 ± 3.2
85U-2M	1.352 ± 0.01	112.01 ± 3.1
85U-3M	1.706 ± 0.02	116.21 ± 3.1
85U-4M	2.087 ± 0.01	114.99 ± 2.2

The shear viscosity is found to increase with acid concentration but a difference in shear viscosity values has been observed for 85U-3M system containing dissociated and associated form of nitric acid. The external force required to accelerate the free ions will be found to be less as per the present value of external force, indicating more force is required compared to

the associated form of acid and thus shear viscosity value becomes higher compared to that the associated form. Alternatively, the present external force becomes higher for associated form of acid and the shear viscosity value is getting suppressed. So, the magnitude of the external force may be decided as per the form of nitric acid used. Further, there are no added advantages in using either dissociated or associated form of nitric acid and hence, any form can be used for simulation study. The surface tension for all the systems has also been calculated and it was found to be almost unaffected by the nitric acid concentration.

Structural:

The structure and probable orientation of uranyl ions, nitrate ions and un-dissociated nitric acid can be described from PCF. The orientation of water around uranyl ion is evaluated from U – Ow and O – Ow PCFs as seen in [Figure 6.20\(a\)](#) and [Figure 6.20\(b\)](#).

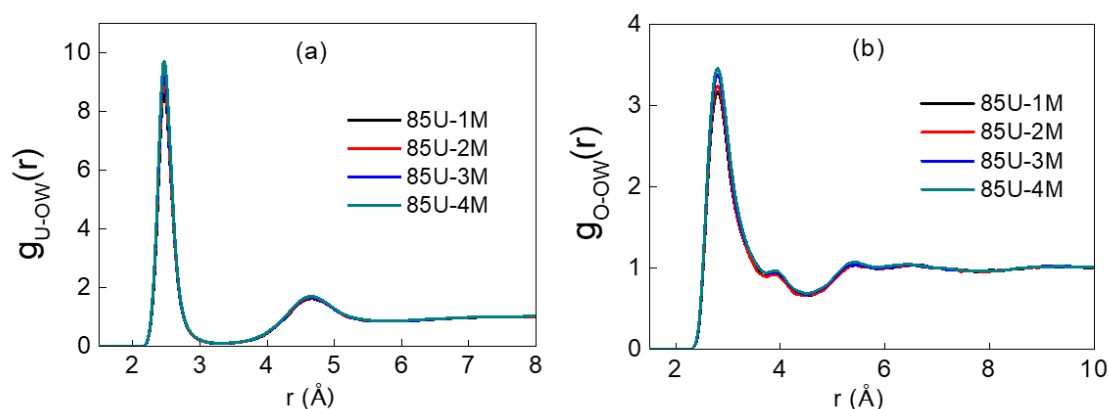


Figure 6.20: Pair correlation function between two interacting (a) U atom and Ow (water oxygen) atom and (b) oxygen atom (O) of uranyl ion and Ow (water oxygen) atom.

The first peaks of U – Ow PCFs are appeared at around 2.45Å which are exactly similar to the results described in preceding section for varying uranyl nitrate concentration. It indicates that the position of water molecules in the first solvation shell of U atom becomes invariable with

the concentration effect of both uranyl nitrate and nitric acid. Thereafter, the first peaks of O – O_w PCFs are located at approximately 2.75 Å which are again quite close to the previous case. The water oxygen is comparatively closer to the U atom as we have already reported earlier. Here, the CNs of U – O_w PCFs are also quite similar like earlier results of the preceding section but the change in CN is negligible as 5.69 - 5.72.

Further, the orientation of nitrate ions around uranyl ion is also discussed by determining the U – O_N and O – O_N PCFs which are shown in **Figure 6.21(a)** and **Figure 6.21(b)**. The first peaks of U – O_N PCFs and O_w – O_N PCFs are located at the same position compared to that of the type-2 system which again confirms that the orientation remains unchanged irrespective of the system conditions. Hence, it can be concluded that the dissociated and associated form of acid have negligible effect on the structural properties.

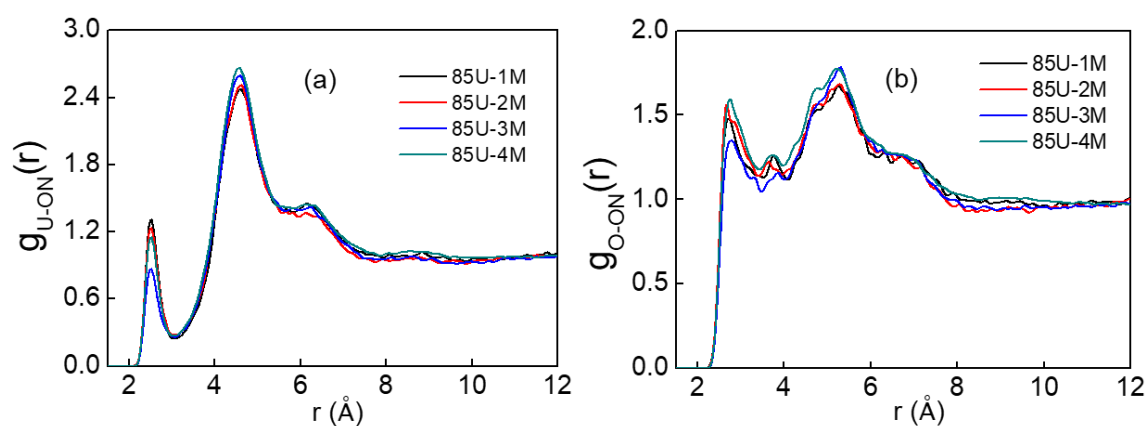


Figure 6.21: Pair correlation function between two interacting atoms (a) U atom and O_N (oxygen atom of NO₃⁻) atom and (b) oxygen atom (O) of uranyl ion and oxygen atom (O_N) of nitrate ion.

Next, the orientation of HNO₃ around uranyl ion has been computed and shown in **Figure 6.22(a)** to **Figure 6.22(d)**. The PCFs between two interacting U atom of UO₂²⁺ and oxygen

atom of HNO_3 are different from other as seen from **Figure 6.22(a)** which displays only one broad peak at around 4.85 to 5.05 Å without passing through any minima. After that, the first peaks of U – N_A PCFs are appeared at approximately 5.25 Å [see **Figure 6.22(b)**] and peak heights are decreased gradually signifies the availability of nitric acids near uranyl ion becomes less at higher concentration of acid. It might be due to change in structural orientation from mono-dentate to bi-dentate which is also reflected in the corresponding CN that varies from 0.83 - 2.26.

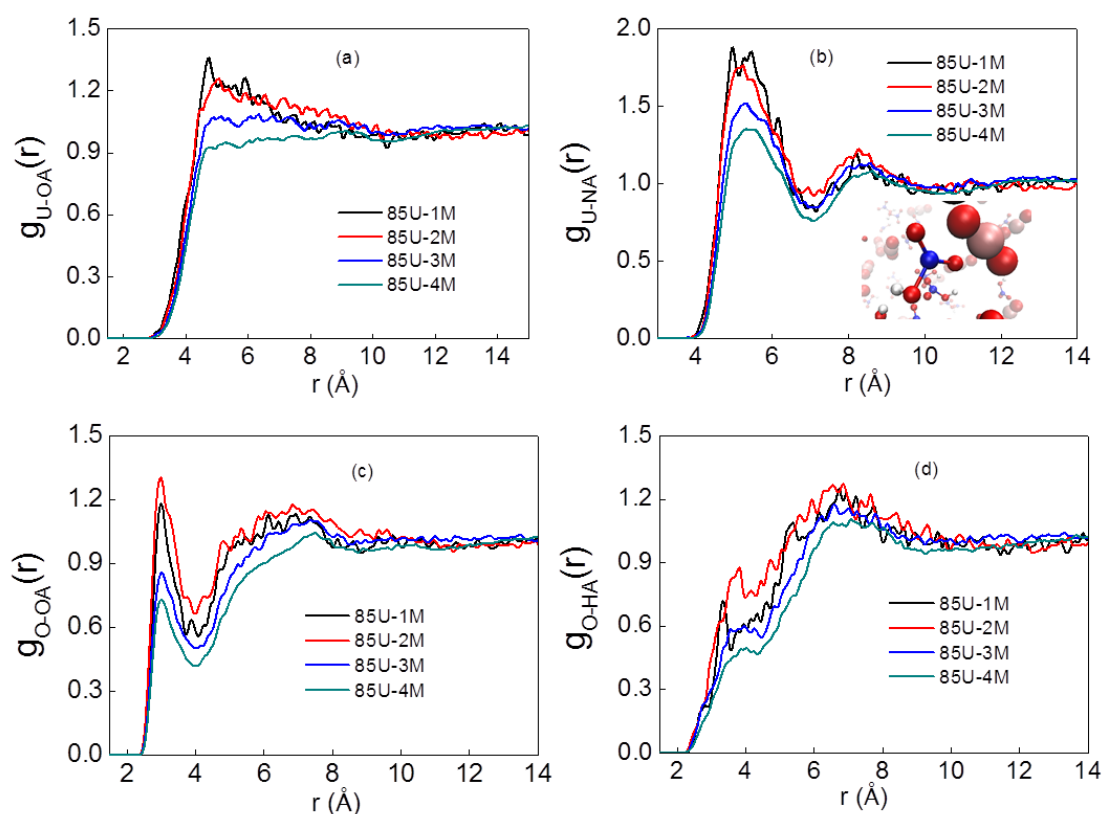


Figure 6.22: Pair correlation function between two interacting (a) U atom and O_A atom (oxygen atom of HNO_3), (b) U atom and nitrogen atom (N_A) of nitric acid, (c) uranyl oxygen (O) atom and oxygen atom (O_N) of nitric acid, (d) uranyl oxygen atom (O) and hydrogen atom (H_A) of HNO_3 . Inset: Snap shot representing the orientation of nitric acid around uranyl ion. Colour code: White-Hydrogen, Red-Oxygen, Pink-Uranium, and Blue-Nitrogen.

The PCFs between two interacting sites of HNO_3 (O_A and H_A) around uranyl oxygen (O) also have been evaluated along with the above two PCFs to get a proper orientation of HNO_3 around uranyl ions [see **Figure 6.22(c)** and **Figure 6.22(d)**]. The first peaks for O – O_A PCFs are located at around 2.95 – 3.05 Å while for O – H_A PCFs at 6.55 – 6.65 Å, indicates that the oxygen atom of HNO_3 is comparatively closer than that of hydrogen atom. Again, the oxygen atom of HNO_3 is relatively closer to that of the nitrogen atom. The proposed orientation is presented in inset of **Figure 6.22(b)**.

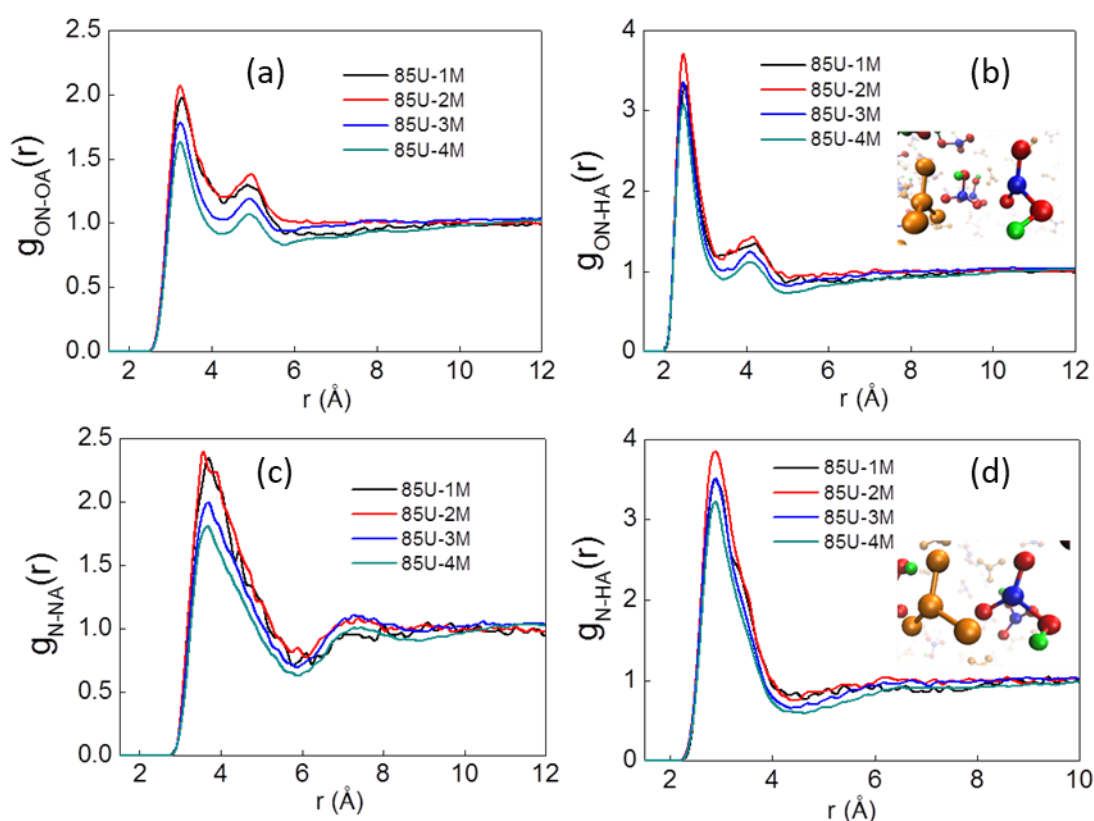


Figure 6.23: Pair correlation function between two interacting (a) oxygen atom (ON) of nitrate ion and oxygen atom (OA) of HNO_3 (b) ON atom of nitrate ion and hydrogen atom (HA) of HNO_3 , (c) nitrogen atoms of nitrate ion and HNO_3 , (d) nitrogen atom (N) of nitrate ion and hydrogen atom (HA) of HNO_3 . Inset: Snap shot representing the orientation of nitrate ion around nitric acid. Colour code: Green-Hydrogen, Blue-Nitrogen, Red-Oxygen and Golden yellow-Nitrate ion.

In addition to that the orientation of nitric acid (N_A , H_A and O_A atoms) around nitrate ions (N and O_N atoms) or vice versa can be produced from the [Figure 6.23\(a\)](#) to [Figure 6.23\(d\)](#). The first peaks of $O_N - O_A$ PCFs are located at around 3.25\AA whereas 2.45\AA for $O_N - H_A$ PCFs [see [Figure 6.23\(a\)](#) and [Figure 6.23\(b\)](#)], indicating the hydrogen atom of nitric acid is comparatively closer to the oxygen atom of nitrate ion. The CNs for $O_N - O_A$ PCFs are increasing from 0.56 to 1.59 and for $O_N - H_A$ from 0.11 to 0.41. After that the first peaks of $N - N_A$ are appeared at a location approximately 3.65\AA while for $N - H_A$ PCFs the peaks are located before 0.8\AA from $N - N_A$ PCFs. So, the nitrogen atom of nitric acid is away from the nitrogen atom of nitrate ion than the hydrogen atom. The CNs are increasing for both the $N - N_A$ and $N - H_A$ PCFs and varies from 0.51–1.55 and 0.27–0.82 respectively.

Potential of mean force (PMF):

The free energy (ΔG_R) related to the release of one water molecule from the solvation shell, has been calculated from the first minimum of the PMF. The PMF has been generated from the PCF using the following relation¹²⁵

$$PMF = -K_B T \ln g(r) \quad (6.2)$$

Where, $g(r)$ denotes PCF. The free energy of release, ΔG_R , which indicates the interaction between ions and water molecules, is equivalent to PMF,

The PMF calculated at the peak of PCF provides the minimum free energy for a system. Therefore the free energy required to release one water molecule or one nitrate ion from the solvation shell of U atom, can be used to explain the competition in the first solvation shell. In addition, it can be also describes the effect of concentration of uranyl nitrate and acid on the competition.

The free energies related to nitrate ions and water molecules are determined using the computing PCF to study the effect of uranyl nitrate and nitric acid concentrations as seen in **Figure 6.24**. If we compare the free energies between water molecules and nitrate ions for both the systems, it has been found that more energy is required to release a water molecule than that of nitrate ion from the solvation shell. It can be explained from the structural properties. The distance between U and O_w atoms is 2.45\AA whereas the O_N atom is around 2.55\AA away from the U atom. For 5-U and 10-U systems the distance is about 4.65\AA having very low free energy. No significant structural differences have been noted for both the systems and thus the free energy values are seen to be very close.

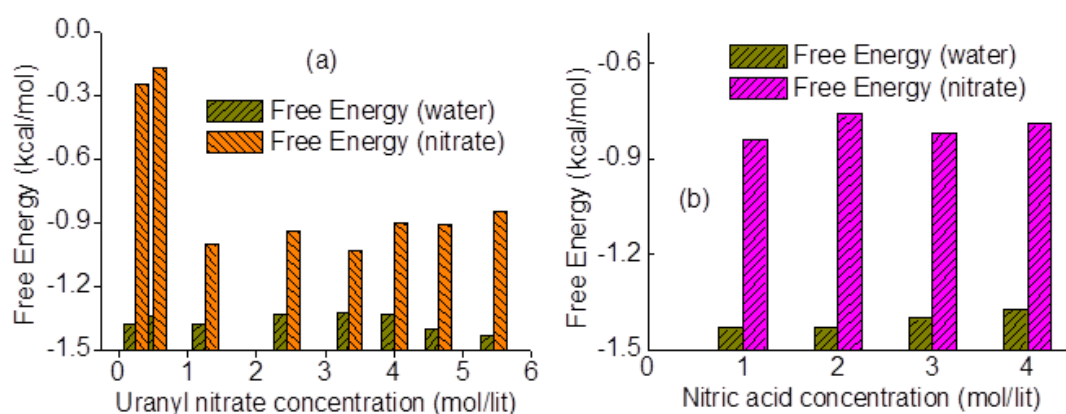


Figure 6.24: Average free energy of uranyl nitrate in 3M nitric acid system as a function of (a) uranyl nitrate concentration and (b) nitric acid concentration

Test of Stoke – Einstein relation in aqueous mixture:

The self-diffusivity (D) of uranyl nitrate was found to be decreased whereas shear viscosity (η) was found to be increased with increasing concentration i.e. D and η are inversely related. Therefore it is worthwhile to investigate the behaviour of the product ($D\eta$) of these two dynamic properties by the well-known Stokes-Einstein (S-E) relation [see [equation 4.3](#)].

The radius of uranyl ion has been computed from volume obtained using COSMOtherm package¹⁰⁹. Therefore, it is worthwhile to check whether the S-E relation is valid or not in this aqueous mixture. In Chapter 4, we had checked the S-E relation for TiAP/dodecane mixture and found the breakdown of S-E relation¹⁸⁵ as the system does not follow either slipping or sticking boundary condition. The S-E relation was found to work well for a new value of $C=2.5$. In a similar fashion, the validity of S-E relation was checked for a varying concentration of uranyl nitrate. The product of self-diffusivity and shear viscosity is plotted against density of the systems and is depicted in **Figure 6.25**.

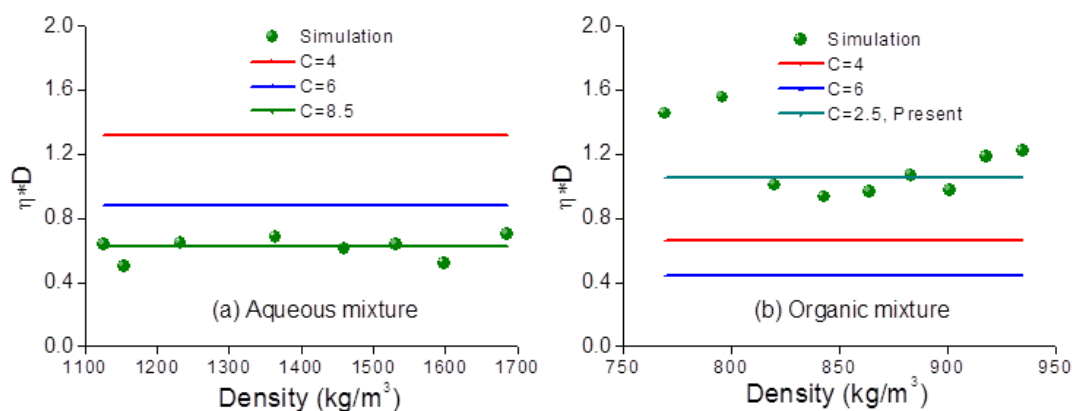


Figure 6.25: Plot of product of diffusivity and shear viscosity ($D\eta$) of (a) aqueous phase containing uranyl nitrate in 3M nitric acid and (b) organic phase containing TiAP in dodecane as a function of calculated density.

Here also, the breakdown of S-E relation was observed as expected because the equation 4.3 does not contain any concentration/density dependent parameter. Thereafter, the value of numerical factor has been computed for aqueous mixture and the value was found to be 8.5 far from the sticking boundary condition. It is quite interesting to mention that the numerical factor for organic mixture was appeared at far slipping region whereas for aqueous mixture the factor appears at far sticking region. It signifies that the TiAP experienced lesser interaction while moving through the dodecane compared to that of uranyl ion moving through 3M nitric acid.

Higher interaction in aqueous medium leads to a higher numerical factor than far sticking boundary condition.²⁵⁷

6.6. SUMMARY

The MD simulations have been carried out for three types of systems. One type is to establish the effect of force field on the structural and dynamical properties using single uranyl ion in water system. The density, self-diffusivity, H-bond dynamics and structural properties calculated for all the models are found to have negligible dependency on the force field whereas the free energy of hydration has shown quite strong effect for the force field as well as the partial charges. Hence it can be concluded that the partial charges do not have significant effect on force field based on the calculated structural and dynamical properties except the free energy of hydration and the GW-model performed well. So, the studies have been extended for second type of systems where a wide range of uranyl nitrate concentration in 3M nitric acid medium have been considered to imitate the feed solution used in PUREX process. The structural and dynamical properties have been calculated to establish the effect of concentration on properties. The bulk density was found to be increased with concentrations and also in excellent agreement with the measured experimental density which ensures the accuracy of the adopted GW type of force field. The self-diffusivities of various ions present in the solution followed the decreasing trend. The self-diffusivity of water is also affected because the uranyl nitrate concentration is responsible for reduction in water shielding around uranyl ion. Further, the activation energy for diffusion calculated from Arrhenius plot shows the higher activation energy for uranyl ion is required compared to that of water molecules which is in accordance with the self-diffusivity values. The structural properties are also affected by the effect of concentration. The CN of water and nitrate ions with respect to U atom was inversely related and both compete to acquire the position in the solvation shell. The nitrate binding mode with uranyl ion was also transformed from bi-dentate to mono-dentate at higher acid concentrations.

The calculated surface tension and shear viscosity were seen to be increased with uranyl nitrate concentrations. At higher concentration of about 4.0 moles/lit, super-saturation effect has been captured by inflection in the surface tension as well as in the shear viscosity due to the solution heterogeneity which was also validated by inflection in the scattering intensity observed by performing dynamic light scattering (DLS) experiment. The surface tension of salt solution was higher than that of the pure water. Acid molarities do not have any significant effect on the structural properties. Again, the uranyl nitrate concentrations and the nitric acid concentrations have negligible effect on the PMF. Finally, the popular S–E relation was found to breakdown in the aqueous mixture like organic mixture.

Chapter 7

Conclusions & Future Work



CHAPTER SEVEN

Conclusions & Future Work

7.1 CONCLUSIONS

DFT derived partial charges on atoms were generated using population analysis methods of Mulliken, Löwdin, NPA and ChelpG and subsequently embedded in OPLS-AA force field to determine the mass density, pair correlation function, free energy of solvation, partition coefficients, diffusion coefficients and dipole moment using MD simulations in order to calibrate the suitable OPLS-AA force field for the tri-alkyl ligands and n-alkane liquids. From overall density analysis for all the ligands and diluent using four different charge models, it can be stated that the OPLS-AA force field using Mulliken charge might be the most suitable force field for determination of density which is within 0.13-1.41% of the experimental results. Further, the different partial charge on the phosphoryl group significantly affect the PCFs of liquid TBP, TiAP and TEP as envisaged from the peak height of PCFs.

Though the predicted density with Mulliken charge is reasonable, the diffusion constant of TBP with Mulliken charge is found to be 4 times smaller than that of experimental value

which suggests that re-parameterization of OPLS-AA force field might be necessary to produce the accurate diffusivity data as estimated by experiments. Overall, from the analysis of diffusivity it is seen that the diffusivity follows the inverse relation with molecular mass i.e.: TEP>TBP>TiAP. The calculated value of $\Delta G_{\text{Hydration}}$ for using Mulliken partial charge is very close to the experimental value indicating that the Mulliken charge model might be useful for estimating the thermodynamic properties. In addition, the calculated partition coefficient of the ligands using MD simulations in water-dodecane system follows the order: TiAP> TBP>TEP which is further corroborated by QESC. Furthermore, the calculated results of partition coefficient are found to be in qualitative agreement with the experimental results. From overall analysis of dipole moment for different charge model, it can be confirmed that the Mulliken charge included OPLS-AA force field might be the suitable choice for the simulations of the present molecular system.

Further, the higher free energy of extraction for TiAP over TBP indicates higher distribution constant of UO_2^{2+} ion with TiAP ($D_{\text{U(VI)}}=29.8$) over TBP ($D_{\text{U(VI)}}=24.5$) and hence TiAP might be used as substitute of TBP in nuclear fuel cycle. Finally, after examining the thermo physical and dynamical properties of the pure liquids employing different Quantum partial charge, Mulliken charge embedded calibrated OPLS-AA force field is perhaps the most reliable one so far as it does not incorporate any arbitrary scaling in the force field or L-J parameters and thus can be used confidently to estimate the liquid state properties of alkyl phosphates and n-alkanes.

The structure, dynamics and thermodynamics of binary mixture of TiAP and dodecane have been determined and reported using the recently developed OPLS-AA potential by performing equilibrium and non-equilibrium MD simulations. The optimized OPLS potential embedding Mulliken partial charge was found to be quite successful in predicting the thermo physical and dynamical properties of pure liquids and mixtures.

The calculated electric dipole moment of TiAP was seen to be mildly altered with TiAP concentration in the dodecane in comparison to pure TiAP. The calculated liquid densities of TiAP-dodecane mixture were shown to be in excellent agreement with the experimental data over the entire range of the mole fraction. The mixture densities at different temperature are also studied which was found to be reduced with temperature as expected. The diffusivities of both TiAP and dodecane were computed and it was established that within the range of 25-30% TiAP in dodecane is perhaps the optimum composition to be used for conducting the solvent extraction experiment. Further, the excess volume of mixing for the TiAP/dodecane mixture was found to be positive over the entire range of mole fraction. In addition, the excess enthalpy of mixing was shown to be endothermic for TBP/dodecane mixture as observed experimentally and similar trend was also predicted for the TiAP/dodecane mixture. The characteristics of spatial pair correlation functions (PCFs) for TiAP–dodecane mixture was also captured over the entire range of the mole fraction. Furthermore, the calculated shear viscosity was in excellent agreement with the experimental values for both pure and mixture. Finally, this study indicates that 20–30% composition of TiAP/dodecane binary mixture is an effective composition for extraction. The newly calibrated OPLS force field was found to be working well even in the mixture and its predictability of experimental results for a wide range of temperature and mole fraction confirms the ability of the new OPLS force field. Further, the present MD simulations results demonstrate that SE relation breaks down at the molecular level.

The excellent matching of the computed results with the experimental results can be further extended to model the water-dodecane biphasic system which finally will be used for the extraction of uranyl ion as practiced in the PUREX process. Work in this direction is in progress in our computational laboratory.

In the present study, MD simulations have been performed for the aqueous-organic biphasic system using a newly developed force field to test its applicability in two phase consisting of four chemical species. The calculated structural and dynamical properties of pure water and water–dodecane like biphasic system using MD simulations are in excellent agreement with the reported experimental values which establishes the validation of Mulliken embedded force field. Again, the study was extended to determine the interfacial properties with the effect of mole fraction of third component (here TiAP) and the acidity of aqueous phase for aqueous-organic biphasic system. It was found that the packing of TiAP as well as the interface thickness is an increasing function of mole fraction of TiAP but after 50% mole fraction there is no significant effect of it. The interfacial tension is a decreasing function of mole fraction of TiAP and the computed values are shown to be in excellent agreement with the reported experimental results. Interfacial tension was found to be maximum in the absence of TiAP molecules and then it decreases gradually indicating TiAP acts as a surface active agent. The system with higher mole fraction of TiAP induces the TiAP molecules to accumulate at the interface and large numbers of water molecules are in contact with them resulting to a large interfacial roughness which facilitates the breaking of hydrogen bonds between water molecules and of making hydrogen bond between phosphoryl group of TiAP and water molecules. Thus, the interaction between water molecules is reduced in the presence of TiAP. The breakage of hydrogen bond among water molecules reduces the surface tension of water and it may help to increase the miscibility of water and organic phases. At higher TiAP concentration, the packing of TiAP at the interface is increased which accelerates the hydration of TiAP thus leads to more reduction of interfacial tension. Further, TiAP-H₂O complex was optimized at the B3LYP/TZVP level of theory using Grimme's dispersion correction. The O---H bond length (1.81Å) in TiAP-H₂O complex (O of P=O and H of water molecule) was found to be quite smaller than that of O---H bond length (2.16Å) in

water dimer which indicates that the TiAP-H₂O interaction is stronger than that of H₂O-H₂O interaction as reflected in the interaction energy for TiAP-H₂O interaction (-10.74kcal/mol) and H₂O-H₂O interaction (-4.63kcal/mol). The O---H bond length in TiAP-H₂O complex (O of P=O and H of water molecule) from MD simulation was found to be 1.55Å whereas O---H bond length in water was found to be 1.95Å, thus compliments the results of QM calculation about H-bond.

The interfacial tension is an increasing function of aqueous phase acidity. In addition to that the interface thickness has been calculated using a model equation and a simple scheme has been suggested for the determination of bulk correlation length. Finally, the interface thickness is correlated with interfacial tension, molecular diameter and bulk correlation length as per the newly proposed scheme. It is worth mentioning that the computed value of the intrinsic thickness is always greater than that of capillary thickness.

Additionally, the stability of the dimer of TiAP with different orientation was established by computing the dimerization energy using DFT. The interaction energy for dimer with orientation of O=P-P=O, P=O-P=O and P=O-O=P was found to be -12.98 kcal/mol, -14.97 kcal/mol and -10.81 kcal/mol respectively indicating that dimer with orientation of P=O-P=O is the most stable which was also captured in the MD simulations. Further, the present MD data shows that the water extraction is enhanced at higher mole fraction of TiAP because of wider interface thickness at higher composition of TiAP which induced the water transport to the organic phase. Again, the calculated values reveal that the water extractability is decreased with increasing aqueous phase acidity as the interface thickness is reduced at higher acidity. Therefore, the interface thickness plays an important role in mass transfer and it may control the transfer processes by choosing the appropriate composition of biphasic mixture.

We anticipate that the present results will assist to illuminate a few dazzling issues on the structure of water-oil interfaces, in particular, the role of interfacial thickness in the kinetics of self-assembly of hydrophobic materials and biomolecules in contact with acidic water. The present MD studies will thus further invite the experimental verification of the calculated results of interfacial tension and interface thickness at a wide variation of composition of third component and acidity. Additionally, it will be worthwhile and challenging to test this force field for ion transfer across the interface. Work in this direction is in progress in our computational molecular engineering laboratory.

MD simulations were conducted to establish the effect of force field on the structural and dynamical properties of uranyl ion-water system. The density, self-diffusivity, H-bond dynamics and structural properties are found to have negligible dependency on the force field whereas the free energy of hydration was found to depend strongly on the force field and partial charges. The GW-model was found to perform well for free energy of hydration and can be considered for systems with wide range of uranyl nitrate concentration in 3M nitric acid medium.

The calculated density using MD simulations was found to be in excellent agreement with the measured experimental density which ensures the accuracy of the adopted GW type of force field. The self-diffusivities of various ions present in the solution followed the decreasing trend. The self-diffusivity of water was also affected because the uranyl nitrate concentration is responsible for reduction in water shielding around uranyl ion. Further, the activation energy for uranyl ion is higher compared to that of nitrate ion which is in accordance with the self-diffusivity values. The CN of water and nitrate ions with respect to U atom was inversely related and both compete to acquire the position in the solvation shell. The nitrate binding mode with uranyl ion was also found to be transformed from bi-dentate to mono-dentate at higher concentrations.

The calculated surface tension and shear viscosity were seen to be increased with uranyl nitrate concentrations. At higher concentration of about 4.0 moles/lit, super-saturation effect has been captured by inflection in the surface tension as well as in the shear viscosity due to the solution heterogeneity which was also validated by inflection in the scattering intensity observed by DLS experiment. The surface tension of salt solution was higher than that of the pure water. Acid molarities do not have any significant effect on the structural properties. Finally, the popular S–E relation was found to breakdown in the aqueous mixture like organic mixture.

The heart of conclusions is that the OPLS – AA force field calibrated with Mulliken atomic partial charges is capable to capture and explain all the thermophysical, dynamical and thermodynamical properties of pure liquids, binary mixtures and biphasic mixtures successfully. So, our main objective of the thesis is the versatility of a single refined force field in the field of radionuclide – ligand – solvent systems pertaining to the fuel reprocessing is achieved. In addition to that TiAP is established as a potential alternative ligand of TBP which can be applied in thermal reactor as well as fast reactor fuel reprocessing. Favourable interfacial properties for metal ion transfer have been suggested and the characteristics of uranyl nitrate along with the limiting concentration of uranyl nitrate in feed solution have been established which useful informations are for fuel reprocessing. Next, the present work can be extended in the direction of extraction of heavy metals with the suggested composition of ligand – solvent system, multicomponent system to understand the co-extraction process, recovery of FP from the waste stream in near future.

7.2 FUTURE WORK

The present ligand – solvent system can be applied to study the reprocessing of spent nuclear fuel. The TiAP can be used as a replacement of widely used TBP in this field. The 20% to 30% composition is suitable for extraction of heavy metal from spent nuclear fuel obtained

from thermal reactor as well as fast reactor. Limited experiments can be done with this composition to validate the simulations results. In addition to that it can be applied to the multicomponent system to understand the co – extraction process. Further, similar extraction system can be tested for recovery of fission product (FP) from the waste steam.

This study can be extended to find out suitable ligand like N,N,N',N'-Tetraoctyl diglycolamide (TODGA), N,N,N',N' Tetra (2 Ethylhexyl) Diglycolamide (TEHDGA), Di-(2-ethylhexyl)phosphoric acid (D2EHPA), Trioctylphosphine oxide (TOPO) or N, N-Di(2-ethyl- hexyl) hexanamide (DOHA) using the similar methodology which is also used for metal extraction. Again, this technique can also be used to study the alternate solvent like ionic liquids in place of dodecane.

REFERENCES:

1. Banerjee, S.; Gupta, H. P., The evolution of the Indian nuclear power programme. *Progress in Nuclear Energy*. **2017**, 101, 4-18.
2. Spent Fuel Reprocessing Options. *IAEA, VIENNA, AUSTRIA 2008, IAEA-TECDOC-1857, ISBN 978-92-0-103808-1..*
3. Vijayan, P. K.; Shivakumar, V.; Basu, S.; Sinha, R., Role of thorium in the Indian nuclear power programme. *Progress in Nuclear Energy* **2017**, 101, 43-52.
4. Nuclear Fuel Cycle Information System. *IAEA, VIENNA, AUSTRIA 2009, IAEA-TECDOC-1613, ISBN 978-92-0-102109-0.*
5. Zabunoglu, O. H., Reprocessing of long-cooled nuclear fuel: Process description and plant design. *Retrospective Theses and Dissertations* **1988**, Digital Repository @ Iowa State University, <http://lib.dr.iastate.edu>.
6. Lo, C. T.; Baird, M. H. I.; Hanson, C., *Handbook of Solvent Extraction*, New York : Wiley, ©1983.
7. Simpson, M. F.; Law, J. D., *Nuclear Fuel Reprocessing*, Idaho National Laboratory, February, **2010**.
8. Paiva, A. P.; Malik, P., Recent advances on the chemistry of solvent extraction applied to the reprocessing of spent nuclear fuels and radioactive wastes. *J. Radioanal. Nucl. Chem.* **2004**, 261, 485 - 496.
9. McKay, H. A. C.; Miles, J. H.; Swanson, The Purex Process. *In Science and Technology of Tributyl Phosphate, Vol III, Applications of Tributyl Phosphate in Nuclear Fuel Reprocessing*; J. L.; Schulz, W. W.; Burger, L. L.; Navratil, J. D.; Bender, K. P., Eds.; CRC Press: Boca Raton, FL 1990; p 8 - 37.

10. Arm, S. T.; Bush, R. P.; McGurk, J. C., Concept for the Reduction of Waste Volumes from Nuclear Fuel Reprocessing. *Prog. Nucl. Energy* **1998**, 32, 389-396.
11. Piotr Mazgaj, P. D., Transmutation: reducing the storage time of spent fuel. *Journal of Power Technologies* **2014**, 94, 27 - 34.
12. Suresh, A.; Srinivasan, T. G.; Rao, P. R. V., The Effect of the Structure of Trialkyl Phosphates on Their Physicochemical Properties and Extraction Behavior. *Solvent Extr. Ion Exch.* **2009**, 27, 258-294.
13. Sawant, R. M.; Rastogi, R. K.; Chaudhuri, N. K., Study on the Extraction of U(IV) Relevant to PUREX Process. *J. Radioanal. Nucl. Chem.* **1998**, 229, 203-206.
14. Spent Nuclear Fuel Reprocessing Flow sheet. **June 2012**, NEA/NSC/WPFC/DOC (2012) 15, Organisation for Economic Co-operation and Development, NEA.
15. Schulz, W. W.; Navratil, J. D.; Bess, T. E., Eds. *Science and Technology of Tributyl Phosphate*; CRC Press: Boca Raton, FL, 1984; Vol. 1, 1984.
16. Wright, A.; Paviet-Hartmann, P., Review of Physical and Chemical Properties of Tributyl Phosphate/Diluent/Nitric Acid Systems. *Sep. Sci. Technol.* **2010**, 45, 1753-1762.
17. Tian, Q.; Liu, H., Densities and Viscosities of Binary Mixtures of TributylPhosphate with Hexane and Dodecane from (298.15 to 328.15) K. *J. Chem. Eng. Data* **2007**, 52, 892-897.
18. Chiarizia, R.; Jensen, M. P.; Borkowski, M.; Ferraro, J. R.; Thiyagarajan, P.; Littrell, K. C., Third Phase Formation Revisited: The U(VI), HNO₃-TBP, n-Dodecane System. *Solvent Extr. Ion Exch.* **2003**, 21, 1 - 27.
19. Rao, P. R. V.; Kolarik, Z., A review of third phase formation in extraction of actinides by neutral organophosphorus extractants. *Solvent Extr. Ion Exch.* **1996**, 14, 955 - 993.

20. Chie Miyake, C.; Hirose, M.; Yoshimura, T.; Ikeda, M.; Imoto, S.; Sano, M., “The Third Phase” of Extraction Processes in Fuel Reprocessing, (I). *J. Nucl. Sci. Technol.* **1990**, *27*, 157 - 166.
21. Hassan, S. H.; Shukla, J. P., Tri-iso-amyl phosphate (TAP): An Alternative Extractant to Tri-butyl Phosphate (TBP) for Reactor Fuel Reprocessing. *J. Radioanal. Nucl. Chem.* **2003**, *258*, 563-573.
22. Sreenivasulu, B.; Suresh, A.; Rajeswari, S.; Ramanathan, N.; Antony, M. P.; Sivaraman, N.; Joseph, M., Physicochemical properties and radiolytic degradation studies on tri-iso-amyl phosphate (TiAP). *Radiochim. Acta* **2017**, *105*, 249–261.
23. Suresh, A.; Sreenivasulu, B.; Jayalakshmi, S.; Subramaniam, S.; Sabharwal, K. N.; Sivaraman, N.; Nagarajan, K.; Srinivasan, T. G.; Vasudeva Rao, P. R., Mixer-settler runs for the evaluation of tri-iso-amyl phosphate (TiAP) as an alternate extractant to tri-n-butyl phosphate (TBP) for reprocessing applications. *Radiochim. Acta* **2015**, *103*, 101–108.
24. Singh, M. L.; Tripathi, S. C.; Lokhande, M.; Gandhi, P. M.; Gaikar, V. G., Density, Viscosity, and Interfacial Tension of Binary Mixture of Tri-iso-amyl Phosphate (TiAP) and n-Dodecane: Effect of Compositions and Gamma Absorbed Doses. *J. Chem. Eng. Data* **2014**, *59*, 1130-1139.
25. Kong, F.; Liao, J.; Ding, S.; Yang, Y.; Huang, H.; Yang, J.; Tang, J.; Liu, N., Extraction and Thermodynamic Behaviour of U (VI) and Th (IV) From Nitric Acid Solution With Tri-isoamyl Phosphate. *J. Radioanal. Nucl. Chem.* **2013**, *298*, 651-656.
26. Rakesh, K. B.; Suresh, A.; Rao, P. R. V., Extraction and Stripping Behaviour of Tri-iso-amyl Phosphate and Tri-n-butyl Phosphate in n-Dodecane With U (VI) In Nitric Acid Media. *Radiochim. Acta* **2014**, *102*, 619-628.

-
27. Das, D.; Juvekar, V. A.; Roy, S. B.; Bhattacharya, R., Co-Extraction of U(VI) and HNO₃ Using TBP and its Higher Homologues TiAP and TEHP: Comparison of Equilibria, Kinetics, and Rate of Extraction. *Separation Science and Technology* **2015**, 50, 411 - 420.
28. Singh, D. K.; Garg, S. K.; Bharadwaj, R. K., Removal of Cr (VI) using tri-isoamyl phosphate. *Indian Journal of Chemical Technology* **2000** 7, 205 – 206.
29. Das, B.; Kumar, S.; Mondal, P.; Mudali, U. K.; Natarajan, R., Synthesis and characterization of red-oil from tri iso-amyl phosphate/n-dodecane/nitric acid mixtures at elevated temperature. *J Radioanal Nucl. Chem.* **2012**, 292, 1161-1171.
30. Suresh, A.; Brahmmananda Rao, C. V. S.; Srinivasulu, B.; Sreenivasan, N. L.; Subramaniam, S.; Sabharwal, K. N.; Sivaraman, N.; Srinivasan, T. G.; Natarajan, R.; Vasudeva Rao, P. R., Development of alternate extractants for separation of actinides. *Energy Procedia* **2013**, 39, 120 – 126.
31. Pal, K. K.; Mishra, S.; Mallika, C.; Mudali, U. K., Evolution in the physiochemical properties of alternate PUREX solvent on hydrolytic and chemical treatment. *Separation Science and Technology* **2017**, 52, 2715 - 2720.
32. Allen, M. P.; Tildesley, D. J., *Computer Simulation of Liquids*. Clarendon Press, Oxford, **1987**.
33. Ye, X.; Cui, S.; de Almeida, V. F.; Khomami, B., Interfacial Complex Formation in Uranyl Extraction by Tributyl Phosphate in Dodecane Diluent: A Molecular Dynamics Study. *J. Phys. Chem. B* **2009**, 113, 9852-9862.
34. Sahu, P.; Ali, S. M.; Shenoy, K. T., The Passage of TBP-Uranyl Complexes From Aqueous-Organic Interface To The Organic Phase: Insights From Molecular Dynamics Simulation. *Phys. Chem. Chem. Phys.* **2016**, 18, 23769-23784.

-
35. Ye, X.; Cui, S.; de Almeida, V. F.; Hay, B. P.; Khomami, B., Uranyl Nitrate Complex Extraction into TBP/Dodecane Organic Solutions: A Molecular Dynamics Study. *Phys. Chem. Chem. Phys.* **2010**, 12, 15406-15409.
36. Baaden, M.; Burgard, M.; Wipff, G., TBP at the Water–Oil Interface: The Effect of TBP Concentration and Water Acidity Investigated by Molecular Dynamics Simulations. *J. Phys. Chem. B* **2001**, 105, 11131-11141.
37. Jayasinghe, M.; Beck, T. L., Molecular Dynamics Simulations of the Structure and Thermodynamics of Carrier-Assisted Uranyl Ion Extraction. *J. Phys. Chem. B* **2009**, 113, 11662-11671.
38. Ye, X. G.; Smith, R. B.; Cui, S. T.; de Almeida, V. F.; Khomami, B., Influence of Nitric Acid on Uranyl Nitrate Association in Aqueous Solutions: A Molecular Dynamics Simulation Study. *Solvent Extr. Ion Exch.* **2010**, 28, 1-18.
39. Wang, J.; Cieplak, P.; Kollman, P. A., How Well Does a Restrained Electrostatic Potential (RESP) Model Perform in Calculating Conformational Energies of Organic and Biological Molecules? *J. Comput. Chem.* **2000**, 21, 1049-1074.
40. Jorgensen, W. L.; Maxwell, D. S.; Tirado-Rives, J., Development and Testing of the OPLS All-Atom Force Field on Conformational Energetics and Properties of Organic Liquids. *J. Am. Chem. Soc.* **1996**, 118, 11225 - 11236.
41. M. J. S. Dewar W. Thiel, Ground states of molecules. 38. The MNDO method. Approximations and parameters. *J. Am. Chem. Soc.* **1977**, 99, 4899 – 4907.
42. Bayly, C. I.; Cieplak, P.; Cornell, W. D.; Kollman, P. A., A well-behaved electrostatic potential based method using charge restraints for deriving atomic charges: the RESP model. *J. Phys. Chem.* **1993**, 97, 10269 – 10280.

-
43. Cui, S.; de Almeida, V. F.; Hay, B. P.; Ye, X.; Khomami, B., Molecular Dynamics Simulation of Tri-n-Butyl-Phosphate Liquid: A Force Field Comparative Study. *J. Phys. Chem. B* **2012**, 116, 305-313.
44. Benay, G.; Wipff, G., Liquid–Liquid Extraction of Uranyl by TBP: The TBP and Ions Models and Related Interfacial Features Revisited by MD and PMF Simulations. *J. Phys. Chem. B* **2014**, 118, 3133-3149.
45. Cui, S.; de Almeida, V. F.; Khomami, B., Molecular Dynamics Simulations of Tri-n-butyl-phosphate/n-Dodecane Mixture: Thermophysical Properties and Molecular Structure. *J. Phys. Chem. B* **2014**, 118, 10750 - 10760.
46. Mu, J.; Motokawa, R.; Williams, C. D.; Akutsu, K.; Nishitsuji, S.; Masters, A., Comparative Molecular Dynamics Study on Tri-n-butyl phosphate in Organic and Aqueous Environments and its Relevance to Nuclear Extraction Processes. *J. Phys. Chem. B* **2016**, 120, 5183 - 5193.
47. Siu, S. W. L.; Pluhackova, K.; Bockmann, R. A., Optimization of the OPLS-AA force field for long hydrocarbons. *J. Chem. Theory Comput.* **2012**, 8, 1459 - 1470.
48. Haughney, M.; Ferrarolo, M.; McDonald, I. R., Molecular-Dynamics Simulation of Liquid Methanol. *J. Phys. Chem.* **1987**, 91, 4934 - 4940.
49. Jamali, S. H.; Ramdin, M.; Becker, T. M.; Rinwa, S. K.; Buijs, W.; Vlugt, T. J. H., Thermodynamic and Transport Properties of Crown-Ethers: Force Field Development and Molecular Simulations. **2017**, 121, 8367 – 8376.
50. Tsuzuki, S.; Shinoda, W.; Saito, H.; Mikami, M.; Tokuda, H.; Watanabe, M., Molecular Dynamics Simulations of Ionic Liquids: Cation and Anion Dependence of Self-Diffusion Coefficients of Ions. *J. Phys. Chem. B* **2009**, 113, 10641 – 10649.

-
51. Nagaoka, M.; Okuno, Y.; Yamabe, T., Chemical Reaction Molecular Dynamics Simulation and the Energy-Transfer Mechanism in the Proton-Transfer Reaction of Formamidine in Aqueous Solution. *J. Phys. Chem.* **1994**, 98, 12506 – 12515.
52. Karplus, M.; Peetsko, G. A., Molecular dynamics simulations in biology. *Nature* **1990**, 347, 631 – 639.
53. Nakata, H.; Kannan, K.; Nasu, T.; Cho, H.; Sinclair, E.; Takemurai, A., Perfluorinated contaminants in sediments and aquatic organisms collected from shallow water and tidal flat areas of the Ariake Sea, Japan: environmental fate of perfluorooctane sulfonate in aquatic ecosystems. *Environ Sci. Technol.* **2006**, 40, 4916 - 4921.
54. Palmer, J. C.; Debenedetti, P. G., Recent advances in molecular simulation: A chemical engineering perspective. *AIChE*, **2015**, 61, 370 - 383.
55. Elliott, J. A., Novel Approaches to Multiscale Modelling in Materials Science. *Int. Mater. Rev.* **2011**, 56, 207-225.
56. Sorenson, J. M.; Hura, G.; Glaeser, R. M.; Head-Gordon, T., What can x-ray scattering tell us about the radial distribution functions of water? . *J. Chem. Phys.* **2000**, 113, 9149-9161.
57. Soper, A. K., The radial distribution functions of water and ice from 220 to 673 K and at pressures up to 400 MPa. *Chem. Phys.* **2000**, 258, 121-137.
58. Odelius, M., Information content in O[1s] K-edge X-ray emission spectroscopy of liquid water. *J. Phys. Chem. A* **2009**, 113, 8176-8181.
59. Wilson, K.R.; Tobin, J. G.; Ankudinov, A. L.; Rehr, J. J.; Saykally, R. J., Extended x-ray absorption fine structure from hydrogen atoms in water. *J. Phys. Rev. Lett.* **2000**, 85, 4289-4292.

-
60. Bosio, L.; Teixeira, J.; Stanley, H. E., Enhanced Density Fluctuations in Supercooled H₂O, D₂O, and Ethanol-Water Solutions: Evidence from Small-Angle X-Ray Scattering. *Phys. Rev. Lett.* **1981**, 46, 597-600.
61. Sturchio, N. C.; Chiarello, R. P.; Cheng, L.; Lyman, P. F.; Bedzyk, M. J.; Qian, Y.; You, H.; Yee, D.; Geissbuhler, P.; Sorensen, L. B., Lead adsorption at the calcite-water interface. *Geochimica et Cosmochimica Acta* **1997**, 61, 251-263.
62. Bosio, L.; Teixeira, J.; Bellissent-Funel, M. C., Enhanced density fluctuations in water analyzed by neutron scattering. *Phys. Rev. A* **1989**, 39, 6612 - 6613.
63. Metropolis, N.; Ulam, S., The Monte Carlo Method. *Journal of the American Statistical Association* **1949**, 44, 335 - 341.
64. Lindahl, E.; Hess, B.; van der Spoel, D., GROMACS 3.0: A package for molecular simulation and trajectory analysis. *J. Mol. Model.* **2001**, 7, 306 - 317.
65. Pronk, S.; Pall, S.; Schulz, R.; Larsson, P.; Bjelkmar, P.; Apostolov, R.; Shirts, M. R.; Smith, J. C.; Kasson, P. M.; van der Spoel, D.; Hess, B.; Lindahl, E., GROMACS 4.5: A High-throughput and Highly Parallel Open Source Molecular Simulation Toolkit. *Bioinformatics* **2013**, 29, 845 - 854.
66. van der Spoel, D.; Lindahl, E.; Hess, B.; Groenhof, G.; Mark, A. E.; Berendsen, H. J. C., GROMACS: Fast, Flexible, and Free. *J. Comput. Chem.* **2005**, 26, 1701 - 1718.
67. Abraham, M.; Hess, B.; van der Spoel, D.; Lindahl, E., *User Manual Version 5.0.7*. The GROMACS development teams at the Royal Institute of Technology and Uppsala University, Sweden, 2015.
68. Cornell, W. D.; Cieplak, P.; Bayly, C. I.; Gould, I. R.; Merz, K. M.; Ferguson, D. M.; Spellmeyer, D. C.; Fox, T.; Caldwell, J. W.; Kollman, P. A., A 2nd Generation Force – Field

for the Simulation of Proteins, Nucleic-Acids and Organic Molecules. *J. Am. Chem. Soc.* **1995**, 117, 5179 - 5197.

69. Ahlrichs, R.; Bar, M.; Haser, M.; Horn, H.; Kolmel, C., Electronic Structure Calculations on Workstation Computers: The Program System Turbomole. *Chem. Phys. Lett.* **1989**, 162, 165 - 169.

70. Becke, A. D., Density-Functional Exchange-Energy Approximation with Correct Asymptotic Behavior. *Phys. Rev. A* **1988**, 38, 3098 - 3100.

71. Perdew, J. P., Density functional approximation for the correlation energy of the inhomogeneous electron gas. *Phys. Rev. B* **1986**, 33, 8822 - 8824.

72. *TURBOMOLE V6.6.*, a development of University of Karlsruhe and Forschungszentrum Karlsruhe GmbH, 1989–2007, TURBOMOLE GmbH, since 2007.

73. Schmidt, M. W.; Baldridge, K. K.; Boatz, J. A.; Elbert, S. T.; Gordon, M. S.; Jensen, J. H.; Koseki, S.; Matsunaga, N.; Nguyen, K. A.; Su, S.; Windus, T. L.; Dupuis, M.; Montgomery, J. A., General Atomic and Molecular Electronic Structure System. *J. Comput. Chem.* **1993**, 14, 1347-1363.

74. Mark, J.; Abraham, M. J.; Gready, J. E., Optimization of Parameters for Molecular Dynamics Simulation using Smooth Particle-Mesh Ewald in GROMACS 4.5. *J. Comput. Chem.* **2011**, 32, 2031 - 2040.

75. Luty, B. A.; Davis, M. E.; Tironi, I. G.; van Gunsteren, W. F., A Comparison of Particle-Particle, Particle-Mesh and Ewald Methods for Calculating Electrostatic Interactions in Periodic Molecular Systems. *J. Mol. Simulation* **1994**, 14, 11 - 20.

76. Toukmaji, A. Y.; Board, J. A., Ewald Summation Techniques in Perspective: A Survey Computer Physics Communications. *Comput. Phys. Commun.* **1996**, 95, 73 - 92.

-
77. Verlet, L., Computer "Experiments" on Classical Fluids. I. Thermodynamical Properties of Lennard-Jones Molecules. *Phys. Rev.* **1967**, 159, 98-103.
78. Hockney, R. W., The potential calculation and some applications. *Meth. Comput. Phys.* **1970**, 9, 136–211.
79. Hess, B.; Bekker, H.; Berendsen, H. J. C.; Fraaije, J. G. E. M., LINCS: A Linear Constraint Solver for Molecular Simulations. *J. Comp. Chem.* **1997**, 18, 1463–1472.
80. Berendsen, H. J. C.; Postma, J. P. M.; van Gunsteren, W. F.; DiNola, A.; Haak, J. R., Molecular dynamics with coupling to an external bath. *J. Chem. Phys.* **1984**, 81, 3684 - 3690.
81. Bussi, G.; Donadio, D.; Parrinello, M., Canonical sampling through velocity rescaling. *J. Chem. Phys.* **2007**, 126, 014101-(1-8).
82. Nose, S., A molecular dynamics method for simulations in the canonical ensemble. *Mol. Phys.* **1984**, 52, 255 – 268.
83. Parrinello, M.; Rahman, A., Polymorphic transitions in single crystals: A new molecular dynamics method. *J. Appl. Phys.* **1981**, 52, 7182-7190.
84. McQuarrie, D. A., Statistical Mechanics, New York : Harper & Row, **1975**.
85. Hansen, J. P.; McDonald, I. R., Theory of Simple Liquids, 2nd ed. (Academic Press, London). **1986**.
86. Chandler, D., Introduction to Modern Statistical Mechanics. *Oxford University Press*, New York, **1987**.
87. Jensen, F., *Introduction to Computational Chemistry*. John Wiley & Sons, England, **1999**.
88. Mulliken, R. S., Electronic Population Analysis on LCAO-MO Molecular Wave Functions. I. *J. Chem. Phys.* **1955**, 23, 1833 - 1840.

-
89. Mulliken, R. S., Criteria for the Construction of Good Self-Consistent-Field Molecular Orbital Wave Functions, and the Significance of LCAO-MO Population Analysis. *J. Chem. Phys.* **1962**, 36, 3428 - 3439.
90. Löwdin, P. O., On the Non-Orthogonality Problem Connected with the Use of Atomic Wave Functions in the Theory of Molecules and Crystals. *J. Chem. Phys.* **1950**, 18, 365-375.
91. Löwdin, P. O., On the Nonorthogonality Problem. *Adv. Quantum Chem.* **1970**, 5, 185-199.
92. Reed, A. E.; Weinstock, R. B.; Weinhold, F., Natural Population Analysis. *J. Chem. Phys.* **1985**, 83, 735 - 746.
93. Martin, F.; Zipse, H., Charge Distribution in the Water Molecule—A Comparison of Methods. *J. Comput. Chem.* **2005**, 26, 97 - 105.
94. Das, A.; Sahu, P.; Ali, S. M., Molecular Dynamics Simulation for the Calibration of the OPLS Force Field Using DFT Derived Partial Charges for the Screening of Alkyl Phosphate Ligands by Studying Structure, Dynamics, and Thermodynamics. *J. Chem. Eng. Data* **2017**, 62, 2280 - 2295.
95. Frenkel, D.; Smit, B., *Understanding Molecular Simulation: From Algorithms to Applications*. **2002** 2nd ed. Academic Press, San Diego.
96. Yarnell, J.; Katz, M.; Wenzel, R.; Koenig, S., Structure factor and radial distribution function for liquid argon at 85 °K. *Phys. Rev. A* **1973**, 7, 2130 - 2144.
97. Trzesniak, D.; Kunz, A. E.; van Gunsteren, W. F., A comparison of methods to compute the potential of mean force. *Chem. Phys. Chem.* **2007**, 8, 162 – 169.
98. Peskir, G., On the Diffusion Coefficient: The Einstein Relation and Beyond. *Stoch. Models* **2003**, 19, 383 - 405.

99. Urban, J. J.; Damewood, J. J. R., Accurate free energy perturbation calculation of the hydration free energies of Fe^{3+} and Fe^{2+} . *J. Chem. Soc., Chem. Commun.* **1990**, 1636 - 1638.
100. Lu, N.; Kofke, D. A., Accuracy of free-energy perturbation calculations in molecular simulation. I. Modeling *J. Chem. Phys.* **2001**, 114, 7303 - 7311.
101. Straatsma, T. P.; Berendsen, H. J. C., Free Energy of Ionic Hydration: Analysis of a Thermodynamic Integration Technique to Evaluate Free energy Differences by Molecular Dynamics Simulations. *J. Chem. Phys.* **1988**, 89, 5876 - 5886.
102. Straatsma, T. P.; McCammon, J. A., Multiconfiguration thermodynamic integration. *The J. Chem. Phys.* **1991**, 95, 1175 - 1188.
103. Straatsma, T. P.; Berendsen, H. J. C.; Postma, J. P. M., Free energy of hydrophobic hydration: A molecular dynamics study of noble gases in water. *The Journal of Chemical Physics* **1986**, 85, 6720 - 6727.
104. Comer, J.; Gumbart, J. C.; Hénin, J.; Lelièvre, T.; Pohorille, A.; Chipot, C., The Adaptive Biasing Force Method: Everything You Always Wanted To Know but Were Afraid To Ask. *J. Phys. Chem. B* **2015** 119, 1129-1151.
105. Darve, E.; Rodríguez-Gómez, D.; Pohorille, A., Adaptive biasing force method for scalar and vector free energy calculations. *THE JOURNAL OF CHEMICAL PHYSICS* **2008**, 128, 144120 (1-13).
106. Kästner, J.; Senn, H. M.; Thiel, S.; Otte, N.; Thiel, W., QM/MM Free-Energy Perturbation Compared to Thermodynamic Integration and Umbrella Sampling: Application to an Enzymatic Reaction. *Journal of Chemical Theory and Computation* **2006**, 2, 452-461.
107. Shirts, M. R.; Pande, V. S., Comparison of Efficiency and Bias of Free Energies Computer by exponential Averaging, the Bennett Acceptance Ratio, and Thermodynamic Integration. *J. Chem. Phys.* **2005**, 122, 144107 (1 - 16).

108. Michel, J.; Orsi, M.; Essex, J. W., Prediction of Partition Coefficients by Multiscale Hybrid Atomic-Level/Coarse-Grain Simulations. *J. Phys. Chem. B* **2008**, 112, 657 - 660.
109. Eckert, F.; Klamt, A., *COSMOtherm, version C2.1*. Release 01.08; COSMOlogic GmbH & Co, KG: Leverkusen, Germany, **2008**.
110. Boda, A.; Ali, S. M.; Shenoi, M. R. K., Partition Coefficients of Macrocyclic Crown Ethers in Water–Organic Biphasic System: DFT/COSMO-RS approach. *Fluid Phase Equilib.* **2010**, 288, 111 - 120.
111. Klamt, A.; Eckert, F., COSMO-RS: A Novel and Efficient Method for the a Priori Prediction of Thermophysical Data of Liquids. *Fluid Phase Equilib.* **2000**, 172, 43.
112. Eckert, F.; Klamt, A., Fast Solvent Screening via Quantum Chemistry: COSMO-RS Approach. *AIChE J.* **2002**, 48, 369 - 385.
113. Ali, S. M.; Joshi, J. M.; Singha Deb, A. K.; Boda, A.; Shenoy, K. T.; Ghosh, S. K., Dual Mode of Extraction for Cs⁺ and Na⁺ Ions with Dicyclohexano-18-Crown-6 and Bis(2-Propyloxy)Calix[4]Crown-6 in Ionic Liquids: Density Functional Theoretical Investigation. *RSC Adv.* **2014**, 4, 22911 - 22925.
114. Ali, S. M., Design and Screening of Suitable Ligand/Diluents Systems for Removal of Sr²⁺ Ion From Nuclear Waste: Density Functional Theoretical Modelling. *Comput. Theor. Chem.* **2014**, 1034, 38 - 52.
115. Ali, S. M., Thermodynamical Criteria of the Higher Selectivity of Zirconium Oxycations over Hafnium Oxycations Towards Organophosphorus Ligands: Density Functional Theoretical Investigation. *Eur. J. Inorg. Chem.* **2014**, 2014, 1533 - 1545.
116. Boda, A.; Ali, S. M., Density Functional Theoretical Investigation of Remarkably High Selectivity of the Cs⁺ Ion Over the Na⁺ Ion Toward Macrocyclic Hybrid Calix-Bis-Crown Ether. *J. Phys. Chem. A* **2012**, 116, 8615 - 8623.

-
117. Pahan, S.; Boda, A.; Ali, S. M., Density Functional Theoretical Analysis of Structure, Bonding, Interaction and Thermodynamic Selectivity of Hexavalent Uranium (UO₂²⁺) and Tetravalent Plutonium (Pu⁴⁺) Ion Complexes of Tetramethyl Diglycolamide (TMDGA). *Theor. Chem. Acc.* **2015**, 134, 41, 1 - 16.
118. Ali, S. M.; Pahan, S.; Bhattacharyya, A.; Mohapatra, P. K., Complexation Thermodynamics of Diglycolamide with f-elements: Solvent Extraction and Density Functional Theory Analysis. *Phys. Chem. Chem. Phys.* **2016**, 18, 9816 - 9828.
119. Cao, X.; Dolg, M., Segmented Contraction Scheme for Small-core Actinide Pseudopotential Basis Sets. *J. Mol. Struct.: THEOCHEM* **2004**, 673, 203 - 209.
120. Petkovic, D. M.; Kezele, B. A.; Rajic, D. R., Dipole moments of some neutral organic phosphates. *J. Phys. Chem.* **1973**, 77, 922 - 924.
121. Estok, G. K.; Wendlandt, W. W., Electric Moments of Some Alkyl Phosphates and Thiophosphates. *J. Am. Chem. Soc.* **1955**, 77, 4767 - 4769.
122. Chiakwelu, O., A theory of transverse current correlations in liquid argon. *Molecular Physics* **1979**, 37, 1941 - 1948.
123. Vogelsang, R.; Hoheisel, C., Computation and analysis of the transverse current autocorrelation function, $C_t(k,t)$, for small wave vectors: A molecular-dynamics study for a Lennard-Jones fluid. *Physical Review A* **1987**, 35, 1786-1794.
124. Palmer, B. J., Transverse-current autocorrelation-function calculations of the shear viscosity for molecular liquids. *Phys. Rev. E* **1994**, 49, 359 – 366.
125. Hess, B., Determining the shear viscosity of model liquids from molecular dynamics simulations. *J. Chem. Phys.* **2002**, 116, 209 - 217.

-
126. Sunda, A. P.; Venkatnathan, A., Parametric dependence on shear viscosity of SPC/E water equilibrium and non-equilibrium molecular dynamics simulations. *Mol. Simul.* **2013**, *39*, 728 - 733.
127. van Buuren, A. R.; Marrink, S.; Berendsen, H. J. C., A molecular dynamics study of Decane/Water Interface. *J. Phys. Chem.* **1993**, *97*, 9206 – 9212.
128. Wen, B.; Sun, C.; Bai, B.; Gatapova, E. Y.; Kabov, O. A., Ionic hydration – induced evaluation of decane – water interfacial tension. *Phys. Chem. Chem. Phys.* **2017**, *19*, 14606 – 14614.
129. Biswas, R.; Ghosh, P.; Banerjee, T.; Ali, S. M.; Shenoy, K. T., Extractive insights in the cesium ion partitioning with bis (2-propyloxy)calyx [4]crown-6 and dicyclohexano-18-crown-6 in ionic liquid – water biphasic systems. *J. Mol. Liq.* **2017**, *241*, 279 – 291.
130. Langevin, D., Capillary-wave techniques for the measurement of surface tension and surface viscoelasticity. *Colloids Surf.* **1990**, *43*, 121 – 131.
131. Tarazona, P.; Checa, R.; Chacón, E., Critical Analysis of the Density Functional Theory Prediction of Enhanced Capillary Waves. *Phys. Rev. Lett.* **2007**, *99*, 196101 (1 - 4).
132. Chacón, E.; Tarazona, P., Intrinsic profiles beyond the capillary wave theory: A Monte Carlo study. *Phys. Rev. Lett.* **2003**, *91*, 166103 (1 - 4).
133. Buff, F.; Lovett, R.; Stillinger, F., Interfacial Density Profile for Fluids in the Critical Region. *Phys. Rev. Lett.* **1965**, *15*, 621 – 623.
134. Rowlinson, J.; Widom, B., *Molecular Theory of Capillarity*; Clarendon Press: Oxford. **1982**.
135. Yuet, P. K.; Blankschtein, D., Molecular Dynamics Simulation Study of Water Surfaces: Comparison of Flexible Water Models. *J. Phys. Chem. B* **2010**, *114*, 13786 - 13795.

136. Starr, F. W.; Nielsen, J. K.; Stanley, H. E., Fast and Slow Dynamics of Hydrogen Bonds in Liquid Water. *Phy. Rev. Lett.* **1999**, 82, 2294 - 2297.
137. Starr, F. W.; Nielsen, J. K.; Stanley, H. E., Hydrogen-bond dynamics for the extended simple point-charge model of water. *Phy. Rev. E* **2000**, 62, 579 - 587.
138. Rapaport, D. C., Hydrogen bonds in water Network organization and lifetimes. *Mol. Phys.* **1983**, 50, 1151 - 1162.
139. Voloshin, V. P.; Naberukhin, Y. I., Hydrogen bond lifetime distributions in computer-simulated water. *J. Structural Chem.* **2009**, 50, 78 - 89.
140. Antipova, M. L.; Petrenko, V. E., Hydrogen Bond Lifetime for Water in Classic and Quantum Molecular Dynamics. *Russian J. Phys. Chem. A* **2013**, 87, 1170 - 1174.
141. Gasparotto, P.; Hassanali, A. A.; Ceriotti, M., Probing defects and correlations in the hydrogen-bond network of ab initio water *J. Chem. Theory Comput.* **2016**, 12, 1953–1964
142. Giberti, F.; Hassanali, A. A., The excess proton at the air-water interface: The role of instantaneous liquid interfaces. *J. Chem. Phys.* **2017**, 146, 244703 (1 - 11).
143. Ansari, N.; Dandekar, R.; Caravati, S.; Sosso, G. C.; Hassanali, A. A., High and low density patches in simulated liquid water *J. Chem. Phys.* **2018**, 149, 204507.
144. Chau, P. L.; Hardwick, A. J., A new order parameter for tetrahedral configurations. *Molecular Physics* **1998**, 93, 511- 518.
145. Errington, J. R. D., P. G. , Relationship Between Structural Order and the Anomalies of Liquid Water. *Nature* **2001**, 409, 318–321.
146. Caleman, C.; van Maaren, P. J.; Hong, M.; Hub, J. S.; Costa, L. T.; van der Spoel, D., Force Field Benchmark of Organic Liquids: Density, Enthalpy of Vaporization, Heat

Capacities, Surface Tension, Isothermal Compressibility, Volumetric Expansion Coefficient, and Dielectric Constant. *J. Chem. Theory Comput.* **2012**, 8, 61 - 74.

147. Johnson, W. F.; Dillon, R. L., Physical Properties of Tributylphosphate-Diluent; Report HW-29086. Hanford Atomic Products Operation Richland, Washington, **1953**.

148. Tsimering, L.; Kertes, A. S., Excess Enthalpies of Tri-nbutylphosphate+ Hydrocarbons. *J. Chem. Thermodyn.* **1974**, 6, 411 - 415.

149. Vo, Q. N.; Dang, L. X.; Nilsson, M.; Nguyen, H. D., Quantifying dimer and trimer formation by tri-n-butyl phosphates in n-dodecane: Molecular dynamics simulations. *J. Phys. Chem. B* **2016**, 120, 6985 - 6994.

150. Abraham, M. H.; Whiting, G. S.; Fuchs, R.; Chambers, E. J., Thermodynamics of Solute Transfer from Water to Hexadecane. *J. Chem. Soc., Perkin Trans. 2* **1990**, 291 - 300.

151. Apostoluk, W.; Robak, W., Analysis of Liquid-Liquid Distribution Constants of Organophosphorus Based Extractants. *Anal. Chim. Acta* **2005**, 548, 116 - 133.

152. Panneerselvam, K.; Antony, M. P.; Srinivasan, T. G.; Vasudeva Rao, P. R., Measurement of enthalpies of vaporization of trialkyl phosphates using correlation gas chromatography. *Thermochim. Acta* **2007**, 466, 49 - 56.

153. Riddick, J. A.; Bunger, W. B.; Sakano, T. K., *Organic solvents. Physical properties and methods of purifications Techniques of Chemistry*. 1986; Vol. 2.

154. Klamt, A.; Schuurmann, G., COSMO: A New Approach to Dielectric Screening in Solvents with Explicit Expressions for the Screening Energy and its Gradient. *J. Chem. Soc., Perkin Trans. 2* **1993**, 2, 799 - 805.

155. Klamt, A., Conductor-like Screening Model for Real Solvents: A New Approach to the Quantitative Calculation of Solvation Phenomena. *J. Phys. Chem.* **1995**, 99, 2224 - 2235.

156. Leay, L.; Tucker, K.; Regno, A. D.; Schroeder, S. L. M.; Sharrad, C. A.; Masters, A. J., The behaviour of tributyl phosphate in an organic diluent. *Mol. Phys.* **2014**, 112, 2203 - 2214.
157. Allen, W.; Rowley, R. L., Predicting the viscosity of alkanes using nonequilibrium molecular dynamics: Evaluation of intermolecular potential models. *J. Chem. Phys.* **1997**, 106, 10273 - 10281.
158. Patil, P. P.; Patil, S. R.; Borse, A. U.; Hundiwale, D. G., Density, excess molar volume and apparent molar volume of binary liquid mixtures. *RASAYAN J. Chem.* **2011**, 4, 599 - 604.
159. Park, S. J.; Gmehling, J., Excess molar volumes at the 308.15 K for constituent binaries of n-decane, n-dodecane, 1-decanol and 1-dodecanol. *Korean J. Chem. Eng.* **1995**, 12, 152 - 155.
160. Tsimering, L.; Kertes, A. S., Enthalpies of mixing of tributyl phosphate with hydrogen bonding solvents. *J. Chem. Eng. Data* **1977**, 22, 163 - 165.
161. Einstein, A., Zur Theorie der Brownschen Bewegung. *Ann. Phys.* **1906**, 324, 371 - 381.
162. Einstein, A., Eine neue Bestimmung der Moleküldimensionen. *Ann. Phys.* **1906**, 324, 289 - 306.
163. Einstein, A., Berichtigung zu meiner Arbeit: "Eine neue Bestimmung der Moleküldimensionen". *Ann. Phys.* **1911**, 339, 591 - 592.
164. Walser, R.; Mark, A. E.; van Gunsteren, W. F., On the validity of Stokes' law at the molecular level. *Chem. Phys. Lett.* **1999**, 303, 583 - 586.
165. Ohtori, N.; Ishii, Y., Explicit expressions of self-diffusion coefficient, shear viscosity, and the Stokes-Einstein relation for binary mixtures of Lennard-Jones liquids. *J. Chem. Phys.* **2015**, 143, 164514 (1 - 7).

166. Banerjee, P.; Yashonath, S.; Bagchi, B., Rotation driven translational diffusion of polyatomic ions in water: A novel mechanism for breakdown of Stokes-Einstein relation. *J. Chem. Phys.* **2017**, 146, 164502 (1 - 11).
167. Chen, B.; Sigmund, E. E.; Halperin, W. P., Stokes-Einstein relation in super cooled aqueous solutions of glycerol. *Phys. Rev. Lett.* **2006**, 96, 145502 (1 - 4).
168. Girault, H. H. J. S., D. J., Electrochemistry of liquid—liquid interfaces. *In: A.J. Bard (Ed.): Electroanalytical Chemistry* **1989**, 15, 1–141.
169. Scott, R. P. W., Liquid Chromatography Column Theory. *Wiley: New York* **1992**.
170. Spiro, M., Interfacial Kinetics in Solution *Faraday Discuss. Chem. Soc.* **1984**, 77, 275-286
171. McUmbur, A. C.; Larson, N. R.; Randolph, T. W.; Schwartz, D. K., Molecular trajectories provide signatures of protein clustering and crowding at the oil/water interface. *Langmuir* **2015**, 31, 5882–5890.
172. He, L.; Lin, F.; Li, X.; Sui, H.; Xu, Z., Interfacial sciences in unconventional petroleum production: from fundamentals to applications *Chem. Soc. Rev.* **2015**, 44, 5446–5494.
173. Jorge, M.; Cordeiro, M. N. D. S., Intrinsic Structure and Dynamics of the Water/Nitrobenzene Interface. *J. Phys. Chem. C* **2007**, 111, 17612 – 17626.
174. Carpenter, I. L.; Hehre, W. J., A molecular dynamics study of the hexane/water interface. *J. Phys. Chem.* **1990**, 94, 531 – 536.
175. Meyer, M.; Mareschal, M.; Hayoun, M., Computer modeling of a liquid–liquid interface. *J. Chem. Phys.* **1988**, 89, 1067 – 1073.
176. Benjamin, I., Molecular structure and dynamics at liquid–liquid interfaces *Annu. Rev. Phys. Chem.* **1997**, 48, 407 – 451.

177. Fernandes, P. A.; Cordeiro, M. N. D. S.; Gomes, J. A. N. F., Molecular dynamics simulation of the water/2-heptanone liquid–liquid interface. *J. Phys. Chem. B* **1999**, 103, 6290 - 6299.
178. Benjamin, I., Theoretical study of the water/1,2-dichloroethane interface: structure, dynamics and conformational equilibrium at the liquid–liquid interface. *J. Chem. Phys.* **1992**, 97, 1432 – 1445.
179. Sahu, P.; Ali, S. M.; Shenoy, K. T., TBP assisted uranyl extraction in water-dodecane biphasic system: Insights from molecular dynamics simulation. *Chemical Prod. Process Modell.* **2017**.
180. Wang, H.; Carlson, E.; Henderson, D.; Rowley, R., Molecular dynamics simulation of the liquid – liquid interface for immiscible and partially miscible mixture. *Molecular Simulation* **2003**, 29, 777 – 785.
181. Mitrinovic, D. M.; Tikhonov, A. M.; Li, M.; Huang, Z.; Schlossman, M. L., Noncapillary-wave structure at the water-alkane interface. *Phys. Rev. Lett.* **2000**, 85, 582-585.
182. Bowers, J.; Zarbakhsh, A.; Webster, J. R. P.; Hutcandhings, L.; Richards, R. W., Neutron Reflectivity Studies at Liquid–Liquid Interfaces: Methodology and Analysis. *Langmuir* **2001**, 17, 140-145.
183. Senapati, S.; Berkowitz, M. L., Computer simulation of the interface width of the liquid/liquid interface. *Phys. Rev. Lett.* **2001**, 87, 176101-1-4.
184. Song, Y.; Dai, L. L., The shear viscosities of common water models by non-equilibrium molecular dynamics simulations. *Mol. Simul.* **2010**, 36, 560 - 567.
185. Das, A.; Ali, S. M., Molecular dynamics simulation for the test of calibrated OPLS-AA force field for binary liquid mixture of tri-iso-amyl phosphate and n-dodecane. *J. Chem. Phys.* **2018**, 148, 074502 (1 - 14).

186. Berendsen, H. J. C.; Postma, J. P. M.; van Gunsteren, W. F.; Hermans, J., Interaction models for water in relation to protein hydration. In: Pullman, B., Ed., *Intermolecular Forces*, D. Reidel Publishing Company, Dordrecht, **1981**, 331 - 342.
187. Mark, P.; Nilsson, L., Structure and Dynamics of the TIP3P, SPC, and SPC/E Water Models at 298 K. *J. Phys. Chem. A* **2001**, 105, 9954-9960.
188. Mills, R., Self-diffusion in Normal and Heavy Water in the Range 1-45o. *The Journal of Physical Chemistry* **1973**, 77, 685 – 688.
189. Wang, J. H., Self-Diffusion and Structure of Liquid Water. I. Measurement of Self-Diffusion of Liquid Water with Deuterium as Tracer *J. Am. Chem. Soc.* **1951**, 73, 510 – 513.
190. Shamay, E. S.; Buch, V.; Parrinello, M.; Richmond, G. L., At the Water's Edge: Nitric Acid as a Weak Acid. *J. Am. Chem. Soc.* **2007**, 129, 12910-12911.
191. Freitas, A. A.; Quina, F. H.; Carroll, F. A., Estimation of Water-Organic Interfacial Tensions. A Linear Free Energy Relationship Analysis of Interfacial Adhesion. *J. Phys. Chem. B* **1997**, 101, 7488 – 7493.
192. Demond, A. H.; Lindner, A. S., Estimation of Interfacial Tension between Organic Liquids and Water. *Environ. Sci. Technol.* **1993**, 27, 2318 – 2331.
193. Ye, X.; Cui, S. T.; Almeida, V. F.; Khomami, B., Molecular Simulation of Water Extraction into a Tri-n-Butyl-Phosphate/n-Dodecane Solution. *J. Phys. Chem. B* **2013**, 117, 14835–14841.
194. Zhang, J.; Dong, Z.; Zhang, Y.; Wang, M.; Yan, Y., Effects of methane content on water-oil interface: insights from molecular level. *Energy & Fuels* **2017**, 31, 7026 – 7036

-
195. Grimme, S.; Antony, J.; Ehrlich, S.; Krieg, H., A consistent and accurate ab initio parametrization of density functional dispersion correction (DFT-D) for the 94 elements H-Pu. *J. Chem. Phys.* **2010**, 132, 154104 (1 - 19).
196. Fukunishi, Y.; Tateishi, T.; Suzuki, M., Octane/water interfacial tension calculation by molecular dynamics simulation *J. Coll. Int. Sci.* **1996**, 180, 188 – 192.
197. Bresme, F.; Chacon, E.; Tarazona, P.; Tay, K., Intrinsic Structure of Hydrophobic Surfaces: The Oil-Water Interface. *Phys. Rev. Lett.* **2008**, 101, 056102 (1 - 4).
198. Zhang, Y.; Feller, S. E.; Brooks, B. R.; Pastor, R. W., Computer simulation of liquid/liquid interfaces. I. Theory and application to octane/water. *J. Chem. Phys.* **1995**, 103, 10252 – 10266.
199. Cordeiro, M. N. D. S., Interfacial Tension Behaviour of Water/Hydrocarbon Liquid–Liquid Interfaces: A Molecular Dynamics Simulation. *Mol. Simu.* **2003**, 29, 817–827.
200. Michael, D.; Benjamin, I., Solute Orientational Dynamics and Surface Roughness of Water/Hydrocarbon Interfaces *J. Phys. Chem.* **1995**, 99, 1530-1536.
201. Luo, G.; Malkova, S.; Pingali, S. V.; Schultz, D. G.; Lin, B.; Meron, M.; Benjamin, I.; Vanysek, P.; Schlossman, M. L., *J. Phys. Chem. B* **2006**, 110, 4527-4530.
202. Benjamin, I., Polarity of the water/octanol interface. *Chem. Phys. Lett.* **2004**, 393, 453–456.
203. Linse, P., Monte Carlo simulation of liquid–liquid benzene–water interface. *J. Chem. Phys.* **1987**, 86, 4177 – 4187.
204. Sood, D. D.; Patil, S. K., Chemistry of nuclear fuel reprocessing: Current status. *J. Radioanal. Nucl. Chem.* **1996**, 203, 547 - 573.

205. Grenthe, I.; Fuger, J.; Konings, R.; Lemire, R.; Muller, A.; Nguyen-Trung, C.; Wanner, H.; Wanner, H.; Forest, I., *Chemical Thermodynamics of Uranium*. Elsevier Science Publishers; Amsterdam (Netherlands), **1992**.
206. Bühl, M.; Wipff, G., Insights into Uranyl Chemistry from Molecular Dynamics Simulations. *Chem. Phys. Chem.* **2011**, 12, 3095 - 3105.
207. Rai, N.; Tiwari, S. P.; Maginn, E. J., Force Field development for Actinyl Ions via Quantum Mechanical Calculations: An Approach to Account for Many Body Solvation Effects. *J. Phys. Chem. B* **2012**, 116, 10885 - 10897.
208. Kerisit, S.; Liu, C., Structure, Kinetics, and Thermodynamics of the Aqueous Uranyl(VI) Cation. *J. Phys. Chem. A* **2013**, 117, 6421 - 6432.
209. Guilbaud, P.; Wipff, G., Force field representation of the UO_2^{2+} cation from free energy MD simulations in water. Tests on its 18-crown-6 and NO_3^- adducts, and on its calix [6]arene 6- and CMPO complexes, (THEOCHEM). *J. Mol. Struct.* **1996**, 366, 55 - 63.
210. Guilbaud, P.; Wipff, G., Hydration of UO_2^{2+} Cation and Its NO_3^- and 18-Crown-6 Adducts Studied by Molecular Dynamics Simulations. *J. Phys. Chem.* **1993**, 97, 5685 - 5692.
211. Frick, R. J.; Hofer, T. S.; Pribil, A. B.; Randolph, B. R.; Rode, B. M., Structure and Dynamics of the UO_2^{2+} Ion in Aqueous Solution: An Ab Initio QMCF MD Study. *J. Phys. Chem. A* **2009**, 113, 12496 - 12503.
212. Frick, R. J.; Hofer, T. S.; Pribil, A. B.; Randolph, B. R.; Rode, B. M., Structure and dynamics of the UO_2^{2+} ion in aqueous solution: an ab initio QMCF-MD study. *Phys. Chem. Chem. Phys.* **2010**, 12, 11736 - 11743.
213. Pomogaev, V.; Tiwari, S. P.; Rai, N.; Goff, G. S.; Runde, W.; Schneider, W. F.; Maginn, E. J., Development and application of effective pairwise potentials for UO_2^{n+} , NpO_2^{n+} ,

- PuO_2^{n+} , and AmO_2^{n+} ($n = 1, 2$) ions with water. *Phys. Chem. Chem. Phys.* **2013**, 15, 15954-15963.
214. Tiwari, S. P.; Rai, N.; Maginn, E. J., Dynamics of actinyl ions in water: a molecular dynamics simulation study. *Phys. Chem. Chem. Phys.* **2014**, 16, 8060 - 8069.
215. Bühl, M.; Diss, R.; Wipff, G., Coordination Environment of Aqueous Uranyl(VI) Ion. *J. Am. Chem. Soc.* **2005**, 127, 13506 - 13507.
216. Bühl, M.; Kabrede, H., Mechanism of Water Exchange in Aqueous Uranyl(VI) Ion. A Density Functional Molecular Dynamics Study. *Inorg. Chem.* **2006**, 45, 3834 - 3836.
217. Bühl, M.; Kabrede, H.; Diss, R.; Wipff, G., Effect of hydration on coordination properties of uranyl (VI) complexes. A first-principles molecular dynamics study. *J. Am. Chem. Soc.* **2006**, 128, 6357 - 6368.
218. Vallet, V.; Wahlgren, U.; Schimmelpfennig, B.; Szabó, Z.; Grenthe, I., The Mechanism of Water Exchange in $[\text{UO}_2(\text{H}_2\text{O})_5]^{2+}$ and $[\text{UO}_2(\text{oxalate})_2(\text{H}_2\text{O})]^{2-}$, as Studied by Quantum Chemical Methods. *J. Am. Chem. Soc.* **2001**, 123, 11999 - 12008.
219. Vallet, V.; Privalov, T.; Wahlgren, U.; Grenthe, I., The Mechanism of Water Exchange in $\text{AmO}_2(\text{H}_2\text{O})_5^{2+}$ and in the Isoelectronic $\text{UO}_2(\text{H}_2\text{O})_5^+$ and $\text{NpO}_2(\text{H}_2\text{O})_5^{2+}$ Complexes as Studied by Quantum Chemical Methods. *J. Am. Chem. Soc.* **2004**, 126, 7766 - 7767.
220. Hagberg, D.; Karlström, G.; Roos, B. O.; Gagliardi, L., The Coordination of Uranyl in Water: A Combined Quantum Chemical and Molecular Simulation Study. *J. Am. Chem. Soc.* **2005**, 127, 14250 - 14256.
221. Spencer, S.; Gagliardi, L.; Handy, N. C.; Ioannou, A. G.; Skylaris, C.; Willetts, A.; Simper, A. M., Hydration of UO_2^{2+} and PuO_2^{2+} . *J. Phys. Chem. A* **1999**, 103, 1831 - 1837.

222. Chopra, M.; Choudhury, N., Effect of Uranyl Ion Concentration on Structure and Dynamics of Aqueous Uranyl Solution: A Molecular Dynamics Simulation Study. *J. Phys. Chem. B* **2014**, 118, 14373 - 14381.
223. Das, A.; Ali, S. M., Understanding of Interfacial Tension and Interface Thickness of Liquid/Liquid Interface at a Finite Concentration of Alkyl Phosphate by Molecular Dynamics Simulation. *J. Mol. Liq.* **2019**, 277, 217 - 232.
224. McCall, D. W.; Douglass, D. C., The Effect of Ions on the Self-Diffusion of Water. I. Concentration Dependence. *J. Phys. Chem.* **1965**, 69, 2001 - 2011.
225. Vallet, V.; Wahlgren, U.; Schimmelpfennig, B.; Moll, H.; Szabó, Z.; Grenthe, I., Solvent Effects on Uranium(VI) Fluoride and Hydroxide Complexes Studied by EXAFS and Quantum Chemistry. *Inorg. Chem.* **2001**, 40, 3516 - 3525.
226. Allen, P. G.; Bucher, J. J.; Shuh, D. K.; Edelstein, N. M.; Reich, T., Investigation of Aquo and Chloro Complexes of UO_2^{2+} , NpO_2^+ , Np^{4+} , and Pu^{3+} by X-ray Absorption Fine Structure Spectroscopy. *Inorg. Chem.* **1997**, 36, 4676 - 4683.
227. Wahlgren, U.; Moll, H.; Grenthe, I.; Schimmelpfennig, B.; Maron, L.; Vallet, V.; Gropen, O., Structure of Uranium(VI) in Strong Alkaline Solutions. A Combined Theoretical and Experimental Investigation. *J. Phys. Chem. A* **1999**, 103, 8257 - 8264.
228. Thompson, H. A.; Brown, G. E.; Parks, G. A., XAFS spectroscopic study of uranyl coordination in solids and aqueous solution. *Am. Mineral.* **1997**, 82, 483 - 496.
229. Neufeind, J.; Soderholm, L.; Skanthakumar, S., Experimental Coordination Environment of Uranyl(VI) in Aqueous Solution. *J. Phys. Chem. A* **2004**, 108, 2733 - 2739.
230. Sémon, L.; Boehme, C.; Billard, I.; Hennig, C.; Lützenkirchen, K.; Reich, T.; Rossberg, A.; Rossini, I.; Wipff, G., Do Perchlorate and Triflate Anions Bind to the Uranyl Cation in an

Acidic Aqueous Medium? A Combined EXAFS and Quantum Mechanical Investigation. *Chem. Phys. Chem.* **2001**, 2, 591 - 598.

231. Hennig, C.; Tutschku, J.; Rossberg, A.; Bernhard, G.; Scheinost, A. C., Comparative EXAFS Investigation of Uranium(VI) and -(IV) Aquo Chloro Complexes in Solution Using a Newly Developed Spectroelectrochemical Cell. *Inorg. Chem.* **2005**, 44, 6655 - 6661.

232. Antonio, R.; Soderholm, L.; Williams, C. W.; Blaudeau, J. P.; Bursten, B. E., Neptunium redox speciation. *Radiochim. Acta* **2001**, 89, 17 - 25.

233. Tsushima, S., Hydration and Water-Exchange Mechanism of the UO_2^{2+} Ion Revisited: The Validity of the "n + 1" Model. *J. Phys. Chem. A* **2007**, 111, 3613 - 3617.

234. Nichols, P.; Bylaska, E. J.; Schenter, G. K.; de Jong, W., Equatorial and Apical Solvent Shells of the UO_2^{2+} Ion. *J. Chem. Phys.* **2008**, 128, 124507.

235. Soderholm, L.; Skanthakumar, S.; Neufeind, J., Determination of Actinide Speciation in Solution Using High-Energy X-ray Scattering. *Anal. Bioanal. Chem.* **2005**, 383, 48 - 55.

236. Aaberg, M.; Ferri, D.; Glaser, J.; Grenthe, I., Structure of the Hydrated Dioxouranium (VI) Ion in Aqueous Solution. An X-ray Diffraction and ^1H NMR Study. *Inorg. Chem.* **1983**, 22, 3986 - 3989.

237. Marcus, Y., Some thermodynamic data concerning the dioxouranium(VI) ion and its compounds and reactions. *J. Inorg. Nucl. Chem.* **1975**, 37, 493 - 501.

238. Gibson, J. K.; Haire, R. G.; Santos, M.; Marçalo, J.; Pires de Matos, A., Oxidation Studies of Dipositive Actinide Ions, An^{2+} (An = Th, U, Np, Pu, Am) in the Gas Phase: Synthesis and Characterization of the Isolated Uranyl, Neptunyl, and Plutonyl Ions $\text{UO}_2^{2+}(\text{g})$, $\text{NpO}_2^{2+}(\text{g})$, and $\text{PuO}_2^{2+}(\text{g})$. *J. Phys. Chem. A* **2005**, 109, 2768 - 2781.

239. Tissandier, M. D.; Cowen, K. A.; Feng, W. Y.; Gundlach, E.; Cohen, M. H.; Earhart, A. D.; Coe, J. V.; Tuttle, T. R., The Proton's Absolute Aqueous Enthalpy and Gibbs Free Energy of Solvation from Cluster-Ion Solvation Data. *J. Phys. Chem. A* **1998**, 102, 7787 - 7794.
240. Halliwell, H. F.; Nyburg, S. C., Enthalpy of hydration of the proton. *Trans. Faraday Soc.* **1963**, 59, 1126 - 1140.
241. Sahu, P.; Ali, S. M., The entropic forces and dynamic integrity of single file water in hydrophobic nanotube confinements. *J. Chem. Phys.* **2015**, 143, 184503 (1 - 14).
242. Chopra, M.; Choudhury, N., Molecular dynamics simulation study of distribution and dynamics of aqueous solutions of uranyl ions: the effect of varying temperature and concentration. *Phys. Chem. Chem. Phys.* **2015**, 17, 27840 - 27850.
243. Prausnitz, J. M.; Lichtenthaler, R. N.; de Azevedo, E. G., *Molecular Thermodynamics of Fluid-Phase Equilibria*. Prentice Hall: NJ, **1998**.
244. D'Agostino, C.; Harris, R. C.; Abbott, A. P.; Gladden, L. F.; Mantle, M. D., Molecular Motion and Ion Diffusion in Choline Chloride Based Deep Eutectic Solvents Studied by 1h Pulsed Field Gradient NMR Spectroscopy. *Phys. Chem. Chem. Phys.* **2011**, 13, 21383 - 21391.
245. Brooker, M. H.; Huang, C. B.; Sylwestrowicz, J., Raman spectroscopic studies of aqueous uranyl nitrate and perchlorate systems. *J. Inorg. Nucl. Chem.* **1980**, 42, 1431 - 1440.
246. Nguyen Trung, C.; Begun, G. M.; Palmer, D. A., Aqueous uranium complexes. 2. Raman spectroscopic study of the complex formation of the dioxouranium(VI) ion with a variety of inorganic and organic ligands. *Inorg. Chem.* **1992**, 31, 5280 - 5287.
247. Chopra, M.; Choudhury, N., Molecular dynamics simulation study of hydration of uranyl nitrate in supercritical water: Dissecting the effect of uranyl ion concentration from solvent density. *Chem. Phys.* **2017**, 495, 48 - 58.

-
248. Hauner, I. M.; Deblais, A.; Beattie, J. K.; Kellay, H.; Bonn, D., The Dynamic Surface Tension of Water. *J. Phys. Chem. Lett.* **2017**, 8, 1599 - 1603.
249. Ismail, A. E.; Grest, G. S.; Stevens, M. J., Capillary waves at the liquid-vapor interface and the surface tension of water. *J. Chem. Phys.* **2006**, 125, 014702.
250. Chen, F.; Smith, P. E., Simulated surface tensions of common water models. *J. Chem. Phys.* **2007**, 126, 221101.
251. Shi, B.; Sinha, S.; Dhir, V. K., Molecular dynamics simulation of the density and surface tension of water by particle-particle particle-mesh method. *J. Chem. Phys.* **2006**, 124, 204715.
252. Lü, Y. J.; Wei, B., Second inflection point of water surface tension. *Appl. Phys. Lett.* **2006**, 89, 164106.
253. Grant, W. E.; Darch, W. J.; Bowden, S. T.; Jones, W. J., The surface tension and viscosity of solutions of uranyl salts. *J. Phys. Chem.* **1948**, 52, 1227 - 1236.
254. Wang, X.; Chen, C.; Binder, K.; Kuhn, U.; Pöschl, U.; Su, H.; Cheng, Y., Molecular dynamics simulation of the surface tension of aqueous sodium chloride: from dilute to highly supersaturated solutions and molten salt. *Atmos. Chem. Phys.* **2018**, 18, 17077 - 17086.
255. Weast, R. C., *CRC Handbook of Chemistry and Physics*. CRC Press: Boca Raton, **1986**.
256. Ben-Naim, A., *Molecular Theory of Solutions*. Oxford University Press: New York, **2006**; pp 56 - 75.
257. Das, A.; Ali, S. M., Unusual behaviour of Stokes–Einstein relation in liquid mixtures. *AIP Advances* **2020**, 10, 045327 (1-10).

APPENDIX

Table A1: Partial atomic charges on 44 atoms of TBP

TBP				
Atom	Mulliken	Löwdin	NPA	ChelpG
P	1.11449	0.75758	2.54813	1.199
O2	-0.48352	-0.43638	-1.03515	-0.647
OS ₁	-0.50244	-0.24731	-0.86562	-0.370
OS ₂	-0.51587	-0.26790	-0.87251	-0.485
OS ₃	-0.47766	-0.23983	-0.86079	-0.502
C1	0.218	0.07962	-0.05113	-0.0296
H1	0.02373	0.10026	0.20285	0.0803
H2	0.02148	0.10017	0.20562	0.0702
C2	0.21673	-0.08825	-0.05203	0.2954
H3	0.01634	0.10089	0.1992	-0.0077
H4	0.0276	0.10498	0.21125	-0.0015
C3	0.22153	-0.08463	-0.05195	-0.2933
H5	0.02279	0.10878	0.20935	-0.005
H6	0.00875	0.09261	0.19717	-0.0394
C4	-0.00441	-0.19799	-0.45048	-0.114
C5	-0.03733	-0.19194	-0.43111	0.3051
H7	0.00348	0.10974	0.2238	0.0024
H8	0.00555	0.10041	0.21793	0.0402
H9	0.00268	0.09743	0.21244	-0.0486
H10	0.01542	0.10424	0.21904	-0.0672

C6	0.00787	-0.31865	-0.62693	-0.3246
H11	0.00894	0.10781	0.20892	0.0693
H12	0.00962	0.10348	0.20981	0.0708
H13	0.01353	0.10941	0.21908	0.0719
C7	-0.00484	-0.18899	-0.45062	-0.0189
C8	-0.03886	-0.18347	-0.43288	0.2905
H14	0.01354	0.1025	0.22334	0.0119
H15	0.00169	0.10126	0.22247	-0.0208
H16	0.02197	0.09958	0.22471	-0.0397
H17	-0.00429	0.09224	0.20782	-0.0491
C9	0.00821	-0.31134	-0.62688	-0.3505
H18	0.01374	0.10393	0.2119	0.0797
H19	0.00669	0.09893	0.20762	0.075
H20	0.01356	0.11191	0.21911	0.0712
C10	-0.00674	-0.19516	-0.45051	0.0116
C11	-0.03241	-0.18615	-0.43275	0.2672
H21	0.00197	0.10726	0.22287	-0.0009
H22	0.00703	0.09924	0.21919	0.0163
H23	0.00562	0.0968	0.21408	-0.0427
H24	0.01787	0.10454	0.22365	-0.0462
C12	0.00569	-0.31016	-0.6272	-0.2836
H25	0.00711	0.104	0.20775	0.0501
H26	0.00931	0.1003	0.20926	0.055
H27	0.01586	0.10748	0.22017	0.0679

Table A2: Partial atomic charges on 53 atoms of TiAP

TiAP				
Atom	Mulliken	Löwdin	NPA	ChelpG
P	0.87129	1.17435	2.50370	1.2561
O2	-0.47594	-0.57325	-1.06142	-0.6595
OS ₁	-0.35822	-0.37738	-0.80729	-0.5337
OS ₂	-0.35002	-0.36331	-0.79896	-0.4351
OS ₃	-0.31221	-0.35876	-0.79283	-0.4375
C1	-0.41556	-0.17103	-0.60829	-0.427
C2	-0.06573	-0.13728	-0.21115	0.4273
C3	-0.17394	-0.13663	-0.40115	-0.2924
C4	-0.17558	0.01852	-0.06738	-0.1125
C5	-0.13148	0.01648	-0.07097	0.1583
C6	-0.18282	-0.13531	-0.40297	0.2754
C7	-0.075	-0.1336	-0.20498	-0.1468
C8	-0.35045	-0.1685	-0.58785	0.6197
C9	-0.15819	0.01544	-0.06451	-0.3429
C10	-0.17455	-0.13498	-0.39947	0.1503
C11	-0.06784	-0.1365	-0.2145	-0.2312
C12	-0.34953	-0.16641	-0.58637	0.4325
H1	0.15655	0.06639	0.18928	0.0277
H2	0.14075	0.06518	0.18133	0.0292
H3	0.10842	0.0772	0.20199	0.0146
H4	0.11318	0.0738	0.20226	0.0318
C13	-0.34959	-0.1672	-0.58593	-0.247
H5	0.1389	0.07257	0.19813	-0.0488

H6	0.11604	0.06868	0.20524	0.0864
H7	0.17954	0.07701	0.22972	0.123
H8	0.10011	0.06365	0.18998	0.0823
H9	0.14716	0.06322	0.1839	-0.0332
H10	0.13504	0.06135	0.17923	0.0335
H11	0.10862	0.0768	0.20121	-0.011
H12	0.11508	0.07549	0.20429	0.0282
H13	0.14757	0.07835	0.20781	-0.1246
C14	-0.40502	-0.16806	-0.5982	-0.3712
H14	0.12078	0.06769	0.20475	0.0583
H15	0.10245	0.06476	0.19277	0.0478
H16	0.11732	0.06683	0.2031	0.0402
H17	0.11386	0.06011	0.16799	0.0379
H18	0.15936	0.0707	0.20163	0.0512
H19	0.11567	0.07898	0.20819	0.0506
H20	0.10999	0.07644	0.20261	0.0686
H21	0.10213	0.06712	0.18407	-0.0621
C15	-0.35075	-0.16817	-0.59522	-0.3153
H22	0.12055	0.06734	0.20427	0.0778
H23	0.10799	0.06721	0.19659	0.0746
H24	0.11564	0.0654	0.20099	0.0749
H25	0.12258	0.06959	0.20719	0.0535
H26	0.14049	0.06747	0.20525	0.0788
H27	0.10722	0.06537	0.19295	0.0516
H28	0.11232	0.06385	0.19849	0.0465
H29	0.13978	0.06879	0.21685	0.0259
H30	0.09924	0.06682	0.19545	0.0559

H31	0.121	0.06728	0.20448	0.0614
H32	0.10333	0.06507	0.19344	0.0577
H33	0.11244	0.06508	0.20029	0.0425

Table A3: Partial atomic charges on 26 atoms of TEP

TEP				
Atom	Mulliken	Löwdin	NPA	ChelpG
P	1.08359	0.90211	2.47744	1.1574
O2	-0.48319	-0.47886	-1.04638	-0.6410
OS ₁	-0.49204	0.27877	-0.80102	-0.4557
OS ₂	-0.46789	-0.27129	-0.78151	-0.5051
OS ₃	-0.50427	-0.2936	-0.78892	-0.5105
C1	-0.0083	-0.06327	-0.6111	-0.3114
C2	0.18941	0.087	-0.07366	0.383
C3	0.18718	0.08568	-0.07386	0.4508
C4	-0.00367	-0.06228	-0.6109	-0.212
C5	0.18402	0.084	-0.07041	0.3641
C6	-0.00695	-0.06405	-0.61105	-0.2459
H1	0.02967	0.031	0.2094	0.0714
H2	0.02257	0.02732	0.21384	0.0756
H3	0.02617	0.01606	0.17548	0.0033
H4	0.01683	0.01484	0.18771	-0.0255
H5	0.01725	0.03162	0.1703	0.0708
H6	0.02346	0.02784	0.1945	0.0924
H7	0.02043	0.01441	0.18182	-0.0501
H8	0.01166	0.01075	0.17955	-0.0323

H9	0.01509	0.03076	0.21361	0.0381
H10	0.02529	0.02891	0.20811	0.0596
H11	0.01127	0.01223	0.21421	-0.0004
H12	0.03189	0.01701	0.21135	0.0006
H13	0.01797	0.03178	0.21252	0.0478
H14	0.02278	0.02792	0.20951	0.0787
H15	0.02977	0.0309	0.20946	0.0964

Table A4: Partial atomic charges on 38 atoms of n-dodecane

n-dodecane	
Atom	Charges
C1	-0.59716
C2	-0.41237
C3	-0.40859
C4	-0.40501
C5	-0.40835
C6	-0.40867
C7	-0.40395
C8	-0.40435
C9	-0.41009
C10	-0.40693
C11	-0.4068
C12	-0.59772
H1	0.19928
H2	0.1997
H3	0.20718

H4	0.20304
H5	0.20145
H6	0.2074
H7	0.20072
H8	0.20152
H9	0.20777
H10	0.20058
H11	0.20277
H12	0.20314
H13	0.20074
H14	0.20759
H15	0.20123
H16	0.20161
H17	0.20791
H18	0.20079
H19	0.20323
H20	0.20128
H21	0.2008
H22	0.20188
H23	0.20195
H24	0.2073
H25	0.1996
H26	0.19958

Table A5: van der Waals and charge parameters of water model

Water (H₂O) SPC/E Model			
Atoms	Sigma (nm)	Epsilon (kJ/mole)	Charge (e)
OW	0.316557	0.650194	-0.8476
HW	0	0	-0.4238
Water (H₂O) Mulliken Model			
Atoms	Sigma (nm)	Epsilon (kJ/mole)	Charge (e)
OW	0.316557	0.650194	-0.52925
HW	0	0	0.26462

Table A6: van der Waals and charge parameters of nitric acid

Atoms	Sigma (nm)	Epsilon (kJ/mole)	Charge (e)
N1	0.33	0.71128	0.21529
OA	0.296	0.87864	-0.12591
OA	0.312	0.71128	-0.21041
OA	0.296	0.87864	-0.17204
HA	0.25	0.12552	0.29307

Table A7: van der Waals parameters of Uranyl ion

Atoms	Sigma (nm)	Epsilon (kJ/mole)
U	0.295	0.53
Ou	0.383	0.57